Faculty of Engineering
Department of Mechanical Engineering

ADVANCED BIOFUELS: OXIDATION KINETICS OF METHYL PENTANOATE AND LIFE CYLCE ASSESSMENT OF TRIACETIN

Thesis submitted in fulfilment of the requirements
of the degree of Doctor in Engineering Sciences

Stefanie Van Damme

Promotors:	prof. dr. ir. Francesco Contino	Vrije Universiteit Brussel
	prof. dr. ir. HervJeanmart	Université catholique de Louvain-la-Neuve
Jury:	prof. dr. ir. Burak Atakan	Universität Duisburg-Essen
	prof. dr. ir. Guillaume Dayma	CNRS Orléans Campus
	dr. ir. Véronique Dias	Université catholique de Louvain-la-Neuve
	prof. dr. ir. Annick Hubin	Vrije Universiteit Brussel
	prof. dr. ir. Roger Vounckx	Vrije Universiteit Brussel

Printed by
Crazy Copy Center Productions
VUB Pleinlaan 2, 1050 Brussel
Tel / fax : +32 2 629 33 44
crazycopy@vub.ac.be
www.crazycopy.be

Dankwoord

Na meer dan vijf jaar is het eindelijk af: mijn doctoraat. Waarin mijn werk over biobrandstoffen staat beschreven. Ik heb geprobeerd mijn mening en bevindingen neer te schrijven. Desalniettemin, dit boek zou niet bestaan zonder de hulp van enkele personen.

Eerst en vooral wil ik mijn promotoren bedanken, Francesco Contino en Hervé Jeanmart. Francesco is er al vanaf het begin van mijn traject bij. We zijn samen gestart aan de VUB en samen probeerden we onze weg te vinden in het kluwen van IWT voorstellen en de werking van de VUB. Twee jaar later, werd Hervé mijn co-promotor, omdat ik experimenteel werk verrichtte op de Botha-Spalding brander in de UCL. Ik zou graag beide bedanken voor de soms urenlange discusssies, het ordenen van mijn gedachten en mij te leren hoe ik mijn resultaten moet presenteren aan het publiek.

De volgende persoon die ik bedank is Véronique Dias. Zij is officieel niet mijn promotor, maar haar expertise in het gebruik van de Botha-Spalding brander is onnavolgbaar. Dankuwel, om mij te leren werken met the experimentele setup en de hulp bij het verwerken van de data.

Zoals de meeste van jullie wel weten: experimenten gaan nooit volgens plan en het oplossen van defecten is een deel van het werk. Gelukkig kon ik rekenen op de hulp van de schitterende UCL techniekers. Merci, Julien, Lily and Frank voor het dichten van lekken, het verhelpen van elektrische storingen en het vervangen van vele gasflessen.

Ik spendeerde niet al mijn tijd naast the brander, ik had ook mijn hoofdburea op de VUB. Op mijn eerste dag aan de VUB, kreeg ik een bureau toegewezen naast mijn mede thermodynamica liefhebber Ward. De daaropvolgende week, werd er een band gesmeed tijdens een autorit naar Brussel, omdat de NMBS staakte op de dag dat ik voor het eerst les moest geven. Het thermodynamica team werd later versterkt door Marina. Die ik me zal herinneren voor haar liefde voor het verbeteren van energy efficiënties en planten.

Naast het thermodynamica team moet ik ook de brunch ladies bedanken. Greet, Karen, Laura en Romy: dankuwel, voor de diepgaande discussies over het echte leven en natuurlijk voor de gezamelijke feestjes.

Niet alle personen die hebben bijgedragen, zijn gerelateerd aan een universiteit. Eerst en vooral wil ik mijn mama bedanken om mij de kans te geven mijn unversiteitsdroom na te streven. Ik wil ook mijn papa bedanken, ook al is hij niet meer onder ons. Hij heeft mij gewezen op het belang van het milieu en hij heeft mij aangespoord om te werken aan een duurzame toekomst. De volgende persoon die ik wil bedanken is mijn partner Dirk. We hebben elkaar voor de eerste keer ontmoet in Brussel en vier jaar later gaat het nog steeds goed. Ik wil ook mijn pluizige huisgenoot Wartje* bedanken, om mijn wekker, luisterend oor en zetelpartner te zijn.

Ik ben bijna op het einde van mijn pagina, dus het is tijd om iedereen te bedanken die er niet op past. Dank u wel aan iedereen om deel uit te maken van mijn leven en zo indirect te helpen aan dit werk.

* Enige gelijkenis op bestaande personen is puur toeval.

Acknowledgement

After more than five years, it is finally there: my PhD, containing my work on biofuels. I tried to put my own opinion and findings in this book. Nevertheless, this book would be non-existing without the help of some people.

First of all I want to thank my promotors, Francesco Contino and Herve Jeanmart. Francesco was present at the beginning of my journey. We were both starting at the VUB. Together we tried to understand the rules of IWT proposals and the VUB life. Two years later, Hervé was added as co-promotor since I did some experimental work on the Botha-Spalding burner at the UCL and his expertise on combustion kinetics was more than welcome. I like to thank both of them for our, sometimes hours-long, discussions, ordening my thaughts and learning me how to present my results to the public.

The next person that I need to thank is Véronique Dias. She is officially not my promotor, but her expertise on the Botha-Spalding burner is far beyond the expertise of anyone else at the UCL. Thank you for learning me how the experimental setup works and helping me by processing the data.

As most of you know, experimental work goes never as planned and fixing breakdowns are part of the job. Luckely, I could count on the help of the wonderfull technicians at the UCL. Merci, Julien, Lily and Frank for solving leakages, electrical problems and changing many gas bottles.

I did not spend all my time next to the burner in UCL, I also had my main office desk at VUB. The first day I arrived at the VUB, I got an office with my fellow thermodynamic lover, Ward. The next week we already bonded during a car ride to Brussels, since the NMBS striked at the day I needed to teach my first WPO session. Our thermodynamica team was later reinforced by Marina. Who I will remember for her love for improving energy efficiency and plants.

Next to the thermodynamic team, I also want to thank the brunch ladies. Greet, Karen, Laura and Romy, thank you for the profound discussions about the real life and of course the parties together.

Not all the persons that contributed are related to an unversity. First of all, I want to thank my mama, for giving me the opportunity to follow my unversity dreams. I also want to thank my papa, even if he is not here with us anymore, to show me the importance of the environment and to nourish my will to work on a sustainable future. The next person that I want to thank is my partner Dirk. We have met each other in Brussel and four years later we are still going strong. I also need to thank my fluffy room mate, Wartje*, for being my alarm clock, listening ear and cuddling partner in crime.

I'm almost at the end of my page, so it is time to thank everyone that didn't fit on it. Thank you all for being a part of my life, helping indirectly with this work.

* Any ressemblance to an existing person is pure coincidence.

The authors thank the Région Wallonne (Belgium) for the financial support (Convention n°1250393). This project is also a part of the IEA (International Energy Agency) Implementing Agreement for Energy Conservation and Emission Reduction in Combustion.

Scientific Contributions

Papers

S. Van Damme, S. Bram and F. Contino, Comparison of biodiesel production scenarios with coproduction of triacetin according to energy and GHG emissions, *Energy Procedia* (61), 1852-1859, 2014

S. Van Damme, V. Dias, H. Jeanmart and F. Contino, Comparison between the Electrical Compensation Method and a Heat Transfer Model for radiation loss quantification by thermocouple measurements in high temperature flames, *Experimental Thermal and Fluid Science*, Under review

S. Van Damme, H. Jeanmart F. Contino, G. Dayma and V. Dias, Oxidation kinetics of methyl pentanoate for different combustion configurations, *Combustion and flame*, preparing for submission

Oral presentations at conferences

S. Van Damme, V. Dias, H. Jeanmart and F. Contino, Assessing radiation losses by temperature measurements in laminar flat flames, *Combura*, Netherlands, 2016

S. Van Damme, V. Dias, H. Jeanmart and F. Contino, Experimental and Kinetic Modeling of a Rich Methyl Pentanoate Flame at Low Pressure, 24^{th} *Journee des études of the Belgian Section of the Comubustion Institute*, Belgium, 2016

S. Van Damme and F. Contino, Energy Balance and Environmental Impact of Biodiesel from Algae with Co-production of Triacetin, 6^{th} *International Conference on Applied Energy*, Taiwan, 2014

S. Van Damme, S. Bram and F. Contino, Energy balance and environmental impact of biodiesel from algae with co-production of triacetin, 3^{th} *International Conference on Algal Biomass, Biofuels and Bioproducts*, Canada, 2013

Poster presentations at conferences

S. Van Damme, V. Dias, H. Jeanmart, F. Contino, Experimental and Kinetic Modelling of Methyl Pentanoate Flames at Low Pressure, 8^{th} *European Combustion Meeting*, Croatia, 2017

S. Van Damme, V. Dias, P. Bréquigny, H. Jeanmart, F. Contino, Comparison of different chemical kinetics modeling codes, 7^{th} *European Combustion Meeting*, Hungary, 2015

S. Van Damme, H. Mbuyi Katshiatshia Mukole, V. Dias, H. Jeanmart, F. Contino, Kinetic modeling of ethyl pentanoate combustion in laminar premixed flames, *Combura*, Netherlands, 2014

Abstract

Biofuels are a part of our current and future energy mix. Bioethanol and biodiesel are blend with our current fuels and despite the strong interest in electric cars, liquid fuels are still needed for heavy transport and aviation. A biofuel is sustainble as less Green House Gases (GHG) are emitted by it use and production compared to fossil fuels and no hazardous molecules and particles are formed by its combustion.

In this thesis two advanced biofuels are investigated: methyl pentanoate (MPE) and triacetin. Both are esters and MPE can be used in gasoline engines without any adjustment. While triacetin can be coproduced with biodiesel and can act as a fuel additive in diesel engines.

The combustion kinetics of MPE are investigated in this work. Investigating which molecules are formed by its combustion. Premixed laminar flat flames with different equivalence ratios were stabilized on a Botha-Spalding burner at a pressure of 55 mbar. The mole fraction profiles of stable species were measured with GC-FID/TCD and the temperature of the flame with a fine wire thermocouple. Radiation losses during the temperature measurements were corrected with both the Electrical Compensation Method (ECM) and a Heat Transfer Method (HTM) method. The corrected temperature profiles obtained with the HTM were used for simulation of the laminar flat flames. A kinetic model for the oxidation of MPE, proposed by Dayma et al., is used for the simulations. The kinetic mechanism is composed of 206 species and 1792 reactions. The OpensMOKE software is used for the simulations. Overall a good fit between experimental and simulated mole fraction profiles was found for the rich and stoichiometric MPE flames. The performance of the mechanism for other combustion configuration is also assessed and in the end some improvements for the kinetic mechanism are suggested.

In the second part, a life cycle assessment for the coproduction of biodiesel and triacetin is made regarding energy and GHG emissions. The system boundaries are set around the production reaction(s) and the production and recovery of the reactant. Data about energy needs and GHG emissions of the processes are extracted from the EcoInvent database. Four scenarios are compared with each other: the biodiesel production from algal oil (BD), and three triacetin coproduction routes: the catalytic interesterification reaction of algal oil with methyl acetate (IRc), the enzymatic interesterification reaction (IRe) and the biodiesel production followed by the esterification of glycerol with acetic acid (ER). The BD scenario scores best in terms of energy and GHG emissions compared to the coproduction scenarios. The main reason is the production of the needed reactants. The production of the reactant used in the coproduction routes consumes more energy and emits more GHG than the production of methanol. Nevertheless, the energy needed for production is less than the energy content of the fuel formed. For the IRe and IR scenarios Enery Return of Investment (EROI) greater than unity is found. Also no waste glycerol is formed with the coproduction reactions and more biofuels is formed, making the coproduction of triacetin a viable process.

Contents

List of Symbols and Acronyms

A pre-exponential or frequency factor of Arrhenius equation $(cm^3 \cdot mole^{-1}s^{-1})$

A_{TC} cross section thermocouple (m)

C correction factor Mass Flow Controller (-)

$C_{i,j}$ contribution of a reaction j to the consumption of species i (%)

E thermo-electric voltage (μV)

E_a activation energy (cal·mole^{-1})

$F_{i,j}$ contribution of a reaction j to the formation of species i (%)

I electrical current (A)

K_p equilibrium constant of a chemical reaction

L length thermocouple (m)

N correction factor that describes the transition from cylindrical to spherical configuration of the thermocouple (-)

R resistance (Ω)

R^2 coefficient of determination (-)

R_f flame radius (m)

R_u universal gas constante (J·mole^{-1} K^{-1})

S_u^0 Laminar flame speed (m·s^{-1})

T temperature (K)

T_i^* reduced temperature of species i

T_0 temperature of the surroundings of the assessed flame (K)

T_∞ temperature of the gas stream, is set to the adiabatic temperature (K)

T_c measured temperature in the flame (K)

T_g actual temperature of the flame (K)

T_m film temperature (K)

V volume (m^3)

X_{Ar} mole fraction argon (mole%)

Z_{rot} rotational relaxation collision number

ΔT_{corr} temperature correction (K)

$\Omega^{(2,2)*}$ collision integral

α polarizability of a molecule

δ dipole moment

δ_i^* reduced dipole moment of species i

$\dot{Q}_{\text{cat}}$ heat released on the thermocouple surface by catalytic reactions (W)

$\dot{Q}_{\text{cond}}$ conduction losses along the thermocouple wires (W)

$\dot{Q}_{\text{conv}}$ convective heat transfer from the flame to the thermocouple (W)

$\dot{Q}_{\text{rad}}$ radiation form the thermocouple to its surroundings (W)

ϵ emissivity (-)

ϵ_{LJ} Lennard-Jones potential well depth

η dynamic viscosity (Pa·s)

κ total stretch rate (s^{-1})

λ thermal conductivity of the fluid ($\text{W}\cdot\text{m}^{-1}\text{K}^{-1}$)

$\mathbb{h}_i$ specific enthalpy of species i

$\mathbb{s}_i$ specific entropy of species i

ϕ equivalence ratio (-)

ρ density (kg m^{-3})

ρ_R resistivity ($\mu\Omega$·cm)

σ Stefan-Botzmann constant ($5.67\cdot10^{-8} Js^{-1}m^{-2}K^{-4}$),

τ mean residence time (s)

b temperature dependency exponent of the Arrhenius equation

$c_{p,i}$ specific heat capacity of species i ($\text{J}\cdot\text{K}^{-1}\cdot\text{kg}^{-1}$)

d diameter thermocouple (m)

h heat transfer coefficient (W m^{-2} K^{-1})

k reaction rate of chemical reaction defined in the Arrhenius equation

k_B Boltzmann constant

n number of measurements (-)

p pressure (Pa)

r_{LJ} Lennard-Jones collision diameter

s standard deviation (-)

t time (s)

v velocity ($cm \cdot s^{-1}$)

w_i molecular weight of species i ($g \cdot mole^{-1}$)

AA acetic acid

AOR Alcohol to Oil Ratio

ASTM American Society for Testing and Materials

AU Absolute Uncertainty

BD biodiesel

CEM Controlled Evaporation and Mixing unit

CFPP Cold Filter Plugging Point

CI Confidence interval

COMR catalyst-to-oil molar ratio

CP Cloud Point

CTH Catalytic Transfer Hydrogenation

DC Direct Current

$\mathbf{E}_V$ the energy content per volume unit ($kJ \cdot Nm^3_{air}$)

ECM Electrical Compensation Method

EL ethyl levulinate

ER esterification reaction of glycerol

EROI Energy Return on Investment

FA Fatty Acid

FAME Fatty Acid Methyl Esters

FFA Free Fatty Acid

FID Flame Ionisation Detector

FS Full scale error

FTIR Fourier-Transform Infra Red spectroscopy

GC Gas Chromatography

GHG Green House Gases

GVL γ-valerolactone

GWP Global Warming Potential

HCCI Homogeneous Charge Compression Ignition

HMF 5-hydroxymethylfurfural

HTM Heat Transfer Model

IC internal combustion

ILUC Indirect Land Use Change

IRc catalytic interesterification

IRe enzymatic interesterification

JSR Jet Stirred Reactor

LA levulinic acid

LCA Life Cycle Assessement

LCIA Life Cycle Impact Assessment

LHV Lower Heating Value

LoD Limit of Detection

LoQ Limit of Quantification

M a neutral third-body that takes part in third body reactions

MA methyl acetate

MAOMR methyl acetate-to-oil molar ratio

ME methanol

MFC Mass Flow Controller

MPE methyl pentanoate

NEV Normalised Energy Value

NIST National Institute for Standards and Technology

NNEV Normalised Net Energy Value

NSC Normalised Sensitivity Coefficient

NTC Negative Temperature Coefficient

Nu Nusselt number

PA pentanoic acid

PAH poly-aromatic hydrocarbons

PBR photo-bioreactors

pdf probability density function

Pr Prandtl number

PRF Primary Reference Fuel

PSR Perfectly Stirred reactor

PUFA Poly-Unsaturated Fatty Acid

RCM Rapid Compression Machine

Rd Reading error

RE Relative error

Re Reynolds number

RF Response Factor

RT Retention Time

RU Relative Uncertainty

SC Sensitivity Coefficient

SCC Spherical Combustion Chamber

sccm standard cubic centimeters per minute

TCD Thermal Conductivity Detector

Tr triacetin

WCO Waste Cooking Oil

WHSV Weight Hourly Space Velocity

Introduction

Biofuels are derived from biomass and are seen as a vital part for the future energy mix. Every CO_2 molecule emitted by their combustion, is captured previously by photosynthesis, making their use carbon neutral. At the moment two kinds of biofuels are produced at industrial scale, namely bio-ethanol and biodiesel. These biofuels are mixable with gasoline and diesel respectively and can be used directly in internal combustion engines. Bio-ethanol is derived mostly by fermentation of sugar or starch rich biomass, while biodiesel is made from vegetable oils via transesterification.

However some disadvantages emerge for both types of biofuels. The main feedstock for both biofuels is high value biomass, like sugar rich biomass or vegetable oil. These types of biomass are edible, leading to the ethical debate if food can be used as fuel. Besides, in order to meet the demand, nature is converted to agricultural land. This land use change leads to an increase in Green House Gases (GHG) emissions, which can nullify the CO_2 neutrality of the biofuels. The increased production of biodiesel also led to an overproduction of the byproduct glycerol, causing its economic value to decline, making the glycerol stream nothing more than a waste stream.

Currently, research is focussing on second and third generation biofuels. Second generation biofuels are produced from lignocellulosic material. The lignocellulosic material can be straw or residues of food crops. The production of second generation biofuels uses biomass that is treated as waste. The whole plant is converted to biofuels and not only the parts with high chemical energy content and food properties. The feedstock for third generation biofuels are algae. In some circumstances the production of algae needs less water and nutrients than terrestrial plants and even a higher biomass yield is achieved.

In this thesis, two biofuels of the new generations are investigated: **pentanoates** and **triacetin**. Pentanoic acid can be formed by hydrolysis and hydrogenation of lignocellosic material and can be esterfied to the wanted pentanoates. The length of the alcohol used for esterification defines whether the pentanoate can replace gasoline (esterification with methanol and ethanol) or diesel (esterification with butanol, pentanol, etc.).

Triacetin can be formed by the esterification of glycerol, a byproduct of the biodiesel production, and acetic acid. A second option is to form biodiesel and triacetin directly, by an interesterification reaction. As feedstock for the biodiesel and triacetin production, the conventional vegetable oil cannot be used. To improve the sustainability of biodiesel, a change in feedstock and a new application or elimination of the formed glycerol is needed. Oil derived from algal biomass, non-edible plants or waste cooking oil, could be good substitute feedstock. Currently, glycerol is seen as a waste stream and esterfying it to triacetin, which can be mixed with biodiesel since they have the same functionality, can be a solution. An increase of 10% in energy content of the produced biofuel can be achieved in this way.

The sustainability of a biofuel is defined by its production process and its combustion kinetics. The biofuel is not sustainable when the production of the biofuel demands more energy than the chemical energy within the biofuel. Also the combustion kinetics of the biofuel are important. They can be used to assess the formation of hazardeous particles and molecules during the biofuel combustion.

In this thesis both requirements are investigated. The combustion kinetics of methyl pentanoate are assessed and a life cycle assessment of the triacetin production is conducted.

In the first Part of this thesis methyl pentanoate (MPE) is investigated. The performance of a kinetic mechanism proposed by Dayma [1] for the combustion of MPE is investigated against different combustion configurations. Data of homogeneours reactors and laminar

flames achieved by other research institutes or taken from literature are used.

We experimentally assessed ourself three flat laminar flames on a Botha-Spalding burner at a pressure of 55 mbar. The experimental setup is described in detail in Chapter 3. The equivalence ratio of the flames are 1.41, 1.15 and 0.88. Samples are taken throughout the laminar flames and analysed by Gas Chromatography followed by a Thermal conductivity Detector and a Flame Ionisation Detector (GC-TCD/FID). Fifteen stable species could be identified in the flame. The uncertainty on the measured mole fraction profiles is quantified to be 10% on the main species, 15% for H_2 and 30% for the intermediate species.

The temperature profile of the laminar flat flame is needed to simulate the flame. The temperature profiles are measured by a fine wire thermocouple of Platinum and Rhodium alloys (Type B). High measured flame temperature are achieved. A maximal temperature of 1765, 1844 and 1893 K is measured in the rich, stoichiometric and lean MPE flame respectively. When flame temperature are measured by a fine wire thermocouple, radiation losses occur and a correction for these losses need to be made. Different correction methods can be applied to correct for the losses. In this work the Electrical Compensation Method (ECM) and a Heat Transfer Model (HTM) are assessed. The HTM performed better, since all the assessed flames could be corrected by this method, while the ECM has a temperature limit of around 1400 K. The temperature measurements in the flames and the correction of the measured temperature is described in Chapter 5.

The laminar flat flames are simulated by the OpenSMOKE software and the simulated mole fraction profiles can be compared to the experimentally measured mole fraction profiles Next to the experimental data we gathered ourself, data of laminar MPE flames at a pressure of 27 mbar and atmospheric pressure, laminar flame velocities, Rapid Compression Machine (RCM) and Jet Stirred Reactors (JSR) are used to check the performance of the mechanism in a broad temperature and pressure range. The comparision between experimental data and simulations can be found in Chapter 6 and 7. Possibilities to improve the kinetic mechanism for the MPE combustion is also discussed in Chapter 7.

In the second Part of this thesis the production of triacetin is investigated. The production of triacetin needs to consume less energy than that there is produced as fuel additive. Therefore an energy balances is made for the different production options for triacetin described in literature.

Three coproduction routes for biodiesel and triacetin are investigated. The (1) catalytic and (2) enzymatic catalysed interesterification reaction of triglycerides with methyl acetate to form biodiesel and triacetin directly. The third option is to perform the conventional transesterification reaction to form biodiesel and glycerol and esterifying the glycerol with acetic acid to triacetin in a next step. The three coproduction routes are compared to the transesterification reaction in terms of fuel produced, energy needed for production and Green House Gas (GHG) emissions during production. Data from literature and the EcoInvent database is used to conduct these calculations.

Overall more biofuel is produced with the coproduction of triacetin. Nevertheless, since the production of the needed reactants, methyl acetate and acetic acid, need more energy compared to the reactant used for the transesterification reaction, methanol, a higher energy input is needed for the coproduction reactions per MJ biofuel produced. The same conclusion is also found for the GHG emissions. During the production of methyl acetate and acetic acid more GHG are emitted compared to the production of methanol, leading the more GHG emissions per MJ biofuel produced.

Part I

Validation kinetic model for methyl pentanoate

1 Part I Introduction

Pentanoates are seen as a new class of biofuels, which can be produced from lignocellulosic biomass with levulinic acid (LA), γ-valerolactone (GVL) and pentanoic acid (PA) as intermediate (Figure 1.1) [2, 3]. The total production process of pentanoates consists of four steps. The first step is the acid hydrolysis of lignocellulosic material to levulinic acid [4]. Different derivatives from levulinic acid have been proposed as biofuel types, like γ-valerolactone and methyl tetrahydrofuran [5, 6]. However these derivates do not mix as good as pentanoates with conventional fuels [3].

The second step in the production of pentanoates is the hydrogenation of levulinic acid to form γ-valerolactone, which is on its turn hydrogenated to pentanoic acid. The acid is then esterified in the final step with an alkyl group to form pentanoates. The full process is already commercialized under the name Biofine [2].

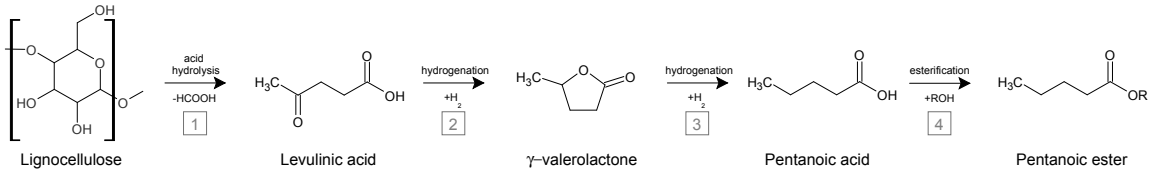

Figure 1.1: Pentanoates can be produced from lignocellosic material in four steps, with levulinic acid, γ-valerolactone and pentanoic acid as intermediates. [3]. The steps are discussed in detail in Chapter 2.

Pure pentanoates and mixtures of pentanoates with conventional fuels can be used in internal combustion engines [3, 7, 8]. In this part, three laminar methyl pentanoate (MPE) flames, at a pressure of 55 mbar, are investigated to validate a newly proposed kinetic mechanism for MPE by Dayma et al. [1]. The flames are stabilised on a Botha-Spalding burner [9] and spatial samples are extracted, separated by Gas Chromatography (GC) and analysed by Thermal Conductivity Detector (TCD) and Flame Ionisation Detector (FID) to achieve the mole fraction profiles. With GC, only stable species can be separated and in total 16 species have been identified. The experimental setup is described in Chapter 3. Special attention is given to an error and uncertainty analysis of the experimental results.

MPE is an ester with the potential to be used as a biofuel in spark ignition engines [10]. It is a short chain ester (Figure 1.2), with five carbon atoms in the acid chain and a methyl group in the alcohol chain. For the stoichiometric combustion of MPE eight molecules of oxygen are needed:

$$C_6H_{12}O_2 \; + \; 8 \; O_2 \; \rightarrow \; 6 \; CO_2 + \; 6 \; H_2O. \tag{1.1}$$

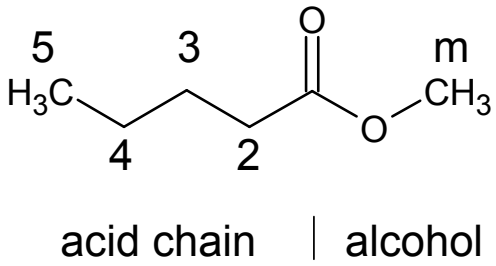

Figure 1.2: Chemical structure of MPE, with the labels for the carbon atoms. The carbon of the carbonyl group is denoted with 1.

Table 1.1: The characteristics of three assessed MPE flames. The rich, stoichiometric and lean MPE flame have an equivalence ratio of 1.41, 1.15 and 0.88 respectively.

ϕ	**MPE (mole%)**	**O_2 (mole%)**	**Ar (mole%)**	**v ($cm \cdot s^{-1}$)**	$\dot{m}$ **($g \cdot s^{-1}$)**	**T_{ad}** (K)
1.41	4.4	24.8	70.8	45.0	0.2260	2461
1.15	4.1	28.8	67.1	47.5	0.2358	2560
0.88	3.8	34.5	61.7	51.7	0.2521	2564

The characteristics of the three assessed MPE flames can be found in Table 1.1. The exact composition, argon dilution, initial flow velocity and mass flow are given.

The equivalence ratio of a MPE flame is defined as

$$\phi = \frac{X_{fuel}/X_{O_2}}{1/8} \tag{1.2}$$

with X_{fuel} and X_{O_2} the initial mole fraction of the fuel and oxidizer. The equivalence ratio of the rich flame is 1.41. The second and third flame have an equivalence ratio of 1.15 and 0.88. Stabilising at stoichiometric conditions proved to be difficult. Therefore a slighter richer and leaner flame has been investigated.

The mass flow of the fuel was kept constant, just as the argon flow rate (5.22 $L_N \cdot min^{-1}$) for the three flames and only the oxygen flow rate was varied from 1.82 to 3.2 $L_N \cdot min^{-1}$. Hereby, flames with varying equivalence ratios, argon dilutions and total mass flows were achieved.

The mole fraction profiles of the assessed laminar premixed flames are simulated with the OpenSMOKE software [11]. Some of the equations behind the simulations are stated in Chapter 4. Also the methods used for the sensitivity and reaction flow analysis are stated in this chapter.

To run simulations of a flat laminar premixed flame, the experimental temperature profile of the flame is needed as an input. The temperature profiles of the three flames were measured with a Type B thermocouple. If the temperature profile is measured with a fine wire thermocouple, a correction for radiation losses is needed. Previously, the ECM was used to quantify the correction experimentally. Nevertheless, due to the high measured temperature of 1844 and 1893 K in the near stoichiometric and lean MPE flame, ECM was not applicable. The temperature correction was therefore computed by a HTM based on forced convection over a wire. For the HTM model, the thermocouples emissivity and the heat transfer coefficient

of the fluid were quantified. The temperature measurement and correction are explained in detail in Chapter 5.

The validation of the MPE kinetic mechanism proposed by Dayma is performed in Chapter 6. The experimental results of the investigated MPE flames are compared with simulations. Also experimental data for other combustion configuration is assessed, together with the results of the sensitivity and reaction flow analysis in Chapter 7. Some improvements for the assessed kinetic mechanism are also stated in this Chapter.

2
Pentanoates as biofuels

The use of pentanoates as biofuels is studied in literature. In the next sections the production process of pentanoates is explained in detail, together with their use in conventional internal combustion engines and the available kinetic mechanisms to simulate their combustion.

2.1 Production process

Three main intermediates are formed by the production of pentanoates from lignocellulosic material: 5-hydroxymethylfurfural (HMF), levulinic acid (LA) and γ-valerolactone (GVL). HMF is produced from the sugar molecules present in the lignocellolosic material by hydrolysis. Pretreatment of the lignocellulosic material is needed to release the sugar molecules. The pretreatment can be mechanical, physical, chemical or biological and has as main purpose to remove the lignin sheet around the cellulose and hemicellulose molecules [12].
Next, the sugar molecules from the biomass are extracted by hydrolysis. The biomass is placed into water and the hydrogen atoms of the water molecule attack the glycosidic oxygen of the cellulose molecule. Cellulose is not easy to hydrolyse and to speed up the reaction the temperature and pressure can be raised or an acidic catalyst or cellulase can be added. Mostly an acid catalyst is added to the reaction mixture. Different acid catalysts options are investigated in literature. The applied process parameters are depending on the characteristics of the biomass and the setup used. Besides, the yield of HMF production is related to the used biomass and the chosen catalyst. A higher yield is found by biomass rich in starch, since less pretreatment and less harsh reaction conditions are needed to produce the important intermediates HMF and LA [4].
A possible pathway to produce LA by hydrolysis of sugar with HMF as intermediate, is given in Figure 2.1. Both 6- and 5-carbon monosaccharides can react to levulinic acid by a chain of acid-catalysed reactions. First, glucose is enolizated to intermediate **(1)**. Further dehydration of intermediate **(1)** yields intermediate **(2)**. Intermediate **(2)** is then also dehydrated to intermediate **(3)**. So two water atoms are abstracted by two reversible reactions and two double bonds are formed. In the next step the double bonds translocate and intermediate **(4)** is obtained, which can react to the cyclic intermediate **(5)**. If again a water atom is substracted from intermediate **(5)**, HMF, an important intermediate, is obtained. HMF **(6)** rehydrates instantly back to intermediate **(5)** in aqueous environment and should be removed from the reaction mixture. In the previous reactions water was removed from the molecule, however when water is added to the bond between C_2 and C_3 in the furan ring in HMF, an unstable intermediate **(7)** is formed, which decomposes to LA **(8)** and formic acid terminating the reaction [2]. Formic acid is formed stoichiometrically as byproduct by the formation of LA from HMF, however more formic acid is found in the reaction products if the full reaction process from biomass to LA is taken into account [13].

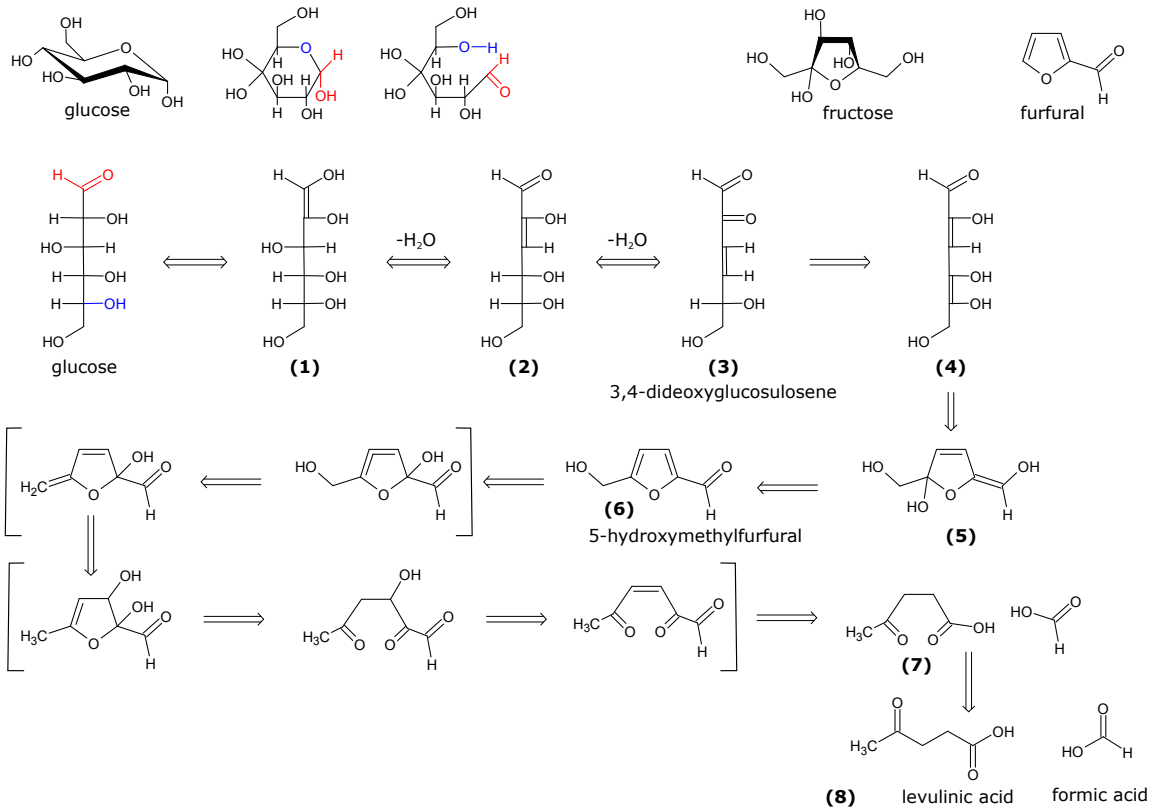

Figure 2.1: A reaction pathway from the monosaccharide glucose to levulinic acid (LA). First the monosaccharide is dehydrated to HMF, which is then hydrated to form the final products LA and formic acid.

Conventionally mineral acid catalysts are used, like HCl, HNO_3, H_2SO_4 etc. The catalysts have a low cost and are easily available. In literature, the LA yield can be found for different biomass feedstocks and mineral acid catalysts (Table 2.1). The numbers in Table 2.1 indicate that the yields with homogeneous catalysts are quite low, not higher than 50% on average. The yield is depending on the concentration of the catalyst used, strength of their primary dissociation constants and the feedstock used. The formation of unwanted byproducts, like humins, also lowers the yield. Humins are dark brown insoluble solids, which have a negative effect on the catalysts and can clog the reactor piping [4].

Heterogeneous solid acid catalysts, like metal catalysts, can also be used. Commonly used catalysts are Amberlyst 70 [26], zeolites [27] and $S_2O_8^{2-}/ZrO_2$-SiO_2-Sm_2O_3 [28]. Their main advantages are that they are easily recovered and no corrosion occur. In literature not a lot of data is found for heterogeneous catalysts. The LA yield tends to be lower than for homogeneous catalyst, not more than 45%, since the LA is adsorpted on the catalyst surface. They are also very selective to the reaction they enhance [4].

The Biofine process in the only semi-commercialised production process of LA from lignocellulosic material. The Biofine process uses dilute sulphuric acid as catalyst [2]. The process consist of two acid-catalysed steps whereby hexose sugars are converted first to HMF. The catalyst added is about 1 to 4% of the mixture, the reaction temperature is between 200 to 230°C and the pressure is ranging from 20 to 25 bar for a few seconds. The process parameters

Table 2.1: Different raw materials used for LA production and their respective yields. The summary is taken from [4] adding the reaction temperature and pressure and some recent studies.

Material	**Acid**	**LA yield** (%)	T (°C)	P (atm)	Cat. (wt%)	time (min)	**Ref.**
Wheat straw	H_2SO_4	19.9	209.3		3.5	37.6	[14]
Corn starch	H_2SO_4	35.4	200		5	60	[15]
Sorghym grain	H_2SO_4	32.6	200		8	40	[16]
Water hyacinth	H_2SO_4	35.0					[17]
Wood	H_2SO_4	16.0	200		5	240	[18]
Pulp slurry	HCl	40.5	160		6	60	[19]
Corn starch	HCl	35.0	200		1.8	30	[19]
Bagasse	HCl	22.8	220		4.45	45	[20]
Paddy straw	HCl	23.7	220		4.45	45	[20]
Rice husk	HCl	59.4	170	56 bar	4.5	60	[21]
Cellulose	H_2SO_4	25.2	250		3	120	[22]
Cellulose	HCl	28.8	250		3	120	[22]
Cellulose	HBr	26.9	250		3	120	[22]
Sucrose	H_2SO_4	61.0	160	1	0.2 M		[23]
Sucrose	H_2SO_4	40-50	140		1.8 mole·L^{-1}	480	[24]
Sucrose	H_2SO_4	42.3	125		9 w/v%	960	[25]

vary due to the variability of the biomass feed. The produced HMF is then transferred to another reactor where it is hydrolysed to LA. The hydrolysation process takes about 15 to 30 min at a temperature of 190 to 220°C and a pressure of 10 to 15 bar [2].

The LA yield of this process lies within 70 to 80 mole%, the highest reported yield in literature. The main disadvantage of the Biofine process is the recovery of the mineral acid catalyst and the separation of the LA from the dilute aqueous solution which also contains the byproduct formic acid [2].

The recovery of the LA is a challenge due to the formation of humins and the difficult separation of LA with the reaction medium. To reduce the formation of humins, the cellulose loading is minimised. However this has a negative effect on the yield and the recovery costs. In most cases the separation and purification of LA is done by vacuum distillation. The LA recovery in the Biofine process uses atmospheric/vacuum distillation combined with steam stripping. The humins are removed before distillation by filtration [2].

Once LA is produced, it needs to react further to GVL and pentanoic acid (PA), which is then esterified to pentanoates. No commercial process is already available, but in literature ample examples of the process on small scale can be found.

GVL is obtained from LA by catalytic hydrogenation (Figure 2.2). Ethyl levulinate (EL) is the other main feestock for the production of GVL from biomass. Cellulose can be converted to alkyl levulinates by alcoholysis in alcohols [29, 30, 31, 32]. The use of EL as feedstock has as main advantage that it easier to separate than LA due to its higher volatility.

The use of GVL as biofuel on itself is investigated by Horvath et al. [33] and they concluded it is a better alternative than ethanol as fuel additive regarding miscibility. Nevertheless, a phase separation occurs when a high concentration of GVL is added to conventional fuels. Also the cetane number of GVL is lower than 10 and the Lower Heating Value (LHV) of 25 $MJ \cdot kg^{-1}$ makes it less suitable as fuel additive [5].

A Ruthenium catalyst is used predominantly to convert LA to GVL using external H_2, since it shows the best selectivity and led to the highest yields. High yields can be obtained, up to 99% with a selectivity higher than 95% (Table 2.2, a) [5, 34].

Another possibility is to not get the hydrogen from external H_2, but to use formic acid (HCOOH) or an alcohol as hydrogen resources. Formic acid is formed by the production of LA from lignocellulose. Using formic acid as H-donor is an example of atom economy and the formic acid does not need to be separated of the LA stream. Different catalyst can be used, but Ruthenium catalysts are again a possibility. The process parameters for this reaction in literature are given in Table 2.2, b [5].

The process using alcohols to convert LA and its esters like EL to GVL is called Catalytic Transfer Hydrogenation (CTH), and is a variation of the Meerwein-Ponndorf-Verley reduction. Some studies about CTH are given in Table 2.2. CTH uses alcohols instead of pressurised H_2 as H-donor, making the reaction more convenient. Also cheaper base metal catalyst can be used for the reaction. The selectivity the GVL is also higher if EL is used as feedstock for CTH compared to the hydrogenation with H_2 [5].

The reaction mechanism to form PA from GVL is shown in Figure 2.3. The first step in the mechanism is the acid-catalyzed ring opening of GVL. Whereby first pentenoic acid is formed, which is hydrogenated to PA. The selectively to PA is high when a low metal loading is applied, however by high catalysts loading the formation of methyl tetrahydrofuran (MTHF), pentanal, pentanol (PeOH), butane and pentane is favored. The pentanol molecule and the pentanoic acid can react to pentyl pentanoate, however the measured concentration of pentyl pentanoate were small in the assessment of Lange et al. [3]. The production of pentanoic acid and related esters out of GVL is studied by different authors, mostly focussing on the production of pentyl pentanoate [3, 6, 35, 36, 37].

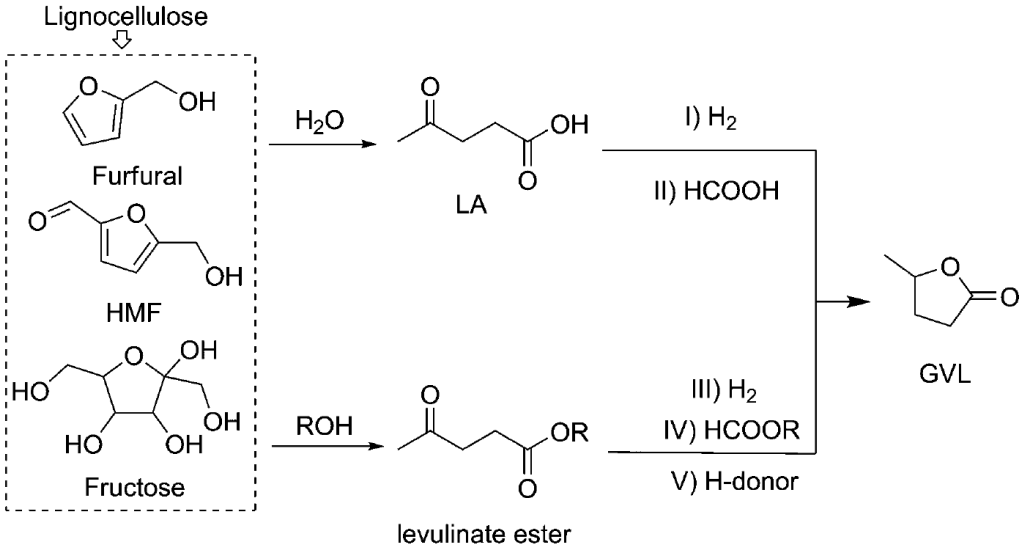

Figure 2.2: Reduction of LA and it ester EL to GVL with different resources of hydrogen [38].

Table 2.2: The reaction conditions together with the obtained yield, conversion and selectivity for the catalytic hydrogentation of LA into GVL, with hydrogen, formic acid and alcohols as H-donors. The table is taken from [5] and [34]. The WHSV denotes the quotient of the mass flow rate of the reactants divided by the mass of the catalyst in the reactor.

a) External hydrogen as H-source		p **H$_2$**	T	**WHSV**	**Time**	**Yield**	**Conv.**	**Select.**	**Ref.**
Catalyst	**LA concentration (m%)**	**(bar)**	**(°C)**	**(h^{-1})**	**(h)**	**(%)**	**(%)**	**(%)**	
Ru (5%)/C	50	35	150	4.8				96	[35]
	50	35	150		4		100	97	[39]
	5	12	130		2.6		92	99	[20]
Ru (5%)/Al_2O_3		145	150		2		99.5	99.7	[40]
Ru (5%)/SiO_2	75	100	200			99			[41]
Ru $(acac)_3$	2	70	140		12	95			[24]
Ru $(acac)_3$/$P(nOct)_3$		100	160		18	99			[42]
$Ru(CO)_4I_2$		100	150		8		85		[43]
$RuCl(PPh_3)_3$	15.8	12	180		24	86	99		[44]
Pt (1%)/TiO_2	$5{\cdot}10^{-3}$ mol/mol H_2	40	200	0.5-1.5				>95	[3]
Re (black)	100	150	106		18	71			[45]
$ReO_2{\cdot}2.5\ H_2O$	100	200	152		12	>99	100		[45]
PtO_2	28	3	24		44	87			[46]
Raney-Ni		60	220		3	94			[47]
Ni-Kat		62	185		4.5	93			[48]
b) Formic acid as H-source			T		**Time**	**Yield**			**Ref.**
Catalyst	**LA source**		**(°C)**		**(h)**	**(%)**			
Na_2SO_4	Synthetic		220		12	11.0			[49]
Ru-NP+Et_3N	Synthetic		130		24	100			[50]
Ag-ZrO_2	Synthetic		220		5	22			
Ni-ZrO_2	Synthetic		220		5	34			
$RuCl_3$/PPh_3+Et_3N	Synthetic		150		12	90			[51]
$RuCl_3$/PPh_3+pyridine	Synthetic		150		12	88			
Ru-P/SiO_2+Ru/TiO_2	Synthetic		150		6	30			[52]
Au/ZrO_2	Synthetic		150		6	99			[53]
Ru/C	Synthetic		150		5	90			[54]
$RuCl_3$/PPh_3+pyridine	Glucose		150		12	48			[51]
Cu/ZrO_2	Synthetic		200		5	100			[55]
Shvo catalyst	Synthetic		95		6	99.9			[56]
Ru/C	Fructose/external		180		16	52			[57]
Au/ZrO_2	Glucose		150		8	51			[53]
Au/ZrO_2	Cellulose		150		8	33			
Cu/ZrO_2	Giant reed		200		12	18.5 wt%			[55]
c) Alcohol as H-source	**Substrate**	**H-donor**	T		**Time**	**Yield**			**Ref.**
Catalyst			**(°C)**		**(h)**	**(%)**			
ZrO_2	LA	2-Butanol	150		16	22			[58]
ZrO_2	BL	2-Butanol	150		16	84.7			[58]
ZrO_2	EL	Ethanol	250		38	1.5			[59]
ZrO_2	EL	2-Propanol	250		1	93.4			[59]
$ZrO(OH)_2$	EL	2-Propanol	200		1	88.5			[60]
$ZrO(OH)_2$	EL	Ethanol	240		3	78.9			[60]
Zr-Beta	LA	2-Pentanol	118		10	96			[61]
Zr-Beta	LA	2-Pentanol	150		6	82			[61]
Zr-Beta	LA	2-Propanol	250			>99			[61]
Zr-Beta	ML	2-Butanol	120		5	>97			[62]
Zr-Beta	LA	2-Butanol	120		11	>98			[62]
Zr-Beta+Al-MFI-ns	furfural	2-Butanol	120		48	78			[62]
Raney Ni	EL	2-Propanol	25		9	99			[38]
Raney Ni	EL	2-Butanol	25		9	92			[38]

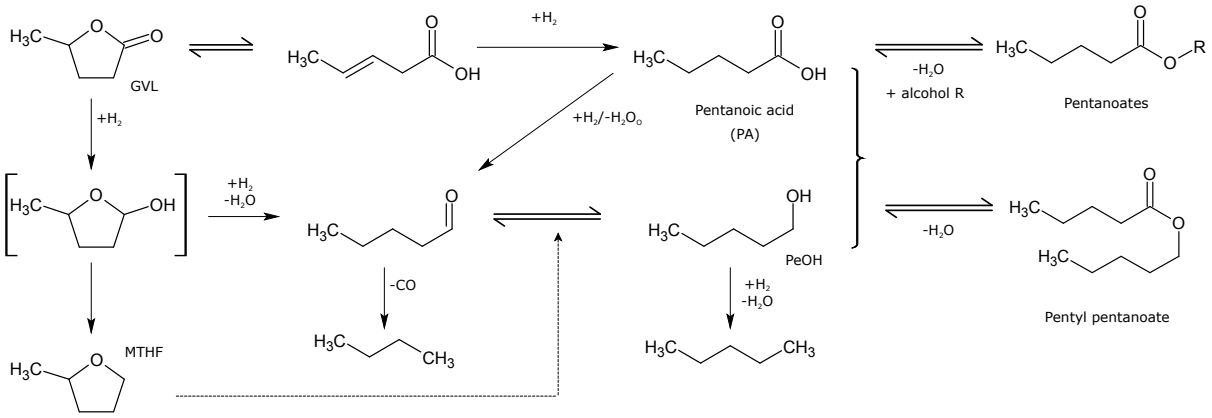

Figure 2.3: The reaction of GVL to pentanoic acid. Pentanoic acid can react with pentanol to form pentyl pentanoate in the same reaction medium. The other option is to separate the pentanoic acid and esterify it with another alcohol to a pentanoate of choice [3].

Chan-Thaw et al. investigated the conversion of GVL to pentyl pentanoate in one pot [6]. They used a 8% Cu-SiZr B catalyst to hydrogenate GVL to PA and let it directly react further to pentyl pentanoate with the extra added pentanoic acid. For a mixture with a ratio of 1 mole GVL per 10 moles of pentanoic acid, a conversion of 93% was found with a pressure of 10 bar for H_2, a temperature of 250°C, a GVL to catalyst ratio of 10:1 wt% and a reaction time of 20 hours. The GVL was converted to 59% of pentyl valerate and 21% penthyl 4-penthoxypentanoate. If only 5 moles of PA was added per mole of GVL, the conversion decreased to 92%, but the selectivity to pentyl valerate increased to 72% [6].

The conversion of LA to GVL and PA is also investigated by Xin et al. [36, 37]. Electrocatalytic hydrogenation is applied on LA to achieve GVL and PA using a non-precious Pb electrode in a single-polymer electrolyte membrane electrocatalytic (flow) cell reactor. The achieved yield for PA is higher than 90% and the Faraday efficiency, the efficiency with which charges are transferred to the system, is above 86%. The selectivity to the reaction product is related to the pH of the mixture. In a neutral mixture the formation of GVL is promoted, while in an acid environment PA is produced.

Lange et al. used a bifunctional catalyst that contains both hydrogenation and acidic functions. They evaluated 150 catalysts in a continuous high-pressure plug-flow reactor. High yields were achieved by zeolites and hydrogenation metals. A promising catalysts is Pt-loaded SiO_2-bound H-ZSM-5 with a yield above 80%, with a selectivity higher than 90%. The performance could be maintained for more than 1500 h with intermittent catalyst regeneration under hot H_2 and/or an airflow at 400°C. Other zeolites that performed well are medium-pore PSH-3 and large-pore mordenite. The conversion of GVL to PA does not need strong acids. Noble metals, like platinum (Pt), palladium (Pd) and rhodium (Rh) can be used. An overview of the production process of pentanoate esters from cellulose suggested by Lange et al. is given in Table 2.3.

Serrano et al. describes the same reaction from GVL to PA and pentyl pentanoate as Lange et al. The GVL reacts in aqueous solution to PA with Pd/Nb_2O_2 as bifunctional catalyst at moderate pressures and temperatures. They repeated the reaction for different catalyst loading, temperatures and WHSV. The found carbon distribution and selectivity for the different reaction conditions can be found in Table 2.4.

Table 2.3: Parameters for the four production steps to produce pentanoates from cellulose, taken from [3]

	Hydrolysis $C_6H_{12}O_2 \rightarrow$LA	Hydrogenation LA$\rightarrow$GVL	Hydrogenation GVL$\rightarrow$PA	Esterification PA$\rightarrow$pentanoates
Catalyst	H_2SO_4	Pt/TiO_2	Pt/ZSM-5	IER
Selectivity	50-60%	>95%	>90%	>95%
Productivity	>0.1 h^{-1}	>10 h^{-1}	>1 h^{-1}	>0.02 h^{-1}
Concentration	<5%	>90%	>50%	>50%

Table 2.4: The carbon distributin and the carbon selectivities for the conversion of GVL to PA over different loading of Pd/Nb_2O_5 catalyst. The feed for all the processes is an aqueous solution containing 50 wt% of GVL. The data is taken from [35]. For process 1 and 3: H_2 at 25 sccm and He at 25 sccm co-feed. In process 2: H_2 co-feed at 100 sccm.

Catalyst	T	P	WHSV	C distribution %		C selectivity %			
	(K)	(bar)	(h^{-1})	Org	Gas	PA	C_9=O	CO_x	C_4+C_5 alkanes
1. $Pd(1\%)/Nb_2O_5$	598	35	1.2	72	28	54	2	6	35
2. $Pd(0.1\%)/Nb_2O_5$	598	35	1.2	79	21	65	3	6	22
3. $Pd(0.1\%)/Nb_2O_5$	598	35	1.2	95	5	92	-	1	5

The effect of the catalyst loading can be deduced from the data in Table 2.4. A loading of $Pd(1\%)/Nb_2O_5$ results in the formation of CO, CO_2, and C_4-C_5 alkanes out of GVL. When the loading is decreased with a factor 10 and the other parameters values stay the same, PA is formed with a yield of 65%. In contrast to LA, PA is not soluble in water and it separates from the aquous reaction medium in an organic layer and can be separated more easily. The organic layer contains around 80% of the carbon of the reaction mixture. The organic oil consist of PA and pentane and butane in a smaller amount, which are dissolved more in the liquid phase due to the high pressure.

Lowering the hydrogen partial pressure in the reactor also improves the PA yield, since hydrogenation is limited under these condition and less decarboxylation products are formed. The best performance is found with a low catalyst loading and hydrogen partial pressure. An equilibrium with more pentanoic acid is reached when the catalyst and hydrogen are limited. A yield of 92% is found for the formation of PA and the organic layer contains 95% of the carbon in the system.

The first reaction steps from biomass to LA or GVL are already well described reactions. Literature data about the reaction of GVL to PA and finally pentanoates are scarce, however the existing data reveals that the process is promising. Pentanoates have a higher energy density compared to the levulinic esters, due to their higher C/O ratio. They mix better with hydrocarbons with longer chain length than with water, due to their low polarity. They do not react with the fuel tank and lines as a result of their apolarity. Their fuel characteristic can be adjusted by the alcohol they are esterfied with. Butyl and pentyl pentanoates are compatible with diesel fuel, even more than Fatty Acid Methyl Esters (FAME) produced from plant oil [34].

Table 2.5: The chemical characteristics of the pentanoates show that ethyl and methyl pentanoate can be used in gasoline engines, while the heavier butyl and pentyl pentanoates are fuels for diesel engines [10].

		Methyl	**Ethyl**	**Propyl**	**Butyl**	**Pentyl**	**PRF95**
Density	($kg \cdot L^{-1}$)	0.875	0.874	0.870	0.868	0.874	0.691
LHV	($MJ \cdot kg^{-1}$)	28.8	30.3	31.5	32.6	33.5	44.7
A/F	(-)	9.52	10.09	10.55	10.92	11.24	15.13
T_{boil}	(°C)	137	142	167	187	206	99

2.2 Use in conventional engines

Next to the production of pentanoates, their use in conventional engines was tested by several authors. Their fuel characteristic can be adjusted by selecting the alcohol for esterification. Short chain alcohols, like methanol and ethanol result in molecules with the same fuel performance as gasoline. While longer chain alcohols like butanol and pentanol result in diesel like molecules. The main difference between the two types of pentanoates is their volatility. Gasoline fuels have a higher volatility and related boiling point than fuel for diesel engines.

A blend of gasoline with 15% ethyl pentanoate was road tested by Lange et al. [3]. They tested the fuel in ten vehicles for a cumulative distance of 250 000 km. No negative impact on the fuel storage or the dispensing system was found. Ethyl pentanoate has a good octane number and some power profits were realised. Nevertheless, a higher volumetric fuel consumption was measured due to the oxygenated nature of ethyl pentanoate, hence a lower energy density.

No significant difference between pure methyl and ethyl pentanoate and Primary Reference Fuel (PRF) was found in a gasoline engine for both performance and emissions [10]. The test were conducted on a traditional spark ignition engine converted to mono-cylinder operation. The flame of the esters propagates faster than PRF95 flames and an adjustment of the ignition time needs to be made to optimise the work output. Contino et al. also summarised the properties of different pentanoates (Table 2.5). Due to the different carbon to LHV ratio of the pentanoates, more CO_2 is emitted compared to PRF95 for the same energy consumed [10].

Contino et al. also tested mixtures of diesel with 20 vol% of butyl and ethyl pentanoate and found no difference in performance and emission. A traditional compression ignition engine converted to mono-cylinder operation was used to test the engine performance. The injection timing was not optimised for the load or fuel, so the fuels could be compared at the same thermodynamic conditions. The pentanoates have a lower cetane number than diesel and adding 20 vol% of esters elongates the ignition delay. The differences between the blends can be reduced if the injection timing is optimised for all of them [7].

Engine test with ethyl, butyl and pentyl pentanoate performed by Koivisto et al. demonstrated that pentanoates have similar engine efficiencies than the reference fuel, however more NO_x and small particles were measured in the exhaust of the pentanoates. They also found a longer ignition delay compared to the ketones, ethers and alkanes that they also have investigated. As explaination for this effect, they suggested that the H-abstraction and isomerisation of an ester is more difficult compared to the other chemical structures [8].

A comparison of ignition delays between pentanoates and iso-octane was done in a Homoge-

neous Charge Compression Ignition (HCCI) engine. The results show that methyl pentanoate is more resistant to auto-ignition than iso-octane, while ethyl pentanoate is almost exactly aligned with iso-octane. The result indicates that ethyl pentanoate has the same sensitivity to pressure and temperature as iso-octane, making it good fuel for gasoline engines. Propyl pentanoate has properties lying between PRF90 and iso-octane. Butyl and pentyl pentanoate are more reactive an their characteristic lie between PRF80 and PRF60 [63].

The engine and road tests with pentanoates revealed no negative effect on the engine performance. The pentanoates are capable of replacing conventional fuels in both spark ignition and compression ignition engines. The volumetric consumption of the pentanoates is higher due to their oxygenated structure and more NO_x is measured in their emission by some authors.

2.3 Kinetic modeling

Different kinetic mechanism are already proposed in literature for esters and also pentanoates. The interest of modeling the combustion of esters started with finding a model to describe the combustion of biodiesel. Biodiesel is usually a methyl ester with between 16 to 20 carbon in the acid chain [64]. The chemical structure of biodiesel is long and complex, so research focussed on surrogate fuels with a smaller size to model the combustion of biodiesel. Shorter methyl esters like methyl butanoate to methyl decanoate are studied.

Opposed-flow diffusions flames of methyl decanoate are investigated by Sarathy et al. They used the experimental data to improve a skeletal mechanism for the methyl decanoate combustion [65]. Glaude et al. investigated the combustion of methyl decanoate in a Jet Stirred Reactor (JSR) at a pressure of 1.06 bar over a broad temperature range and at a stoichiometric equivalence ratio. The data was used to improve the kinetic mechanism developed for the combustion of methyl hexanoate and methyl heptanoate [66].

The kinetic mechanism for the oxidation of methyl hexanoate and methyl heptanoate was investigated by Dayma et al. [67, 68]. They studied the combustion of both in a JSR at a pressure of 10 atm over a temperature range of 500 to 1000 K and for equivalence ratios ϕ from 0.6 to 2. A kinetic model for the combustion of methyl hexanoate and heptanoate was achieved for the low and high temperature range and could describe the experimental data well.

The same research group also investigated the laminar burning velocities of C_4 to C_7 ethyl esters in a Spherical Combustion Chamber (SCC) at a pressure ranging from 1 to 10 bar. A pressure dependency for the laminar velocity of $p^{-0.215}$ is found for ethyl pentanoate at a stoichiometric equivalence ratio and a temperature of 423 K. The data was combined with data of other combustion configuration to achieve a kinetic model for the ethyl esters. A sensitivity analysis on the laminar flame speed demonstrated that the laminar flame speed is most sensitive to the chemistry of the small species and radicals, like H, O_2, OH, HO_2, CO and CO_2 [69].

Laminar flames of ethyl pentanatoate were investigated by Mbui Katshiatshia et al. on a Botha Spalding burner at a pressure of 55 mbar for equivalence ratios of 0.81, 0.95 and 1.31. A kinetic model containing 211 species and 1368 reactions was established to describe the ethyl pentanoate combustion [70].

Our work will focus on the validation of a kinetic mechanism for methyl pentanoate (methyl pentanoate (MPE)). In literature experimental data for different combustion configuration are

already available, just as kinetic mechanisms for the combustion of MPE. The use of MPE ($C_6H_{12}O_2$) as additive is investigated by Dmitriev et al. [71]. The addition of MPE on a premixed fuel-rich *n*-heptane/toluene flame at atmospheric pressure decreases the formation of intermediates important for the creation of polycyclic aromatic hydrocarbons, so MPE could diminish the soot formation in rich flames [71].

Korobeinichev et al. investigated a rich (ϕ= 1.5) and stoichiometric (ϕ= 1.0) flame at a pressure of 27 mbar and atmospheric pressure. Several stable species could be detected and a good fit between simulations with their established kinetic model for MPE and experimental results was found [72].

The extinction limits of C_2 to C_{11} methyl ester diffusion flames have been measured by Diévart et al. [73]. The data was used to build a kinetic mechanism. He found that formaldehyde and ethylene are important intermediates by the combustion of methyl esters larger than methyl butanoate and that smaller esters have a distinctive reaction mechanism which is different from that of biodiesel [73].

The autoignition of MPE is investigated by Weber et al. in a Rapid Compression Machine (RCM) The following equivalence ratios were assessed at a pressure of 15 bar: 0.25, 0.50, 1.00 and 2.00. Data at 30 bar was also gathered for the stoichiometric mixture [74].

Weber et al. wanted to compare his experimental data with simulations. Models for the combustion of MPE are established by different authors [72, 73, 74]. However the performance of the kinetic models was not satisfactionary for the RCM data [74]. The results from the mechanism that he established himself, differs with the ignition delays modeled with the mechanism from Diévart et al. Weber believes that the differences between the two models are related to the difference in enthalpy of formation for the radical directly formed from MPE with hydrogen abstracted on position 2. The enthalpy of formation for the other radical directly formed from MPE by hydrogen abstraction and MPE itself do not differ significantly between the two models (Table 2.6). He also stated that missing reaction pathways, incorrect rate estimates or incorrect thermodynamic properties could be the reason for the poor performance of the mechanisms. So overall, more research is needed to obtain a kinetic mechanism for the MPE combustion that is able to reproduce experimental data for different combustion configurations by simulations.

Table 2.6: Enthalpies of formation of MPE and its radicals, labeled according to the convention used in Figure 1.2, calculated by the THERM software by Diévart and the RMG software by Weber.

Radical site	Diévart et al. [73]		Weber et al. [74]	
	($kJ \cdot mol^{-1}$)	($kcal \cdot mol^{-1}$)	($kJ \cdot mol^{-1}$)	($kcal \cdot mol^{-1}$)
MPE	-470.98	-112.57	-472.53	-112.94
2	-297.16	-71.02	-273.63	-65.40
3	-277.03	-66.21	-273.63	-65.40
4	-277.03	-66.21	-278.61	-66.59
5	-265.94	-63.56	-267.53	-63.94
m	-270.51	-64.65	-270.12	-64.56

3

Experimental set-up

The experimental setup on which laminar flat flames can be stabilised, consists of three main parts: an evaporation system for the liquid fuel, the Botha-Spalding burner and Gas Chromatography (GC) equipment with detectors to analyse the samples (Figure 3.1).

Besides these parts, a control system for the gas supply and a compression system before the GC analysis are present in the experimental setup. Furthermore, an analysis of the error and uncertainty on the experimentally achieved mole fraction profiles is performed in this chapter.

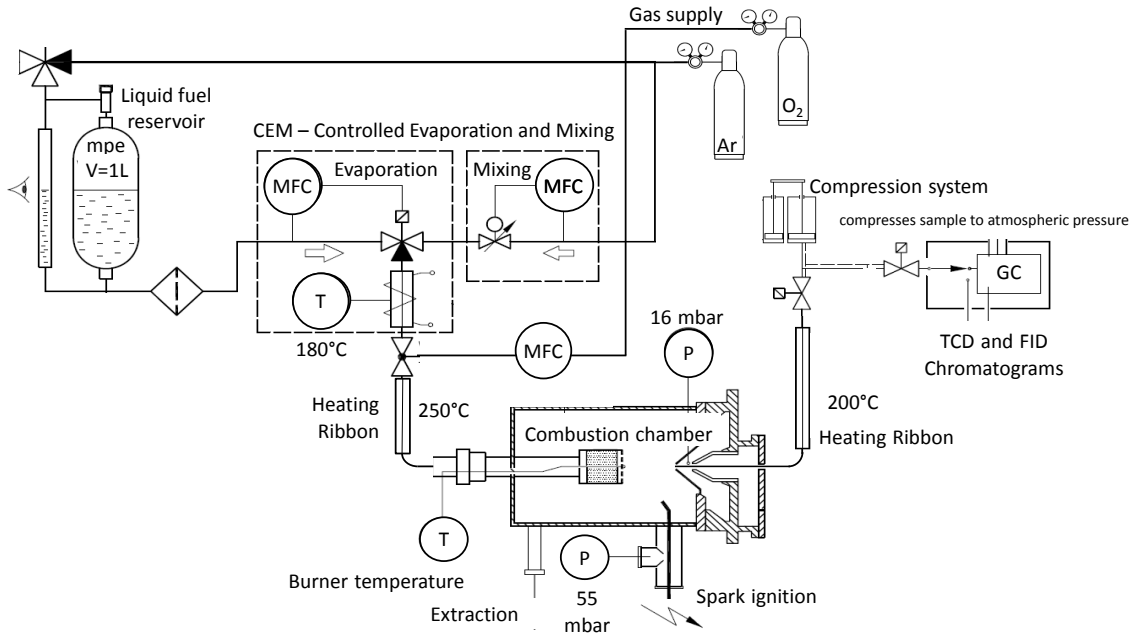

Figure 3.1: An overview of the experimental setup. The three main parts of the experimental setup are the evaporation system, the Botha-Spalding burner and the sampling and analysing part.

3.1 Evaporation system

Methyl pentanoate is a liquid at ambient conditions and its boiling temperature is 410 K [75]. To obtain a premixed flame, the fuel needs to be vaporised preceding the mixing with oxygen and argon. Argon is chosen as diluent since it is inert and stable flames can be achieved with it over a broad temperature and pressure range [76]. To achieve a constant gas flow of the fuel and to avoid condensation prior the combustion chamber, the evaporation system shown in Figure 3.1 is used. The liquid fuel is stored in a stainless steel reservoir of 1 liter, pressurised by argon at 3 bar. A mass flow controller, a mini cori-flow from Bronkhorst, controls the liquid entering the Controlled Evaporation and Mixing unit (CEM). The maximum mass flow rate of the fuel is 120 g·h^{-1} and a filter is placed between the storage tank and the CEM to avoid impurities entering the CEM [77]. A second controller, a EL-FLOW from Bronkhorst, regulates the amount of argon that enters the CEM, which is set to the maximum flow rate of 2 L_N·min^{-1} during experiments.

The CEM is a capilar tube, heated to 453 K, which is 43 K higher than the boiling point of methyl pentanoate (MPE). At the CEM exit, the fuel is vaporised and already mixed with a fraction of the argon. The fuel mass flow rate during the experiments is set to 100 g·h^{-1}. One liter of fuel is enough to provide for 8 hours of experiments, since the density of MPE is 875 kg·m^{-3} at 298 K and approximately 0.1 L of fuel is consumed per hour [78].

To avoid condensation of the fuel in the connection between the CEM and the combustion chamber, a heating ribbon set at 523 K is used. The mixture leaving the CEM has a MPE content of around 14 mole% at a pressure that varies between 50 and 60 mbar. The condensation temperature can be calculated via the Antoine equation and appears to be between 283 to 306 K, well below the temperature of the heating ribbon.

3.2 Gas supply to the combustion chamber

The incoming gas to the Botha-Spalding burner is a mixture of the fuel, oxygen and argon. During experiments, the oxygen and one of the argon streams are controlled by a Mass Flow Controller (MFC), a Bronkhorst F-201CV. The MFC contains a thermal mass flow sensor, that regulates the mass flow by measuring the temperature at different places in the stream.

The used MFC are calibrated for nitrogen. A correction factor is applied to make the calibration valid for oxygen and argon. The correction factor C is defined as the ratio of the product of specific heat and density at normal conditions of the gas for which the MFC is calibrated and of the gas that is controlled in reality,

$$C = \frac{c_{p,1}\rho_1}{c_{p,2}\rho_2}, \tag{3.1}$$

where, in our case, $c_{p,1}$ and ρ_1 are the heat capacity and density for nitrogen at normal conditions and $c_{p,2}$ and ρ_2 are the heat capacity and density for oxygen or argon at normal conditions, which is a temperature of 273 K and a pressure of 1 atm [79]. For the conversion of N_2 to Ar, the factor C has a value of 1.4, while for O_2 the factor C is 0.98 [80].

Other gases needed for the experiments and calibration are ethylene, methane, propane, CO, CO_2 and hydrogen. Ethylene and hydrogen gas bottles are part of the experimental setup. The mass flow controllers for ethylene and hydrogen are thermal MFCs and are especially calibrated for these gases. There is no further correction needed. For the calibration of

methane, propane, CO and CO_2, their gas bottles were connected via the hydrogen or the ethylene supply. The correction factors for these gas stream are calculated in Appendix 1.

The error on the flow rates controlled by the MFC is also given in the datasheets provided by Bronkhorst and is determined as a percentage of full scale (0.1% FS) added with a percentage of reading (0.5 % Rd). In Section 3.6 the experimental error and uncertainty is investigated more into detail.

3.3 Combustion chamber

The combustion chamber contains a Botha-Spalding burner [9] with a circular diameter of 8 cm on one side and a quartz sampling cone on the opposite side (Figure 3.2). The burner disk is cooled to stabilise the flame [9].

A Botha-Spalding burner can produce flat flames over the entire range of mixture ratios. The flat shape of the flames makes it possible to determine the flame speed without arbitrary assumptions related to a curved flame front. If the flame is ignited downstream of the disk, the flame will stabilise when the stream velocity of the premixed fresh gases equilibrate with the flame speed. More information is given in Section 4.1 [9].

The position of the burner can be adjusted manually with an accurancy of 0.1 mm, so samples can be taken along the flame. Due to the characteristics of the investigated laminar flat flames and the burner, samples at different distances from the burner are related to different steps in the combustion process. The samples close to the burner surface are related to fresh gases, while samples further away from the burner are burnt gases. By this way, the mole fraction profiles of the reactants, combustion products and intermediates can be obtained.

During the experiments, the pressure of the combustion chamber is kept constant at 55 mbar. The low pressure is achieved by means of two vacuum pumps. The primary vacuum pump stabilises the experimental pressure at 55 mbar, while a second vacuum pump is placed after the sampling cone, subtracting a stream for sampling from the flame at an even lower pressure of around 16 to 20 mbar. The pressure in the combustion chamber and after sampling are measured with two pressure sensors, both Pfeiffer Vacuum Type CMR 361.

To ignite the flame, a retractable ignition spark is located at the bottom of the combustion chamber. For ignition, the igniter is placed in front of the burner surface at a distance of 1 cm. Once the flame is ignited, it is retracted to avoid any influence and contact with the flame. Ethylene is used as fuel for ignition. The ethylene flame can be gradually switched to the flame of interest.

The burner is heated up to 318 K by water circulation on the inside to avoid condensation of the fuel in the burner. When a laminar flame is established, the heat released leads to a higher equilibrium temperature in the burner and the water circulation serves as cooling, just as additional cooling circuit with tap water, to keep the heat losses to the burner constant and the flame at a stable position during the experiments. The combustion chamber and the sampling cone are also cooled on the outside with the tap water circuit. The combustion chamber is therefore not adiabatic and the temperature profile needs to be measured experimentally to conduct kinetic modeling. The temperature of the burner surface is measured by a type K thermocouple and the temperature of the assessed flames is measured with a type B thermocouple. The temperature measurements are explained in detail in Chapter 5.

For security reasons, an automatic pneumatic valve is installed at the entrance of the

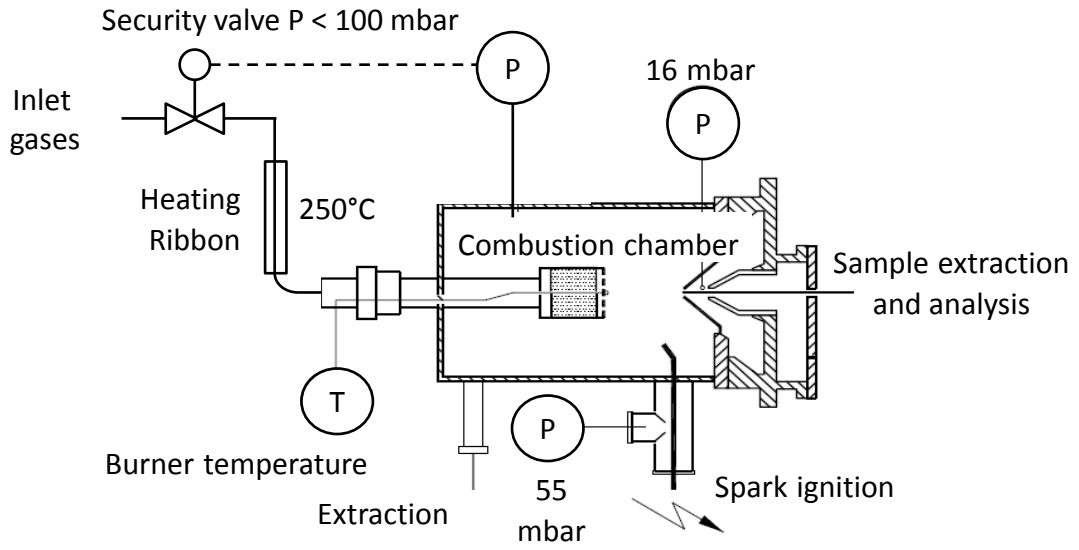

Figure 3.2: The combustion chamber consists of an adjustable Botha-Spalding burner opposite to a quartz sampling cone. The pressure in the combustion chamber is set to 55 mbar, while after the sampling cone the pressure is 16 mbar to extract a molecular beam and quench the reaction [81].

combustion chamber. If the pressure inside the combustion chamber rises up to 100 mbar, the valve closes automatically, so no premixed gases can enter the combustion chamber and cause an explosion. The valve also closes automatically if there is no cooling water running.

Sampling is performed by a quartz cone with an entrance diameter of 0.2 mm and an angle of 45°. A sample stream goes continuously through the sampling cone. The position of the sampling cone is fixed in front of the movable burner. After the sampling cone, a higher vaccuum is attained, to quench the combustion reaction. However, a sample at atmospheric pressure is needed and the sampling stream is led to the compression system by a heating ribbon set to 523 K to avoid condensation of some of the sample gas (unburned fuel, water, etc.).

3.4 Compression system

An online compression system is used to increase the pressure of the sample (16 mbar) to the working pressure of the GC (atmospheric pressure). The compression system consists of a cylinder with a volume varying between a maximum of 2006 ml before compression and 33 ml after compression (compression ratio of 61). The cylindrical piston needs to be heated to avoid condensation.

The compression process is regulated by four valves (Figure 3.3), which are controlled by a LabView program. During normal operation, when the a gas stream is extracted but not sampled, valves 5b, 6, 7 and 8 are closed. The sample stream is extracted by the second vacuum pump, through valve 5a and the manual valve which are open. At the start of the sampling, the compression system is placed under vacuum by opening valve 8 to extract gas residues. Then valve 5a is closed, while the counteracting valve 5b opens, leading the sample stream to the compression system instead of extraction. Valve 6 is activated and compressed air at 8 bar moves the piston of the compression system upwards. After 45 s of filling, the

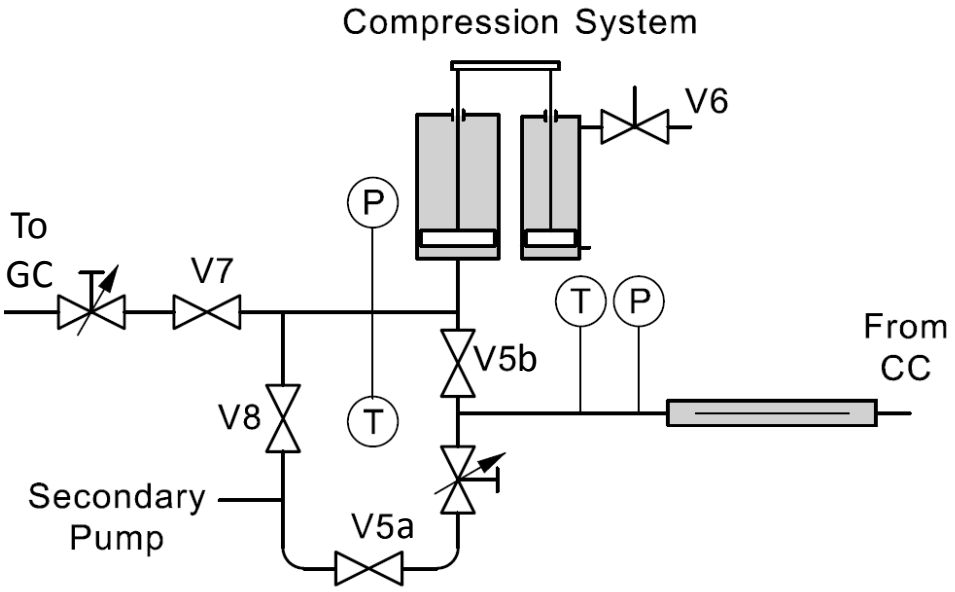

Figure 3.3: Detail of the valves regulating the compression system. When the sample is extracted from the combustion chamber (CC) the manual valve and valve 5a are open. During sampling, valve 5a closes and a sequence of opening and closing valves 5b, 6, 7 and 8 is followed to obtain a sample at atmospheric pressure [81].

positions of valve 5a and 5b switches again, stopping the sampling.

Valve 6 is also closed after 45 s and the sample is compressed. The compressed sample is led to the GC equipment by opening valve 7. The compressed sample expands and when the sample has a pressure around atmospheric pressure, the sample is finally injected in the GC. After injection valve 8 is opened to evacuate the lines. To monitor the temperature and pressure in the compression system a thermocouple is placed between valve 6 and 8 together with a pressure sensor.

In case of condensation, the mole fractions of the sample components change, leading to incorrect chromatogram results. To find a temperature high enough to avoid condensation, the Antoine equation can be used, if the partial pressure of the condensating species are known. The condensation temperature for water and fuel is calculated in the following paragraphs, since these two species can condensate.

The Antoine equation describes the relation between partial pressure and temperature for pure components. The Antoine equation for water is

$$\log_{10}(P(\text{bar})) = 4.6543 + \frac{1435.264}{T(\text{K}) - 64.848} \tag{3.2}$$

with P the partial pressure related to the temperature T. This equation is valid between 255.9 and 373 K [82]. Unfortunately, Antoine equation parameters for methyl pentanoate were not found. Only the boiling point at atmospheric pressure is stated on the National Institute for Standards and Technology (NIST) chemistry webbook page, which is 410 K [75]. Therefore molecules with the same functionality as methyl pentanoate are selected: one with a lower boiling temperature and one with a higher boiling temperature as methyl pentanoate, namely n-butyl acetate ($T_{b,atm}$=400 K) and methyl hexanoate ($T_{b,atm}$=423 K) (Figure 3.5, a). The

Antoine equation is given for both molecules in the NIST database [83, 84].

$$\text{n} - \text{butyl acetate} \qquad \log_{10}(P(\text{bar})) = 4.26803 + \frac{1440.231}{T(\text{K}) - 61.362} \tag{3.3}$$

$$\text{Methyl hexanoate} \qquad \log_{10}(P(\text{bar})) = 4.95409 + \frac{1935.423}{T(\text{K}) - 31.421} \tag{3.4}$$

The saturation pressure of MPE in function of the temperature is assumed to lie between the partial pressures found for n-butyl acetate and methyl hexanoate.

The saturation pressure of MPE can be calculated if the atmospheric boiling temperature and the critical point are known. The vapor pressure behavior of n-alkanes can be described by the analytical expressions suggested by Ambrose and Walton for the Pitzer expansion [85]

$$ln\left(\frac{P_{vp}}{P_c}\right) = f^{(0)} + \omega f^{(1)} + \omega^2 f^{(2)} \tag{3.5}$$

with

$$f^{(0)} = \frac{-5.97616\tau + 1.29874\tau^{1.5} - 0.60394\tau^{2.5} - 1.06841\tau^5}{T_r} \tag{3.6}$$

$$f^{(1)} = \frac{-5.03365\tau + 1.29874\tau^{1.5} - 5.41217\tau^{2.5} - 7.46628\tau^5}{T_r} \tag{3.7}$$

$$f^{(2)} = \frac{-0.64771\tau + 2.41539\tau^{1.5} - 4.26979\tau^{2.5} - 3.25259\tau^5}{T_r} \tag{3.8}$$

where P_{vp} is the vapor pressure, P_c is the critical pressure, T_r is the reduced temperature ${}^{T}/_{Tc}$ with T_c the critical temperature, τ is defined as $1 - T_r$ and ω is the acentric factor defined by Pitzer as

$$\omega = -log_{10}\left[\lim_{(T/T_c)=0.7} {}^{P_{vp}}/_{P_c}\right] - 1.0. \tag{3.9}$$

The acentric factor describes the centricity of a molecule. No value for the acentric value is found in literature for MPE. Nonetheless, the Pitzer expansion can be solved since the boiling temperature and the critical point are known and the vapor pressure curve can be fitted through these points. A value of 0.75 for the acentric factor is found by optimising the fit. This value is also found when Equation 3.9 is solved. So the partial pressure of both MPE and water can be calculated.

The partial pressure of water or MPE needs to be below the saturation pressure found with the Antoine equations for the temperature of the compression system to avoid condensation. From the composition of the flames, the mole fraction of the fuel is maximal 4.4 mole% for the rich MPE flame (Table 1.1). While from assessing the equilibrium concentration of the reaction products the mole fraction of the water will vary between 15 and 18 mole%.

To calculate the partial pressure of water and MPE the pressure after compression needs to be known. During sampling the extraction is stopped for 45 s (Figure 3.6). As a result the pressure after the sampling cone rises to a pressure of 42.34 ± 1.90 mbar on average. Then the sample is compressed rapidly. The sample consists mostly of argon, so the molecular weight of the sample is estimated to be 40 g·mol^{-1}. If we assume that the sample behaves as an ideal gas, with a temperature of 363 K and a pressure of 42 mbar, the sample mass is 0.1 g. The compression process is assumed isothermal and the pressure will rise to 2.58 bar (Figure

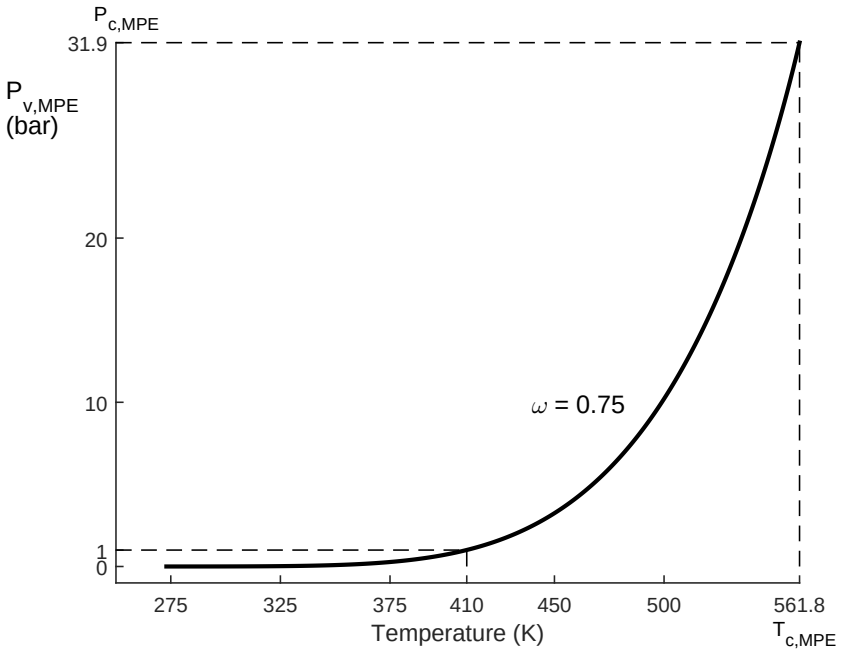

Figure 3.4: The vapor pressure of MPE in function of the temperature can be calculated by the expressions suggested by Ambrose and Walton [85].

3.6). With this end pressure, the partial pressure of the fuel will be 0.114 bar and the partial pressure of water will range between 0.387 and 0.464 bar.

With these partial pressures, the minimum temperature to avoid condensation of the fuel will lie between 338 K and 360 K, when we are assessing the rich MPE flame flame (Figure 3.5, b). The result of the Ambrose-Walton method lie between the partial pressure of n-butyl acetate and methyl hexanoate, indicating that the results are correct. The temperature to avoid the condensation of water varies from 348 to 353 K (Figure 3.5, c). So to avoid condensation during the sampling of the MPE flames, the compression system should be heated above 360 K. A heating device is connected to the compression system and a temperature of 363 K is achieved during experiments, reducing the risk of condensation significantly.

The pressure after compression (2.58 bar) is higher than the operating pressure of the GC equipment. So before the actual injection of the sample in the GC-column, the compressed sample is expanded gradually to atmospheric pressure. This process can be seen in Figure 3.6. The compression happens after 45 s of sampling, the sample than gets 28 s to expand to atmospheric pressure. No pressure drop occurs between the GC-colums and the atmospheric pressure at injection, so unskewed chromatograms are achieved.

If the injected sample is still at a higher pressure, the obtained chromatograms are unreliable [86]. To proof the influence of sample pressure on the chromatogram, a sample with a known concentration was injected at different pressures. The areas of the found chromatogram increase linearly with the pressure applied (Appendix 1, Figure 13.7).

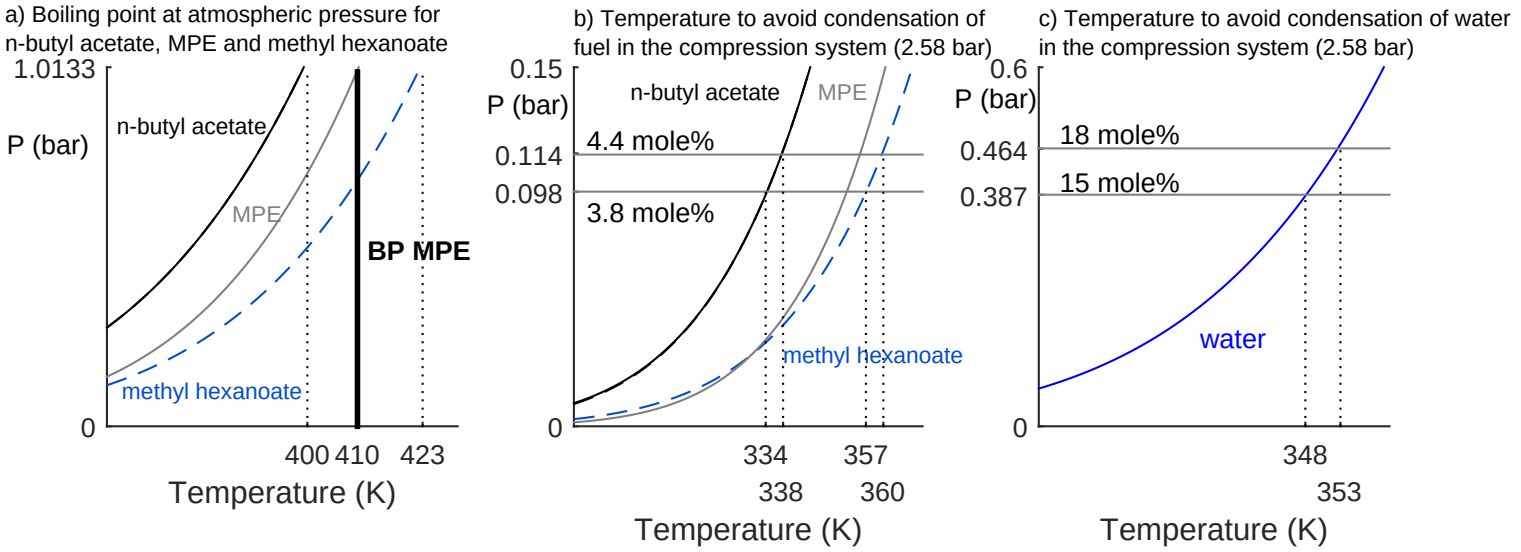

Figure 3.5: Via the Antoine equation and the Ambrose Walton method the temperature at which the MPE and water start condensating in the compression system can be calculated. To check the correctness of the results obtained by the Ambrose Waltond equations, the Antoine equations for two molecules, with the same functionality as MPE but different boiling points are also shown. The two selected molecules are n-butyl acetate, with an atmospheric boiling temperature of 400 K, and methyl hexanoate, with an atmospheric boiling temperature of 423 K. The boiling temperature of MPE ($T_{b,atm}$=410 K) lies between these values (Figure a). The vapor pressure of MPE obtained by the Ambrose Walton method lies between the values of n-butyl acetate and methyl hexanoate.
A temperature of 360 K is needed to avoid condensation of the fuel in the assessed MPE flames, since this temperature is related to the partial pressure of the MPE in the rich flame (Figure b). Water condensation can be a problem if the compression system is not heated until 353 K (Figure c).

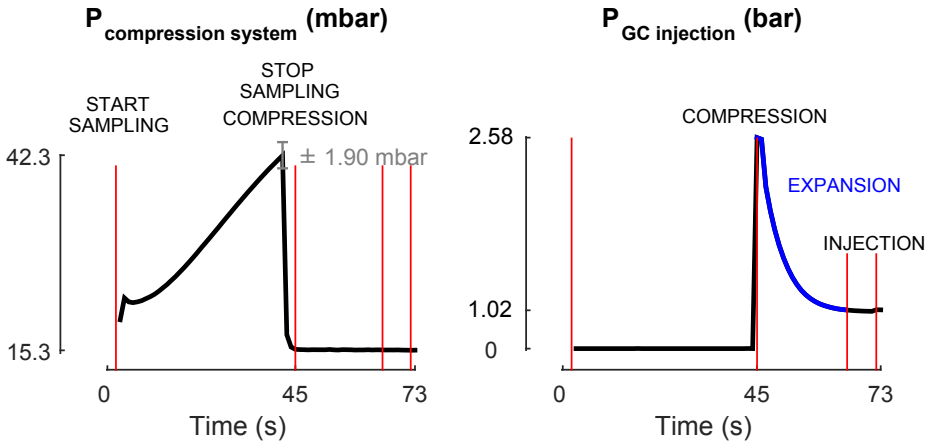

Figure 3.6: The pressure rises during sampling in the compression system. After 45 s of sampling a pressure of 42.3 mbar is achieved and the sample is compressed rapidly in the compression system. Valve 7 is opened and the sample is led to the GC entrance, where a pressure higher than atmospheric pressure is measured. The sample is expanded for 28 s and no pressure difference between the pressure in the GC-columns and the atmospheric pressure is found.

With the current experimental setup, it is not possible to obtain exact atmospheric pressure after compression of the sample. The sample has a mass of 1 g, which is 0.003 mole and the minimum to be quantified by the GC-TCD/FID. Also the temperature of 363 K cannot be lowered due to the risk of condensation. The pressure on which the flame is stabilised cannot be changed, because the thickness and the structure would change too. The only other solution is to change the plunger, which should be tested in future work.

3.5 Analysing the samples by GC-FID/TCD

When Gas Chromatography (GC) is used as separation method, the identified and quantified species are limited to stable ones. Separation by GC is based on species having a different affinity for the mobile (carrier gas) or stationary (GC column) phase. Species with a higher affinity for the stationary phase will tend to elute later. The affinity is depending on the polarity of the species, the applied temperature and flow rate of the carrier gas and the interaction of the species with both the mobile and stationary phase. So choosing the right column, carrier gas and temperature is important to obtain a good separation of the species [87].

After the separation, the species will emerge separatly and are detected by two detectors in serie. The first detector is a Thermal Conductivity Detector (TCD). The sample is not destructed by this detector and it can be analysed by the second detector, a Flame Ionisation Detector (FID). The sample is burned in a H_2/Air flame in the FID detector. Both detectors measure a change in signal when a species elutes, resulting in a chromatogram profile. Due to the different working principle, certain species are only detected by one of the detectors, argon for example is not an hydrocarbon and cannot be burned and is therefore only detected by the TCD. Both detection methods are described in Section 3.5.2. Helium is used as carrier gas for most of the experiments. With this carrier gas, the fuel, stable intermediates and some permanent gases can be detected by the FID. The diluent argon can be detected by the TCD

with helium as carrier gas.

Other detection techniques, like Molecular Beam Mass Spectrometry (MBMS), could also be an option to analyse the samples. Mass spectrometry (MS) has some advantages compared to GC. The MS process takes place under vacuum and no compression system is needed, minimalising the risk of condensation. MS is a faster method than GC and can also detect radicals. Nevertheless, the fuel investigated is quite complex and different radicals with the same mass-to-charge ratio are expected. When radicals have the same mass-to-charge ratio, they cannot be detected separately. So, MS could give some more information of the radicals formed, but the data should be handled with care. Overall, GC-FID/TCD and detection techniques with MS are both viable detection techniques. They have both their disadvantages, but are both able to quantify mole fraction profiles.

The time when a species elutes is called the retention time. To identify species, retention times found for species in the sample are compared with retention times of pure species samples. When the same retention time is found, it is admissible that the species is the same as in the pure sample.

The obtained chromatogram areas can be converted to mole fraction by calibration. Samples with different concentrations are analysed and the Response Factor (RF) is defined as the slope of the linear correlation between the species mole fraction, x_i and the detected chromatogram area:

$$\mathrm{RF} = \frac{d\mathrm{Area}}{dx_i}. \tag{3.10}$$

All these steps of sample analysis will be discussed in detail in the following sections.

3.5.1 Separation

The injected samples are separated by the CP-SIL 5CB column from Agilent for oxygenated species and the HP-MOLSIEVE column produced by Sigma Aldrich for permanent gases. The sample is then retained in the RTX-1 column with a very small internal diameter of 0.1 μm before the TCD, to reduce the mass flow. The used TCD is a μ-TCD, which needs a reduced sample flow. The characteristics of the three used columns are given in Table 3.1.

The temperature of the oven is programmed to obtain a good separation of the intermediates. First, the oxygentated species in the CP-SIL 5CB column are eluted, the starting temperature is 40°C which is increased to 120°C in two steps (Table 3.2). After 30 min all the intermediates on the CP-SIL 5CB column are eluted and the GC switches to the HP-MOLSIEVE column. The permanent gases are separated on this column. The starting temperature is again 40°C and the temperature is increased to 250°C in two steps, to separate CO_2, C_2H_4 and C_2H_2. Afterwards the temperature of the oven is decreased to 90°C. In total the method takes around 80 minutes to achieve a full chromatogram [70].

Three 6-way valves are present in the GC equipment to switch between the three columns (Figure 3.7). The first valve, E2, controls the injection of the sample to the columns and the detectors, while E3 and E4 control which columns is used. The default position of the valves is 'off', which means that the carrier gas goes through the column. If a sample is present the species are separated on the column. In the 'on' position, the carrier gas is bypassing the column. At the beginning of the separation, valve E3 is at the 'off' position and the CPSIL 5CB column elutes. After 30 min E3 is switched to the 'on' position and E4 to 'off', so the species on the HP-MOLSIEVE column can elute.

Table 3.1: Characteristics of the three used GC columns

Column	Length (m)	Internal diameter (μm)	External diameter (mm)	Maximum temperature (°C)
CP-SIL 5CB	25	5	0.53	350
HP-MOLSIEVE	30	50	0.53	300
RTX-1	15	0.1	0.32	350

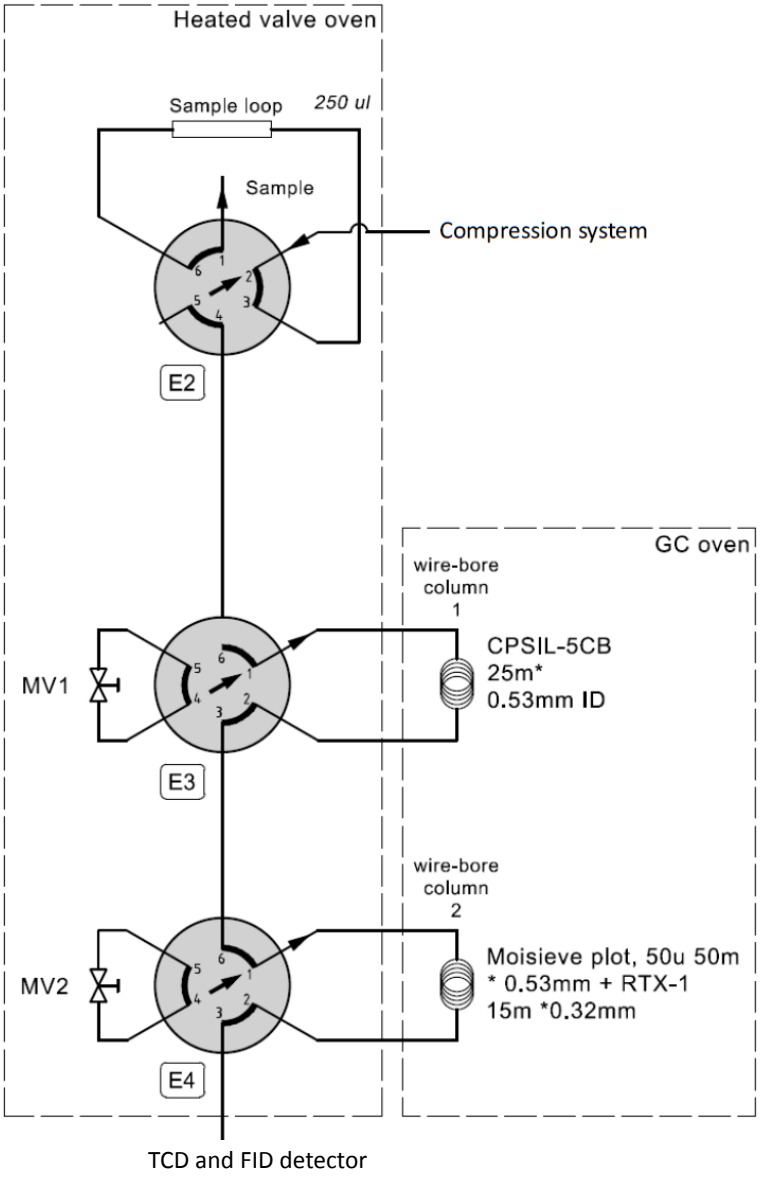

Figure 3.7: Three 6-way valves are implemented in the GC equipment. The first valve E2 controls the injection, while valve E3 and E4 control when the sample on the CP-SIL 5CB or HP-MOLSIEVE column are eluted.

Table 3.2: The temperature profile of the oven is made of 6 ramps. The first 3 ramps apply on the elution of the CP-SIL 5CB column, for which the temperature starts at 40°C and gradually increases to 120°C. The oven temperature is lowered before the permanent gases are eluted from the HP-MOLSIEVE column. Afterward, the oven temperature is increased until a maximum temperature of 250°C is reached.

	Oven rate ($^\circ$**C** $\cdot$**min**$^{-1}$)	**Hold temperature** ($^\circ$**C**)	**Hold time** (**min**)
Initial		40	7.00
Ramp 1	80	65	10.00
Ramp 2	10	120	5.00
Ramp 3	40	40	10.00
Ramp 4	120	90	9.57
Ramp 5	50	250	22.00
Ramp 6	100	90	3.40
			66.97
TOTAL	12.74 min		79.71

3.5.2 Detection

The first detector, a TCD, is a non-destructive universal but not very sensitive detector. This detector is based on the different thermal conductivities of species. The TCD is a katharometer, measuring the difference in thermal conductivity between a reference, the carrier gas, and the sample. When only the carrier gas is eluting no voltage will be registered, however when another species with a different thermal conductivity is co-eluting a difference in voltage will be measured. In this work, the TCD chromatogram shows peaks for all gases. The sampling rate of the TCD is fixed to 50 Hz, with a signal to noise ratio of 2. The temperature of the filament is set to 280°C and the detected signal is expressed in μV. The chromatogram achieved by TCD in the rich MPE flame at a distance of 4 mm is given in Figure 3.8. The main peak is related to argon.

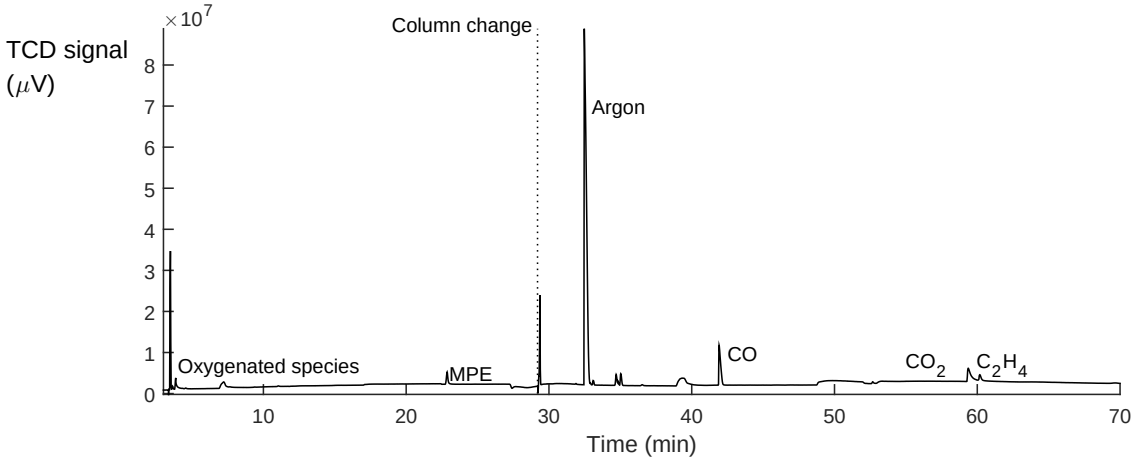

Figure 3.8: Chromatogram achieved by the TCD at a distance of 4 mm in the rich MPE flame

The second detector is the FID, which is used for the detection of hydrocarbons. The sample is burned in a H_2/Air flame and the electric conductivity is measured. When a species elutes, the measured electric conductivity changes, resulting in a peak of the signal. The flow rate of the H_2 flow is set to be 70 ml·min^{-1} and the air flow is 350 ml·min^{-1}. A make up flow of Helium (25 ml·min^{-1}) is added to increase the resolution. The increase in flow rate leads to less band broadening. With this detector the hydrocarbons, even oxygenated ones, can be detected. In total 12 species could be distinguished in the FID chromatogram. A list of them can be found in Table 3.3.

The FID can also detect CO and CO_2, since they are converted to CH_4 by a methaniser. The methaniser is a heterogenous catalyst which can hydrogenate CO and CO_2 to methane. The main advantage is that CO and CO_2 can be quantified with the FID detector, which is a more sensitive detector than the TCD detector. The peaks of the different species can still be identified, since they eluete at different Retention Time (RT).

In Figure 3.9 a FID chromatogram achieved for a sample of the rich flame at a distance of 4 mm is shown. The peak of the fuel MPE, CO, CO_2, C_2H_4 and C_2H_2 are very distinctive. The peaks of the oxygenated species are found at the beginning of the chromatogram and can be distinguished from each other.

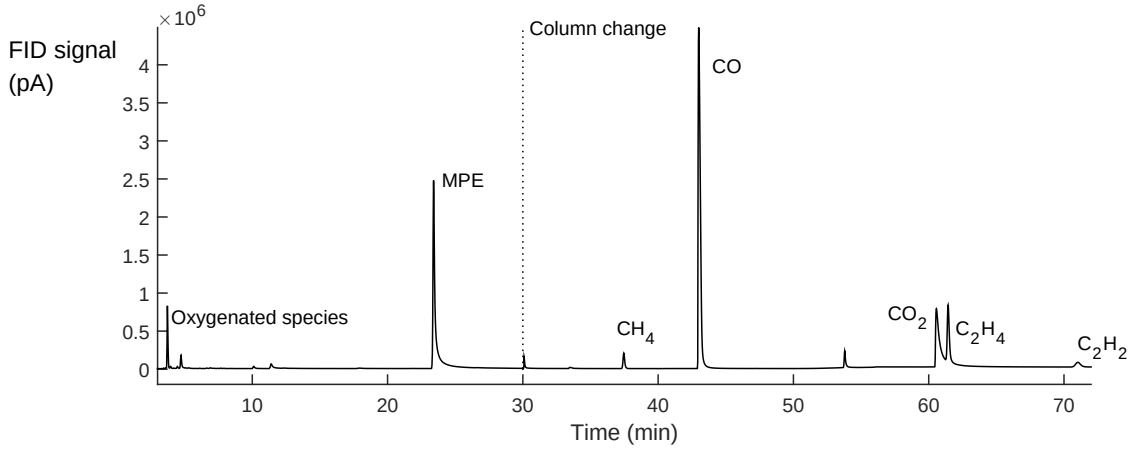

Figure 3.9: Chromatogram achieved by the FID at a distance of 4 mm in the rich MPE flame

3.5.3 Identification and quantification of the detected species

To identify species, their RT needs to be calibrated by injecting a pure sample of the species and see when it elutes. The signal peak should be higher than the Limit of Detection (LoD) to correctly detect a species. The LoD is usually defined as 2 to 3 times the peak to peak baseline value [88]. Species with a chromatogram peak above this limit can be identified by their RT. In overall, 16 species are identified. The RT can be found in Table 3.3, together with the column the species elutes from, the carrier gas used and the detector.

To quantify the concentration of a species, its chromatogram peak should be ten times the noise to signal ratio [88]. This limit is called the Limit of Quantification (LoQ). In Figure 3.10, the LoD and LoQ are visualised together with the maximal peak values found in the chromatograms. Formaldehyde, propane, acetaldehyde, ethanol, methane and acetylene have chromatogram peaks well above the LoD and LoQ. The peaks of acetic acid, formic acid, acetone and isopropanol on the other hand, are close to the LoQ. Their mole fraction

profiles are therefore not reliable and will not be used further, but it can provide qualitative information.

A linear relation is obtained for each species between the injected mole fraction profile and the measured chromatogram area. It is set that the linear regression curve intersects with the origin and the Response Factor (RF) is defined as the slope of the regression curve. Once the RF of a species is known, the mole fraction profile of the species in a sample can be acquired by dividing the found chromatogram area by the related RF.

Table 3.3: Retention times of the identified species, with the column, the carrier gas and the detector used.

Species		Column	Carrier gas	Detector	Retention time (min)
Formaldehyde	CH_2O	CPSIL5 CB	Helium	FID	3.8
Propane	C_3H_8	CPSIL5 CB	Helium	FID	4.0
Acetaldehyde	CH_3CHO	CPSIL5 CB	Helium	FID	4.5
Ethanol	C_2H_5O	CPSIL5 CB	Helium	FID	4.7
Acetic acid	CH_3COOH	CPSIL5 CB	Helium	FID	6.1
Formic acid	HOCHO	CPSIL5 CB	Helium	FID	6.6
Acetone	CH_3COCH_3	CPSIL5 CB	Helium	FID	6.9
Methyl pentanoate	$C_6H_{12}O_2$	CPSIL5 CB	Helium	FID	23.0
Methane	CH_4	HP-MOLSIEVE	Helium	FID	37.4
Carbon monoxide	CO	HP-MOLSIEVE	Helium	FID	44.0
Carbon dioxide	CO_2	HP-MOLSIEVE	Helium	FID	60.7
Ethylene	C_2H_4	HP-MOLSIEVE	Helium	FID	62.6
Acetylene	C_2H_2	HP-MOLSIEVE	Helium	FID	71.3
Argon	Ar	HP-MOLSIEVE	Helium	TCD	33.2
Water	H_2O	HP-MOLSIEVE	Helium	TCD	38.8
Hydrogen	H_2	HP-MOLSIEVE	Argon	TCD	5.4
Oxygen	O_2	HP-MOLSIEVE	Argon	TCD	5.9

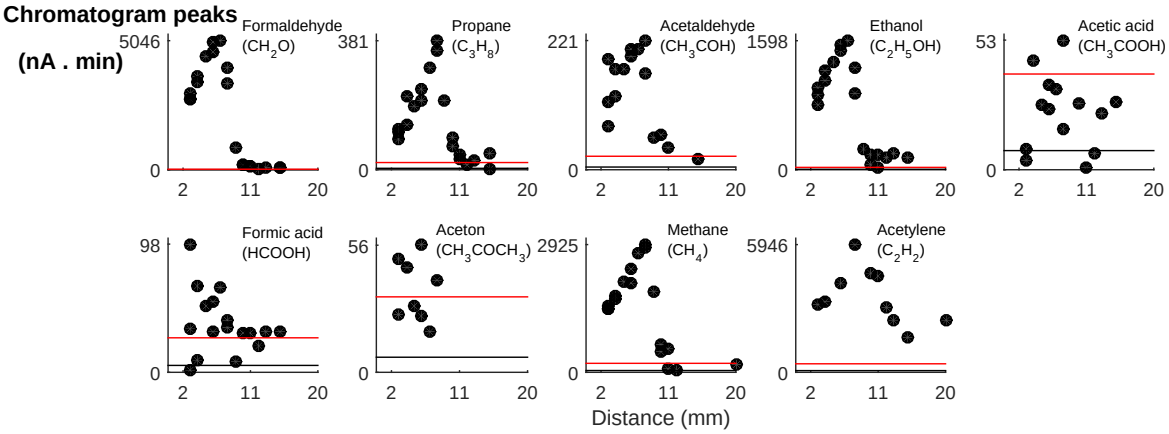

Figure 3.10: The Limits of Detection and Quantification (LoD and LoQ) visualised for intermediates. Most of the intermediates have chromatogram peaks higher than the LoQ, only acetic acid, formic acid, acetone and isopropanol have data points below LoQ, so their mole fraction profiles are not used to assess the performance of the MPE mechanism.

Response factors, the slope of the calibration curve, were obtained for the following permanent gases O_2, H_2, CO_2, CH_4, C_2H_4 and C_3H_8 (Figure 3.11). Mixtures with different mole fractions of the target gas added to Ar and O_2, were injected in the GC using the same compression method as during flame sampling and the pressure in the combustion chamber was maintained at 55 mbar. An overview of the experimental conditions and the repeatability of the experiments can be found in Appendix 1.

The values for the RF of the assessed permanent gases are given in Table 3.4. An absolute difference of only 3% has been found between the RF of CO_2 and CH_4. This can be explained by the use of a methanizer before FID. Since the two RF values of CO_2 and CH_4 are very close, the efficiency of the methanizer is close to 100%. It is assumed that CO has the same RF as CO_2, as this molecule is also hydrogenated by the methanizer to CH_4.

For C_2H_4 and C_3H_8 higher RF are found compared to CO_2 and CH_4. The sensitivity of the FID is 4.1 times higher for C_3H_8 and 1.5 times higher for C_2H_4 compared to CH_4. The FID detector is more sensitive to molecules with longer carbon chains, due to more ions formed by their combustion.

Hydrogen and oxygen are detected by TCD instead of FID. To calibrate H_2 and O_2 the GC carrier gas needs to be switched from helium to argon. The thermal conductivity of argon differs sufficiently with the one of hydrogen and oxygen The TCD is considerably more sensitive to H_2 than to O_2. The RF of H_2 is 8.6 times higher than the RF of O_2.

To check the linearity of the RF the coefficient of determination R^2 can be calculated,

$$R^2 = 1 - \frac{\sum_i (y_i - x_i)^2}{\sum_i (y_i - \bar{y})^2}, \tag{3.11}$$

where the dependent parameter y_i is the chromatogram area, the independent variable x_i the mole fraction of the species in the sample. The available model $\bar{y}$ is the linear regression of the data. When the value of the coefficient of determination is close to unity, the linear regression is valid and explains fully the deviation of the experimental data. For the calibration curves the coefficients of determination ranges from 0.90 for C_2H_2 to 1.00 for C_3H_8. The low value of R^2=0.90 for C_2H_2 is due to the experimental variability (Appendix 1).

The 95% uncertainty interval on the RF, can be calculated and is shown on Figure 3.11.

Table 3.4: The Response Factors (μV min·mole%$^{-1}$ or pA min·mole%$^{-1}$) for the six assessed permanent gases: O_2, H_2, CO_2, CH_4, C_2H_4 and C_3H_8. The gases containing carbon are detected by the FID, O_2 and H_2 are detected by TCD.

Species	Response Factor
CO_2	759 885 791
CH_4	781 591 418
C_2H_4	1 153 860 089
C_3H_8	3 127 321 676
H_2	1 062 783 830
O_2	124 082 490

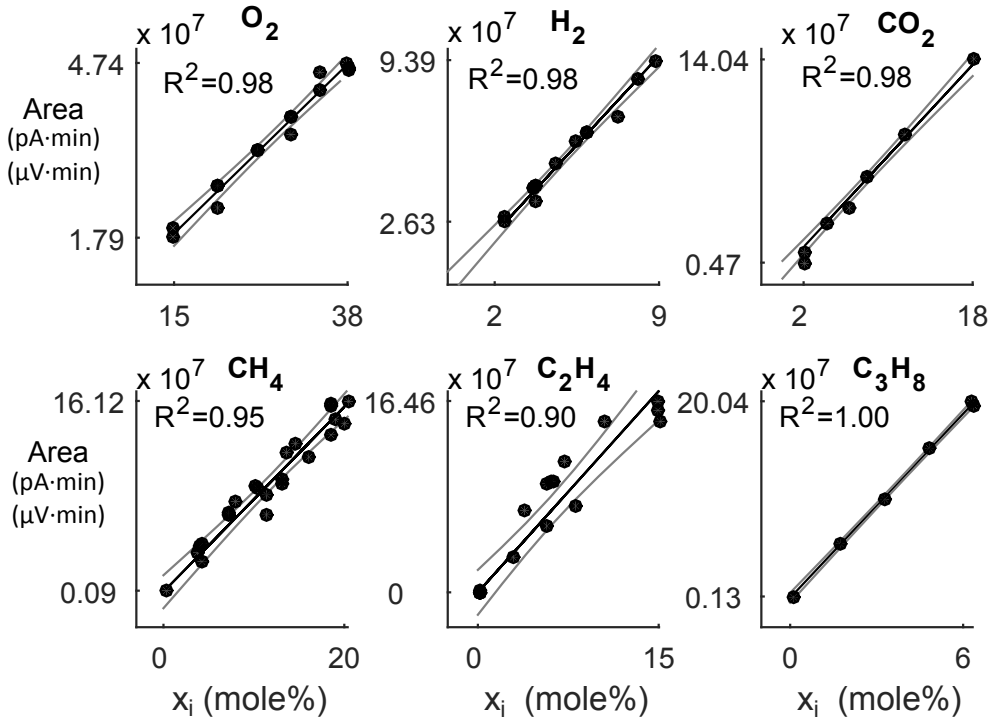

Figure 3.11: The calibration curve is obtained for six permanent gases: O_2, H_2, CO_2, CH_4, C_2H_4 and C_3H_8. The coefficient of determination R^2 is a measure for deviation of the experimental value from the found correlation. The lowest R^2 value of 0.9 was found for C_2H_4, meaning that 10% of the experimental deviation cannot be explained by the linear regression. Next to the R^2 values, the 95% uncertainty interval on the RF was calculated to use further in the uncertainty analysis.

The 95% confidence interval for each calibration curve can be expressed as

$$\hat{y} \pm t_{\alpha/2,n-2}\ \hat{\sigma}\ \sqrt{\frac{1}{n} + \frac{(x-\bar{x})^2}{\sum_{i=1}^{N}(x_i-\bar{x})^2}}, \tag{3.12}$$

with $\hat{y}$ the estimation of the dependent variable, the chromatogram area, x the independent variable, the mole fraction of the assessed species. $\bar{x}$ is the mean value of the assessed mole fractions and α is 5%. The Student's t distribution is applied as probability density functions, since the sample sizes are rather small, even for the t distribution. The t statistic, $t_{\alpha/2,n-2}$, is depending on the chosen confidence interval (1-α)100% and the degrees of freedom $n-2$, with n the sample size. The confidence interval is set to be 95%, so $\alpha = 0.05$. The standard deviation $\hat{s}$ is defined as

$$\hat{\sigma} = \sqrt{\frac{1}{n-2}\sum (y_i - \hat{y}_i)^2}. \tag{3.13}$$

The achieved uncertainty intervals are shown in Figure 3.11 and they are minimal at the mean mole fraction value. The assessed mole fraction range for calibration must lie around the expected mole fractions in the flame, to achieve a RF with a low uncertainty.

In Figure 3.12, the absolute values for the 95% confidence intervals related to the calibration curves in Figure 3.11 are shown in a different way. The absolute values of the confidence

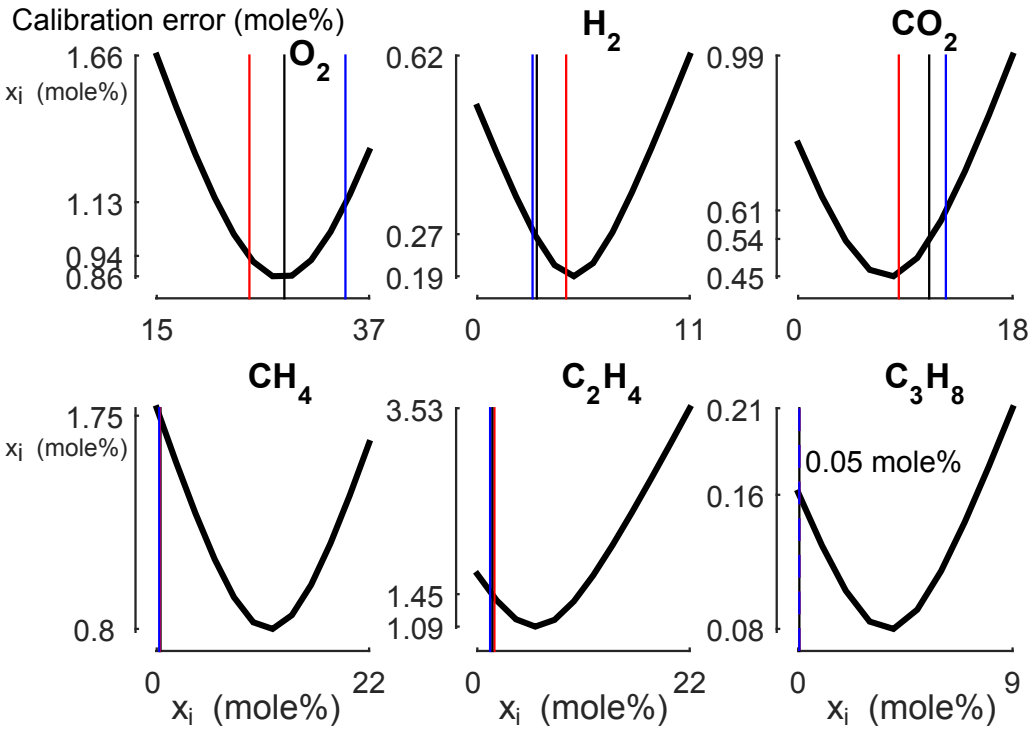

Figure 3.12: The absolute uncertainty related to calibration is expressed in mole fraction for the six calibrated permanent gases by dividing the areas related to the 95% uncertainty interval in Figure 3.11 by the RF. In addition, the input mole fraction for oxygen are shown for the rich (red line), stoichiometric (black line) and lean (blue line) flame, as well as the simulated equilibrium concentrations for H_2 and CO_2 and the maximal simulated mole fraction for CH_4, C_2H_4 and C_3H_8. The uncertainty by calibration on the oxygen and CO_2 mole fraction is relatively low, due to a good choice of the concentration range for the calibration. However, high uncertainties are found for the intermediates since the calibration is conducted for concentrations far higher than the samples. The uncertainty due to calibration is maximal for CH_4. An uncertainty of 1.75 mole% is found for all the flames, while the maximal simulated concentration is only 0.3 mole%.

intervals are divided by the related RF, resulting in a confidence interval expressed in mole fraction instead of chromatogram area. The red line is the inlet oxygen mole fraction of the rich flame, the black one of the stoichiometric flame and the blue one of the lean flame. The uncertainty due to the calibration on the fresh oxygen mole fraction ranges between 0.86 mole% to 1.13 mole% for the MPE flames, which is relatively low compared to the inlet mole fraction ranging from 24.6 to 34.6 mole%.

The maximal simulated mole fractions are shown for H_2 and CO_2 in the three MPE flames. The uncertainty for these mole fraction values does not exceed 1 mole%, since the calibration range is well chosen. Calibration leads to an uncertainty of 0.27 mole% on the maximal H_2 mole fraction in the stoichiometric and lean MPE flame. The uncertainty on the CO_2 mole fraction lies withing 0.45 to 0.61 mole%.

The other permanent gases have a higher uncertainty on the calibration, even in the range of their experimental measured mole concentrations. The maximal simulated mole fraction for C_2H_4 is 1.3, 1.6 and 1.8 mole%, for the lean, stoichiometric and rich MPE flame respectively.

Table 3.5: Due to calibration, an absolute uncertainty (AU) of maximum 1 mole% is found for O_2, H_2 and CO_2. The highest relative uncertainty (RU) of 673% is found for H_2 in the stoichiometric flame. A RU of 12.6% is found, due to the low equilibrium concentration of 2.45 mole% for H_2 in the stoichiometric MPE flame.
For the intermediates CH_4, C_2H_4 and C_3H_8, the uncertainty due to calibration has the same order of magnitude or even higher than the simulated mole fraction profiles.

Equivalence ratio	O_2 mole%	AU	RU	H_2 mole%	AU	RU	CO_2 mole%	AU	RU
ϕ=1.41	24.51	±0.94	3.8%	4.56	±0.20	4.4%	8.77	±0.47	5.4%
ϕ=1.15	28.02	±0.86	3.0%	2.45	±0.31	12.6%	11.5	±0.56	4.9%
ϕ=0.88	34.55	±1.13	3.3%	2.45	±0.28	12.1%	12.3	±0.61	5.0%
Equivalence ratio	CH_4 mole%	AU	RU	C_2H_4 mole%	AU	RU	C_3H_8 mole%	AU	RU
ϕ=1.41	0.44	±1.73	393%	2.0	±1.38	69%	0.03	±0.16	533%
ϕ=1.15	0.35	±1.74	497%	1.6	±1.44	90%	0.03	±0.16	533%
ϕ=0.88	0.26	±1.75	673%	1.32	±1.50	114%	0.03	±0.16	533%

The related error due to calibration is 1.45 mole% for the lean and stoichiometric flame and 1.1 mole% for the rich MPE flame. The calibration error is the same order of magnitude as the simulated mole fraction. For CH_4 and C_3H_8, the uncertainty due to calibration is even higher than the expected concentration. The uncertainty due to calibration can be lowered, if the calibration is conducted for a lower concentration range.

Another source of uncertainty related to the calibration that is not quantified is the difference in temperature between the flame samples and the samples used for calibration. The pressure achieved by compressing a flame sample is higher than the pressure found for a calibration sample, since its temperature is higher. This can have an effect on the GC injection pressure. Nevertheless, the injection pressure was monitored and no substantial differences between both set of samples was found.

A different calibration method is used for the intermediates that are not permanent gases. Formaldehyde, acetaldehyde, formic acid and acetone are liquid at standard conditions. The calibration has been conducted by Mbuyi [70]. The method is as follows: a sample of the liquid compounds is equilibrated at a temperature of 295 K. With the Antoine equation for these liquids, the partial pressure in the bottle can be calculated. Mbuyi took a sample with a syringe of the airspace of the bottles and diluted it with air before injection. Different dilutions result in different mole fractions of the species of interest, and the calibration curves can be obtained. The achieved RF for the species in liquid state at ambient conditions can be found in Table 3.6, together with the coefficient of determination, R^2. No uncertainty analysis is conducted on the obtained RF's of these intermediates.

A separate calibration is performed for MPE using the full experimental setup. If mixtures of vaporised fuel/O_2/Ar are injected without a flame, condensation risks occur (Figure 3.5). Therefore, the calibration of MPE should be done with caution.

The results for the MPE calibration compared with the measurements in the stoichiometric MPE flame can be found in Figure 3.13. Condensation in the compression system of the

Table 3.6: Response factors for liquid compounds with their coefficient of determination R^2 [70]

Species		Response Factor	R^2
Formaldehyde	CH_2O	9 584	0.99
Acetaldehyde	CH_3CHO	25 944	0.94
Formic acid	$HCOOH$	78 047	0.99
Acetone	CH_3COCH_3	61 068	0.98

$MPE/O_2/Ar$ mixture happens at a concentration of 0.87 mole% MPE, leading to a constant area measured for samples with a higher fuel concentration. The MPE concentrations measured in the stoichiometric flame are below 0.46 mole%, so the obtained areas can be converted by the obtained calibration curve.

Next to the 95% uncertainty interval is calculated and converted to mole fraction. The uncertainty, due to calibration, of the maximum concentration of 0.45 mole% measured in the stoichiometric flame is 0.06 mole% or around 13% relatively. The uncertainty on the lower concentrations even increases.

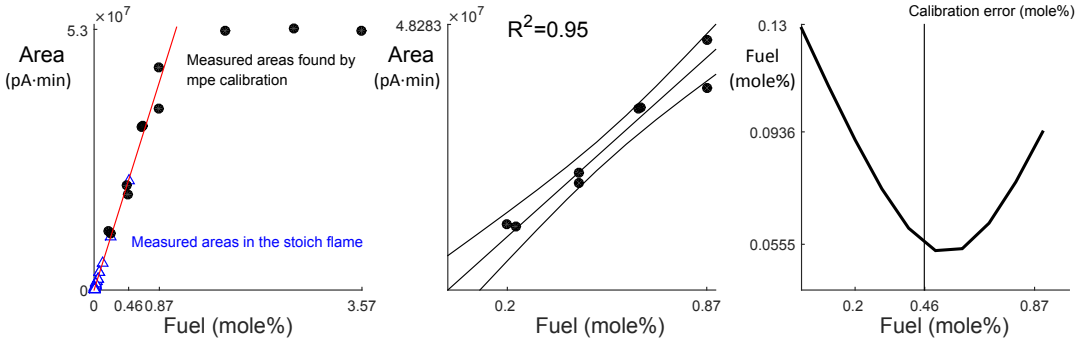

Figure 3.13: The calibration of MPE in the stoichiometric MPE flame. Samples with increasing fuel concentration are injected, however condensation occurs at a concentration of 0.87 mole%

3.6 Error and uncertainty from experimental setup

The obtained mole fraction profiles are affected by errors and uncertainties related to the experimental setup. The total uncertainty on the mole fraction profiles needs to be determined. Different experimental parameters and variables are monitored or controlled during the experiments. Controlled parameters are the mass flow rate of the fuel, the volume flow rate of the gases and the pressure in the combustion chamber. The monitored variables are the temperature of the burner surface, the temperature and pressure after the sampling cone and the pressure and temperature at the inlet of the GC equipment. The error and uncertainty on these parameters and variables indicate the quality and reliability of the measurements.

Uncertainty is not the same as error. Error is the difference between the measured value and the true value of the measurand, while uncertainty expresses a range in which the true values may lie [89]. To perform error and uncertainty analysis, some definitions are needed,

like measurand and influence quantities. The measurand is a well-defined physical property, like the pressure in the combustion chamber or the mass flow of the fuel. The value of the measurand is determined by measurement, however the measured values are only an estimation of the real value of the measurand, due to influence quantities: parameters or variables that affects the measurement, e.g. the temperature of the combustion chamber if the pressure in the combustion chamber is measured.

3.6.1 Error analysis

Error is defined as the true value of the measurand minus the result of the measurement. Errors occur since measurements are imperfect. An error has two components: a random and systematic component. The random error appears as influence quantities vary unpredictably and affect the measurement. It is impossible to correct this effect, even if this type of error can be reduced by increasing number of observations. In this case, the expected value for random error curtails to zero if the amount of measurements increases. Systematic errors are related to effects of influence quantities which can be identified and quantified. If the size of the systematic error is significant, a correction can be applied. Calibration or adjustments of measuring devices can eliminate systematic errors.

In the case of the assessed experimental setup, the random errors are assumed zero due to the contineous monitoring. From analysis of the monitoring data, the values for the parameters and variables are constant during experiments and sampling. The controlled parameter with the highest variation during sampling is the mass flow of the fuel (Figure 3.14 and Appendix 2). For the stoichiometric MPE flame the fuel mass flow is set to 100 $g{\cdot}h^{-1}$ and has a standard deviation of 1 $g{\cdot}h^{-1}$, which is assumed to be more an uncertainty than an error. For every other controlled or monitored parameter, less variation during sampling is found and the variations are seen as uncertainty and not as a random error.

The systematic errors of the experimental setup is related to the calibration of the controllers. The systematic error of a controller is given by the manufacturer. Two types of errors are stated by Bronkhorst, the manufacturer of the used mass and flow controllers. The first type is a full scale error, which is defined as a percentage of the maximum value. Next to a Full scale error (FS), a Reading error (Rd) is denoted. This is a percentage of the value the controller is set to. The values for the two errors of the controllers are given in Table 3.7.

Table 3.7: The systematic error of a controller is defined as the addition of a full scale and a reading error. The full scale and reading error for the used MFCs and pressure sensors can be found in the technical data sheets. Once the total systematic error is known, the relative error (RE) of a parameter can be calculated.

Controlled Parameter		Accuracy		Full scale		Set value		RE
	Type	Full scale	Reading				Total error	(%)
$\dot{m}_{fuel}$	Mini Coriflow		0.20%	120	$g{\cdot}h^{-1}$	100	± 0.2	0.2
$\dot{v}_{Ar_1}$	Bronkhorst F-201CV	0.10%	0.50%	4	$L{\cdot}min^{-1}$	2	± 0.014	0.7
$\dot{v}_{Ar_2}$	El-flow	0.10%	0.50%	2	$L{\cdot}min^{-1}$	2	± 0.012	0.6
$\dot{v}_{O_2}$	Bronkhorst F-201CV	0.10%	0.50%	4	$L{\cdot}min^{-1}$	2	± 0.014	0.7
						2.45	± 0.016	0.65
						3.2	± 0.020	0.63

For the volume flow controllers, a full scale and reading error are given. For the fuel mass flow controller only a reading error is defined in the technical data sheets. The FS and Rd can be added, as clarified in following calculation example:
The maximum flow for a Bronkhorst F-201CV stream is 4 L·min^{-1}. The FS error is 0.1%, so 0.004 L·min^{-1}. The Rd is 0.5%, which is 0.02 L·min^{-1}. The total error is adding up the FS and Rd error, resulting in 0.024 L·min^{-1}. If the flow is changed to 2 L·min^{-1} the 0.1% FS stays the same and 0.5% Rd is 0.01 L·min^{-1}. The total error is now 0.014 L·min^{-1}.

The error on the fuel mass flow rate only consists of an Rd error, resulting in an experimental error of 0.2 g·h^{-1}, or a relative error of 0.2%. The two argon flows are controlled by different MFCs, with the same FS and Rd error. However, due to a different full scale value, the error on the argon flow controlled with the Bronkhorst F-201CV is 0.014 L·min^{-1} and the error on the EL-FLOW controlled stream is 0.012 L·min^{-1}. Since the error of the oxygen volume flow is depending on the set value, the total experimental error varies between the different MPE flames, ranging from 0.014 to 0.020 L·min^{-1}. All these experimental errors are lower than 1% of the set value.

The error on the mole fraction of the measured species and the equivalence ratio ϕ of the samples can be calculated from the MFC systematic errors by error propagation. Errors of different controlled variables cannot be added together, since error propagation is based on probability. If two parameters, which errors δa and δb are random and uncorrelated, are added together, their combined error δQ propagates in quadrature:

$$\delta Q = \sqrt{(\delta a)^2 + (\delta b)^2}. \tag{3.14}$$

When the parameters are multiplied or divided by each other, the fractional errors add in quadrature.

$$\frac{\delta Q}{|Q|} = \sqrt{\left(\frac{\delta a}{|a|}\right)^2 + \left(\frac{\delta b}{|b|}\right)^2} \tag{3.15}$$

where $|a|$ and $|b|$ are the values for parameter a and b and Q the measured value.

To calculate the error on the total mole flow, the errors of the mass flow of the fuel and the volume flows of O_2 and Ar need to be added. To make the addition possible, the unit of all the flows are converted to mole·s^{-1}. The error on the total mole flow is

$$\delta\dot{n} = \sqrt{(\delta\dot{n}_{Ar,1})^2 + (\delta\dot{n}_{Ar,2})^2 + (\delta\dot{n}_{O_2})^2 + (\delta\dot{n}_{fuel})^2} \tag{3.16}$$

with $\delta\dot{n}_{Ar,1}$, $\delta\dot{n}_{Ar,2}$, $\delta\dot{n}_{O_2}$ and $\delta\dot{n}_{fuel}$ the error on the argon, oxygen and fuel mole flow respectively.

The error on the mole fraction of a reactant is depending on the error of the total mole flow and the mole flow of the specific reactants.

$$\delta X_{Ar} = |X_{Ar}| \cdot \sqrt{\left(\frac{\delta\dot{n}_{Ar,1}}{|\dot{n}_{Ar,1}|}\right)^2 + \left(\frac{\delta\dot{n}_{Ar,2}}{|\dot{n}_{Ar,2}|}\right)^2 + \left(\frac{\delta\dot{n}_{O_2}}{|\dot{n}_{O_2}|}\right)^2 + \left(\frac{\delta\dot{n}_{fuel}}{|\dot{n}_{fuel}|}\right)^2} \tag{3.17}$$

$$\delta X_{O_2} = |X_{O_2}| \cdot \sqrt{\left(\frac{\delta\dot{n}_{Ar,1}}{|\dot{n}_{Ar,1}|}\right)^2 + \left(\frac{\delta\dot{n}_{Ar,2}}{|\dot{n}_{Ar,2}|}\right)^2 + \left(\frac{\delta\dot{n}_{O_2}}{|\dot{n}_{O_2}|}\right)^2 + \left(\frac{\delta\dot{n}_{fuel}}{|\dot{n}_{fuel}|}\right)^2} \tag{3.18}$$

$$\delta X_{fuel} = |X_{fuel}| \cdot \sqrt{\left(\frac{\delta\dot{n}_{Ar,1}}{|\dot{n}_{Ar,1}|}\right)^2 + \left(\frac{\delta\dot{n}_{Ar,2}}{|\dot{n}_{Ar,2}|}\right)^2 + \left(\frac{\delta\dot{n}_{O_2}}{|\dot{n}_{O_2}|}\right)^2 + \left(\frac{\delta\dot{n}_{fuel}}{|\dot{n}_{fuel}|}\right)^2} \tag{3.19}$$

The error of the equivalence ratio ϕ is based on the error of the fuel and oxygen flow.

$$\delta\phi = |\phi| \cdot \sqrt{\left(\frac{\delta\dot{n}_{O_2}}{|\dot{n}_{O_2}|}\right)^2 + \left(\frac{\delta\dot{n}_{fuel}}{|\dot{n}_{fuel}|}\right)^2} \tag{3.20}$$

The theoretical values for the total mass flow, mole fraction and equivalence ratio with their absolute and relative error can be found in Table 3.8. The errors between the flames differ due to the O_2 stream. The O_2 stream is the only changing parameter and its relative error increases with the equivalence ratio. Overall, the systematic errors are less than 1% of the parameter value.

The error on the pressure in the combustion chamber and after the sampling cone are presented in Table 3.9. The pressure in the combustion chamber has an influence on the flame structure, especially on the flame thickness. Another error that affects the position of flame is the reading error on the position of the burner. The position of the burner is manually adjusted, and a reading error of 0.01 mm can occur. Next to these direct errors, the shape and nozzle size of the sampling cone can have an effect on the sampling position [90, 91]. The error on the pressure, position of the burner and the nozzle, affect the position of the flame more than the error due to manually adjustments. The main purpose of the uncertainty analysis is to quantify the error on the mole fraction profiles and not on the position of the flame. Therefore, these errors will not be quantified further.

3.6.2 Uncertainty analysis

Once the systematic errors are quantified, the uncertainty on the flame parameters can be determined. Uncertainty is related to the measurement results and expresses the scattering of the measured values which could be attributed to the measurand. Uncertainty can be expressed by statistical methods (Category A) or by other means (Category B). Uncertainty of Catagory A is characterised by the estimated variance σ^2 and the number of degrees of freedom $n-2$. If parameters are dependent on each other, the covariance should also be given. When the variance cannot be conducted from data, an approximation of the variance can be made, u^2. The uncertainty is then from Category B [89].

In this case, the uncertainty of the experimental setup is defined as the standard deviation of the monitoring data, so the uncertainty is Category A. The analysis focuses on the composition of the sample.

The composition of the flame is determined by the equivalence ratio ϕ and the argon dilution X_{Ar}. Amid the sampling, which takes 45 s, the input parameters are measured 45 times. The mean parameter values during sampling are given in Figure 3.14 for the rich, stoichiometric and lean MPE flames. To see the average parameters values of the samples distinctively, they are plotted with distance to the burner on the x-axis. By representing the samples spatially, we can see if parameters are affected by the distance to the sampling cone.

The 95% confidence interval of the mean value is calculated assuming a normal distribution of the measurements. The confidence interval is than

$$95\%CI = 1.96\frac{s}{n}, \tag{3.21}$$

where s is the standard deviation of the data, n the number of measurements. The intervals are visualised in Figure 3.14.

Table 3.8: Systematic error on the total mass flow, mole fraction profiles of the reactants and the equivalence ratio for the assessed MPE flames

ϕ	$\dot{n}_{\text{total}}$ (mole·s^{-1})	%	X_{Ar} (mole%)	%	X_{O_2} (mole%)	%	X_{MPE} (mole%)	%	ϕ (-)	%
ϕ=1.41	0.0055 $\pm 2.03 \cdot 10^{-5}$	0.37	70.84 ±0.42	0.59	24.79 ±0.20	0.79	4.37 ±0.03	0.72	1.41 ±0.01	0.94
ϕ=1.15	0.0058 $\pm 2.10 \cdot 10^{-5}$	0.36	67.09 ±0.39	0.59	28.77 ±0.22	0.76	4.14 ±0.03	0.72	1.15 ±0.01	0.91
ϕ=0.88	0.0063 $\pm 2.25 \cdot 10^{-5}$	0.36	61.66 ±0.36	0.58	34.57 ±0.25	0.72	3.81 ±0.03	0.72	0.88 ±0.01	0.88

Table 3.9: The systematic error on the pressure sensors.

Monitored Parameter	Type	Accuracy Error of Reading	Set value		Total error	RE (%)
P_{comb}	Pfeiffer Vacuum Type CMR 361	0.20%	55	mbar	± 0.11	0.2
P_{cone}	Pfeiffer Vacuum Type CMR 361	0.20%	16	mbar	± 0.032	0.2

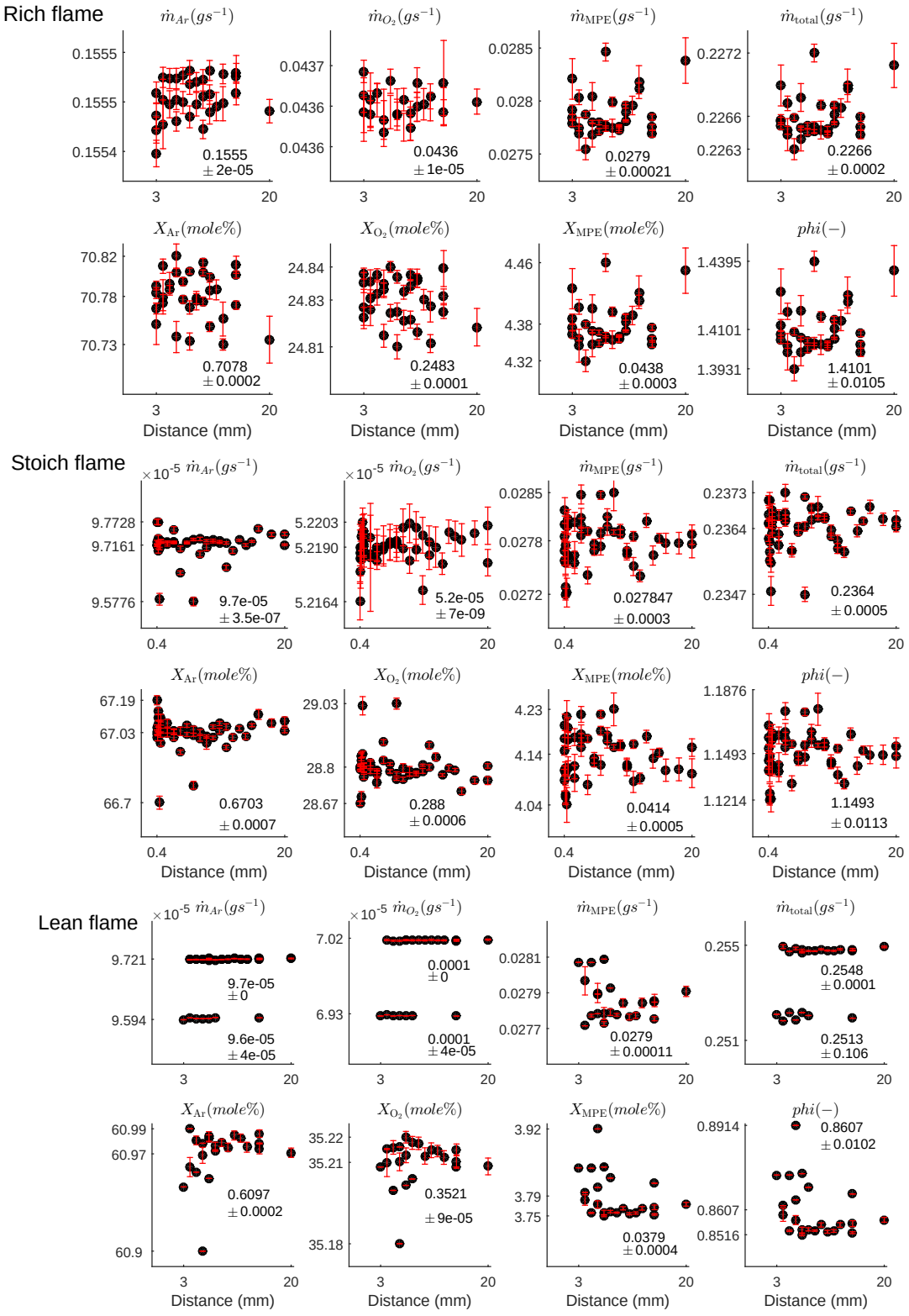

Figure 3.14: The mean input value and their experimental uncertainty for each sample. Overal, the mass flow of the fuel influences the equivalence ratio, composition and total mass flow of the sample. Nevertheless, the experimental uncertainties are small compared to the systematic error related to the accuracy of the mass flow controllers.

For the rich MPE flame, the volume flow of argon and oxygen does not vary during sampling and between the different samples. The mass flow of the fuel is more affected by sampling (Appendix 2), leading to a maximal variation of 2.5 $g \cdot h^{-1}$ between the average values for every sample in the rich flame. The variation of the fuel mass flow affects the equivalence ratio ϕ of the samples and the mole fraction profiles of Ar, O_2 and MPE (Figure 3.14). The equivalence ratio of the rich flame samples ranges between 1.39 and 1.44, while the mean value is the theoretical value of 1.41. Although the volume flow of argon and oxygen do not vary significant, their mole fraction profiles are affected by the variation of the fuel mass flow, leading to a variation of 0.1 mole% for argon and 0.03 mole% for oxygen. Besides the equivalence ratio, the total mass flow is related to the mass flow of the fuel, with a variation of 0.4%.

In the stoichiometric MPE flame, there is more variation in the flow of the gases and the fuel. The average equivalence ratio of the samples ranges between 1.12 and 1.19. The greater uncertainty is caused mainly by the variation in mass flow of the fuel. Besides, the repeatability of the argon volume flow is not as good as in the rich flame. For four samples, the volume flow of argon drops, leading to an argon dilution lower than 67 mole%. This is due to the EL-FLOW MFC, which is not able to maintain a constant mass flow due to blockages in the ECM. The effect on the four measurements are assessed small enough to withhold the four measurements.

The mean values for the mass flows and mole fraction profiles in the lean flame can also be found in Figure 3.14. The measurements were done at two different time periods, due to technical problems. The setup was dismantled and after maintenance a difference in parameter values is seen. The argon and oxygen mole flow differs with 0.003 and 0.002 $mole \cdot s^{-1}$ respectively, which is around 1 to 1.5% of the total value. The difference can be explained by the dismantling and different ambient conditions on the days of the experiments. The changes have an effect on the total mass flow rate, nevertheless the equivalence ratio and mole fraction profiles are less affected by the changes. Since the sample is compressed to atmospheric pressure and the pressure in the combustion chamber is constant (55.4±0.06, Figure 3.15) for all samples, it is assumed that the changes have a minimal effect on the achieved samples and all the measurements are kept.

The uncertainty on the pressure in the combustion chamber, the pressure of the sample by injection to the GC and the temperature at the injection in the GC can be found in Figure 3.15. In the rich MPE flame, an average value of 55.4 ± 0.09 mbar is found for the pressure in the combustion chamber, with a minimum value of 55.3 mbar and a maximum value of 55.8 mbar, meaning that the pressure only fluctuates with 0.7% experimentally. Values with the same order of magnitude are found for the stoichiometric flame. For this flame, an overal average of 55.5 ± 0.21 mbar is found and between the samples, the pressure only varies with 1.6% between the maximum and minimum pressure. The same results were found for the lean MPE flame.

The pressure difference between the injected sample and the atmospheric pressure is very low, indicating that the obtained chromatograms are reliable. The injection pressure is also almost the same for all the three flames, indicating that there is little variation in the compression process between the flames. The temperature of the compression system is only for the stoichiometric flame high enough to prevent condensation fully. For the other two flames, the temperature measured at the compression system is not high enough to prevent condensation. The heating of the compression system could not be increased due to limitation of the electrical circuit. Therefore, a separate electrical circuit is needed in further research,

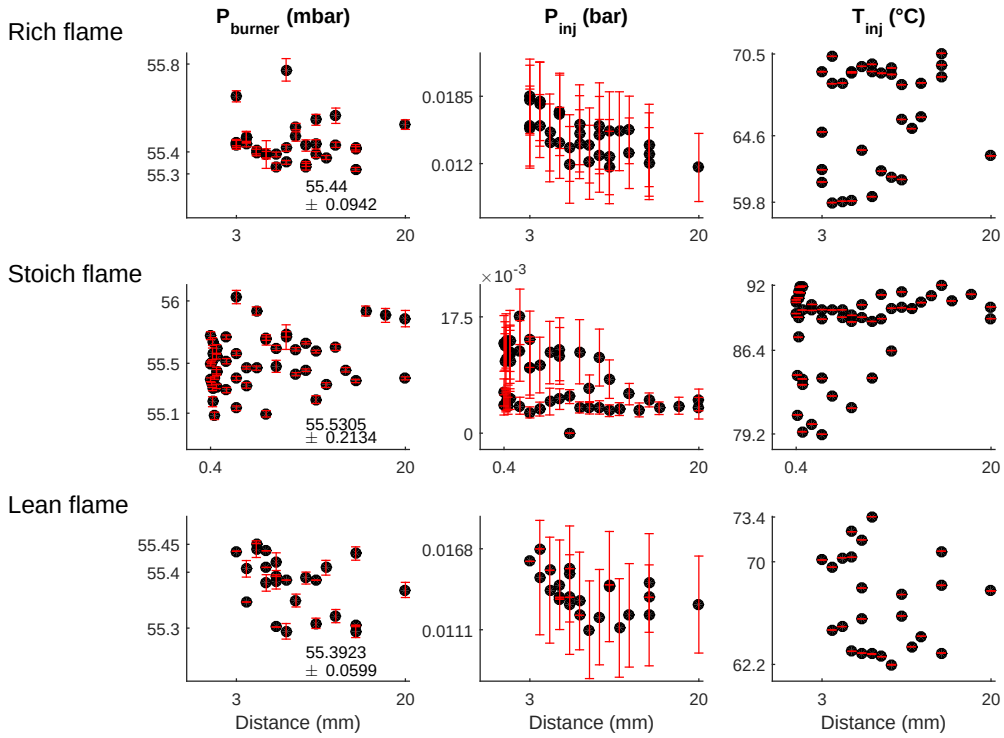

Figure 3.15: The pressure in the combustion chamber does not vary between the measurements and during the sampling. The pressure of the sample injection is low enough to not skew the chromatogram. The injection system is heated at different temperatures during the measurements, this can have an influence on the amount of moles injected in the GC. However, the injection column of the GC is kept at a constant temperature of 40°C

to be able to heat the compression system enough to prevent condensation. The condensation of MPE is seen in the chromatogram. Nevertheless, after cleaning the compression system, the same mole fraction profiles for other species were measured at the same flame position, indicating that the condensation of MPE have only a small effect on the mole fraction profiles of the other species.

3.7 Total uncertainty

The theoretical parameter values with their error related to the accurancy of the MFCs and the experimentally measured parameter values with the standard deviation, are presented in Table 3.10. Overall, the experimental uncertainty is smaller than the systematic error. Only for the mole fraction of the fuel and the equivalence ratio, they have the same order of magnitude. They are added together by error propagation to obtain the total uncertainty.

The total uncertainty on the equivalence ratio ϕ, argon dilution and total mass flow affects the composition of the samples. To quantify the effect of these variations on the mole fraction profiles, simulations with the total uncertainty extremities are conducted.

Simulations for an equivalence ratio ranging from 1.38 to 1.44, an argon dilution varying from 70.4 to 71.2 mole% and a total mass flow between 0.2258 and 0.2274 g·s^{-1} are conducted

Table 3.10: The experimental error related to the accuracy of the MFCs and uncertainty on experimental parameters during experiments. The total error is mostly defined by the accuracy of the MFCs, the experimental variability is negligible.

	$\dot{m}_{total}$ (g·s^{-1})	X_{Ar} (mole%)	X_{O_2} (mole%)	X_{MPE} (mole%)	ϕ (-)
			ϕ = **1.41**		
Error	0.226±5.4·10^{-3}	70.84 ±0.42	24.79 ±0.20	4.37 ±0.03	1.41 ±0.01
Uncertainty	0.227±4.8·10^{-6}	70.78±0.02	24.83±0.01	4.38±0.03	1.41 ±0.01
TOTAL	0.226±5.4·10^{-3}	70.8±0.42	24.8 ±0.20	4.4 ±0.04	1.41 ±0.02
			ϕ = **1.15**		
Error	0.236±5.3·10^{-3}	67.09 ±0.39	28.77±0.22	4.14 ±0.03	1.15 ±0.01
Uncertainty	0.236±1.2·10^{-5}	67.03±0.07	28.8±0.06	4.14±0.05	1.15±0.01
TOTAL	0.236±5.3·10^{-3}	67.1 ±0.40	28.8± 0.23	4.1 ±0.06	1.15 ±0.02
			ϕ = **0.88**		
Error	0.253±5.3·10^{-3}	61.66 ±0.36	34.57 ±0.25	3.81 ±0.03	0.88 ±0.01
Uncertainty	0.252±1.1·10^{-5}	60.97±0.01	35.2 ±0.005	3.79±0.03	0.86 ±0.01
TOTAL	0.252±5.3·10^{-3}	61.7 ±0.36	34.5 ±0.25	3.8 ±0.04	0.88 ±0.01

for the rich MPE flame with the OpenSMOKE software. The kinetic mechanism proposed by Dayma et al. is used. The same simulation is done for the stoichiometric and lean MPE flame with the total uncertainties stated in Table 3.10.

The uncertainty on the mole fraction profiles of eight permanent gases, is assessed and the results are shown in Table 3.11. The assessed species are: oxygen (O_2), carbon monoxide (CO), carbon dioxide (CO_2), hydrogen (H_2), methane (CH_4), ethylene (C_2H_2), acetylene (C_2H_4), and propane (C_3H_8).

The main contribution to the uncertainty on the mole fraction profiles is the calibration. For some of the intermediates with a low concentration, the uncertainty is even higher than the expected mole fraction. The variation in total mass flow in the rich and stoichiometric MPE flame has only an effect smaller than 1%. The experimental uncertainty on the equivalence ratio ϕ has a greater effect, especially on intermediate species like H_2, CH_4, C_2H_4 and C_2H_2. The lean MPE flames seems more sensitive to variation in the argon dilution than the other MPE flames.

The relative uncertainty for a certain species changes between the flames, mainly due to differences in calibration uncertainty and systematic error. The uncertainties found for O_2, CO_2, CO and H_2 can be used directly on the mole fraction profiles in the flames. However, for the other assessed permanent gases, the uncertainty due to calibration is higher than their expected mole fraction. The uncertainty due to the systematic error on these compounds is maximal 8% (C_2H_2 in the stoichiometric flame).

If zero is seen as part of the calibration curve, an overestimation of the uncertainty due to calibration is made for species with a low concentration. Applying the 95% uncertainty interval of the calibration curve results can lead to an uncertainty which is higher than the measured concentration, a relative uncertainty higher than 100%. Therefore, an relative uncertainty limit of 25% is implied for species with a low concentration.

Table 3.11: Relative uncertainty on the mole fraction profiles for 9 of the measured permanent gases due to the experimental setup and calibration. The uncertainty due to the experimental setup is related to the uncertainty on the total mass flow $\dot{m}$, the argon dilution Ar and the equivalence ratio ϕ For the intermediates, CH_4,C_2H_2, C_2H_4 and C_3H_8 the uncertainty due to calibration is higher than the measured mole fraction, resulting in relative uncertainties higher than 100%. The total relative uncertainty is calculated using error propagation.

	O_2	CO_2	CO	H_2	CH_4	C_2H_2	C_2H_4	C_3H_8
RU (%)	Rich MPE flame							
Calibration	3.8	5.4	5.0	4.4	*393*	*366*	*69*	*533*
$\dot{m}$	0.009	0.03	0.04	0.05	0.23	0.20	0.22	0.32
Ar	0.54	0.45	0.41	0.40	0.43	0.32	0.39	0.27
ϕ	0.11	2.79	2.84	5.34	3.86	7.39	2.84	1.50
TOTAL	3.84	6.10	5.76	6.93	393	366	69	533
without calibration	0.55	2.83	2.87	5.35	3.89	7.40	2.87	1.50
RU (%)	Stoichiometric MPE flame							
Calibration	3.0	4.9	4.9	12.6	*497*	*683*	*90*	*533*
$\dot{m}$	0.03	0.08	0.10	0.18	0.19	0.40	0.31	0.38
Ar	0.57	0.52	0.44	0.44	0.48	0.36	0.45	0.29
ϕ	0.14	0.86	3.07	4.71	3.47	7.66	3.44	0.31
TOTAL	3.06	5.00	5.80	13.46	497	683	90	533
without calibration	0.59	1.01	3.10	4.74	3.51	7.68	3.48	0.56
RU (%)	Lean MPE flame							
Calibration	1.13	5.0	5.1	12.1	*673*	*1179*	*114*	*533*
$\dot{m}$	2.20	1.51	0.10	0.88	0.57	2.25	0.36	0.38
Ar	5.96	5.57	4.59	4.57	4.98	3.64	4.63	3.24
ϕ	2.11	2.00	2.30	3.05	2.97	3.95	2.63	1.34
TOTAL	6.79	7.89	7.23	13.32	673	1179	114	533
without calibration	6.69	6.11	5.13	5.56	5.83	5.82	5.34	3.53

4
Numerical simulations

The description of the Botha-Spalding burner and mathematical equations related to laminar premixed flames are given in Section 4.1. The laminar flat flame simulations are conducted by OpenSMOKE is a framework written in object-oriented C++, created by the Politechnico di Milano to perform detailed kinetic numerical simulations of reacting flows [11].

The framework of simulation software OpenSMOKE is a set of C++ libraries, which contains functions to run the simulations based on the implied kinetic mechanism, thermodynamic and transport properties and computional preferences like the wanted level of convergence [11].

Different combustion configurations can be simulated with the OpenSMOKE software. Some examples are homogeneous ignition delay, perfectly stirred reactors, premixed burner stabilised flames or laminar flame velocity calculations. No graphical interface is available, the solvers are run by command line.

In Section 4.2, the equations which the OpenSMOKE software use to determine the flame properties, are discussed in detail. The content of the input files in CHEMKIN format [92] and how to use the CHEMKIN input files are also described.

Next, the MPE mechanism is described in Section 4.3 and the methodology of the sensitivity and reaction flow analysis applied on the simulation results are explained in Sections 4.4 and 4.5. In Section 4.7 the use of OpenSMOKE is explained.

4.1 Mathematical description of premixed laminar flat flames

The burner on which the laminar flame is stabilised, is a poreus disk. The flame is ignited downstream the burner disk. The flame travels to the burner when the flame speed is higher than the stream velocity of the fresh gases. If the flame speed does not exceed the stream velocity of the fresh gases, the flame will not be able to stabilise and is blown off.

The burner disk is cooled and the closer the flame propagates to the burner the more heat losses occur. When the flame looses heat, it flame speed reduces. The flame stabilises at the position where the flame speed velocity and the flow velocity of the unburned gases equilibrate. In Figure 4.1 a, different positions at which a flame can stabilise are visualised, with in Figure 4.1 the related temperature profiles of the flames. When the flame front is not in contact with the burner disk, the same temperature profile will be found. However, if the flame stabilises closer to the burner disk, e.g. flame 4, more heat is extracted and the flame temperature decreases.

Three conservation equations apply on laminar flat flames. When the flame effects at the edge of the burner are neglected and only the flat flame front is taken account, the properties of the laminar flame only depend on the distance from the burner. Only one spatial coordinate z is needed to describe the laminar flat flame [93].

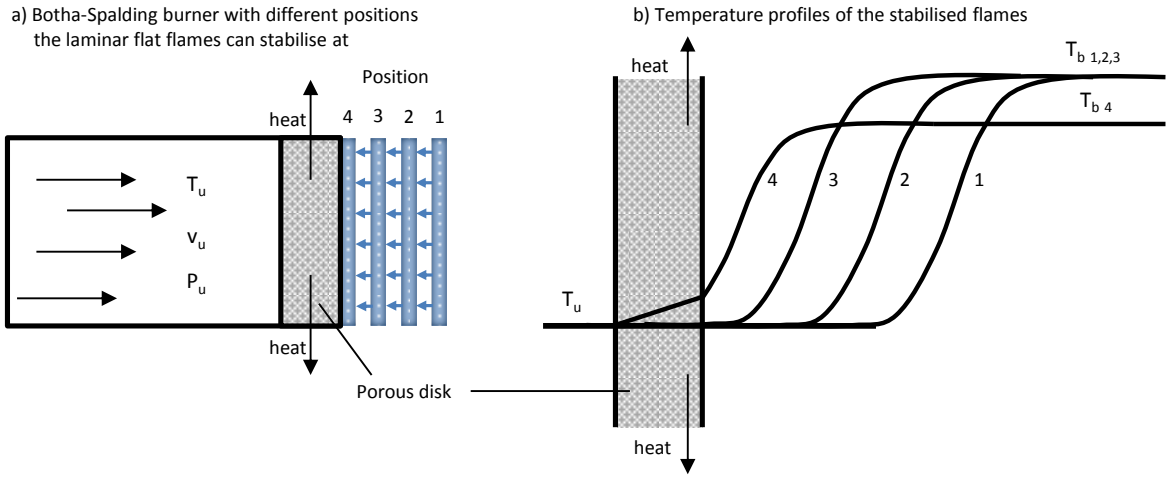

Figure 4.1: a) The laminar flame can stabilise at different positions. The position is related to the equilibrium between the stream velocity of the unburned gases, characterised by the temperature T_u, pressure P_u and velocity v_u, and the flame speed. The cooling of the burner decreases the flame velocity to aid the stabilisation. b) The related temperature profiles of the position the flame stabilises on. [9]

To simplify the derivation of the conservation equations some assumptions are made. It is assumed that the ideal gas law is valid and that external forces, like gravity, can be neglected. The mean free path of the molecules needs to be small compared to the flame thickness, leading to a continuous system. We should be able to discard the kinetic energy of the gas flow and the Dufour effect, the energy flux due to a mass concentration gradient. The pressure need to be constant and the system need to be in local thermal equilibrium and stationary. In a non-sooting flame the heat flux caused by the radiation of gases and particles should be neglectable [93].

The general relation for a conservation equation is

$$\frac{\delta W}{\delta t} + \frac{\delta J}{\delta z} = Q, \tag{4.1}$$

where W denotes the density of a conserved variable, J is the flux density of the conserved variable and Q is a source or sink of the conserved variable.

The conservation of mass m in the laminar flat flame can be written as

$$\frac{\delta \rho}{\delta t} + \frac{\delta \rho v}{\delta z} = 0. \tag{4.2}$$

The density W is the total mass density ρ. The movement of mass, the flux J, is the product of the density and the mean mass velocity v. During chemical reaction no mass is created or destroyed, so the source term in the mass conservation equation is zero. The conservation equation for mass is also called the continuity equation.

Next to the total mass m, the mass of species i m_i is conserved. The density is now the partial density ρ_i of species i, which can also be written as ρw_i, where w_i is the mass fraction of species i. The flux therm is the partial velocity multiplied with the mass velocity v_i of species i. Species i can be produced or consumed during the combustion reaction. Therefore the source term is not zero, but the chemical rate of production of species i, stated as r_i. The

conservation of mass m_i of species i can be written as

$$\frac{\delta \rho w_i}{\delta t} + \frac{\delta \rho w_i v_i}{\delta z} = r_i. \tag{4.3}$$

The third conservation equation is the conservation of enthalpy h of the mixture. The different terms of the general equation are $W = \sum_i \rho_i h_i$, $J = \sum_i \rho_i v_i h_i + j_q$ and Q is zero since energy is conserved. Here h_i is the specific enthalpy of species i and j_q is a heat flux, corresponding to the transport of energy due to a temperature gradient. The full conservation equation can be written as

$$\sum_i \frac{\delta}{\delta z}(\rho v w_i h_i) + \sum_i \frac{\delta}{\delta z}(\rho V_i w_i h_i) + \frac{\delta j_q}{\delta z} + \sum_i \frac{\delta}{\delta z}(\rho w_i h_i) = 0. \tag{4.4}$$

The full derivation of the equation can be found in [93]

Besides the conservation equations, the equations describing the heat and mass transport are important. The transport of mass due to concentration gradients is called diffusion and can be described by the law of Fick. An extended form of the law of Fick regarding the mass flux j_i can be written as

$$j_i = \frac{c^2}{\rho} M_i \sum_j M_j D_{ij} \frac{\delta x_j}{\delta z} - \frac{D_i^T}{T} \frac{\delta T}{\delta z}, \tag{4.5}$$

where c is the molar concentration, D_{ij} are multicomponent diffusion coefficients, x_j denotes the mole fractions and D_i^T is the thermal diffusion coefficient of the species i based on the temperature gradient [93].

The transport of heat due to temperature gradients is called conduction. The empirical law of Fourrier describes the heat flux j_q by

$$j_q = -\lambda \frac{\delta T}{\delta z}, \tag{4.6}$$

where λ is the heat conductivity of the gas mixture [93].

A laminar flat flame can be completely described if the temperature T, pressure P, velocity v, the overall density ρ and the $S-1$ linearly independent mass fraction $w_i, ..., w_{S-1}$ are known in function of the spatial coordinate z. The pressure is the same as the surrounding pressure and assumed constant, the density ρ can be calculated from the perfect gas law. Since the flame is stationary, the continuity equation, Equation 4.2, reduces to

$$\frac{\delta \rho v}{\delta z} = 0, \tag{4.7}$$

meaning that ρv is constant and the velocity v can be calculated from the unburnt gases throughout the flame. The mass fractions are determined by solving conservation equations, with the restriction that the sum of the mass fractions need to be unity [93].

To solve the stated equations the properties of the reacting gas need to be known. In the next sections the derivation of some of the mentioned properties is explained in more detail.

4.2 Determination of gas properties

Before performing simulations, the thermodynamic and transport properties of the assessed flames need to be determined. Different equations to calculated the reacting gas properties are available in literature and the parameters needed for these equations are stated in two files in CHEMKIN format. One file contains the parameters to calculate the thermodynamic properties of the species in the reacting gas, these parameters are the coefficients of the JANAF polynomials [94]. The second file consists of molecule characteristics of the species, such as the Lennard-Jones collision diameter and the dipole moment, which are used to obtain the transport properties of the reacting gas. A third file contains the names of the species in the assessed mechanism and the parameters for the Arrhenius equations for all the reactions in the mechanism. The three files are written in CHEMKIN format.

4.2.1 Thermodynamic properties

The JANAF coefficients [94], are used to calculate the molar heat capacity $c_{p,i}$, the enthalpy $\mathbb{h}_i$ and the entropy $\mathbb{s}_i$ at a given temperature (T) and 1 atm for each species i by .

$$c_{p,i} = R_u \left(a_1 + a_2 T + a_3 T^2 + a_4 T^3 + a_5 T^4\right) \tag{4.8}$$

$$\mathbb{h}_i = R_u \; T \left(a_1 + \frac{a_2 T}{2} + \frac{a_3}{3} T^2 + \frac{a_4}{4} T^3 + \frac{a_5}{5} T^4 + \frac{a_6}{T}\right) \tag{4.9}$$

$$\mathbb{s}_i = R_u \left(a_1 ln(T) + a_2 T + \frac{a_3}{2} T^2 + \frac{a_4}{3} T^3 + \frac{a_5}{4} T^4 + a_7\right) \tag{4.10}$$

where R_u is the universal gas constant, T is the temperature and a_1 to a_7 are the coefficients of the JANAF polynomials.

Next to the JANAF coefficients, the file also contains two adjacent temperature intervals and for both a set of coefficients are stated. So the file contains in total 14 coefficients per species. The first seven coefficients are for the high-temperature range, the other seven for the low-temperature range.

To calculate the enthalpie, entropie and heat transfer coefficient of an ideal mixture, the Gibbs theorem is applied. The thermodynamic properties of the mixture is averaged by the mole fraction x_i of the species. For example, the specific mole enthalpy of a mixture containing n species is given by

$$\tilde{\mathbb{H}} = \sum_{i=1}^{n} x_i \tilde{\mathbb{H}}_i. \tag{4.11}$$

4.2.2 Transport properties

The macroscopic transport properties of the gas mixture in the assessed flames are needed for simulation. Pressure and temperature can be easily regulated or measured. Nevertheless, the thermal conductivity, viscosity and diffusion coefficients are also needed to simulate the laminar flat flames. Simulation software derives these macroscopic properties from microscopic quantities associated with the molecules of the gas mixture. These microscopic quantities are the mass, the geometry of the molecule, the Lennard-Jones potential well depth and the collision diameter, the dipole moment, the polarizability and the rotational relaxation collision number. All these quantities are stated in the transport file.

The Lennard-Jones potential well depth ϵ_{LJ} and the Lennard-Jones collision diameter r_{LJ} are given in the third and fourth column of the transport file. Both parameters are part of the Lennard-Jones potential, a model for the interaction between two neutral molecules.

A molecular dipole moment δ exists if the positive and negative charges are unevenly distributed within the molecule. The unit of molecular dipole moment is debye and the dipole moment value is stated for every species in the fifth column of the transport file. In the sixt and seventh column of the transport file, the polarizability and the rotational relaxation collision number of the species is given.

Most gas properties are calculated based on the standard kinetic theory described by Hirschfelder et al. [95]. Some numerical solvers have also the possibility of taking the energy levels of the species into account, making the solution more exact. This solution method is called the multi-component method. In OpenSMOKE, however, the energy levels are not taken into account and the solution is obtained by the mixture-averaged approximation.

The calculation of three needed macroscopic transport properties: the viscosity, the diffusion coefficient and the thermal conductivity, can be found in the next paragraphs. They are explained in more detail, since they are used to calculate the heat transfer coefficient h. The temperature dependency of h is needed for the Electrical Compensation Method (ECM) to correct the measured flame temperature for radiation losses. With the equations for the viscosity, the diffusion coefficients and the thermal conductivity, the temperature dependency of h can be defined.

Viscosity

The dynamic viscosity η_i of a species i expressed in $\mathrm{g{\cdot}cm^{-1}s^{-1}}$ in the gas state can be calculated from the Lennard-Jones collision diameter r_{LJ}, the molecular mass m_i, the Boltzmann constant k_B and the collision integral $\Omega^{(2,2)*}$ as a function of the temperature T by

$$\eta_i = \frac{5}{16}\frac{\sqrt{\pi m_i k_B T}}{\pi r_{LJ}^2 \Omega^{(2,2)*}} \tag{4.12}$$

The collision integral $\Omega^{(2,2)*}$ depends on the reduced temperature T_i^* and the reduced dipole moment δ_i^* given by

$$T_i^* = \frac{k_B T}{\epsilon_{LJ}} \tag{4.13}$$

$$\text{and} \quad \delta_i^* = \frac{1}{2}\frac{\eta_i^2}{\epsilon_{LJ} s_i^3} \tag{4.14}$$

with s_i the reduced collision diameter of the species i. To achieve the collision integral value, the Stockmayer potentials stated by Monchick and Mason are quadraticly interpolated [96]. The Stockmayer potential is the Lennard Jones potential extended for molecules with a dipole moment.

OpenSMOKE uses a polynomial fit of the logarithm of the dynamic viscosity versus the logarithm of the temperature. This polynomial fit is proposed by Kee et al. [97, 98]

$$ln\ \eta_i = \sum_{k=1}^{N} b_{i,k}^{\eta} (ln\ T)^{k-1} \tag{4.15}$$

A third order polynomial fit is used. The average error of this fit is between 1% compared by applying the full calculations. However, fitting at the beginning of each problem reduces the calculation time drastically [97].

The viscosity of a mixture of species i and k is calculated by the Wilke formula adjusted by Bird et al. [99, 100].

$$\eta = \sum_{k=1}^{K} \frac{x_k \ \eta_k}{\sum\limits_{j=1}^{K} x_j \ \Phi_{kj}} \tag{4.16}$$

$$\text{where} \quad \Phi_{kj} = \frac{1}{\sqrt{8}} \left(1 + \frac{w_k}{w_j}\right)^{-1/2} \left(1 + \left(\frac{\eta_k}{\eta_j}\right)^{1/2} \left(\frac{w_j}{w_k}\right)^{1/4}\right)^2, \tag{4.17}$$

w_i and w_k are the mass fraction of species i and k, x_i and x_k are the mole fraction of species i and k.

Diffusion coefficient

The binary diffusion coefficient related to a species j and k is depending on the pressure and temperature [95]

$$D_{jk} = \frac{3}{16} \frac{\sqrt{2\pi k_B^3 T^3 / m_{jk}}}{p\pi s_{jk}^2 \Omega^{(1,1)*}} \tag{4.18}$$

where s_{jk} is the reduced collision diameter and m_{jk} is the reduced molecular mass of species j and k, which can be calculated by

$$m_{jk} = \frac{m_j m_k}{m_j + m_k}. \tag{4.19}$$

The collision integral $\Omega^{(1,1)*}$ is related to the reduced temperature T_{jk}^* and the reduced dipole moment δ_i^*. Since now two species are involved, the formulas for the reduced parameters differ with the ones defined for the viscosity calculations. The equations for the reduced quantities are also different for the combinations of polar or apolar species.

Two polar or non-polar species j and k

$$\frac{\epsilon_{LJ,jk}}{k_B} = \sqrt{\left(\frac{\epsilon_{LJ,k}}{k_B}\right)\left(\frac{\epsilon_{LJ,j}}{k_B}\right)} \qquad s_{jk} = \tfrac{1}{2}(s_j + s_k) \qquad \eta_{jk}^2 = \eta_j \eta_k$$

Combination of a polar p and non-polar n species

$$\frac{\epsilon_{LJ,np}}{k_B} = \xi^2 \sqrt{\left(\frac{\epsilon_{LJ,n}}{k_B}\right)\left(\frac{\epsilon_{LJ,p}}{k_B}\right)} \quad s_{np} = \tfrac{1}{2}(s_n + s_p)\xi^{-1/6} \quad \eta_{np}^2 = 0$$

$$\xi = 1 + \tfrac{1}{4}\alpha_n^* \eta_p^* \sqrt{\frac{\epsilon_{LJ,p}}{\epsilon_{LJ,n}}} \qquad \alpha_n^* = \frac{\alpha_n}{r_{LJ,n}^3} \qquad \eta_p^* = \frac{\eta_p}{\sqrt{\epsilon_{JL,p} s_p^3}}$$

where α is the polarizability of a molecule, s_{jk} is the reduced collision diameter, k_B is the Boltzmann constant, ϵ_{LJ} is the Lennard-Jones potential well depth and η is the viscosity. The reduced temperature and dipole moment are defined as

$$T_{jk}^* = \frac{k_B \ T}{\epsilon_{LJ,jk}} \tag{4.20}$$

$$\text{and} \quad \delta^*_{jk} = \frac{1}{2}\mu^{*2}_{jk} \tag{4.21}$$

Again, a polynomial of the third order of the binary diffusion coefficients is used in the simulations to reduce the calculation time:

$$ln\ D_i = \sum_{k=1}^{N} b^D_{i,k} (ln\ T)^{k-1}. \tag{4.22}$$

The mixture-averaged diffusion coefficient for a species j is computed as

$$D_{km} = \frac{\sum\limits_{j\neq k}^{K} x_j\ w_j}{\bar{w} \sum\limits_{j\neq k}^{K} {}^{x_j}/_{D_{jk}}}. \tag{4.23}$$

If the mixture is a pure species, the formula will be undefined. Therefore a small quantity of each species is always retained.

Thermal conductivity

The individual species thermal conductivities λ are composed of translational, rotational and vibrational contributions as stated by Warnatz [101].

$$\lambda_k = \frac{\eta_i}{w_i}(f_{trans} C_{v,trans} + f_{rot} C_{v,rot} + f_{vib} C_{v,vib}) \tag{4.24}$$

where η_i and w_i are respectively the viscosity and the molecular weight of species i. f_{trans}, f_{rot} and f_{vib} are the translational, rotational and vibrational contributions. The pure species formulas are used for calculating mixture-averaged thermal conductivities. The different energy contributions can be written as:

$$f_{trans} = \frac{5}{2}\left(1 - \frac{2}{\pi}\frac{C_{v,rot}}{C_{v,trans}}\frac{\frac{5}{2} - \frac{\rho D_{k,k}}{\eta_k}}{Z_{rot} + \frac{2}{\pi}\left(\frac{5}{3}\frac{C_{v,rot}}{R_u} + \frac{\rho D_{kk}}{\eta_k}\right)}\right), \tag{4.25}$$

$$f_{rot} = \frac{\rho D_{kk}}{\eta_k}\left(1 - \frac{2}{\pi}\frac{\frac{5}{2} - \frac{\rho D_{k,k}}{\eta_k}}{Z_{rot} + \frac{2}{\pi}\left(\frac{5}{3}\frac{C_{v,rot}}{R_u} + \frac{\rho D_{kk}}{\eta_k}\right)}\right), \tag{4.26}$$

$$f_{vib} = \frac{\rho D_{kk}}{\eta_k}, \tag{4.27}$$

where C_v is the molar heat capacity, which is specific for each contribution, R_u is the universal gas constant, Z_{rot} is the rotational relaxation collision number, ρ is the density, $D_{k,k}$ the 'self-diffusion' coefficient and η_k the viscosity.

The relationships for the molar heat capacity C_v, for the translational, rotational and vibrational energy contributions are depending on the geometry of the species of interest. The geometry of a species can be unimolecule (e.g. Ar), linear (e.g. O_2) or non-linear (e.g. MPE). The related values for the molar heat capacity can be found in Table 4.1.

Table 4.1: Molar heat capacity C_v relationships for different molecule geometries and translational, rotational and vibrational energy contributions

Geometry	$C_{v,trans}$	$C_{v,rot}$	$C_{v,vib}$
Spherical	$^3/_2\ R_u$	-	-
Linear	$^3/_2\ R_u$	R_u	$C_v - {}^5/_2\ R_u$
Non-linear	$^3/_2\ R_u$	$^3/_2\ R_u$	$C_v - 3\ R_u$

For an unimolecular species i, there are no rotational or vibrational contribution for C_v, causing the thermal conductivity equation to simplify to

$$\lambda_i = \frac{\eta_i}{W_i}\left(\frac{5}{2}\frac{3}{2}R_u\right). \tag{4.28}$$

The 'self-diffusion' $D_{k,k}$ coefficient in Equation 4.25 and Equation 4.26 is defined as

$$D_{kk} = \frac{3}{16}\frac{\sqrt{2\pi k_B^3 T^3/m_k}}{p\pi r_{LJ}^2 \Omega^{(1,1)*}}, \tag{4.29}$$

where k_B is the Boltzmann constant, m_k is the molecular mass of species k, r_{LJ} is the Lennard-Jones diameter and $\Omega^{(1,1)}$ a collision integral. The density ρ in Equation 4.25 and 4.26 comes from the equation of state for a perfect gas

$$\rho = \frac{p w_i}{R_u T} \tag{4.30}$$

where p is pressure, R_u is the universal gas constant, T is the temperature and w_i is the molecular weight of the species.

The last unknown parameter in Equation 4.25 and 4.26 is the rotational relaxation collision number Z_{rot}. A value for Z_{rot} at 298 K is available in the transport database and the temperature dependency is given by [102, 103]

$$Z_{rot}(T) = Z_{rot}(298K)\frac{F(298K)}{F(T)} \qquad with$$
$$F(T) = 1 + \frac{\pi^{3/2}}{2}\left(\frac{\epsilon/k_B}{T}\right)^{1/2} + \left(\frac{\pi^2}{4}+2\right)\left(\frac{\epsilon/k_B}{T}\right) + \pi^{3/2}\left(\frac{\epsilon/k_B}{T}\right)^{3/2}. \tag{4.31}$$

Again, a polynomial fit for the thermal conductivity is used to reduce the computational time, the temperature dependency proposed by Kee is implemented in OpenSMOKE:

$$ln\ \lambda_i = \sum_{k=1}^{N} b_{i,k}^{\lambda} (ln\ T)^{k-1}. \tag{4.32}$$

To achieve the mixture-average property a combination averaging formula is applied [104]:

$$\lambda = \frac{1}{2}\left(\sum_{k=1}^{K} X_k \lambda_k + \frac{1}{\sum_{k=1}^{K} X_k/\lambda_k}\right). \tag{4.33}$$

4.2.3 Kinetic mechanism

The kinetic mechanism containing all the reactions of the combustion process is given in a third file in CHEMKIN format. The file consists of three sections. In the first section the elements are given. C, H, O, Ar and N are stated in the MPE mechanism. Next, the names of all the species are given. The last section contains the reactions of the mechanism with their Arrhenius equation parameters. The reaction rate k of a reaction at a certain temperature T can be approximated with the Arrhenius equation.

$$k = AT^b exp\left(\frac{E_a}{R_u T}\right) \tag{4.34}$$

where A is the pre-exponential factor, b is the temperature dependency exponent and E_a is the activation energy expressed in cal·mole^{-1} [93]. The gas constant R_u and the temperature T are also a part of the Arrhenius equation.

A reversible reaction can be depicted as

$$A + B \rightleftharpoons_{k_b}^{k_f} C + D, \tag{4.35}$$

where species A and B react with each other to C and D and vice versa. The parameters in the kinetic file are only valid to calculated the forward reaction rate k_f. The reverse reaction rate k_b can be calculated from the gas equilibrium constant $K_c(T)$ in elementary reactions.

$$K_c(T) = \frac{k_f}{k_b} = \frac{P_C \cdot P_D}{P_A \cdot P_B} = exp\left(\frac{-\Delta H + T\Delta S}{R_u T}\right) \tag{4.36}$$

where P_A, P_B, P_C and P_C are the partial pressure of the reactants, T is the temperature, R_u is the universal gas constant and ΔH and ΔS are the differences in enthapy and entropy between the reactants and the reaction products. $\Delta H + T\Delta S$ is the definition of the Gibbs free energy. At chemical equilibrium the Gibbs free energy is minimal. For irreversible reactions only the forward reaction rates k_f is needed.

Most reactions in the mechanism are described by the simple Arrhenius equation. Exceptions are third body reactions, where the third body can be a different species with specific reaction characteristics. These reactions are mostly recombination and dissociation reactions and can be pressure dependent. A neutral third-body M is inserted in the reaction, to be able to account for the pressure dependency. The energy-rich intermediate, M, initiates the dissociation and terminates the recombination reactions.

Dissociation

$$\begin{aligned} \mathrm{AB + M} &\rightarrow \mathrm{AB^* + M} \quad (1) \\ \mathrm{AB^* + M} &\rightarrow \mathrm{AB + M} \quad (-1) \\ \mathrm{AB^*} &\rightarrow \mathrm{A{+}B} \quad (2) \end{aligned}$$

Recombination

$$\begin{aligned} \mathrm{A{+}B} &\rightarrow \mathrm{AB^*} \quad (-2) \\ \mathrm{AB^*} &\rightarrow \mathrm{A + B} \quad (2) \\ \mathrm{AB^* + M} &\rightarrow \mathrm{AB + M} \quad (-1) \end{aligned}$$

The energetically excited species AB* has different possible energy distributions. Nevertheless, when steady-state conditions are assumed, the same values for the formation rate coefficients k_1, k_{-1}, k_2 and k_{-2} related to the steps (1), (-1), (2) and (-2) respectively can be assumed. For the dissociation reactions, the net production rate of AB* can be found in steady-state conditions. In the first reaction, AB* is produced, while in the following 2 reactions, it is consumed. The rate of production and consumption of AB* in the three reactions can be written as:

$$\frac{d[AB^*]}{dt} = [AB] \cdot [M] \cdot k_1 \qquad (1)$$

$$\frac{-d[AB^*]}{dt} = [AB^*] \cdot [M] \cdot k_{-1} \quad (-1)$$

$$\frac{-d[AB^*]}{dt} = [AB^*] \cdot k_2 \qquad (2)$$

and since steady-state conditions are assumed, the production equals the consumption, so

$$[AB] \cdot [M] \cdot k_1 = [AB^*] \cdot [M] \cdot k_{-1} + [AB^*] \cdot k_2 \tag{4.37}$$

and the concentration of AB* can be written as

$$[AB^*] = \frac{k_1 \cdot [AB] \cdot [M]}{k_{-1}[M] + k_2} \tag{4.38}$$

The overall reaction rate of the dissociation and recombination reaction can be written as

$$k_{dis} = k_2 \cdot [AB^*] = -\frac{1}{[AB]}\frac{d[AB]}{dt} = k_1[M]\left(\frac{k_2}{k_2 + k_{-1}[M]}\right)$$

$$k_{rec} = k_{-1} \cdot [AB^*] \cdot [M] = +\frac{1}{[A][B]}\frac{d[AB]}{dt} = k_{-2}\left(\frac{k_{-1}[M]}{k_2 + k_{-1}[M]}\right)$$

The ratios between brackets in the expressions for k_{dis} and k_{rec}, are probabilities related to the termination of the reaction. The probabilities become 1 for the dissociation at low pressure and the recombination at high pressure. They also turn zero at high pressure by dissociation and low pressure for recombination, since the concentration of the third-body [M] is present in both reaction rates and that is related to the pressure or density of the combustion system.

The equilibrium constant K_c between the dissociation and recombination reactions can also be determined

$$K_c = \frac{k_{diss}}{k_{rec}} = \frac{k_1}{k_{-1}}\frac{k_2}{k_{-2}} = \left(\frac{[A][B]}{[AB]}\right)_{eq} \tag{4.39}$$

The fall-off curve of a thermal unimolecular dissociation or recombination is defined as the relation between the logarithm of the reaction rate $log(k)$ and the logarithm of the third-body concentration $log([M])$ (Figure 4.2). At low concentrations of [M], the reaction rate is related

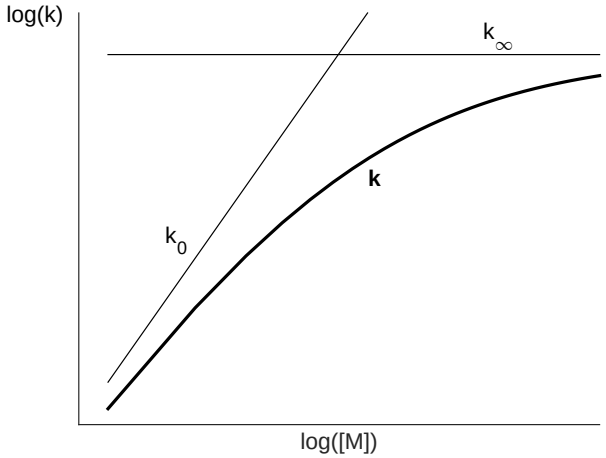

Figure 4.2: The fall-off-curve of an unimolecular dissociation or recombination reaction is defined as the relation between the logarithm of the third-body concentration log([M]) and the logarithm of the reaction rate log(k).

to [M] and the limiting reaction rate is k_0. At higher concentrations of [M], the reaction rate k is independent of [M] and have a limit value of k_∞. The reaction rates are substituted by k_0 and k_∞.

The reaction rate k can then be written as the Lindemann-Hinshelwood's equation.

$$k = \frac{k_0 k_\infty [M]}{k_0[M] + k_\infty} \tag{4.40}$$

The Lindemann-Hinshelwood's equation is depending on the reaction rate k_0 valid when the pressure tends to vaccuum and reaction rate k_∞ related to an infinite pressure. However, it does not describe the intermediate pressures well. To define where in the pressure range we are, the concentration of the third body [M] is incoperated, calculated via the ideal gas law.

$$[M] = \frac{n}{V} = \frac{P}{RT}. \tag{4.41}$$

The application of pressure dependency of a reaction in the mechanism file is done by some text additions. If the pressure dependency is evaluated by the Lindemann-Hinshelwood's equation, the reaction is written as:

```
A+B+M = C + M          2.3E14   0.0    156.2
                LOW/   6.3E27   -2.6   -54.3/.
```

The first line of contains the reaction and the Arrhenius equation parameters at normal and high pressures. The LOW keyword indicates that the second line contains the Arrhenius parameters for the low-pressure limit.

The temperature dependency can also be determined by the Troe's formula [105, 106], where the broadening of the reduced fall-off curves related to collision efficiencies the is taken into account by a broadening factor F,

$$k = k_\infty \left(\frac{k_0[M]}{\frac{k_0}{k_\infty}[M] + 1} \right) F. \tag{4.42}$$

The broadining factor F is composed of strong and weak broadening factors, F^{sc} and F^{wc}. The logarithm of F can be calculated as follows

$$log(F) = \frac{log(F_{cent})}{1\left[\frac{log(X)+c}{N-d(log(X)+c)}\right]^2} \tag{4.43}$$

where F_{cent} is the center broadening factor, d is 0.14 and the other parameters are

$$N = 0.75 - 1.27 \cdot log(F_{cent}), \tag{4.44}$$

$$c = -0.4 - 0.67 \cdot log(F_{cent}), \tag{4.45}$$

$$X = \frac{[M]}{k_\infty/k_0}, \tag{4.46}$$

$$\text{and} \quad F_{cent} = (1-\alpha)\exp\left(-\frac{T}{T^{***}}\right) + \alpha\ \exp\left(-\frac{T}{T^{*}}\right) + \exp\left(-\frac{T^{**}}{T}\right). \tag{4.47}$$

The parameters α, T^{***}, T^{*} and T^{**} are given in the mechanism file after the key word TROE. In the example below, T^{**} is not given, since it is not mandatory and the term containing T^{**} in Equation 4.47 can be omitted.

```
A+B+M = C + M                2.3E+14     0.0    156.2
              LOW/           6.3E+27    -2.6   -54.3/
             TROE/             0.604  6980.0    132./
```

The pressure dependency of a reaction is also related to the dilutent or the buffer gas at low pressures. This is implemented by a enhancement factor with which the low-pressure rate constant is multiplied.

```
A+B+M = C + M                 2.3E14          0.0        156.2
              CO/1.9/  H2/1.7/  /CO2/3./  H2O/5./
```

In the example above the low-pressure rate constant is multiplied with 1.9 if the buffer gas is CO.

Since the flames in this work are stabilised at a pressure of 55 mbar, the LOW, TROE and enhancement factors can have an effect on the simulations results, because they define the low-pressure rate constant.

4.3 Mechanism for MPE combustion

The MPE mechanism investigated in this work is based on a kinetic mechanism for methyl butanoate [107] completed by a submechanism to model the oxidation of methyl pentanoate written by Dayma [1]. The full mechanism contains 206 species and 1792 reactions. It has a hierarchical structure and most of the rate constants were estimated by structure-reactivity relationships. For instance, rate constants for H-abstractions on carbon 3, 4, or 5 were taken from Fisher et al. [107], while H-abstractions on carbon 2 were evaluated assuming carbon 2 behaves as an allylic carbon atom. Similarly, for the beta-scissions of the primary radicals, rate constants were taken from [67] and [68].

The notation of the species in the mechanism, is based on the notation used by Fisher et al. [107]. In the MPE molecule, the hydrogen and the carbon atoms on the acid chain are reffered to by a number, with number 1 being the carbon of the carbonyl group (Figure 1.2). The

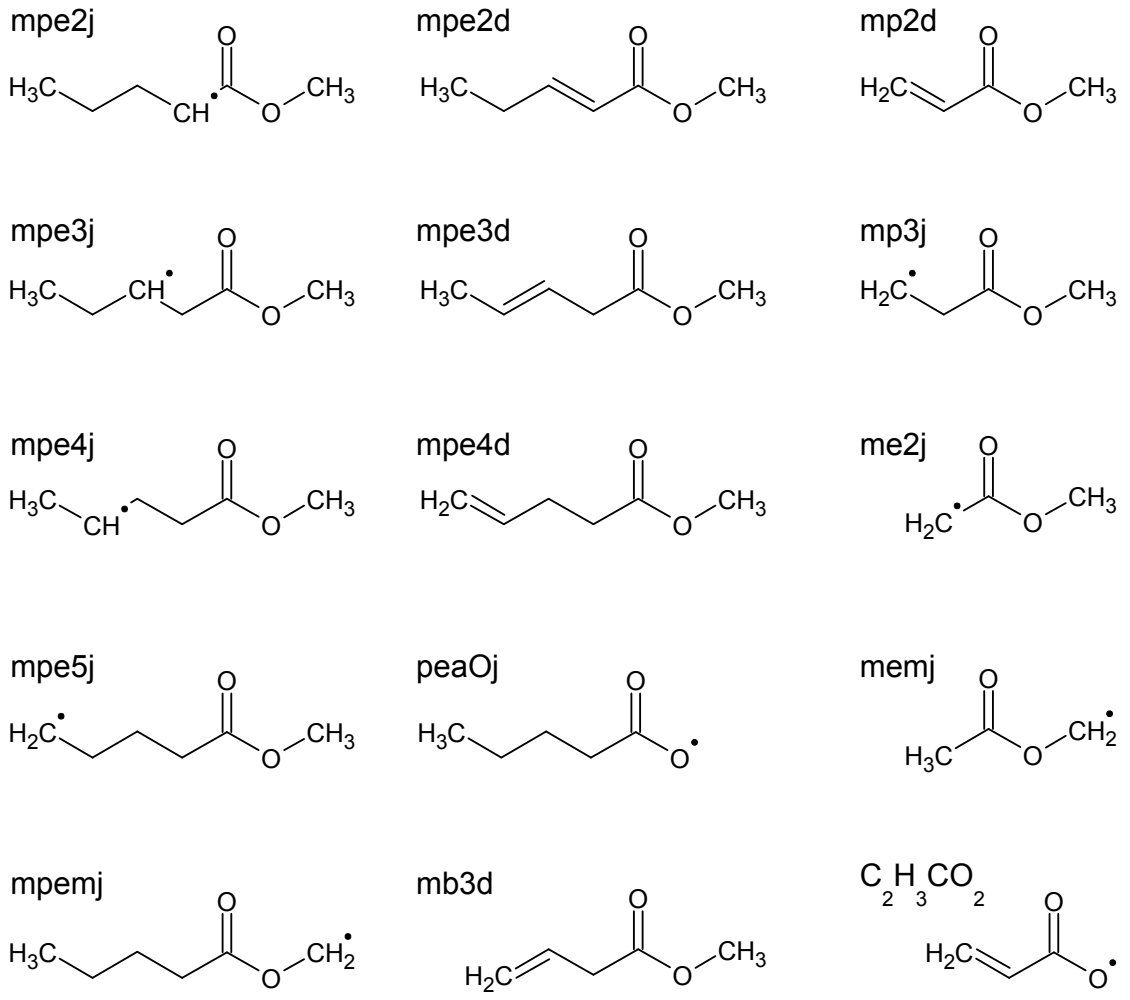

Figure 4.3: Chemical structure and nomenclature for intermediate species derived from the fuel MPE

hydrogen and carbon atoms in the methyl group are denoted m, while the other hydrogen atom are numbered the same as the carbon atom they are bounded on.

If an hydrogen atom is abstracted, the intermediate radical name contains a j prior the number of the carbon atom where the hydrogen atom is abstracted from. So mpe2j is the radical formed if a hydrogen atom is abstracted from the carbon atom next to the carboxyl group. A d in the intermediates name means that a double bond is present. One of the intermediates is mp2d. The full name of this intermediate is methyl prop-2-enoate, or methyl acrylate, and it has a double bound at position 2. The structures and names of some of the important intermediates directly formed from MPE are given as an example in Figure 4.3.

4.4 Sensivity of the achieved mole fraction profiles

A sensitivity analysis quantifies the influence of an input parameter on the result of the model. With the OpenSMOKE software, a sensitivity analysis for the pre-exponential factor A of the

Arrhenius equation as input parameter can be conducted. The pre-exponential value of each reaction is changed by a factor and afterwards the simulation is performed again to obtain the simulation result with the adjusted pre-exponential value. Once both results are known the Sensitivity Coefficient (SC) can be calculated

$$\mathrm{SC}_{ij} = \frac{\Delta w_i}{\Delta A_j} \tag{4.48}$$

where w_i is the mass fraction of the species and A the pre-exponential factor of the reaction.

The SC is the ratio of the difference in the found mass fraction w_i for a species i, and the related change of the pre-exponential factor A_j of reaction j. The SC is calculated not only for every reaction and species combination but also for every spatial gridpoint related to burner distance x_k. In total i x j x k SC are obtained. In this work, there are 206 species x 1881 reaction x 297 data points $\approx$ 115 million coefficients.

The SC is normalised by the pre-exponential A and the simulated mass fraction w_i. The Normalised Sensitivity Coefficient (NSC) are dimensionless and can be used to compare the influence of different reactions. Without normalisation reactions with a high pre-exponential A will be most influential. A post-processor is available in the OpenSMOKE software to calculate the NSC and to acquire plots showing the NSC in descending order for a chosen species. The dimensionless NSC are achieved by multiplying the SC by the ratio of the nominal pre-exponential factor A and the mass fraction w_i

$$\mathrm{NSC}_{ij} = \frac{A}{w_i}\frac{\partial w_i}{\partial A_j}. \tag{4.49}$$

The mass fraction profile of a species is most sensitive to reactions with the highest absolute NSC values. The sign of the NSC indicates if an increase of the pre-exponential factor A, has a positive or a negative effect on the mass fraction of the assessed species. The highest 200 NSC's can be shown by the OpenSMOKE postprocessor, not more. There is also an option for a global or local analysis. The global analysis takes all the found NSC for an assessed species and reaction into account. It searches the NSC with the highest absolute value and presents the maximal NSC value with the sign for the assessed species and reaction. An example is shown in Figure 4.4. The local method on the other hand, needs a distance to the burner x_k as input. The NSC found for that distance is shown as final NSC. Nevertheless, higher NSC values can occur at other distances.

Due to the amount of SC related to the mechanism the post-processor failed to convert them to NSC. As a solution, I wrote a code in MATLAB to convert the xml-files with the SC to NSC and achieve the characteristic sensitivity analysis figures. With the MATLAB code it is possible to achieve the NSC of all the reactions and not the 200 most important ones. The MATLAB code is validated by smaller mechanism GRI3.0 for which the NSC could be calcated in both ways and compared.

4.5 Reaction flow analysis

A reaction flow analysis can be conducted by the OpenSMOKE software and the results can be used to determine the formation and consumption pathways for the species in the mechanism. An integrated reaction flow analysis is performed, considering the overall formation and consumption during the combustion process. This is performed by an Excel files with a macro

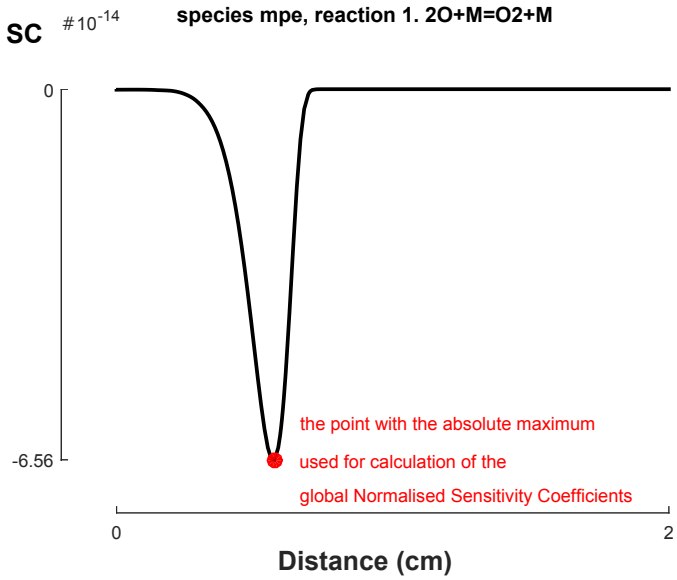

Figure 4.4: The Sensitivity Coefficients (SC) for the MPE mass fraction profile obtained by changing the pre-exponential factor of reaction 2O+M=O2+M. The absolute maximum of the SC is used to further calculate the NSC in the global analysis setting.

made by Ancia [108]. The macro retrieves the reaction rates of all the reactions containing the assessed species i. Next, the macro integrates the reaction rates over the full spatial interval. Reactions with a negative integration result contribute to the consumption of species i, while reactions with a positive integration value assist to the formation of the species.

The integrated areas are normalised by the total sum of the integrated areas to identify the reactions which contributes the most to the formation or the consumption of a species. The contribution of a reaction j to the formation or the consumption of a species i is given by

$$F_{i,j} = \frac{|A_{F,i,j}|}{\sum_{j=1}^{N} |A_{F,i,j}|} \tag{4.50}$$

$$C_{i,j} = \frac{|A_{C,i,j}|}{\sum_{j=1}^{N} |A_{C,i,j}|} \tag{4.51}$$

where $F_{i,j}$ is the contribution to the formation of species i by reaction j, $C_{i,j}$ is the contribution to the consumption of species i by reaction j, $A_{F,i,j}$ is the positive area under the reaction rate profile of reaction j and $A_{F,i,j}$ is the negative integrated area of the reaction rate profiles of reaction j.

$F_{i,j}$ and $C_{i,j}$ express the contributions of a reaction to the formation or consumption of species i in percentage. They can be used to establish a reaction flow analysis, whereby the formation and consumption reaction pathways can be visualised. The reaction pathways can be used to identify the kinetics of the fuel consumption and if these pathways change with equivalence ratio ϕ. The formation and consumption pathways of tje three MPE flames are discussed in Section 7.2.1.

4.6 Selection of the simulation software

Our research group has experience with different simulation softwares. The COSILAB software from SoftPredict [109] was used in different papers [110, 111]. **Besides, the Cantera Catherine Duynslaeghers [112].** Both softwares are capable of simulating burner stabilised laminar flat flames.

In 2014, our research group had the possibility to try out the OpenSMOKE code, which can simulate different combustion configurations. The results obtained by the OpenSMOKE code for burner stabilised laminar flames were compared with the simulation results achieved by COSILAB. No difference between the simulation results of both programs was found and it was opted that the COSILAB software, for which yearly a license fee needed to be paid, was replaced by the OpenSMOKE software.

The Cantera software can be ran from Python or MATLAB. The installation of Cantera on a WINDOWS computer is not straight forward, but the implementation of Cantera with MATLAB is an advantage. The Cantera software is not directly used to simulate laminar flat flames, but it is used to simulate the temperature correction, which will be discussed in Chapter 5, in MATLAB. The Cantera software makes it possible to use physical properties of the reacting gas mixture during MATLAB calculations if the pressure, temperature and flame composition are known.

4.7 OpenSMOKE software

The OpenSMOKE software [11] will be used for the simulations of 1D laminar flames, laminar burning velocities and Perfectly Stirred reactor (PSR). In this section, the different steps to run the simulations are explained.

4.7.1 Preprocessing of kinetic files

The three earlier discussed input files are needed to simulate with OpenSMOKE. However, the CHEMKIN format cannot be directly used by OpenSMOKE and the files are pre-processed to a format that can be used by OpenSMOKE.

The **'OpenSMOKE_CHEMKINInterpreter'** program is used for the pre-processing. The input files with the transport data, thermodynamic data and mechanism are loaded into the program and are processed to a folder containing files which can be used by OpenSMOKE. The folder with the processed kinetic mechanism data can then be copied to folders where the model is needed.

4.7.2 OpenSMOKE solvers

To simulate laminar flames, the **'OpenSMOKE_LaminarFlame1D'** program is used. This program needs three textfiles as input. In a first text file, called *Data* by default, the flame properties, like composition, equivalence ratio, mass flow etc., are stated together with computational options, like enabling the Soret effect, a reaction flow analysis or a sensitivity analysis. Also, the parameters for conversion can be altered in the *Data* file. The second file is called *Operations* by default and contains the amount of iterations and the conditions to add gridpoints. Checking the convergence of one iteration is done automatically by OpenSMOKE, however the convergence of the final result need be check manually. The

amount of iterations and gridpoints can be changed in the *Operations* file. The third text file contains the experimental temperature profile of the assessed laminar flame. Without referring to the temperature profile in the *Data* file, the energy equation is solved and mole and mass fraction profiles for an adiabatic flame are obtained.

The same program can also be used for simulations of laminar flame speeds. To achieve the laminar flame speed, the temperature profile is not stated in the *Data* file and the position of the flame front is defined in coding. No changes in the *Operations* file are needed. OpenSMOKE solves the energy equation and the laminar flame velocity is found as the velocity stated for the the first gridpoint. The adiabatic flame temperature is found as the temperature of the last grid point.

The **'OpenSMOKE_PerfectlyStirredReactor'** solver is used to simulate perfectly stirred reactor configurations. Two input files are needed for this solver. In the *InletStream*-file the temperature, the pressure the equivalence ratio ϕ and the compostion of the flame are stated. In the second text file, *PSR*, the residence time is given and whether or not the conditions are isothermal. With this data, OpenSMOKE can simulate the mole fraction profiles.

The **'OpenSMOKE_Batch'** solver can simulate the behaviour of Rapid Compression Machine (RCM). In a *Data* file the pressure, the temperature, the equivalence ratio and the mixture composition is stated. In a second file, the *Batch* file, the residence time, the volume and the reaction conditions are given. The Batch process can be solved with constant pressure or with constant volume. For RCM simulations the pressure is kept constant.

4.7.3 Postprocessing of the simulations results

The mole and mass fractions obtained after each iteration step are saved by OpenSMOKE in the Steady output folder. The convergence of the results can be checked by comparing the result of two last consecutive iterations.

The SC and reaction rates needed for the sensitivity analysis and the rate of production analysis are saved in a folder called *Additional*.

The performance of the OpenSMOKE solver is checked by comparing the obtained simulation results with the results of other simulation codes. The laminar flat flames results were compared with the results obtained by COSILAB [109] and no substantial differences between the mole fraction profiles are found. The simulations of laminar flame speed are also compared with the COSILAB software. Differences up to 5 $cm \cdot s^{-1}$ are found between the simulations. These difference can be explained by the determination of the flame front position. In COSILAB, the flame front is fixed in the middle of the defined spatial axis and the value for the first temperature gradient need to be determined. In OpenSMOKE, both the position and gradient are defined manually and the flame front lies at one third of the spatial axis by default. This different definition for flame front position can result to the found differences. The obtained adiabatic flame temperature with OpenSMOKE are compared by the results of Cantera [112] and no substantial differences are found. The same is observed for 0D ignition delay simulations, conducted by OpenSMOKE and COSILAB.

The OpenSMOKE software can be used to simulate the laminar flat flames, with the same results as other simulation codes. However, if laminar flames velocities are calculated, the position of the flame front position should be defined with care and the settings for convergence need to be checked.

5
Temperature measurement

The assessed laminar flat flames are not adiabatic. Heat losses to the burner and combustion chamber occur. The flame temperature profile is needed as input for the OpenSMOKE solver.To measure the temperature of the assessed MPE flames, different methods can be used. The options can be divided into invasive and non-invasive methods. Thermocouples are an invasive method. They are emerged in the flame of interest and can change the nature of the flame, leading to a difference between the measured temperarture values and temperature of the undisturbed flame. Non-invasive methods are based on laser induced changes in vibrational state and energy level of the molecules. The main advantage of lasers is that they do not disturb the flame. Nevertheless, their initial cost is substantial [113].

Our research group is experienced with thermocouples and a Type B thermocouple is used in this work. The thermocouple can be easily inserted into the flame. However, the measurement should be corrected for of radiation losses to the environment [114]. Different options exists to quantify the correction and in this chapter two correction options will be compared with each other and their performance will be assessed.

The first correction method is a Heat Transfer Model (HTM) that can predict the temperature correction ΔT_{corr} in function of the flame composition and the thermocouple characteristics. The model has no temperature limitation and could be applied on all the assessed flames. It is based on a Nusselt number correlation valid for forced convection over the thermocouple. Special attention is given to the shape of the thermocouple, which is a combination of a sphere, the junction bead, and a cylinder, the thermocouple wire. In Section 5.5 the HTM model is explained in detail.

Another correction method, the experimental Electrical Compensation Method (ECM), is based on a temperature increase due to a current. The current results in extra stress in the thin thermocouple wire, which can lead to thermocouple breaking. To avoid failing the maximal current is restricted to 0.6 A, related to a temperature of 1400 K in vacuum. As a result, the measured temperature in high temperature flames cannot be corrected by this method, since no extra current to compensate for the radiation losses can be applied on the thermocouple without breaking it. In our case, the method was not applicable to the stoichiometric and lean MPE flame. The method is described in detail in Section 5.1.

The ECM has been used by our research group to correct for radiation losses in previous research [110, 115, 111], however for the MPE flames the measured temperatures are too high to be reliably corrected by ECM and a new correction method, Heat Transfer Model (HTM), needed to be established. To assess the performance of both correction methods, they are applied on flames with different equivalence ratios, argon dilutions and initial flow velocities. The rich MPE flame is the only MPE flame on which both methods can be applied, therefore additional flames with an overall lower temperature profile were investigated. Ethylene was

chosen as fuel for these flames, since it was already part of the experimental setup. Five ethylene flames, with different flame characteristics, are investigated to assess the effect of changes in argon dilution, equivalence ratio and initial velocity on the temperature correction.

5.1 Correction for radiation losses in literature

In literature, three methods are described to correct for radiation losses when flame temperatures are measured with fine wire thermocouples. Two of them are experimental methods: the Electrical Compensation method (ECM) and the method using different thermocouples with reducing bead size. The third method is based on heat transfer calculations related to the forced convective heat transfer from the flame to the fine wire thermocouple and the radiation of the thermocouple to its environment. This correction method is called the Heat Transfer Method (HTM).

In this Chapter two of them, the experimental ECM and the HTM based on theoretical equations are applied on high temperature flames. The performance of both methods is assessed and the dis- and advantages of both are identified. To our knowledge, it is the first time that ECM and HTM are applied on the same flames and a comparison between their performances is made.

The ECM and HTM are based on the power balance over the thermocouple when submerged in a flame. The power balance can be written as [114]:

$$\dot{Q}_{\text{cat}} + \dot{Q}_{\text{conv}} + \dot{Q}_{\text{rad}} + \dot{Q}_{\text{cond}} = \rho c_p V \frac{dT_c}{dt}, \tag{5.1}$$

where $\dot{Q}_{\text{cat}}$ is the heat flow rate released by catalytic reactions on the thermocouple surface, $\dot{Q}_{\text{conv}}$ is the convective heat flow rate from the flame to the thermocouple, $\dot{Q}_{\text{cond}}$ are the conduction losses along the thermocouple wires and $\dot{Q}_{\text{rad}}$ is the radiation flow rate from the thermocouple to its surroundings. The right hand term is the transient heating or cooling of the thermocouple, where ρ, c_p, V and T_c are the density, the specific heat capacity, volume and temperature of the thermocouple.

A non-catalytical coating is applied to minimise the catalytic reactions on the thermocouple surface, so $\dot{Q}_{\text{cat}}$ can be discarded from the power balance [116]. Three coatings are mostly mentioned in literature: silica base coatings, BeO-Y_2O_3 coatings and alumina coatings. Silica-based coatings are prone to reduction by hydrogen if the temperature is higher than 1100°C. The ceramic BeO-Y_2O_3 coating is not affected by hydrogen, but is extremely toxic and safety precautions need to be made. The alumina-base ceramic coatings can be other option, which is less toxic and more stable than silica [117]. Due to the position and characteristics of the thermocouple, the conduction losses can also be discarded. Heitor et al. have found that if the length-to-diameter ratio is above 200, conduction losses can be neglected [117]. In our case the diameter of the thermocouple wire is 0.1 mm and its length is around 120 mm, implying that our length-to-diameter ratio is well above the limit to discard conduction losses. So, only the term for convection and radiation are kept and when steady state is reached, Equation 5.1 simplifies to:

$$h(T_g - T_c) = \sigma\epsilon(T_c^4 - T_0^4), \tag{5.2}$$

where, at the left hand side h is the convective heat transfer coefficient, T_g is the unknown flame temperature and T_c is the measured flame temperature. At the right hand side, describing the radiation term, σ is the Stefan-Boltzmann constant, ϵ is the emissivity of the thermocouple

and T_0 is the temperature of the surroundings, which is the combustion chamber in our case [114].

Equation 5.2 can be converted to

$$T_g = T_c + \frac{\sigma\epsilon(T_c^4 - T_0^4)}{h}, \tag{5.3}$$

where the actual flame temperature T_g is expressed in function of the measured flame temperature T_c. Equation 5.3 implies that the temperature measured by the thermocouple is lower than the actual flame temperature, due to the radiation losses from the thermocouple to its surroundings.

To check if the applied coating is preventing catalytic heating on the thermocouple the temperature hysteris can be assessed. The measured temperature profile should be the same for both starting in the fresh gases as starting in the post flame zone. If a higher temperature is found for the fresh gases when the thermocouple is first placed in the post flame zone, catalytic heating is still happening [117].

The correction for radiation losses is depending on three parameters: the emissivity of the thermocouple ϵ, the heat transfer coefficient of the flame h and the temperature of the surroundings T_0. All three of these parameters can be deduced from measurement or literature, making it possible to calculate the temperature correction. The Heat Transfer Model (HTM) which is further explained in Section 5.5, follows this working principle.

ECM on the other hand, is an experimental method which does not need the values for ϵ, h and T_0 as input. ECM is based on the difference between the power balance over the thermocouple at vacuum and in the flame of interest [118]. During ECM, the temperature of the thermocouple is increased artificially by applying a current, which increases the risk of thermocouple breaking. Thus, the main disadvantage of ECM is that experimental data can only be gathered at relatively low temperatures.

ECM quantifies the radiation losses experimentally in two steps. The first step is to obtain the characteristic curve of the thermocouple in vacuum. Since the thermocouple is placed in vacuum, no convection can occur. The temperature of the thermocouple is increased by applying a current on the wire. This form of heating is called Joule heating. The characteristic curve, expressing the equilibrium between the Joule heating and the heat transfer from the thermocouple by radiation, can be written as

$$RI^2 = A\sigma\epsilon(T_c^4 - T_0^4) \tag{5.4}$$

or

$$I^2 = \frac{A\sigma\epsilon(T_c^4 - T_0^4)}{R}, \tag{5.5}$$

where R is the thermocouples resistance, I the applied current, A the area of the thermocouple, ϵ the emissivity of the thermocouple, T_c the measured temperature and T_0 the temperature of the surroundings. The shape of the characteristic curve is depending on the quality of the vacuum created, the characteristics of the thermocouple (A , ϵ and R) and the temperature of the surroundings (T_0). The characteristic curve obtained with the used thermocouple is given in Figure 5.1

Once the characteristic curve is determined, the thermocouple is placed into the flame of interest for the second step of ECM. The thermocouple is now heated by convection of the flame and by the Joule heating together. The power balance of this second step contains a

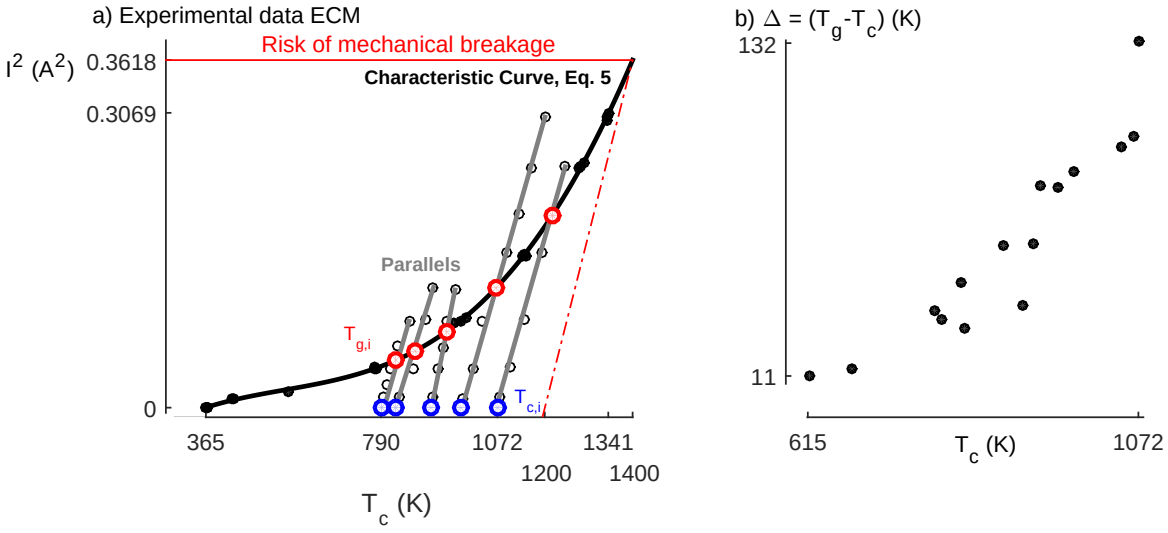

Figure 5.1: a) The characteristic curve derived in vacuum with five of the measured parallels for the rich MPE flame. The measured temperatures T_c are the blue markers when no current is applied and the corrected temperatures $T_{g,i}$ are the red markers at the intersections. b) The temperature correction Δ as a function of the measured temperature T_c for the rich MPE flame increases with the measured temperature T_c.

convection and a Joule heating term in the left hand side and a radiation term to describe the losses from the thermocouple to its surroundings in the right hand side:

$$RI^2 + Ah(T_{g,i} - T_c) = A\sigma\epsilon(T_c^4 - T_0^4). \tag{5.6}$$

where $T_{g,i}$ is the actual temperature of the flame related to the measured temperature T_c.

The measurements are repeated for different positions in the laminar flat flame, related to different starting measured temperatures T_c. T_c is the temperature measured when no extra current is applied and heating only occurs by convection. $T_{g,i}$ is the actual flame temperature related to the measured temperature T_c and can only be measured if a current is applied, which is compensating the energy loss by radiation. When Equation 5.6 is converted to a correlation of I^2 as a function of the measured temperature T_c, the following is found:

$$I^2 = \frac{A\sigma\epsilon(T_c^4 - T_0^4) - Ah(T_{g,i} - T_c)}{R} \tag{5.7}$$

Several correlations between I^2 and different T_c are collected. These experimental curves will further on be called parallels (Figure 5.1).

We now have two equations that expresses I^2 as a function of the measured temperature T_c derived for different measuring conditions. When we equal Equation 5.5 and 5.7 at each other, we get:

$$I^2 = \frac{A\sigma\epsilon(T_{c,i}^4 - T_0^4)}{R} = \frac{A\sigma\epsilon(T_{c,i}^4 - T_0^4) - Ah(T_{g,i} - T_c)}{R}. \tag{5.8}$$

Equation 5.8 can be simplified by discarding the radiation terms and the resistance of the thermocouple, implying that only the convection term equalling zero, $Ah(T_{g,i} - T_c) = 0$, remains at the intersection of the characteristic curve and the parallels. The convection term only equals zero when the measured temperature T_c is equal to the real flame temperature $T_{g,i}$.

This means that at the intersections, the measured temperature T_c is increased sufficiently by the Joule heating to compensate for the radiation losses of the thermocouple, and the actual flame temperature $T_{g,i}$, the temperature that we want to know, is measured.

A visualisation of the working principle of ECM can be found in Figure 5.1, where the characteristic curve and some parallels for the temperature correction in the rich MPE flame are shown. The red markers at the intersection of the characteristic curve and the parallels are the corrected temperatures $T_{g,i}$, the blue markers are the measured temperatures T_c when no current is applied. The difference between the measured temperature T_c and the actual flame temperature T_g increases with the measured temperature T_c. This can also be seen in the correction curve (Figure 5.1 b), defined as the relation between T_c and the temperature correction ΔT_{corr}.

ECM is used as temperature correction method at different occasions in literature. Bonne et al. used ECM to measure the temperature profile of laminar hydrogen and methane flames. Finding no significant difference between the temperature profiles obtained by ECM and by analysing the OH radical concentration profile [118]. Bakali et al. corrected for radiative losses in rich premixed n-heptane and iso-octane flames at atmospheric pressure with ECM [119]. Hayhurst used ECM not only to correct for radiative energy losses but also to determine the emissivity of the thermocouple junction and the heat transfer coefficients [120]. He used the Kramers Nusselt number correlation, which was validated by Bradley et al. [121], to calculate the heat transfer coefficients [122]. The calculated h values lie within 10% of the measured values. The corrected temperatures were compared by Hayhurst with temperatures measured by the sodium D-line reversal method. The sodium D-line reversal method is explained in [123], and derives the flame temperature from excited Na atoms measurements when sodium is added to mostly nitrogen containing flames. The difference between both methods could be explained by the error resulting from the catalytic heating effect on the thermocouple [120].

The temperature in laminar premixed Ethanol/Methane/Oxygen/Argon flames were measured with a type B thermocouple by Tran et al. [124]. The diameter of the thermocouples was 0.1 mm and it was coated by a 0.05 mm layer of BeO-Y_2O_3 to reduce the heating due to the catalytic effect on the thermocouple. The correction was done with ECM and a uncertainty of $\pm$20 K was assumed on the corrected temperature in the burned gases.

Pousse et al. used a coated type B thermocouple with a diameter of 0.2 mm to measure the temperature in an indane/CH_4/O_2/Ar flame with and without the sampling probe present. The presence of the probe had a cooling effect in the flame front, however the same equilibrium temperature corrected for radiation losses by ECM was measured by both conditions [125].

A Pt/Pt-13%Rh themocouple coated by BeO-Y_2O_3 was used by Lamoureux et al. to measure the temperature in CH_4/O_2/N_2 flames at 5.3 kPa [126]. A temperature of 1770 K was reached in the burned gases after temperature correction with ECM and the uncertainty was estimated to be $\pm$5%.

Our own research group measured the temperature in different low pressure flames with a Pt/Pt-Rh 10% thermcouple coated with BeO-Y_2O_3. The flames that were investigated are formaldehyde flames [110], acetone added to H_2/O_2/Ar flames [115] and benzene and benzene/ethanol flames [111]. The temperature of all these flames were corrected by ECM.

A second method quantifies the correction by calculating the radiation losses, by solving Equation 5.3. To achieve the corrected temperature T_g the value of T_0, ϵ and h need to be determined. A value for the heat transfer coefficient h between the flame and the thermocouple is estimated by a Heat Transfer Model (HTM) together with the determination of the temperature of the surroundings T_0 and the emissivity ϵ of the thermocouple [127].

Sato et al. describes an iterative procedure to find the conductive and radiative heat losses for thermocouple measurements in flames [128]. The temperature in Hydrogen/Air and town gas/Air flames at atmospheric pressure were measured with three uncoated Pt/13%PtRh thermocouples with varying diameter. The measured temperatures were corrected iteratively and the achieved temperature profiles were the same for all thermocouples. The emissivity from the gas to the thermocouples was found negligible, since the mass of the reacting gas is low. However, if soot is present in the flame, this term cannot be neglected [121]. Sato used the equation of Eckert for the convective heat transfer coefficent on the wire surface and the Ranz and Marshall equation for the heat transfer on the surface of the bead.

The temperature profile in sooting premixed ethylene/O_2/Ar flames were measured by Abid et al. at atmospheric pressure [129]. The equivalence ratio of the flames was 2.07 and only the mass flow rate of the unburned gas was changed between the flames from 4.5 to 13 cm·s^{-1}. The higher the initial velocity of the flame, the higher the measured temperature in the flame, since the heat transfer coefficient is positively related to the velocity of the fluid. The temperature was measured by a type S thermocouple coated by BeO-Y_2O_3 to prevent catalytic heating. The wire diameter of the thermocouples is 0.3 mm. The radiation corrections were calculated using the energy balance equation (Equation 5.3). To calculate the heat transfer coefficient h a cylindrical configuration was assumed and the Nusselt number correlation based on Andrews et al. [130] was applied. The effect of soot deposits increasing the emissivity of the thermocouple was taking into account in the calculations and the uncertainty on the absolute temperature is estimated to be around 50 K.

Shaddix wrote a review article about the temperature correction by HTM on fine wire thermocouples [114]. He concluded that different assumptions in the HTM calculations can lead to errors in the order of 50 to 100 K.

The third method uses multiple thermocouples with diminishing bead diameters [131, 132]. If thermocouples with different bead diameters, but with geometrically the same beads, are used to measure the flame temperature, a linear correlation between bead size and measured temperature is found. The corrected flame temperature is found when an extrapolation to a bead diameter equal to zero is made [132].

Next to the correction method, the choice of thermocouple alloys has an effect on the temperature measurements. In our work alloys of platinum and rhodium are used, due to their good properties in both oxidizing and reducing enviroments. However, the thermocouple needs more time to reach the equilibrium by measurements and has a temperature limit of 1800°C. Other alloys combinations, like iridium/rhodium, iridium/tungsten or tungsten/rhenium, can go to higher temperature, but are limited to an oxidizing or a reducing enviroment and since we are measuring both lean and rich flames over the full flame profile they are not an option [121].

5.2 Thermocouple characteristics

A type B thermocouple is used for this work, composed of PtRh6% and PtRh30%. Both PtRh-alloy wires have a diameter of 0.1 mm and a length of around 6 cm. The welding point of the thermocouple wires is the actual thermocouple and this junction bead has a diameter of around 1.7 times the thermocouple wire diameter. To connect the thermocouple with the measuring devices, supporting wires with the same composition but with a diameter of 0.5 mm and a length of around 35 cm are used (Figure 5.2). The supporting wires are placed in a U-shaped metal containment for protection.

Table 5.1: The measured thermoelectric voltage over the thermocouple can be converted to temperature in selected temperature and voltage ranges, by Equation 5.9. The coefficients needed for Equation 5.9 are given in this table [134].

Temperature range	250 to 700°C	700 to 1820°C
Voltage range	291 to 2431 μV	2431 to 13820 μV
c_0	$9.8423321 \cdot 10^{1}$	$2.1315071 \cdot 10^{2}$
c_1	$6.9971500 \cdot 10^{-1}$	$2.8510504 \cdot 10^{-1}$
c_2	$-8.4765304 \cdot 10^{-4}$	$-5.2742887 \cdot 10^{-5}$
c_3	$1.0052644 \cdot 10^{-6}$	$9.9160804 \cdot 10^{-9}$
c_4	$-8.3345952 \cdot 10^{-10}$	$-1.2965303 \cdot 10^{-12}$
c_5	$4.5508542 \cdot 10^{-13}$	$1.1195870 \cdot 10^{-16}$
c_6	$-1.5523037 \cdot 10^{-16}$	$-6.0625199 \cdot 10^{-21}$
c_7	$2.9886750 \cdot 10^{-20}$	$1.8661696 \cdot 10^{-25}$
c_8	$-2.4742860 \cdot 10^{-24}$	$2.4878585 \cdot 10^{-30}$
Error range	-0.02 to 0.03°C	-0.01 to 0.02°C

A coating of BeO-Y_2O_3 of 0.01 mm is applied on the thermocouple wires to avoid radical reactions on the thermocouple surface [133]. This ceramic layer material is available as a chlorhydric acid solution in which 7% of Beryllium oxide and 93% of Yttrium oxide are blended at 100°C. The coating is applicated in layers and after each layer the coating is dried in a Bunsen burner flame [133]. The layer application is stopped when the coating is 0.01 mm thick, which is measured by a microscope.

This type of thermocouple can be used continuously at a temperature of 1600°C and intermittently to 1800°C and is therefore suitable for flame temperature measurements [113]. The welding point of the platina alloys is the actual thermocouple and is placed in parallel to the flame close to the sampling cone as shown in Figure 5.2.

When a thermocouple is submerged in a flame a thermoelectric voltage E occurs, due to the two different platina rhodium alloys. The measured temperature T_c can be derived from this measured thermoelectric voltage by

$$T_c = c_0 + c_1 E + c_2 E^2 + ... + c_i E^i, \tag{5.9}$$

where E is in μV and T_c is in degrees Celsius. The needed coefficients $c_0 ... c_i$ to solve Equation 5.9 for a temperature range from 250 to 1820°C, can be found in Table 5.1 [134].

The uncertainty of the temperature measurement is depending on the error of the voltage measurements. The thermoelectric voltage E, which is a Direct Current (DC), is measured with a multimeter 3458A from Keysight Technologies, with a resolution of 8.5 numbers. During temperature measurements the voltage varies between 2 and 11 mV. The Keysight Technologies multimeter was recalibrated and certificated before the measurements and an uncertainty of 0.76 μV was found when the multimeter was set to measuring potentials lower than 100 mV [135]. The error mentioned in the datasheet of the multimeter for DC voltage measurements lower than 100 mV, is 2.5 ppm of reading and 3 ppm of the full scale. An auto-calibration of

the multimeter is conducted before starting the measurements eliminating errors due to time drift and temperature changes [136].

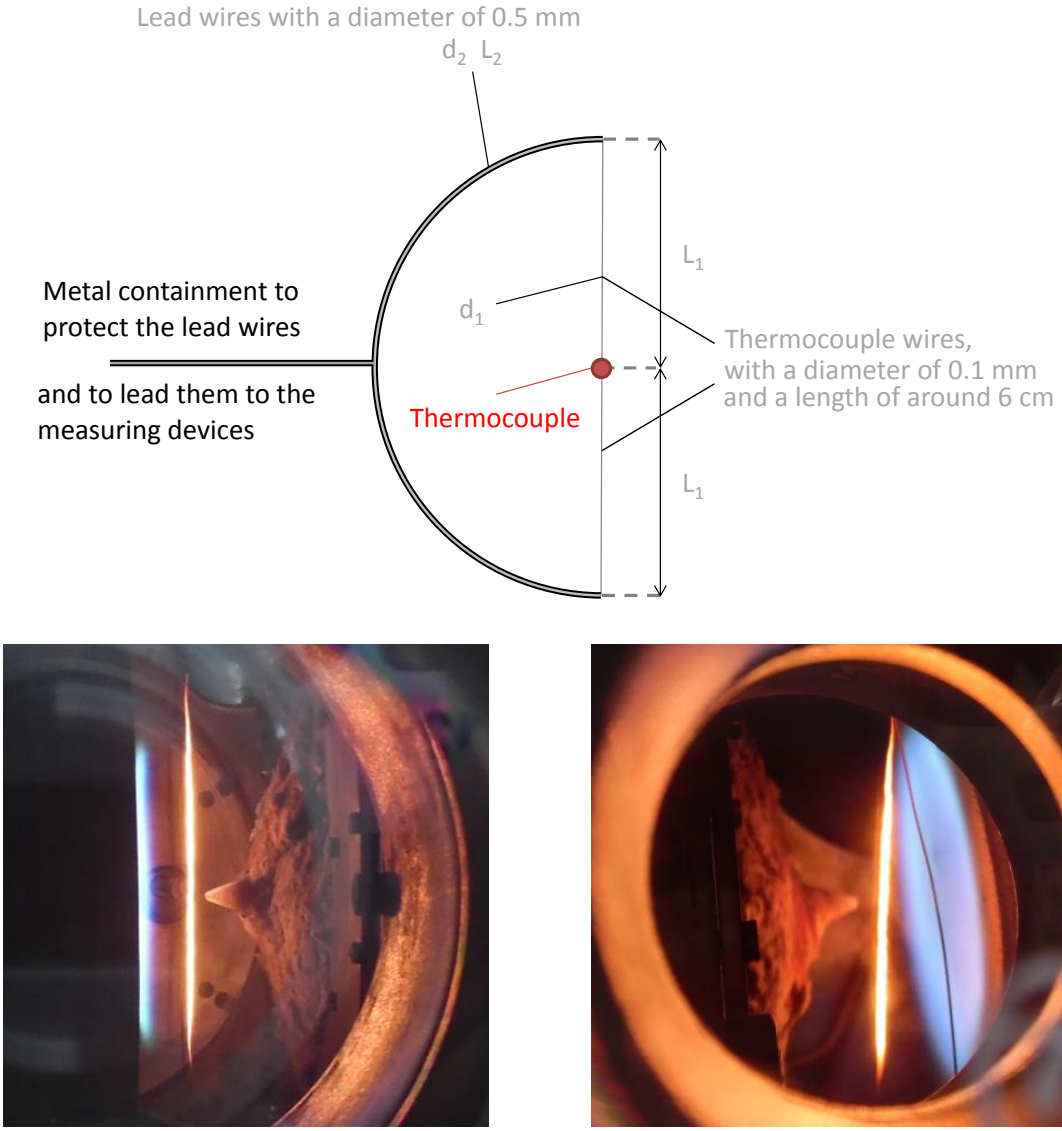

Figure 5.2: The PtRh6% and PtRh30% wires of the thermocouple have a approximatly length of 6 cm, leading to a total length of approximatly 12 cm. The diameter of these wires is around 0.1 mm. To connect the thin PtRh-alloys with the measuring devices, supporting wires with the same composition, but with a greater diameter (0.5 mm) are used. The welding point of both PtRh wires is the actual thermocouple. To avoid radical reactions on the thermocouple surface, a coating is applied until the diameter of the thermocouple wires is 0.11 mm. The thermocouple is placed parallel to the burner while measuring the temperature. The welding point, the actual thermocouple is placed in front of the sampling cone. A U-shaped metal containment is placed around the supporting wires for protection.

The uncertainty on the measured voltage is also related to the ambient temperature variations

during measurement. If the temperature variation is within ±1°C of the temperature the auto-calibration is conducted on, the previous stated uncertainties and errors are valid. So during measurements the ambient temperature should not be varying. An extra error term is added when auto-calibration is applied and the temperature varies more than ±1°C. The extra error term is 0.15 ppm of reading and 1 ppm of full scale multiplied with the difference between the actual ambient temperature and the temperature the multimeter is calibrated for.

As an example: the absolute error ranges between 0.30 and 0.33 μV over the measured range of 0 to 12.8 mV (0 to 2005 K) when the ambient temperature only varies with one degree. If the temperature variation is larger, the error increases. In the case of a variation of 5 K, the error is 0.80 and 0.83 μV over a range of 0 to 12.8 mV.

If we transform the error on the measured voltages to temperatures by Equation 5.9, the effect of the error is rather small. Due to the temperature conversion, the experimental error converges to a minimum value at higher temperatures (Figure 5.3 a). A error of 0.029 K is found for a temperature of 2005 K, which is related to a voltage of 12.8 mV, when the ambient temperature varies within 1°C. When the ambient temperature is 10°C off from the calibration temperature the error due to measurement at 2005 K is still only 0.115 K.

The error on the conversion of voltage to temperature varies from -0.02 to 0.03°C when the temperature is lower than 700°C and from -0.01 to 0.02°C for higher temperatures (Table 5.1). In Figure 5.3 a the conversion error is added to the experimental errors of measurement (dashed lines). The conversion error plays a role at higher temperatures. If the ambient temperature does not vary during measurement, the conversion error is of the same order of magnitude as the experimental error on the measurement.

Next to the error on the voltage measurement, the uncertainty during the temperature measurements in the flames need to be taken into account. Due to fluctuations in the total mass flow, pressure and position of the thermocouple the measured voltage is varying with a standard deviation of 0.02 mV. This standard deviation corresponds to a temperature of 14 K if a temperature of 372 K is measured and decreases to 2 K for measured temperatures around 2000 K (Figure 5.3 b). The experimental uncertainty on the measured temperature is greater than the measuring error, especially at the low temperatures that are measured in the fresh gases and the flame front.

From this uncertainty and error analysis, we can concluded that the uncertainty on the measured temperature due to the multimeter, the conversion of the signal and the uncertainty on the experimental parameters will not be greater than ±14 K at low temperatures and around ±2 K at temperatures close to 2000 K.

A second thermocouple is placed within the burner and is able to measure the temperature at the burner surface. A Type K thermocouple is used, made from nickel-chromium/nickel-alumel. The thermocouple itself does not touch the burner, so no conduction losses occur.

5.3 Assessed flames

The characteristics of the three assessed MPE flames, already described in Section 1, and the characteristics of five assessed ethylene flames are given in Table 5.3. The ethylene flames are investigated since flames where both ECM and HTM can be applied on, are needed to compare the performance of ECM and HTM.

The equivalence ratio of the investigated MPE flames ranges from 0.88 to 1.41. Also the argon dilution and the initial flow velocity vary between the MPE flames, making it possible

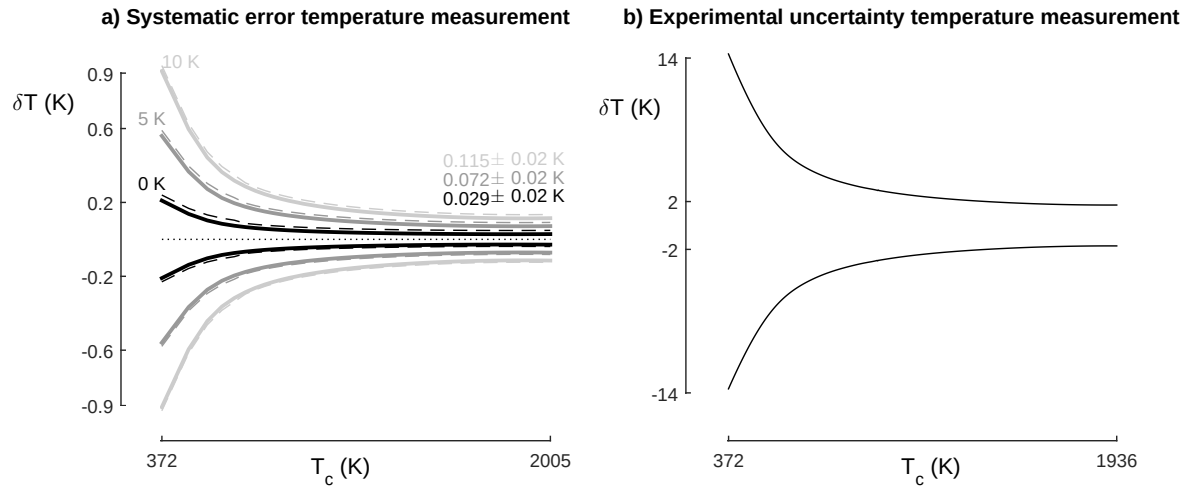

Figure 5.3: a) The systematic error on the temperature measurement decreases with the measured temperature T_c. The conversion error is from the same order of magnitude as error on the measured voltage at high temperatures. Changes in ambient temperature affect the error in the low temperature region more. b) The experimental uncertainty on the temperature measurements ranges from 2 K at a measured temperature of 372 K to 14 K at 1936 K. The uncertainty is due to variation in total mass flow, combustion chamber pressure, thermocouple position, etc. The systematic error is negligible compared to the experimental uncertainty and the total uncertainty is greater for the temperature ofs in the fresh gases and the flame front.

to assess the effect of one of the flame properties on the heat transfer coefficient h achieved by HTM. Therefore, the ethylene flames characteristics are chosen to approximate the MPE flames and only one flame characteristic differ between each C_2H_4 flame.

The equivalence ratio of the C_2H_4 flames ranges between 1.00 and 1.43, with 1.43 as standard value, which is close to the equivalence ratio of the rich MPE flame. The argon dilution is standard 70.8 mole%, also the argon dilution of the rich MPE flame, but is lowered to 59.2 mole% for Flame 7 to be able to assess the effect of the argon dilution on the heat transfer coefficient. The flow velocity is set to 42.7 cm·s^{-1} for Flame 4 to 7 and is increased to 49.7 cm·s^{-1} for Flame 8.

The uncertainty on the flame composition, initial flame velocity and equivalence ratio due to the experimental setup can be found in Table 5.2. The error stated in the user manual for the ethylene MFC is 0.1% of the full scale value, which is 8 L·min^{-1}, and a reading error of 0.5%. The combination of both errors lead to the uncertainty given in Table 5.2. The standard deviation of the parameters during experiments is not taken into account, since there is no sampling or liquid fuel involved and the experimental uncertainty is negligible.

5.4 Measured temperature profiles

The measured temperature profiles of the rich, stoichiometric and lean MPE flame are discussed together with the measured temperature profiles of the ethylene flames. The temperature profiles of the three MPE flames were measured using the Type B thermocouple decribed in Section 5.2.

Table 5.2: Error due to the controllers on the total mole flow, the mole fractions of the reactants and the air fuel equivalence ratio for the five assessed ethylene flames, expressed as standard deviation and relative error (RE)

	$\dot{m}_{total} \pm \sigma$ ($g{\cdot}s^{-1}$)	RE %	$X_{Ar} \pm \sigma$ (mole%)	RE %	$X_{O_2} \pm \sigma$ (mole%)	RE %	$X_{C_2H_4} \pm \sigma$ (mole%)	RE %	$\phi \pm \sigma$ (-)	RE %
Flame 4	0.238 ±0.0011	0.48	70.8 ±0.45	0.64	19.8 ±0.10	0.50	9.4 ±0.05	0.51	1.43 ±0.003	0.22
Flame 5	0.234 ±0.0011	0.48	70.8 ±0.45	0.64	20.8 ±0.11	0.51	8.5 ±0.04	0.51	1.22 ±0.003	0.22
Flame 6	0.229 ±0.0011	0.48	70.8 ±0.45	0.64	21.9 ±0.11	0.51	7.3 ±0.04	0.50	1.00 ±0.002	0.22
Flame 7	0.250 ±0.0011	0.45	59.2 ±0.34	0.58	27.6 ±0.14	0.49	13.2 ±0.06	0.49	1.43 ±0.004	0.26
Flame 8	0.277 ±0.0013	0.47	70.8 ±0.44	0.62	19.8 ±0.10	0.49	9.4 ±0.05	0.49	1.43 ±0.003	0.20

Table 5.3: Composition and characteristics of the three MPE flames, for which the corrected temperature profiles need to be determined for further use in kinetic modelling. Together with the characteristics of the five ethylene flames. One parameter changes for each ethylene flame compared to the default flame Flame 4. The ethylene flames are used to assess the effect of changes in equivalence ratio, argon dilution and initial flow velocity on the temperature correction.

		MPE			**C_2H_4**				
		Flame 1	Flame 2	Flame 3	Flame 4	Flame 5	Flame 6	Flame 7	Flame 8
Equivalence ratio	ϕ	1.41	1.15	0.88	**1.43**	**1.22**	**1.00**	1.43	1.43
Argon dilution	mole%	70.8	67.1	61.7	70.8	70.8	70.8	**59.2**	70.8
Velocity	$cm{\cdot}s^{-1}$	45.0	47.5	51.7	42.7	42.7	42.7	42.7	**49.7**
Mass flow	$g{\cdot}s^{-1}$	0.2260	0.2358	0.2521	0.1935	0.1937	0.1939	0.1879	0.2249
Volume flow	$m^3{\cdot}s^{-1}$	0.42	0.45	0.49	0.42	0.42	0.42	0.42	0.49
T_{burner}	K	535	757	720	624	672	707	751	672
T_{ad},T_{in}=T_{523K}	K	2459	2523	2535	2520	2538	2521	2633	2520

The uncorrected temperature profiles are shown in Figure 5.4. The highest temperature was measured for the lean MPE flame, due to lowest argon dilution of 61.7 mole% (Table 1.1). The temperature of the unburned gasses could not be sampled for the lean and stoichiometric flame flames. However, the temperature in the post flame zone could be measured for all the flames. The temperature profiles were measured twice for each flame. The thermocouple was placed in front of the sample cone as close as possible without touching the sampling cone or induced moving of the thermocouple due to sample extraction. At this position the measured and corrected temperature will be the closest to the actual temperature of the extracted sample. The burner was moved upon the sampling cone, with the thermocouple placed in between them. At this position the thermocouple is close to the burner surface and the lowest temperature, related to the fresh gases or the flame front, is measured. Then the burner is moved away, making it possible to measure the temperature at different positions in the flame. The temperature profile measurement was stopped if a temperature decrease was noticed, indicating the post flame zone was reached. Between the measurements of the temperature profiles, the thermocouple could cool down to decrease the risk of breakage.

5.4.1 Methyl pentanoate flames

The temperature profiles measured in the MPE flames are shown in Figure 5.4. The temperature of the flame front and the unburned gases could be measured for the rich MPE flame, resulting in an uncorrected temperature profile ranging from 940 to 1765 K.

The combustion process in the lean and stoichiometric flame starts closer to the burner and the temperature of the unburned gases could not be measured. The higher expected flame velocity for these flames compared to the rich flame, can be an explaination. The flames stabilise to close to the burner and the total flow rate cannot be increased due to experimental restrictions. Also the cooling of the burner cannot be adjusted. The lowest uncorrected temperature T_c measured in the stoichiometric flame is 1507 K, while the measured post flame zone temperature is 1844 K. The post flame zone temperatures measured in the lean flame vary from 1385 K to 1893 K.

As temperature of the unburned gases in the MPE flames, the temperature measured with the type K thermocouple on the burner surface is chosen. A temperature of 535 K is measured at the burner surface for the rich MPE flame, for the stoichiometric and lean MPE flame a temperature higher than 700 K is measured. The temperature difference can be explained by the position of the flame. The rich flame is stabilised further away from the burner than the other two flames, leading to a lower temperature at the burner surface.

The same difference between the post flame zone temperature and the adiabatic temperature is found for the three flames, suggesting that the flames are losing the same amount of heat to their surroundings. The highest temperature of 1893 K temperature is measured in the lean flame, while we expect the stoichiometric flame to be the hottest. An explanation can be found in the lower argon dilution in the lean flame, since also a higher adiabatic flame temperature is found for this flame, which is only related to the flame composition. To conduct ECM, the measured temperature profile needs to be elevated by applying a current to compensate for the radiation losses. So ECM can only be applied in the flame front of the rich MPE flame, since there the measured temperatures there can be increased deliberately by applying a current without the risk of breaking the thermocouple. However the stoichiometric and lean MPE flame cannot be corrected by ECM, since the temperatures are above or close to 1400 K. In addition, the post flame temperature measured in the lean flame is even higher than the maximum temperature for continuous measurement (1873 K).

5.4.2 Ethylene flames

The temperature measurements in the C_2H_4 flames have as purpose to investigate the influence of the flame composition, the argon dilution and the flow rate on the temperature correction found with ECM and HTM. The temperature profiles of the ethylene flames are measured with the same Type B thermocouple as for the MPE flames and are shown in Figure 5.4. The highest temperature is found by the flame with the lowest argon content, as expected since the related adiabatic flame temperatures is also the highest.

Flame 1 and Flame 5 have the same composition, nevertheless a higher temperature of 30 K is found by Flame 5, due to the greater fresh gases velocity which lead to a greater heat transfer to the thermocouple. This effect is in accordance with literature [129].

The maximum measured temperatures for the five ethylene flames only differ 70 K and a difference of the same order of magnitude is found in the measured temperatures on the burner surface, which are set as initial temperature of the temperature profiles.

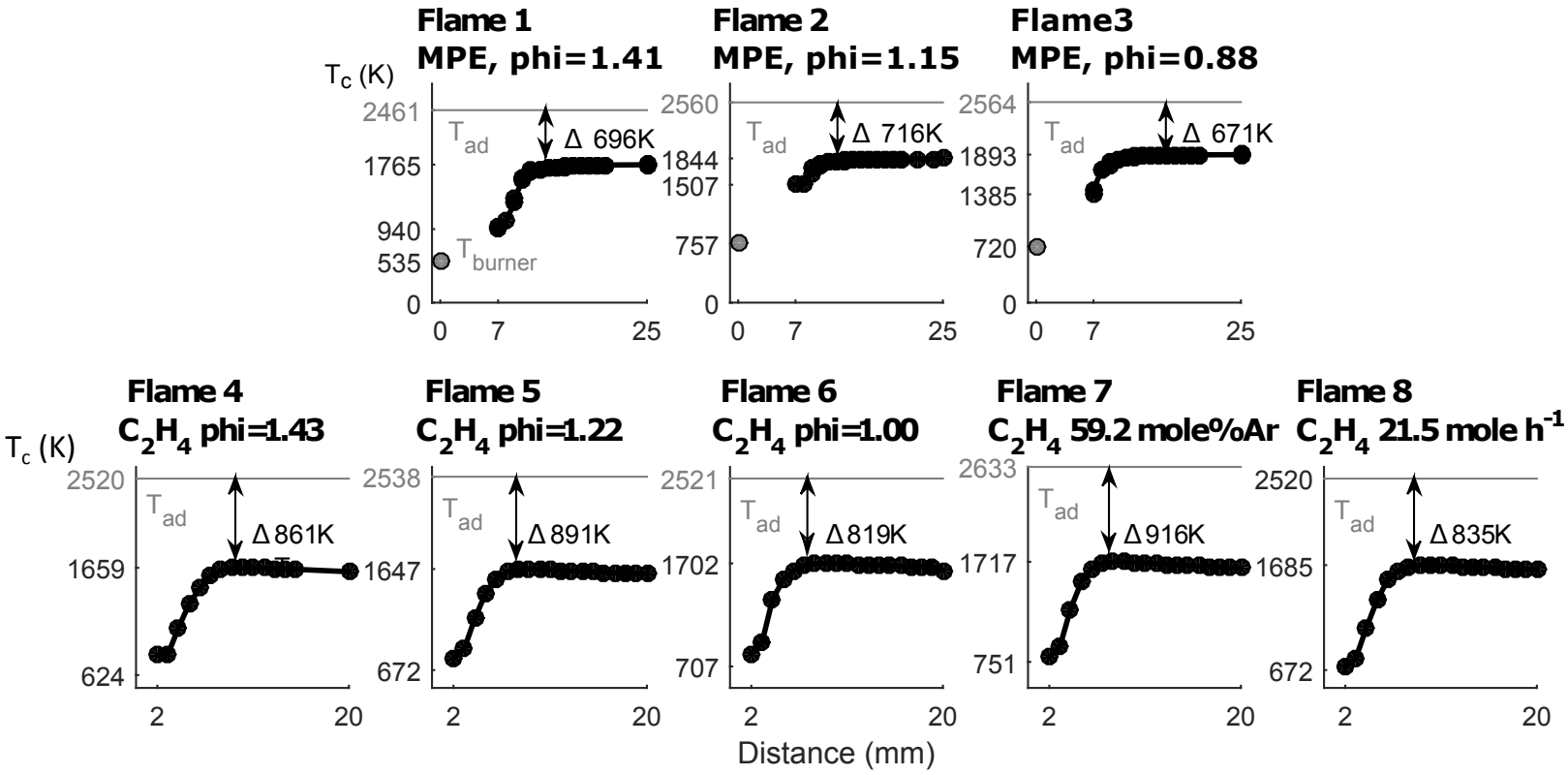

Figure 5.4: The measured temperature profiles for the three assessed MPE flames and the five ethylene flames, without the correction for radiation losses. Similar differences between the measured equilibrium temperature and the adiabatic temperature are found for the three MPE flames, indicating that losses to the burner are similar. The lean MPE flame has a higher temperature compared to the rich and stoichiometric flame, due to its low argon dilution. The same conclusion can be made for the ethylene flame temperature profiles. A decrease in argon dilution leads to a higher measured temperature. Higher heat losses to the experimental setup are found with the ethylene flames compared with the MPE flames, since a greater difference between adiabatic flame temperature and measured temperature in the ethylene flame is found.

5.5 Heat Transfer Model

The Heat Transfer Model (HTM) calculates directly the corrected temperature from the measured temperature by Equation 5.3. The unknown parameters are the emissivity ϵ of the thermocouple, the temperature of the surroundings T_0 and the heat transfer coefficient h of the gas stream to the thermocouple.

The temperature of the surroundings T_0 can be deduced from measurements, while the emissivity ϵ of the thermocouple can be obtained from the characteristic curve of the thermocouple [114, 127] and literature data [137]. To find the heat transfer coefficient h, Nussselt number correlations valid for the experimental geometry and conditions are assessed [114, 127, 138]. In the end the temperature correction ΔT_{corr} is found.

5.5.1 Temperature of surroundings

The temperature of the surroundings T_0 is assumed to lie between the temperature of the burner and the ambient temperature outside of the combustion chamber. The combustion chamber is cooled by tap water and on the outside it is not hotter than 333 K. The temperature at the burner surface and behind the sampling cone is measured during experiments. The temperature at the burner surface ranges between 509 and 746 K for the assessed MPE flames. The temperature after the sampling cone is varying between 323 and 473 K (Appendix 2). From these indirect data, it is assumed that the inner wall of the combustion chamber has a temperature around 398 K on average, within a range of 75 K. A sensitivity analysis will be performed, to assess if these assumptions affect the temperature correction ΔT_{corr}.

5.5.2 Emissivity of the thermocouple

The emissivity of the thermocouple is related to the coating and the material the thermocouple is made from. Different methods exist to quantify the emissivity. A thermal infrared camera can be used to measure the emissivity directly, or an electrical heating method can be applied in vaccuum as done previously in literature [127, 137, 139].

At vacuum, the convection term of the power balance (Equation 5.2) can be omitted. The temperature of the thermocouple is now increased by applying a current instead of convection from the flame. The power balance over the thermocouple does now have a term for the Joule heating, which replaces the convection term, to heat up the thermocouple wire:

$$RI^2 = A\sigma\epsilon(T_c^4 - T_0^4), \tag{5.10}$$

where R is the resistance of the thermocouple, I is the applied current, A is the area of the thermocouple, σ is the Stefan Boltzmann constant, ϵ is the emissivity of the thermocouple, T_c is the measured temperature and T_0 is the temperature of the surroundings. This curve is also called the characteristic curve of the thermocouple and is determined experimentally.

Hence, the emissivity of the thermocouple can be derived from the characteristic curve:

$$\epsilon = \frac{RI^2}{A\sigma(T_c^4 - T_0^4)}. \tag{5.11}$$

The resistance R of the thermocouple needs to be quantified to obtain the emissivity ϵ.

The resistance R of the thermocouple increase with temperature. Experimental resistance data has been measured in a oven over a temperature range of 300 to 1211 K. The achieved

resistance increases from 3.24 to 12.11 Ω (Figure 5.5 a). The measured resistance can be verified by assessing the dimensions of the thermocouple and the resistivity ρ_R of the two different PtRh-alloys the thermocouple consists of. The resistivity ρ_R is a constant specific for the material the thermocouple is made of and for PtRh30% and PtRh6% a value of 19.0 and 17.5 $\mu\Omega$·cm at 20°C is found respectively [140]. If we combine these values with the dimensions of the thermocouple (Figure 5.2), the resistance R can be achieved by

$$R = \rho_R \frac{L}{A_{TC}} \tag{5.12}$$

where L the length of the thermocouple wire and A_{TC} is the cross-sectional area of the thermocouple. The length of the thermocouple wires can vary between the thermocouples, so for the thermocouple wire length an error of 1 cm is assumed and for the lead wires length an error of 5 cm. The diameter of the thermocouple and lead wire is measured with a microscope, an error of 0.01 mm is assumed for both wires. The theoretical resistance varies between 2.8 and 4.2 Ω at 293 K taking into account the uncertainties. This interval contains the value of 3.24 Ω which is measured at 293 K. The thermocouple wires are responsible for more than 80% of the total resistance at 293 K.

The emissivity obtained from Equation 5.11 ranges from 0.32 to 0.53 over a temperature range from 773 to 1341 K. These values are higher than the emissivity values found in literature for uncoated Type B thermocouples, which are ranging from 0.082 to 0.184 [139, 141, 142]. Emissivity values for the BeO-Y_2O_3 coating are ranging from 0.25 to 0.75 in literature, with 0.6 as the most common value [137]. So the coating is determining the emissivity of the thermocouple and not the composition of the thermocouple wires. The measured flame temperatures are higher than 1341 K and an extrapolation to temperatures up to 1900 K is needed. The coating is a ceramic and a maximum value for the emissivity is expected at high temperatures [143, 144].Therefore the value stated by Peterson et al., 0.60±0.08, will be used for further calculations at temperatures higher than 1341 K.

5.5.3 Heat transfer coefficient

The model to predict the heat transfer coeffient h in function of the flame properties is based on the forced convection of a cross flow over a thermocouple wire, where the convective heat transfer coefficient h can be calculated from the Nusselt number (Nu). The Nusselt number is the ratio of convectieve to conductive heat transfer at a boundary layer within a fluid

$$\mathrm{Nu} = \frac{h \cdot d}{\lambda} \tag{5.13}$$

where d is the characteristic length of the assessed configuration, the diameter for a cylinder and sphere, and λ is the thermal conductivity of the fluid. The Nusselt number can on itself be derived from emperical correlations as a function of the Reynold and Prandtl number. However it must be verified that the used emperical correlation, is valid for the assessed configuration and the Reynold and Prandtl number values of the assessed fluid.

Nusselt correlation The first step is to find a Nusselt number correlations which is valid for the the shape of the thermocouple and the characteristics of our flames. There are two possibilities to define the shape of the thermocouple: the junction bead can be seen as a sphere, or the thermocouple wire is taken into account as a cylinder. For both shapes different

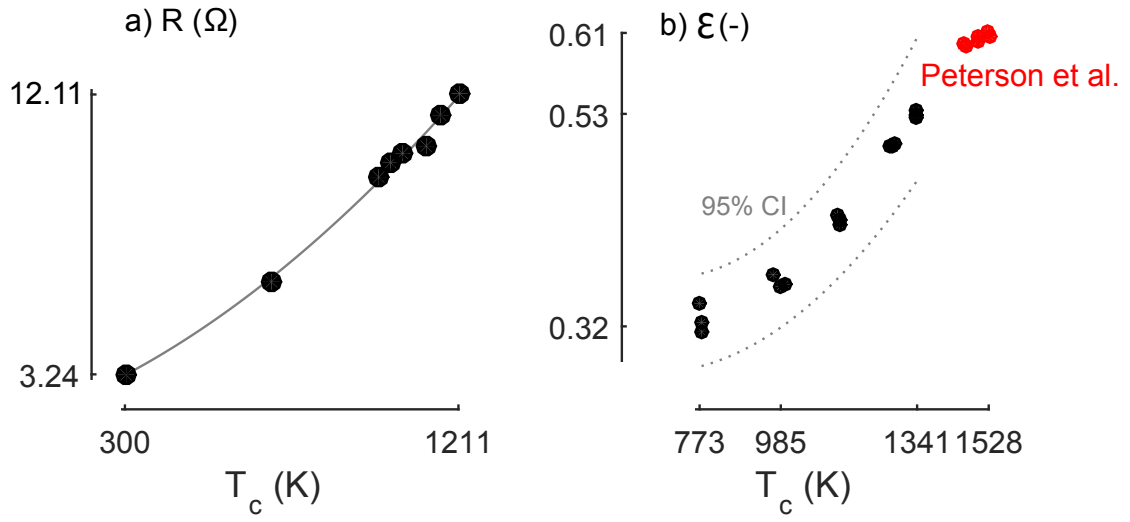

Figure 5.5: a) The thermocouple resistance increases from 2.58 to 11.45 Ω over a temperature range of 300 to 1211 K. b) Once values for R are determined the thermocouples emissivity can be achieved from the characteristic curve. The emissivity increases with temperature and values between 0.32 and 0.53 are found for a temperature range from 778 to 1341 K. The measured flame temperature are higher. Peterson et al. states that the emissivity of BeO-Y_2O_3 coating is around 0.6±0.08 for a temperature of 1500 K and this value will be used further [137].

Nusselt correlations are valid and they have another limit value when the Reynolds number limits to zero.

Shaddix suggests that the decision between shapes is based on the ratio bead-to-wire diameter. If the diameter of the bead is less than three time the diameter of the wire ($d_b/d_w < 3$), the temperature of the fine thermocouple wire and the junction bead can be assumed the same. The heat transfer over the wires will than dominate the energy balance and the Nusselt correlations for a cylinder are valid [114]. Shaddix stated that for nearly all thermocouples, cylindrical heat transfer is the most appropriate. He suggests that the Nu number correlation of Collis and Williams is used, with the known or estimated local flow velocity [114, 145].

Assuming that the thermocouple has a cylindrical configuration, is not completely correct, as the welding bead will always have an influence. Hibshman investigated the transition of a cylindrical thermocouple to a spherical one and concluded that the transient behaviour of the Nusselt number can be described by a correction factor N,

$$N = \frac{\mathrm{Nu_{sph}} - \mathrm{Nu_{real}}}{\mathrm{Nu_{sph}} - \mathrm{Nu_{cyl}}} \tag{5.14}$$

where $\mathrm{Nu_{sph}}$ is the Nusselt number found with a correlation valid for a spherical configuration, $\mathrm{Nu_{cyl}}$ is the Nusselt number valid for a cylindrical configuration and $\mathrm{Nu_{real}}$ is the real Nusselt number valid for the thermocouple in the transition phase [138].

Hibshman investigated thermocouples with bead-to-wire ratios varying from 1.59 to 9. He placed the thermocouples in a hydrogen/air/oxygen premixed flame and measured with all the thermocouples the temperature at the same place in the flame. The measured temperatures varied due to changes in radiation losses since the thermocouples configurations differ. He assumed that the thermocouple with a bead-to-wire ratio of 9 had a pure cyclindrical configuration and calculated the corrected temperature for this thermocouple using the

Whitaker correlation [146]. Once he knew the corrected temperature T_g, he could calculate the real Nusselt number valid for all the thermocouples by

$$\mathrm{Nu}_{\mathrm{real}} = \frac{\sigma\epsilon(T_c^4 - T_0^4)}{(T_g - T_c)}\frac{d}{\lambda}, \tag{5.15}$$

where σ is the Stefan-Boltzmann constant, ϵ is the emissivity of the thermocouple, T_c is the measured temperature, T_0 is the temperature of the surroundings, T_g the real flame temperature, d the diameter of the thermocouple and λ the thermal conductivity of the fluid.

Afterwards he calculated the Nusselt numbers for a cylindrical or spherical configuration for all the thermocouples using the Collis and Williams correlation and the Whitaker correlation respectively. With the Collis and Williams correlation a lower Nusselt number, $\mathrm{Nu}_{\mathrm{cyl}}$, was achieved than the real Nusselt number, while with the Withaker correlation a higher Nusselt number, $\mathrm{Nu}_{\mathrm{sph}}$, was achieved.

Hibshman then calculated the correction factor N for all the thermocouples, and plotted the values of N against the bead-to-wire ratio of the thermocouples (Figure 5.6). Data for both uncoated and SiO_2 coated type B thermocouples were gathered. From the data a transition phase from cylindrical to spherical behaviour can be seen. A linear regression was made through the data, only forcing it through the unity point and a 95% uncertainty interval was established. The coating does not have a considerable effect on the transition as all measurements with or without coating lie within the confidence interval.

Our thermocouple has a bead-to-wire ratio of 1.7 and for this ratio a correction factor of 0.92 ± 0.2 is suggested by Hibshman. In the further simulations a value for N will be selected between 0.72 and 1. The lower limit of the 95% uncertainty interval is 0.72 and physically a maximum value of 1 can be applied. Before choosing a Nusselt correlation valid for a cylindrical of spherical configuration, the Reynolds and Prandtl numbers of the reacting streams are calculated to check which Nusselt number correlations are valid.

Reynolds number The Reynolds number (Re) is defined as the ratio of inertial forces to viscous forces and it characterises the flow regime of the fluid.

$$\mathrm{Re} = \frac{v \cdot d \cdot \rho}{\eta} \tag{5.16}$$

where v is velocity of the fluid, d is the characteristic length, η is the dynamic viscosity of the fluid and ρ is the density of the fluid. At low Reynolds numbers, a laminar regime occurs where the viscous forces are more important. A turbulent regime exists when the inertial forces are dominant with a Reynolds number higher than the threshold value stated.

Since we are investigating laminar flat flames, we expect to find low Reynolds numbers. To calculate the Reynolds numbers for the assessed MPE flames, the velocity v of the streams is needed, just like the dynamic viscosity η and the density ρ of the fluid and the diameter d of the thermocouple wire.

The velocity of the MPE flames ranges between 45.0, 47.5 and 51.7 $\mathrm{m{\cdot}s^{-1}}$ at 293.15 K and 55 mbar for the rich, stoichiometric and lean flame respectively. The velocity of the ethylene flames is either 42.7 or 49.7 $\mathrm{cm{\cdot}s^{-1}}$ regarding the fresh gases stream at 55 mbar. However in the combustion chamber the temperature increases significantly due to the combustion process, and we expect an increase in velocity. The cross section of the burner used for the calculations is circular with a diameter of 8 cm.

The needed density ρ and dynamic viscosity η are calculated from the transport data of the kinetic mechanism for MPE combustion and the Cantera software [112]. The Cantera software is chosen since it is compatible with the MATLAB software [147] and the gas properties can be directly used in further calculations. The pressure, total mole flow and compositions of the flame are needed as input parameters for the calculations. The experimental uncertainty on these three parameters, discussed in Section 3.7, are included in the calculations by means of a Monte Carlo analysis.

A Monte Carlo analysis is a global uncertainty method, based on the sampling of parameter values [148]. A process is simulated n times within a Monte Carlo analysis. For each simulation parameter values are selected from a given range by the implied probability density function (pdf). The results of the simulations give an overview of all the possible outcomes. In this case, 100 samples are run and an uniform distribution is chosen as pdf, except for the emissity. An overview of the implied parameter ranges is given in Table 5.5.

In Figure 5.7, the convergence of the Monte Carlo analysis is proven. The mean value of the achieved Re numbers is shown after each iteration, together with their standard deviation and this for the rich MPE flame. The Collis and Williams Nusselt number correlation is used for these calculations. After 100 iterations both the mean value and the standard deviation converge, proofing that 100 runs are enough.

The temperature at which the flame properties are evaluated is depending on the assessed configuration. Nusselt number correlations valid for a sphere need to be evaluated at the temperature of the free stream gas T_∞, which is assumed to be the adiabatic flame temperature. The Nusselt relation applying on a cylindrical configuration, must be evaluated at the film temperature T_m, which is defined as the mean of the measured temperature T_c and the actual flame temperature T_g.

For a first calculation, the Nusselt number correlations of Collis and Williams correlation [145] and Ranz and Marshall are selected [149]. If we calculate the Reynolds numbers for both configurations in function of the temperature for the MPE flames and the ethylene flames, we find that they vary between 0.05 and 0.5 (Figure 5.8). The Reynolds number value decreases with the temperature, due to the decreasing density and the increasing viscosity. Lower Reynolds numbers are found for the cylindrical configuration, which is related to the lower temperature T_m they are evaluated on.

Hibshman used the Whitaker correlation for a spherical configuration with the junction bead diameter as characteristic length. The Whitaker correlation is valid for Reynolds numbers between 3.5 and 76 000 (Table 5.4) [146]. Due to this limits the Whitaker correlation cannot be used for the assessed flames. The Ranz and Marshall correlation for spheres is valid for Reynolds numbers between 0 and 200 [149]. The Reynolds numbers of our flames lie within this range, so this correlation can be used for further calculations. No substantial difference between both Nusselt numbers correlations was found, so it is assumed that the transient relation found by Hibshman is also valid if the Ranz and Marshall correlation is used.

The Collis and Williams correlations is valid over a Reynolds number range of 0.02 to 44, so the Collis and Williams correlation is valid for our flames. Other valid correlations are the Kramers correlation and the Andrews correlation [122, 130]. All three Nusselt number correlations for a cylinder will be assessed and the effect of Nusselt number correlations choice on the corrected temperature can be deduced.

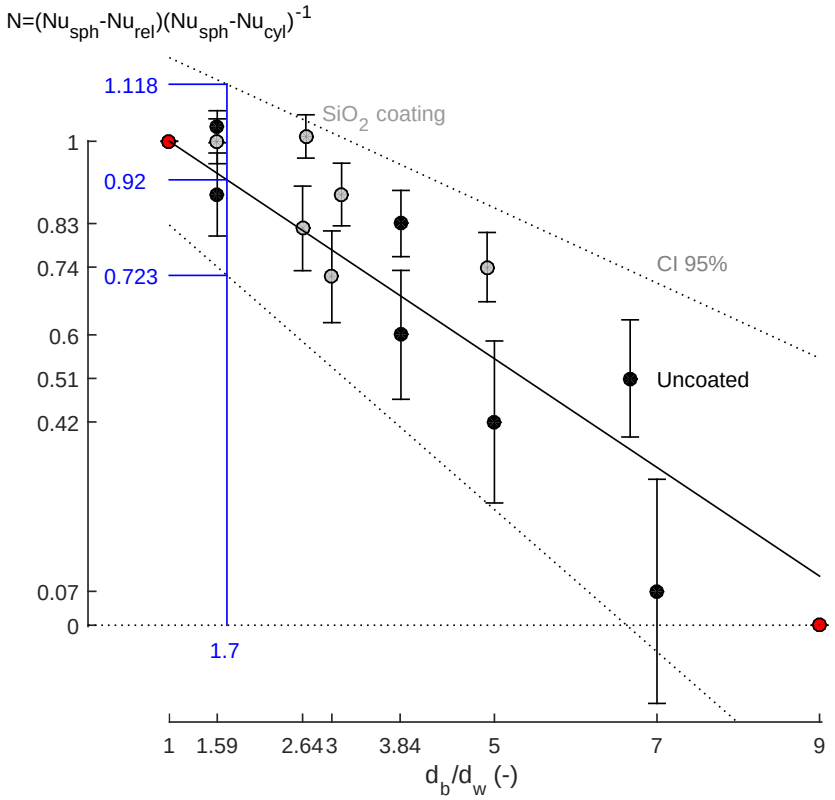

Figure 5.6: Hibsman determined the correction factor N for 14 thermocouples with different bead-to-wire ratios (d_b/d_w). He assumed that if the bead-to-wire ratio is unity, the correction factor N is also unity and when the bead-to-wire ratio is nine a cylindrical configuration is appropriate, related to a correction factor N of zero. A linear regression was made through the data provided in [138] and a 95% confidence interval was established. The thermocouple used for the flame temperature measurements has a bead-to-wire ratio of 1.7, related to a value for N of 0.92±0.2.

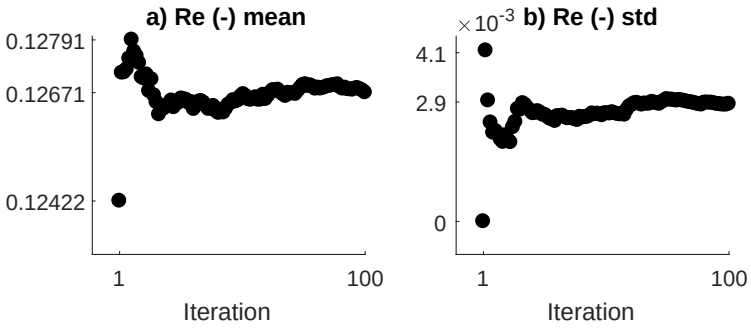

Figure 5.7: The mean Reynolds numbers after each iteration step of the Monte Carlo analysis. The Reynolds number is calculated for the rich MPE flame with the Collis and Williams correlation.

Table 5.4: Nusselt correlations valid at low Reynolds numbers for forced convection over a cylindrical and spherical configuration. The Nusselt correlations valid for a cylinder are evaluated at T_m, while the equations valid for a sphere are evaluated at T_∞.

Configuration	Nusselt correlation		Re range	T	Ref.
Cylinder	Collis and Williams	$Nu = (0.24 + 0.56\ Re^{0.45}) \left(\frac{T_m}{T_\infty}\right)^{0.17}$	$0.02 < \mathrm{Re} < 44$	T_m	[145]
	Kramers	$Nu = 0.42\ Pr^{0.2} + 0.57\ Pr^{1/3}\ Re^{1/2}$	$0.01 < \mathrm{Re} < 10\,000$	T_m	[122]
	Andrews	$Nu = 0.34 + 0.65\ Re^{0.45}$	$0.02 < \mathrm{Re} < 20$	T_m	[130]
Sphere	Ranz and Marschall	$Nu = 2.0 + 0.60\ Re^{1/2}\ Pr^{1/3}$	$0 < \mathrm{Re} < 200$	T_∞	[149]
	Whitaker	$Nu = 2.0 + \left(0.4\ Re^{1/2} + 0.06\ Re^{2/3}\right) Pr^{0.4} \left(\frac{\mu_\infty}{\mu_s}\right)^{1/4}$	$3.5<\mathrm{Re}<76\,000$	T_∞	[146]

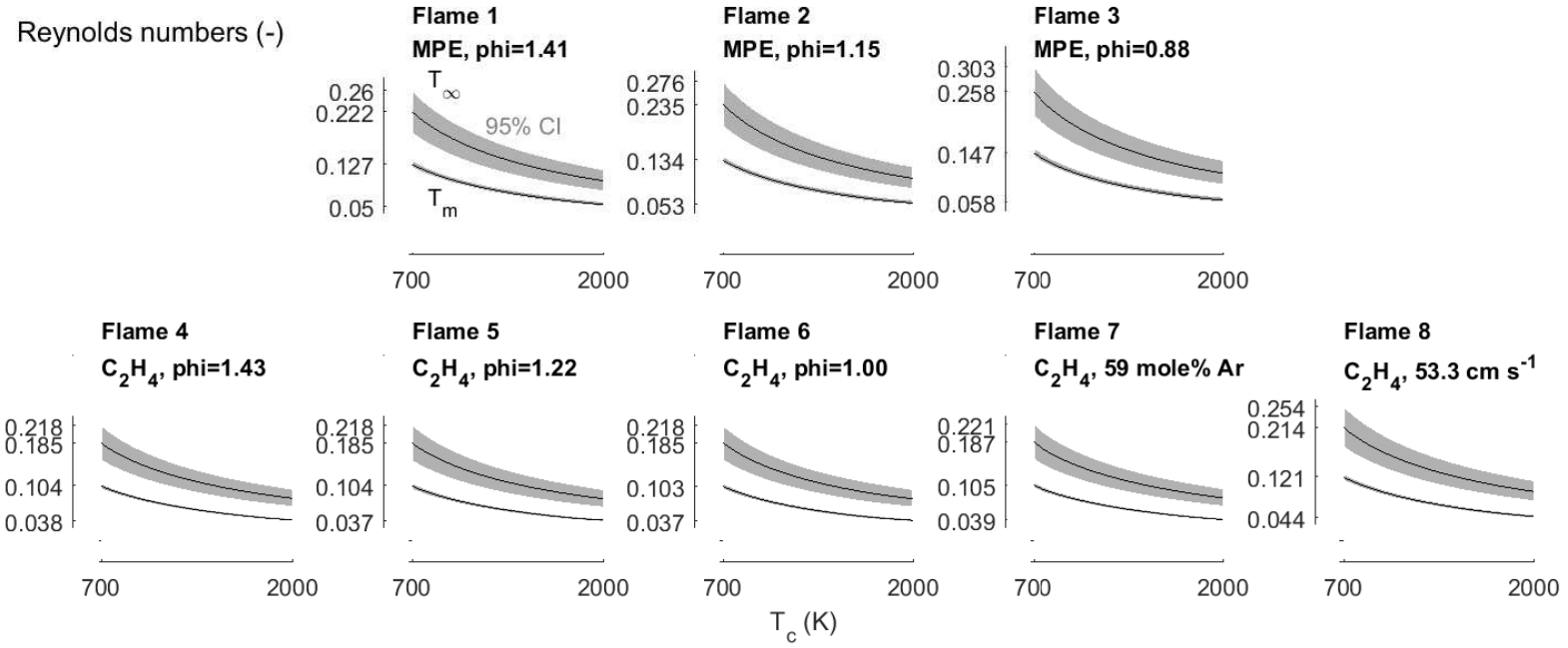

Figure 5.8: The Reynolds numbers for the MPE flames calculated at the film temperature T_m with the Collis and Williams correlation [145] and at the free stream temperature T_∞ with the Ranz and Marschall correlation [149].

Prandtl number The Nusselt correlations of Kramers, Ranz and Marshall and Whitaker are also depending on the Prandtl number (Pr) (Table 5.4). The Prandtl number is a dimensionless number, defined as the ratio of momentum diffusity to thermal diffusity:

$$\mathrm{Pr} = \frac{c_p\ \eta}{\lambda}, \tag{5.17}$$

where c_p is the specific heat, η is the dynamic viscosity and λ is the thermal conductivity. The gas properties are determined by the Cantera software at the temperature defined by the Nusselt correlation their are needed for.

Real Nusselt number Once the Nusselts numbers for both configurations are obtained the real Nusselt number can be calculated with the correction factor N. The heat transfer coefficient h can then be determined by

$$h = \frac{\mathrm{Nu}_{\mathrm{real}}\lambda}{d}, \tag{5.18}$$

where λ is the thermal conductivity of the fluid and d is the characteristic length of the assessed configuration. Since the thermocouple is behaving more as a cylinder, the diameter of the thermocouple wires is chosen as characteristic length.

The heat transfer coefficient h, the emissivity of the thermocouple ϵ and the temperature of the surroundings T_0 are now known and the corrected temperature T_g can be calculated with Equation 5.3.

5.5.4 HTM applied on flames

Before we can calculate the temperature correction with the model, the Nusselt number for the thermocouple and the heat transfer coefficients h are calculated.

The Nusselt numbers achieved by the Kramers and the Ranz and Marschall correlations are shown in Figure 5.9 over a temperature range of 700 to 2000 K. Due to the low Reynolds numbers of the flames the Nusselt numbers tend to their theoretical limit. The Nusselt number limit for a spherical configuration is 2, while for a cylinder it is around 0.3 if the Re number curtails to zero [114]. Since the temperature correction ΔT_{corr} is directly related to the Nusselt number, the temperature correction can differ with a factor 6 between both configurations. However, the used thermocouple will behave more like a cylinder due to the low bead-to-wire ratio of 1.7. The real Nusselt numbers are calculated by Equation 5.15, which is shown on Figure 5.9 as the black lines. The found Nusselt numbers for the flames do not differ by more than 2%, since there is no variation between the Re numbers of the flames.

The standard deviation for all Nusselt numbers are shown by a dashed lines and is the result of taking the uncertainty on the flame composition, initial velocity, pressure, the correction factor N, the emissivity and diameter of the thermocouple into account. The uncertainty on all these parameters are found in Table 5.5. The uncertainty on the Nusselt number is calculated by a Monte Carlo analysis with 100 runs. For each run a value is sampled from the uncertainty range of the parameter. An uniform distribution is applied for most of the parameters, only for the emissivity ϵ a normal distribution is applied and for the correction factor N a triangular distribution is assumed, with the mean value of 0.92 and the limit values 0.72 and 1. The uniform distribution is chosen for most of the parameters, since the pdf of the uncertainty on the parameters is not known. By using the uniform distribution, all the

possible parameters values are weighted the same. A normal distribution is applied for the emissivity, as this distribution is stated by [137]. The triangular distribution is chosen for the correction factor N, since with this distribution no outliers which are physically impossible can occur. A greater uncertainty is found on the real Nusselt number, compared tot the Nusselt number achieved by the Ranz and Kramers correlations, since the uncertainty on the correction factor N is taken into account for its calculations.

In Figure 5.10, the achieved heat transfer coefficients h for the eight assessed flames at the maximum measured temperature T_c are shown together with their standard deviation. The mean values for the heat transfer coefficients achieved by the combination of the Collis and Williams and the Ranz correlations, range from 734 and 759 $\mathrm{W{\cdot}m^{-2}K^{-1}}$ in the MPE flames. An increase of about 90 $\mathrm{W{\cdot}m^{-2}K^{-1}}$ is found for h with the Andrews and Kramers correlations.

The effect of the equivalence ratio, argon dilution and initial flame velocity on the heat transfer coefficient h can be deduced from the simulated values for the ethylene flames. A change from rich to lean conditions leads to a decrease in heat transfer coefficients h values, while a decrease in argon dilution has a positive effect on h. These changes are related to the thermal conductivity of the reacting flame. Increasing the initial velocity has a positive effect of around 100 $\mathrm{W{\cdot}m^{-2}K^{-1}}$ on the heat transfer coeffient, due to a change in the Reynolds numbers and related Nusselt number.

Once the heat transfer coefficient h is determined the corrected temperature T_g can be calculated by Equation 5.3. The temperature corrections ΔT_{corr} for different cylindrical Nusselt correlations in function of the measured temperature are shown in Figure 5.11. The temperature correction ΔT_{corr} is specified for the maximal measured temperature T_c in the flame. The temperature correction in the rich MPE flame is 476±142 K if the Collis and Williams correlation is chosen and 417±108 K for both the Kramer and Andrews correlations. Higher temperature corrections are found with the Collis and Williams correlations since lower heat transfer coefficients were found earlier.

The correction found with the Collis and Williams correlation even surpasses the adiabatic flame temperature for Flame 3, the lean MPE flame. The temperature is surpassed by 173 K, a value close to the uncertainty of the correction (± 182 K). The mean average of the Collis and Williams corrections stays below the adiabatic flame temperature. The Kramers and Andrews correlations result in a lower temperature corrections, whose standard deviations are surpassing the adiabatic temperature limit with 42 K, well within the uncertainty limit (± 134). Therefore the Kramers correlation is chosen as Nusselt number correlations for further correction. The Collis and Williams correlations is suggested by Shaddix and Hibshman [114, 138], however the found correction for Flame 3 is surpassing the adiabatic temperature limit. Shaddix also accepted the Kramers and Andrews correlations as possibilities. These two correlations result in a higher Nusselt number, there is no substantial difference between the correction found with both these correlations. The Kramers correlations is chosen since it is validated by Bradley et al. for fine wire thermocouples [121].

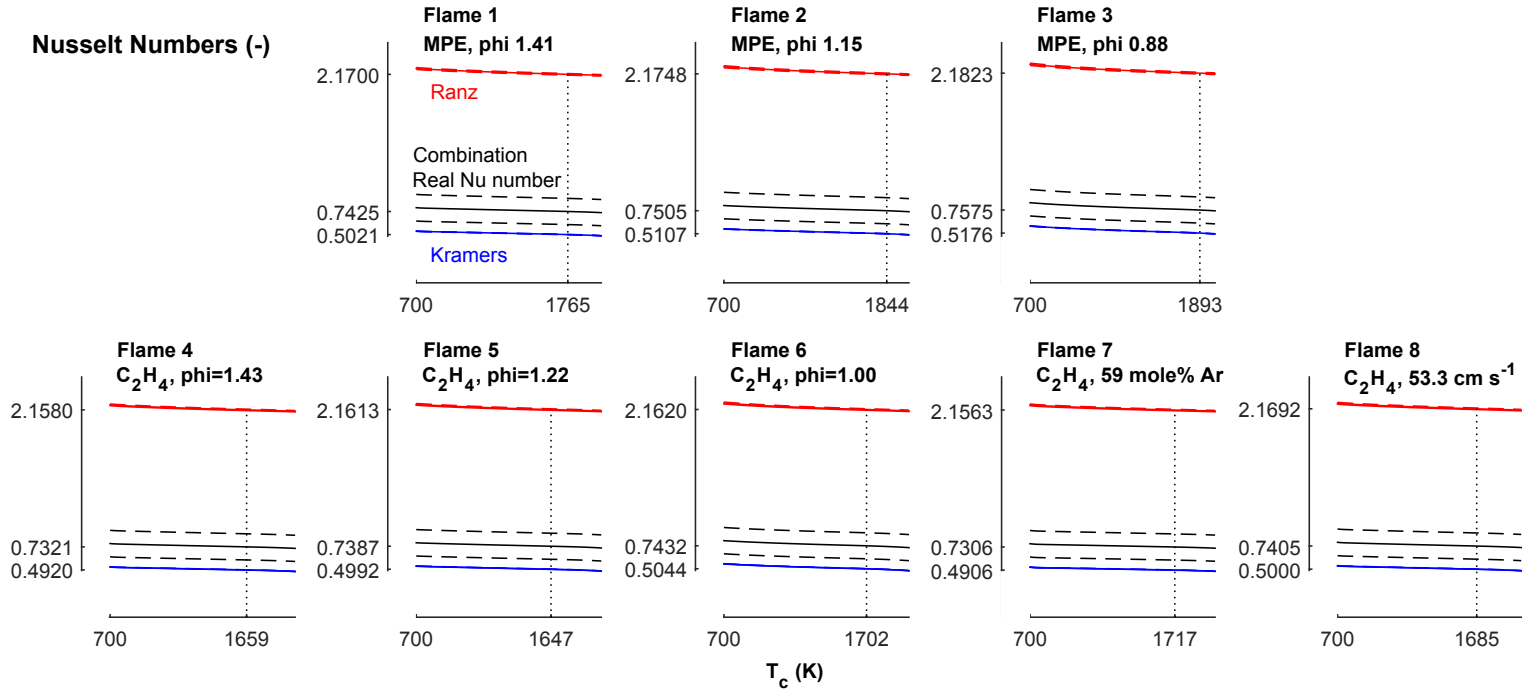

Figure 5.9: The Nusselt numbers achieved by the Kramers and Ranz correlations [122, 149] and the combination of these two correlations to the Nusselt number valid for the thermocouple, whose configuration is between a cylinder and a sphere. The standard deviations are also shown as dashed lines. The standard deviation on the real Nusselt numbers is greater due to the uncertainty on the correction factor N. The temperature dependency of the Nusselt numbers is rather small due the related low Reynolds numbers.

Table 5.5: The expected values and their uncertainty range for the HTM parameters. A uniform distribution is assumed for all the parameters except for the emissivity ϵ, for which a normal distribution is assumed, and the correction factor N for which a triangular distribution is assumed.

		MPE			**C_2H_4**				
Parameter	Unit	ϕ=1.41	ϕ=1.15	ϕ=0.88	ϕ=1.43	ϕ=1.22	ϕ=1.00	59 mole% Ar	53.3 cm· s^{-1}
X_{Ar}	mole%	70.8±0.42	67.1±0.59	61.7±0.58	70.8±0.45	70.8±0.45	70.8±0.45	59.2±0.34	70.8±0.44
X_{O_2}	mole%	24.8±0.20	28.8±0.22	34.5±0.25	19.8±0.10	20.8±0.11	21.9±0.11	27.6±0.14	19.8±0.1
X_{mpe}	mole%	4.4±0.03	4.1±0.03	3.8±0.03					
$X_{C_2H_4}$	mole%				9.4±0.05	8.5±0.04	7.3±0.04	13.2±0.06	9.4±0.05
$\dot{n}_{total}$	mol·min^{-1}	0.33±0.0012	0.35±0.0013	0.38±0.0014	0.31±0.0015	0.31±0.0015	0.31±0.0015	0.31±0.0014	0.36±0.0017
p	mbar	55±0.28	55±0.28	55±0.28	55±0.28	55±0.28	55±0.28	55±0.28	55±0.28
T_0	K	398± 75	398± 75	398± 75	398± 75	398± 75	398± 75	398± 75	398± 75
d	mm	0.11±0.003	0.11±0.003	0.11±0.003	0.11±0.003	0.11±0.003	0.11±0.003	0.11±0.003	0.11±0.003
ϵ	(-)	0.60 ± 0.08	0.60 ± 0.08	0.60 ± 0.08	0.60 ± 0.08	0.60 ± 0.08	0.60 ± 0.08	0.60 ± 0.08	0.60 ± 0.08
N	(-)	0.72:0.92:1.00	0.72:0.92:1.00	0.72:0.92:1.00	0.72:0.92:1.00	0.72:0.92:1.00	0.72:0.92:1.00	0.72:0.92:1.00	0.72:0.92:1.00

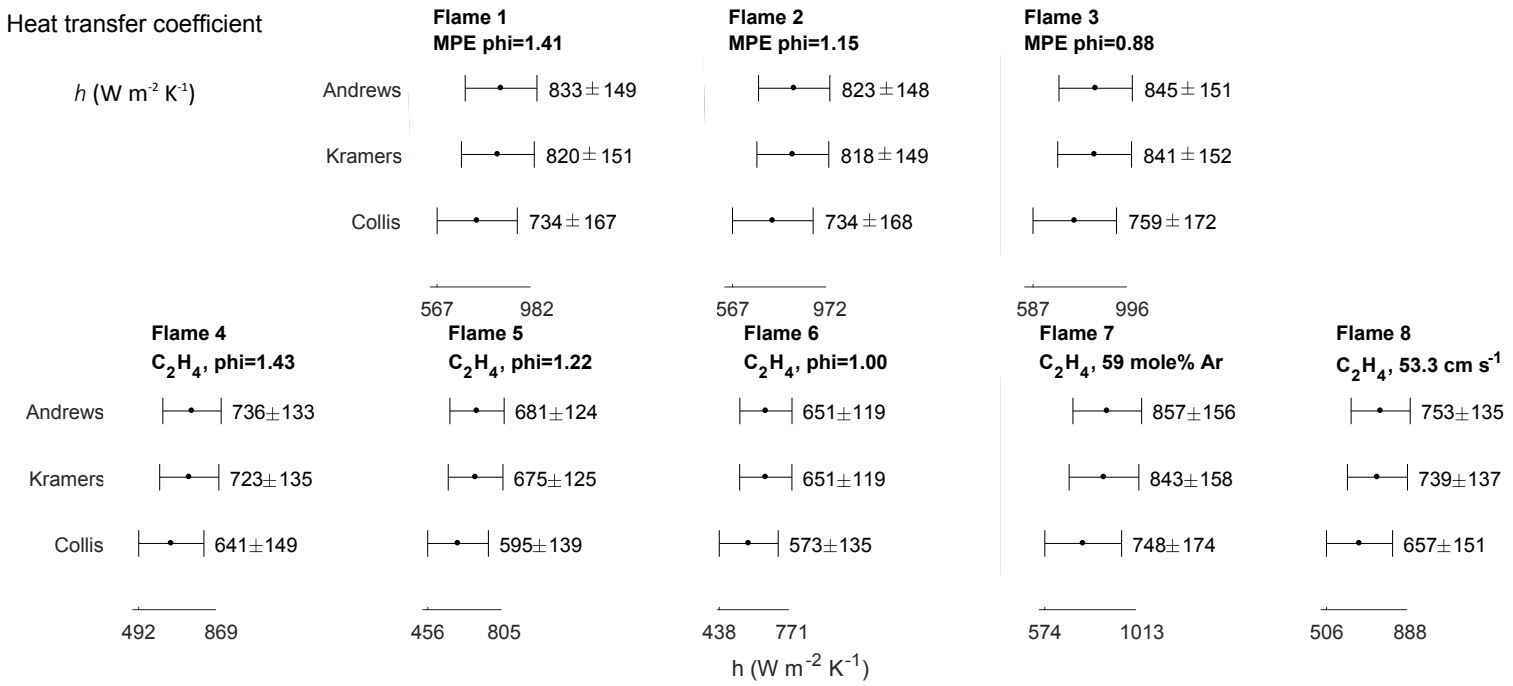

Figure 5.10: The heat transfer coefficients h modeled for the MPE and ethylene flames calculated by the method described in Section 5.5 and this for three combinations of valid Nusselt number correlations. The Ranz and Marschall correlation for a spherical configuration is always used [149]. Three correlations are valid related to a cylindrical configuration: Andrews, Kramers and Collis and Williams [122, 130, 145], just as the transient behavior of the thermocouple configuration. The uncertainty on the heat transfer coefficient is shown as the standard deviation.

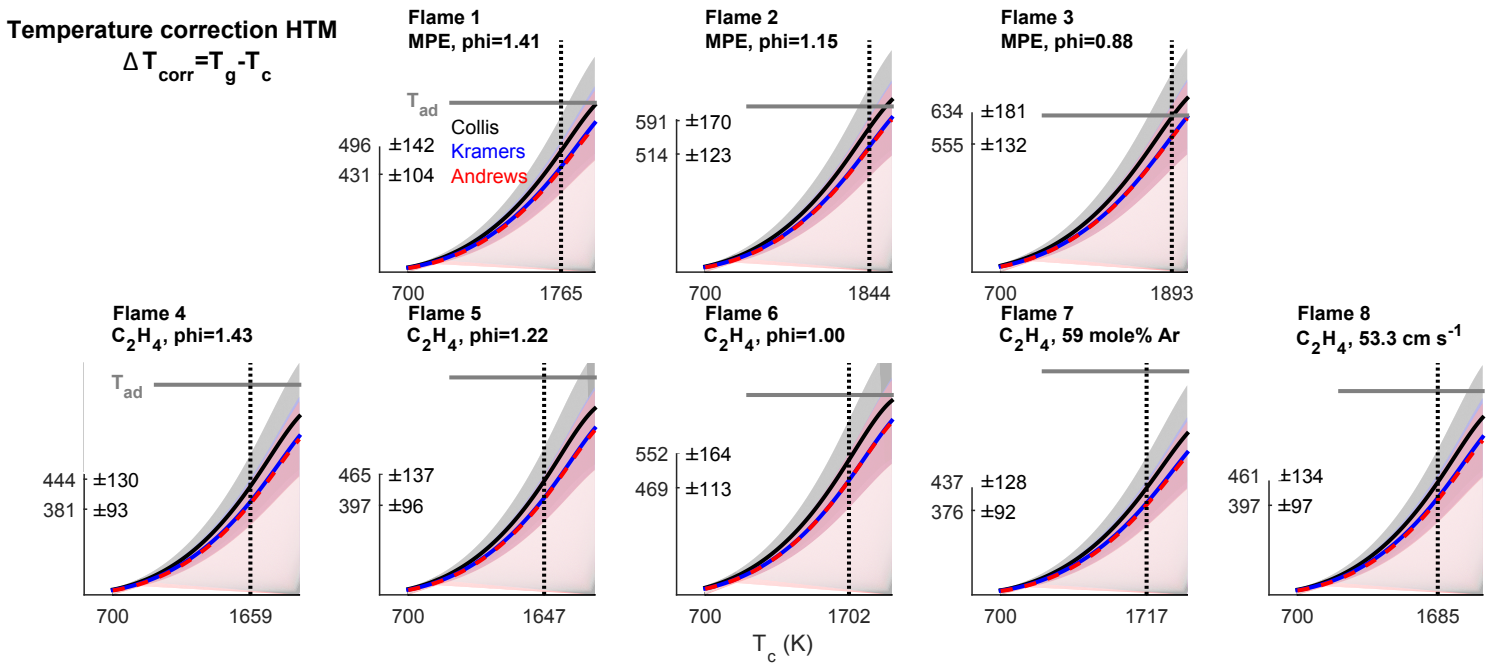

Figure 5.11: The temperature correction ΔT_{corr} in function of the measured temperature T_c achieved by different Nusselt correlations combinations for a thermocouple with a transient behaviour between a sphere and a cylinder. The standard deviation of the correction is shown as areas. Grey is the uncertainty on the Collis and Williams correction and blue and red are the uncertainties on the Kramers and Andrews corrections. Since the correction factor N can be one, high temperature corrections related to a cylindrical configuration can be found. For Flame 3, the lean MPE flame, the uncertainty goes 173 K beyond the adiabatic flame temperature with the Collis and Williams correlation, which is the same order of magnitude as the uncertainty on the correction. The expected mean value stays below the adiabatic flame temperature with only 8 K. The Kramers and Andrews correlations performs better, their uncertainty ranges do not cross the adiabatic flame temperature limit substantially.

5.5.5 Uncertainty analysis

The obtained uncertainty on the temperature correction ΔT_{corr} increases with the measured temperature T_c as can be seen in Figure 5.11. The uncertainty can be caused by the three parameters in Equation 5.3: the emissivity of the thermocouple ϵ, the heat transfer coefficient h and the temperature of the surroundings T_0. The contribution of each parameter to the total uncertainty as a function of the measured temperature T_c is given in Figure 5.12. The heat transfer coefficient is the main source of uncertainty at the maximum T_c. It is responsible for 76 to 78% of the uncertainty, since it bundles the uncertainty on the velocity, flame composition, correction factor N, etc. The emissivity is responsible for the rest. The temperature of the surrounding T_0 has no effect at the assessed high temperature, but at a temperature of 700 K it is responsible for 3% of the uncertainty on the HTM result.

5.5.6 Sensitivity analysis

The sensitivity of the corrected temperature is calculated for the MPE flames and the ethylene flames. The sensitivity to eight independent parameters are assessed. The parameters are the diameter d and emissivity ϵ of the thermocouple, the temperature of the surroundings T_0, the argon dilution X_{Ar}, the measured temperature T_c, the fluid velocity v, the pressure p and the correction factor N.

One after another, the value of each parameter is increased by 1% and a NSC is calculated by

$$\text{NSC} = \frac{x}{T_g}\frac{\Delta T_g}{\Delta x}, \tag{5.19}$$

where x is the expected value of one of the assessed independent parameters stated in Table 5.5, T_g is the initial corrected temperature, ΔT_g is the difference in corrected temperatures of the simulations and Δx is the difference in input parameter.

In Figure 5.13, the results of the sensitivity analysis on the flames can be found. The model is most sensitive to the measured temperature T_c as expected. A NSC of 1.48 to 1.52 is found for the different MPE flames. The term ${T_c}^4$ in the radiation term is responsible for this sensitivity.

The effect of increasing the diameter results in a temperature correction increase, however the explanation is less straightforward. The diameter is used to calculate both the Reynolds number and the heat transfer coefficient h. The increase of the temperature correction indicates that the direct effect on the heat transfer coefficient h by Eq. 5.13 is more important. The low Reynolds numbers are related to almost constant Nusselt numbers and have therefore almost no effect on the temperature correction.

Changing the argon dilution affects the thermal conductivity λ and the related heat transfer coefficient h. The increase in argon mole fraction, has a greater effect in flames where the argon dilution is already high, like Flame 1, since the relative change is greater. That an increase in argon content has a positive effect on the thermal conductivity can also be seen in Flame 7.

The model is less sensitive to the emissivity ϵ, correction factor N, initial stream velocity v and pressure p. The model is insensitive for only one parameter: the temperature of the combustion chamber T_0.

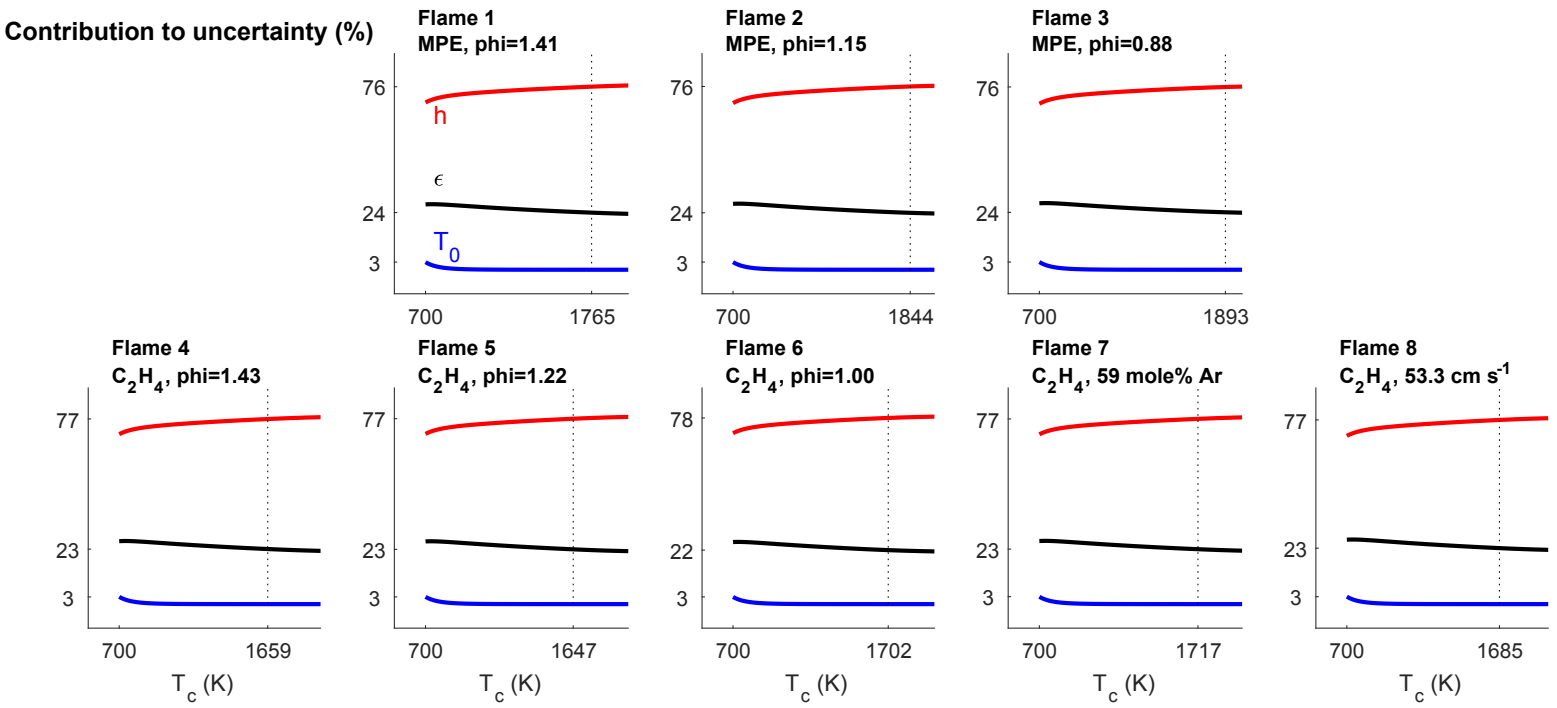

Figure 5.12: The contribution to the uncertainty on the temperature correction ΔT_{corr} of ϵ, h and T_0 as a function of the measured temperature T_c. The heat transfer coefficient contributes to 76 to 78% of the uncertainty, the emissivity is responsible for the rest. The temperature of the surroundings has no effect on the uncertainty.

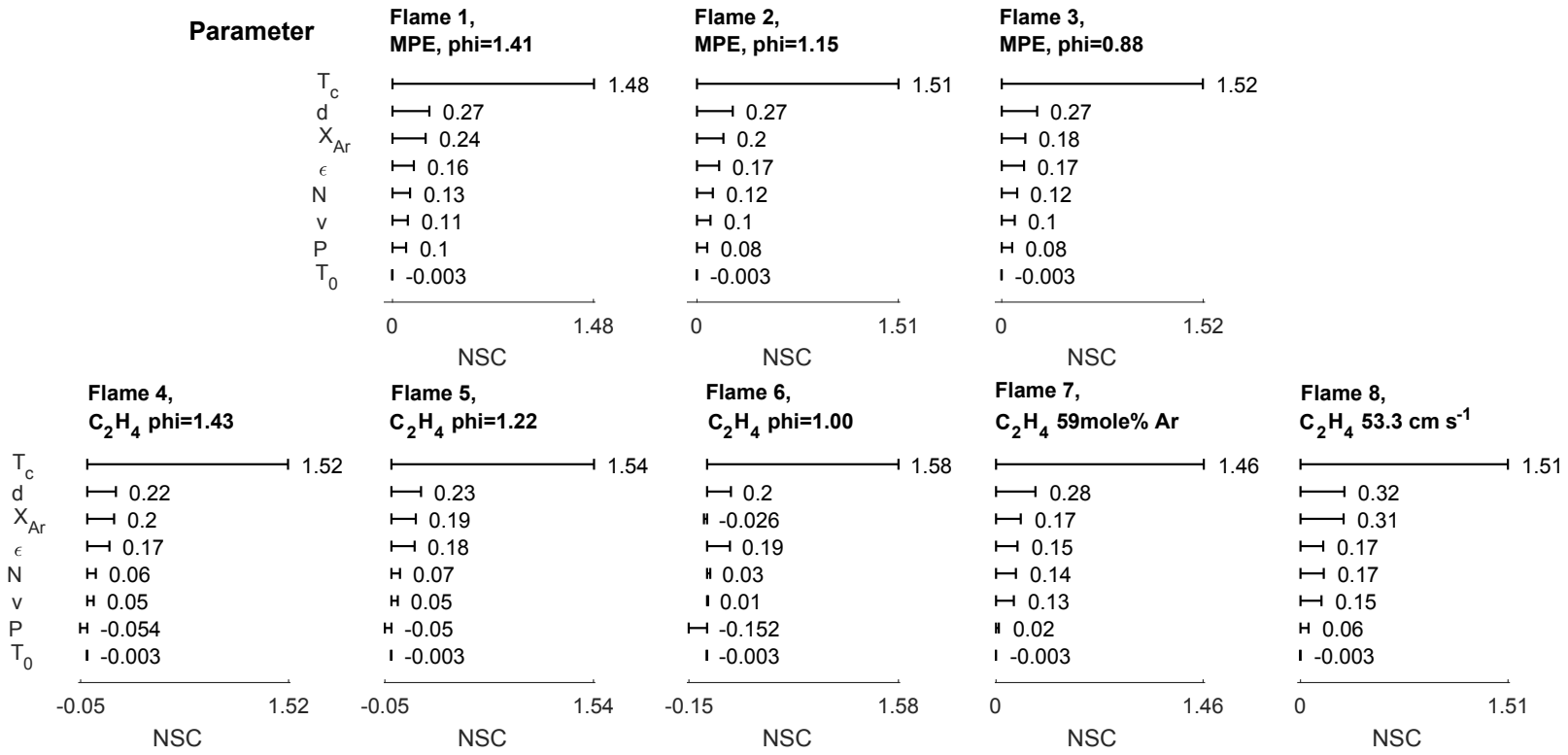

Figure 5.13: The model is most sensitive to the measured temperature T_c. The other parameters also have an effect, only for the temperature of the surroundings T_0 the model is insensitive.

5.6 Electrical Compensation Method

ECM could not be applied on all the flames. Only in the rich MPE flame and the ethylene flames the measured temperature in the flame front was low enough to apply ECM without a considerable risk of thermocouple failing. From experience the measured temperature is limited to 1400 K, to avoid thermocouple breakage. The starting temperature of a parallel should be around 1200 K to not cross this limit during measurements.

In total 15 parallels have been obtained in the rich MPE flame. In Figure 5.14, the parallels are shown, together with the characteristic curve. At the starting points of the parallels no current is applied, so the measured flame temperatures T_c is visualised. The values for T_c range from 616 to 1104 K. The intersections of the parallels with the characteristic curve, are the corrected temperatures T_g. Values between 626 and 1204 K are found for T_g and the temperature correction ΔT_{corr} increases with the measured temperature T_c.

ECM is not applicable in the stoichiometric and lean MPE flame and the temperature corrections are unknown. The minimal temperature measured in the stoichiometric flame is 1507 K, which is above the safe working temperature for current application. In the lean flame a minimum temperature of 1385 K is measured, which is below the safe temperature of 1400 K. However, no parallel could be established, as for a safe parallel a starting temperature of 1200 K is needed. A possibility is to assume that the same temperature correction as for the rich MPE flame is valid. However different heat transfer coefficient h values came forward from the HTM analysis, since their composition and velocity differ, resulting in different temperature corrections. So no experimental temperature correction could be applied on the lean and stoichiometric flames. The temperature profile measured in the ethylene flames is low enough for ECM and three parallels were established in each flame (Figure 5.14).

The extrapolation of the experimental data to the flame temperatures is another drawback of the ECM. The temperature correction is quantified for temperatures lower than 1350 K, the maximal temperature the characteristic curve is defined for (Figure 5.1), while higher flame temperatures are measured. An extrapolation is needed, increasing the uncertainty on the temperature correction.

The shape of the characteristic and Equation 5.3 imply that the temperature correction ΔT_{corr} is not linear depending on the temperature. However the correct order of the polynomial that should be fitted through the data is not known. To deduce the order of the correction curve, the temperature dependency of the emissivity ϵ and the heat transfer coefficient h need to be taken into account.

The temperature dependency of the emissivity ϵ can be found in literature. The temperature dependency of Type B uncoated emissivity is mostly assumed linear [139, 141]. The emissivity of the BeO-Y_2O_3 coating was determined by Peterson et al. to be 0.60±0.08 by an electrical heating experiment, ranging from 1464 to 1528 K. Other experimental data derived for BeO and Y_2O_3 separately, indicates that a maximum value at temperatures higher than 1600 is achieved [143, 144]. The emissivity of the thermocouple is defined by the coating (Section 5.5.2) and is therefore assumed constant at high temperatures. So the temperature dependency of the temperature correction is only depending on the heat transfer coefficient h and the measured temperature T_c.

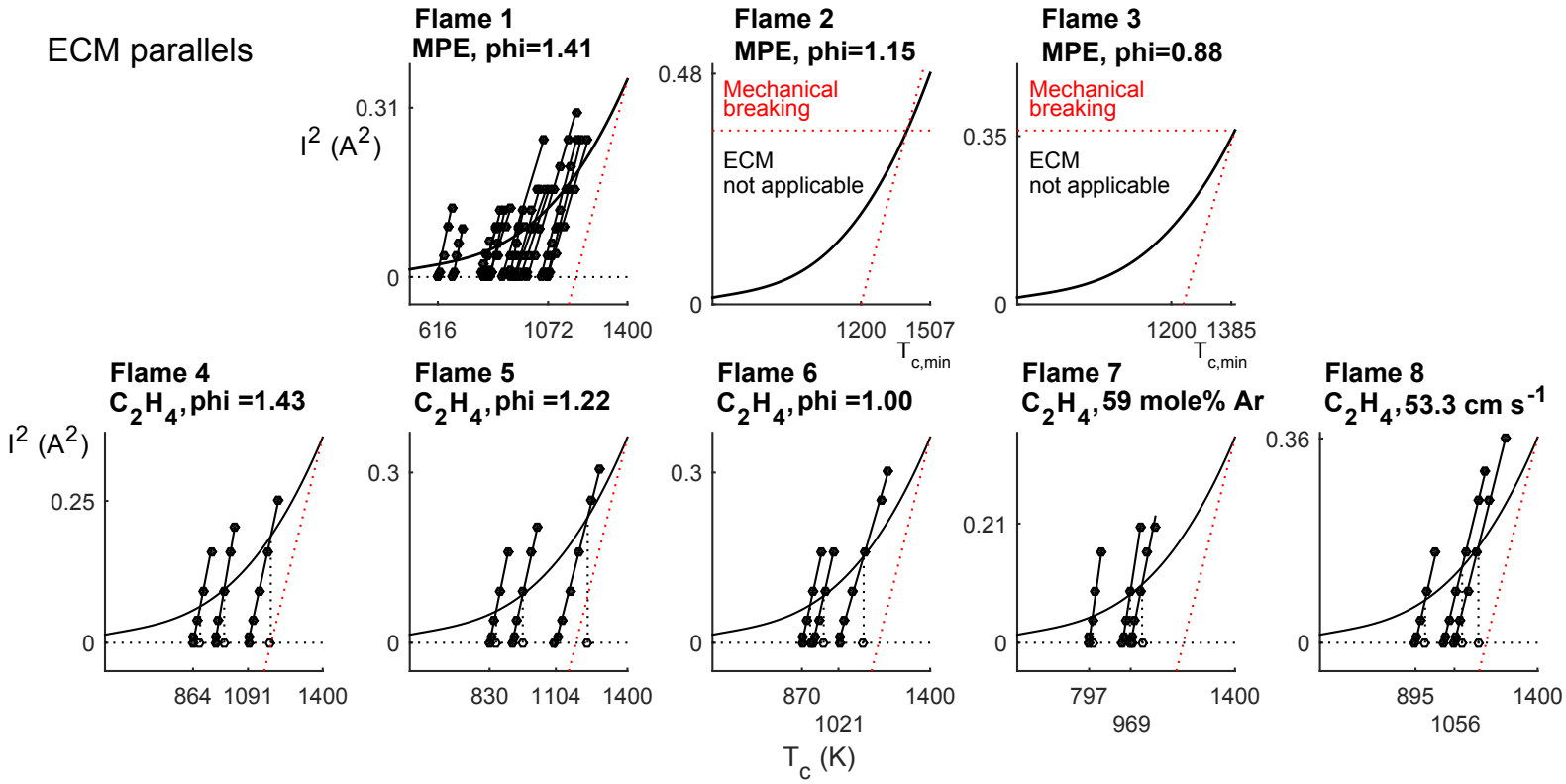

Figure 5.14: ECM results for the assessed flames. Fifteen parallels were established in the rich MPE flame. The temperatures in the stoichiometric and lean MPE flame were higher than 1200 K and ECM could not be applied. Three parallels were established for each ethylene flame.

The temperature dependency of heat transfer coefficient h is related to the chosen Nusselt number correlation (Section 5.5.3) and macroscopic properties of the flames like the thermal conductivity (Section 4.2.2), which makes the determination of the temperature dependency less straightforward.

The temperature dependency of ΔT_{corr} can be determined by curve fitting through the available experimental data. A residual analysis is done to determine the best order of the fitting. In Figure 5.15, the residuals of different order polynomials fitted through the experimental temperature correction ΔT_{corr} can be seen. The equations of the 2^{nd}, 3^{rd} and 4^{th} order polynomial are

$$T_{\text{corr}} = 8.40 \cdot 10^{-4} T^2 - 1.18T + 418.70 \tag{5.20}$$

$$T_{\text{corr}} = 2.17 \cdot 10^{-6} T^3 - 0.0047T^2 + 3.48T - 860.09 \tag{5.21}$$

$$T_{\text{corr}} = 1.00 \cdot 10^{-8} T^4 - 3.22 \cdot 10^{-4} T^3 + 0.039T^2 - 20.91T + 4174 \tag{5.22}$$

No substantial difference can be seen between the polynomials residuals. A higher order polynomial does not describe the experimental ECM data better. Nevertheless, the residuals increases with measured temperature, so the fit is worse at higher temperature.

To compare the performance of the different fittings, they are applied on the rich MPE flame (Figure 5.16), also the temperature correction achieved by HTM for this flame is shown on the figure. The ECM data points indicate a higher temperature correction than the simulations by HTM suggest. Leading to already a difference of 119 K in temperature correction at a measured temperature of 1072 K. The extrapolation of the ECM data leads to a higher temperature correction and for all the assessed orders the correction surpasses the adiabatic temperature limit.

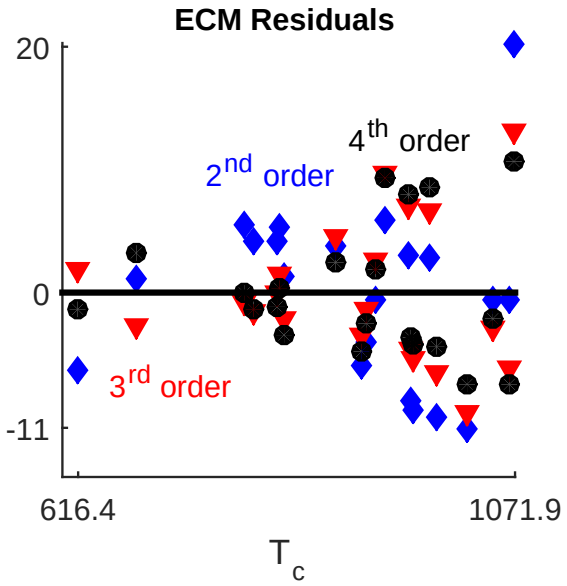

Figure 5.15: The residuals related to the difference between the experimental data for ECM and the polynomials of the 2^{nd}, 3^{rd} and 4^{th} order fitted through the data. No polynomial is performing better than the other ones.

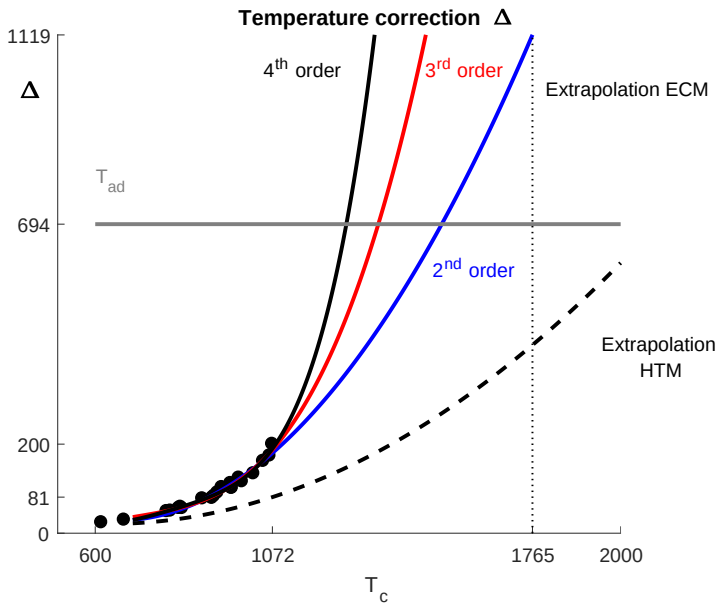

Figure 5.16: The extrapolation of the ECM data with different polynomials, together with the temperature correction achieved by HTM with the combination of the Kramers and the Ranz and Marshall correlations. The polynomial of the 2^{nd} order is the best choice to extrapolate the ECM data, but still an unrealistic temperature correction which surpasses the adiabatic temperature is found. A much lower temperature dependency is found by the HTM simulations and a difference of 123 K is found between the ECM and HTM correction at 1072 K.

From this analysis no correct order of the extrapolation can be selected. It seems that the temperature dependency cannot be described by a polynomial fitted through the experimental data. The order of the temperature dependency seems to change with temperature. The correct correlation for high temperature regions cannot be deduced, since no experimental data is available. For further calculations a polynomial of the second order is fitted through the ECM data, since this seems the best option and no experimental data to improve the order of the fit is available.

The temperature correction ΔT_{corr} is depending on the heat transfer coefficient h. The equations to derive h are given in Section 4.2.2. The equations are related to the composition of the flame and their temperature dependency changes with composition and therefore temperature. In the HTM simulations, these changes can be captured, but the experimental ECM data is unable quantify this effect.

Now that the order of the temperature dependency of the temperature correction is assumed to be two, the temperature correction ΔT_{corr} in function of the measured temperature T_c can be calculated (Figure 5.17). The uncertainty due to extrapolation is taken into account by the standard deviation shown as a dashed line.

Unrealistic high temperature corrections are found for Flame 1 and 6. For both flames the adiabatic temperature limit is exceeded. These results shows that the amount of experimental data points at temperatures below 1100 K have almost no effect on the performance of the correction at flame temperatures above 1600 K. Even for the rich MPE flame were 15 measurements were conducted an unrealistic T_g was obtained, while for the ethylene flames, for which only three data points have been established, valid temperature corrections of the same order of magnitude have been found.

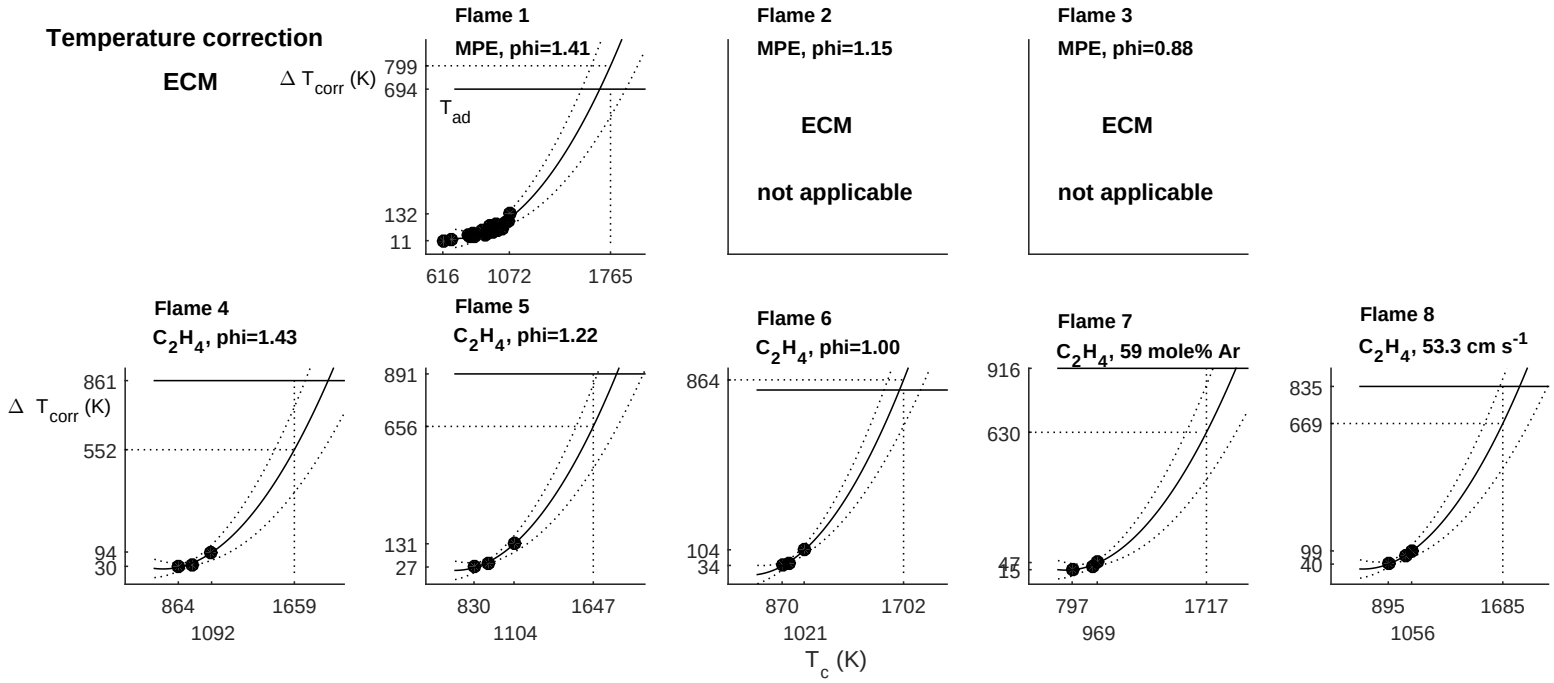

Figure 5.17: The temperature correction ΔT_{corr} in function of the measured temperature T_c, with the 95% uncertainty interval. The adiabatic temperature limit is shown as a black line, which is crossed by the correction of Flame 1 and 6, meaning that the temperature correction is physically impossible.

A low pass filter of the second order is needed to measure the thermo-electric voltage when a current is applied over the thermocouple (Figure 5.18). The implied current is alternative current with a frequency of 8 kHz. This high frequency is needed to heat up the thermocouple. However to measure the related thermo-electric voltage, which is DC, a low-pass filter of the second order is needed to cut-off the applied current with a high frequency. The calculations for the effect of the low-pass filter can be found in Appendix 3. The filter cuts off frequencies higher than 159 Hz, so the thermo-electric voltage can be measured without it is affected by the applied current.

A pressure of 0.001 mbar was achieved in the combustion chamber during the measurements for the characteristic curve. The pressure was measured by a Pfeiffer Vacuum Type CMR 373 sensor with a reading error of 0.15%. The mininum value that can be measured with this sensor, 0.001 mbar, is measured, indicating that the vacuum is from high quality. Next, the flame of interest is ignited and the parallels are measured. The flames are stabilised at a pressure of 55 mbar, the same pressure for the mole fraction measurements. The uncertainty on the ECM measurements will be further discussed, together with the experimental results in Section 5.6.

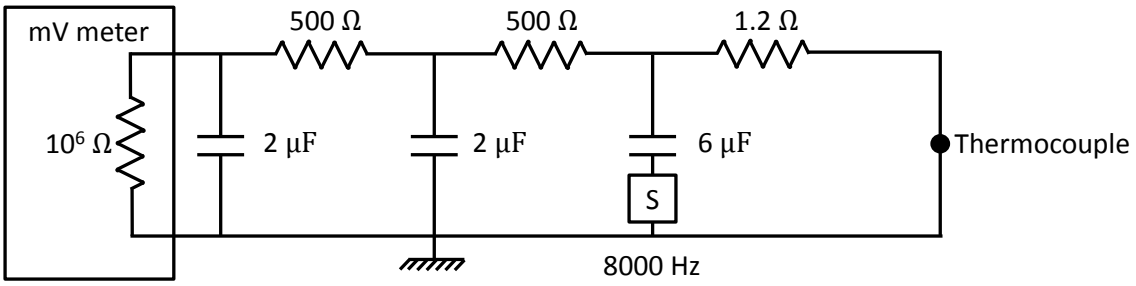

Figure 5.18: The electrical setup for the ECM consist of generator S which produces a current of 8 kHz varying from 0 to 0.6 A. The current is directly applied to the thermocouple, resulting in an increasing temperature due to the Joule heating. The thermo-electric voltage over the thermocouple is quite small and measured by a multimeter of Keysight Technologies. The multimeter can measure the voltage at direct current, so the frequency of the current needed the be lowered, which is done by the low-pass filter of the second order (Appendix 3).

5.6.1 Error and uncertainty analysis

The experimental error on the ECM is depending on both the measurement of the applied current and induced voltage. An Agilent 34401A multimeter is used to measure the applied current. A maximum current of 0.6 A is applied during the experiments, so the multimeter is set to the 1 A range. The uncertainty on the Agilent multimeter by this setting is stated to be 0.10% of reading value and 0.04% of full scale value [150]. The current applied on the thermocouple for ECM varies between 0 and 0.6 A, so the error on the applied current varies from 0.0004 A to 0.001 A. The error on the measured temperature is already discussed in Section 5.2 and is around 1 K. However, the uncertainty on the measured temperature is around 14 K in the flame front and 2 K in the post flame zone, due to flame and thermocouple pertubations.

The shape of the characteristic curve is also affected by the pressure in the combustion

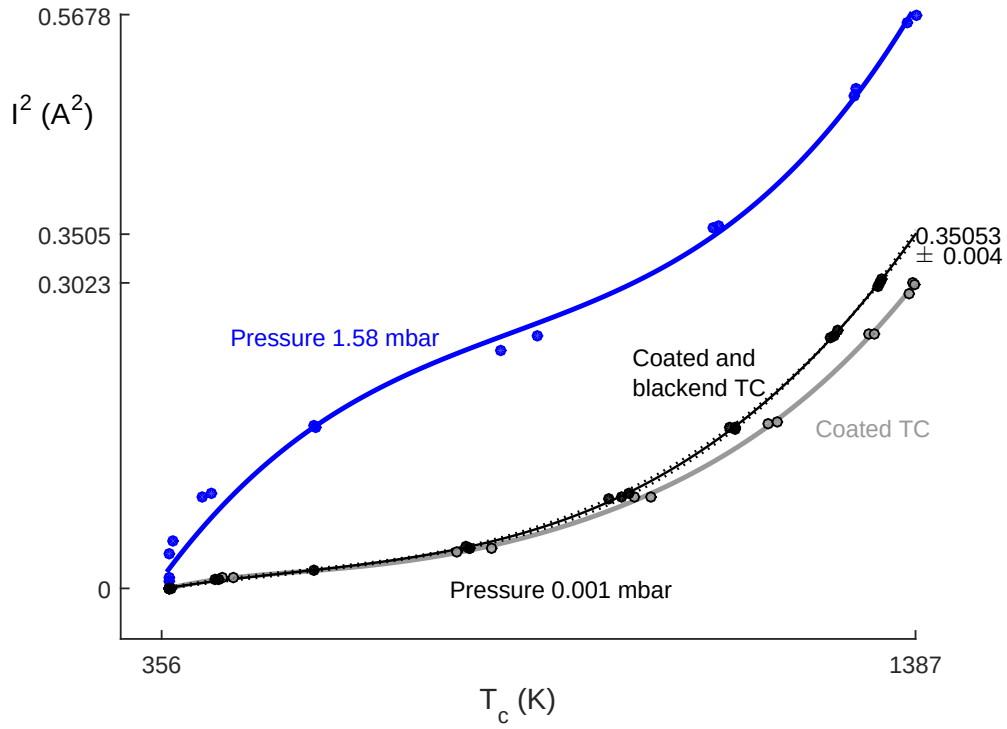

Figure 5.19: The characteristic curve for ECM was measured for different pressures in the combustion chamber. When the pressure is around 1.58 mbar instead of 0.001 mbar, the shape of the vacuum curve changed considerabelly. Also different characteristic curves were obtained before and after the flame has been in a flame. After flame contact, soot particles increases the emissivity of the thermocouple, leading to higher values for the characteristic curve (Equation 5.5, [151]). In the end a polynomial of the third order was obtained as characteristic curve, with a standard deviation of 0.004 A^2 at 1387 K.

chamber. The pressure in the combustion chamber is an influence quantity which can be regulated easily and when the characteristic curve was established a stable pressure of 0.001 mbar was measured. The characteristic curves was also determined at a pressure of 1.58 mbar and a totally different curve was established (blue line, Figure 5.19). The difference between the characteristic curves can be explained by heat transfer through convection if no perfect vacuum is sustained.

The emissivity of the thermocouple is another parameter that affects the shape of the characteristic curve. When the thermocouple was coated with the ceramic layer of BeO-Y_2O_3, the characteristic curve was measured three times (Figure 5.19, grey curves). The characteristic curve was also measured three times at vacuum after the thermocouple had been in a flame (Figure 5.19, black curves). A higher characteristic curve was found. This can be explained by an increase in emissivity ϵ and junction diameter caused by soot deposits [151].

The found uncertainty of the characteristic curve determination with the thermocouple, which was already aged in the flame, contains the effects and uncertainty of all influence quantities. Through each set of measuring points a polynomial of the third order was fitted. From the variations between the measurements a standard deviation could be obtained.

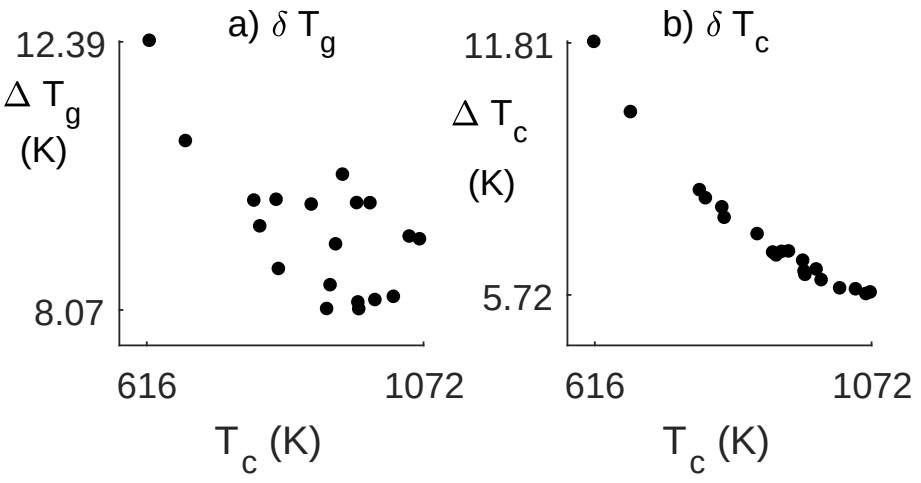

Figure 5.20: The uncertainty on the corrected temperature T_g due to the ECM parallels is related to the uncertainty on the measured temperature T_c. For both decreasing uncertainties are found, related to the lower uncertainty on the temperature measurements at high temperatures.

The standard deviation increases with temperature and a maximum value of 0.004 A^2 for a temperature of 1387 K is found. If we assume a normal distribution for the data the 95% Confidence interval (CI) can be calculated by

$$95\%CI = 1.96\frac{s}{\sqrt{n}} \tag{5.23}$$

where s the standard deviation of the measurements and n the number of measurements, in this case three. If we assess the effect of the uncertainty of the characteristic curve position on the temperature correction, a uncertainty due to the characteristic curve δCC of maximum 3K is found.

The parallels established by ECM contribute also the uncertainty on the ECM results. The linearity of the slopes is assessed for the rich MPE flame. The coefficient of determination is used to express the linearity. R^2 values ranging from 0.92 to 1 are found, implying that the linearity of the parallels is high. However to assess the uncertainty of the parallels on the temperature correction, 95% CI are calculated for the parallels, taking also the uncertainty on the temperature measurements into account. The intersections of the confidence intervals with the characteristic curve, are the limits of the 95% CI for the corrected temperature.

When the range of the 95% uncertainty interval on T_g due to the parallels is plotted in function of the measured temperature T_c, an decrease in uncertainty with measured temperature is found, ranging from 12.4 to 8.1 K (Figure 5.20 a). There is also an error on the measured temperature T_c (Figure 5.20 b), decreasing from 11.8 to 5.72 K with the measured temperature T_c. The uncertainty on the actual flame temperature T_g due to the parallels is related to the uncertainty on the temperature measurements. As a result the uncertainty decreases with the measured temperature T_c, just like in Figure 5.3.

The last contribution to the uncertainty on the ECM data is the extrapolation. The uncertainty stated as a standard deviation related to extrapolation is given in Figure 5.21 as a function of the measured temperature T_c. The extrapolation is the main contribution to the ECM uncertainty and is added together with the uncertainty due to the characteristic

curve and the parallels by error propagation. For the assessed flames the uncertainty on the maximum measured temperature is ranging between 154 and 187 K.

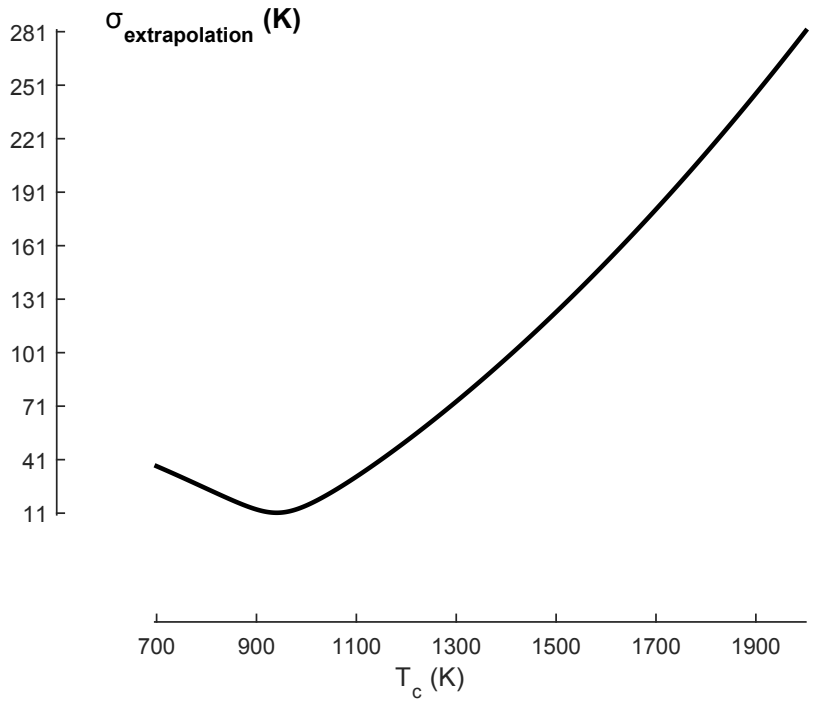

Figure 5.21: The uncertainty on the temperature correction due to the extrapolation in ECM. The standard deviation of the correction rises to 281 K for the measured flame temperature.

5.7 Comparison of the ECM and HTM results

Once the measured temperatures are corrected with both HTM and ECM, the temperature correction found with both methods can be compared. In Figure 5.23, the corrections for the maximal measured flame temperatures, achieved by the different methods, are shown, together with their standard deviation.

Overall, a higher temperature correction is found by ECM, due to the uncertainty on the extrapolation of the experimental data. The total uncertainty on the ECM correction is also higher compared to HTM. Physically impossible flame temperatures are found for Flame 1 and 6 with ECM, since the correction surpasses the calculated adiabatic flame temperature.

The temperature corrections found by HTM are close to the calculated adiabatic flame temperatures for Flame 2 and 3. A part of the standard deviation range related to the correction found with the Collis and Williams Nusselt number correlation even exceeds the adiabatic temperature limit. Therefore, the Kramers and Andrews Nusselt number correlations are considered more reliable. The temperature corrections found by Kramers and Andrews correlation do not differ by more than 2.5%, just like the uncertainty on them, so one of the correlations is chosen for further use. The Kramers correlation is selected, since it is validated by Bradley et al. [142] and the difference between both correlations is not more than 2.5%.

In Figure 5.22 the measured temperature profile of the flames where ECM and HTM could be applied on are shown, together with the corrected temperature profile obtained by HTM

and ECM. As said before higher corrected flame temperatures are derived with the ECM. It can also be seen that no overlap between the uncertainty ranges of both methods is found.

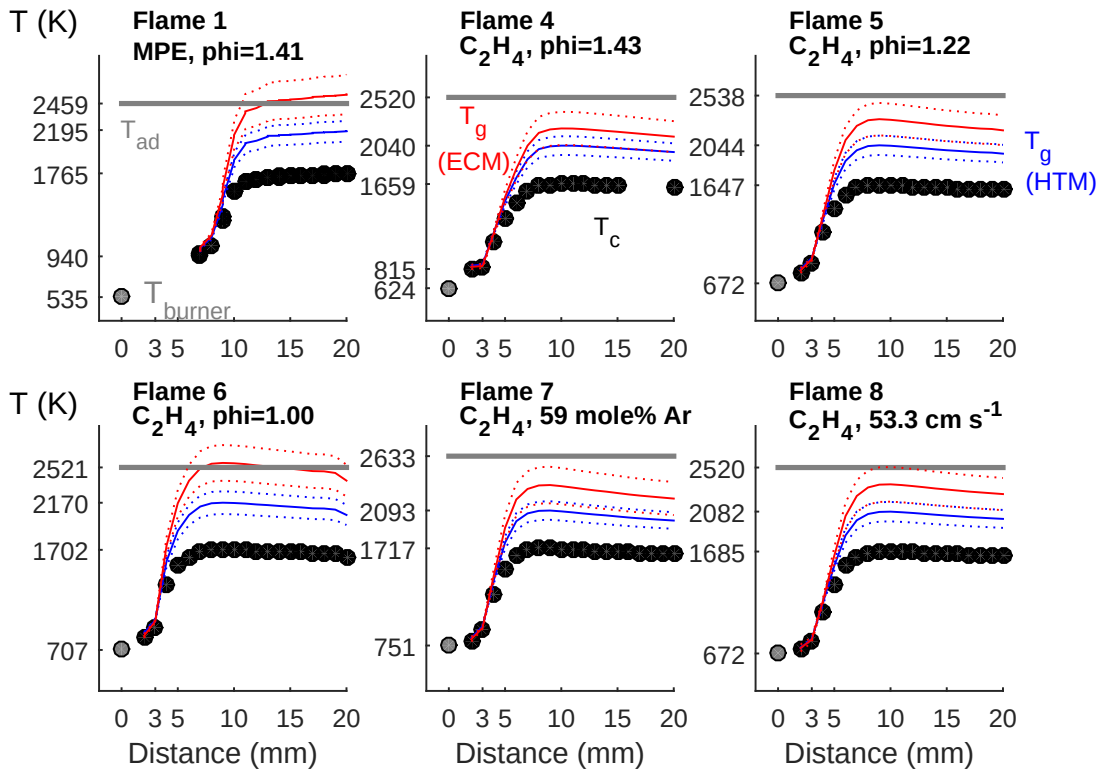

Figure 5.22: The measured temperature T_c profiles in the rich MPE flame and in the ethylene flames, together with the corrected temperature T_g obtained by HTM (blue lines) and ECM (red lines).

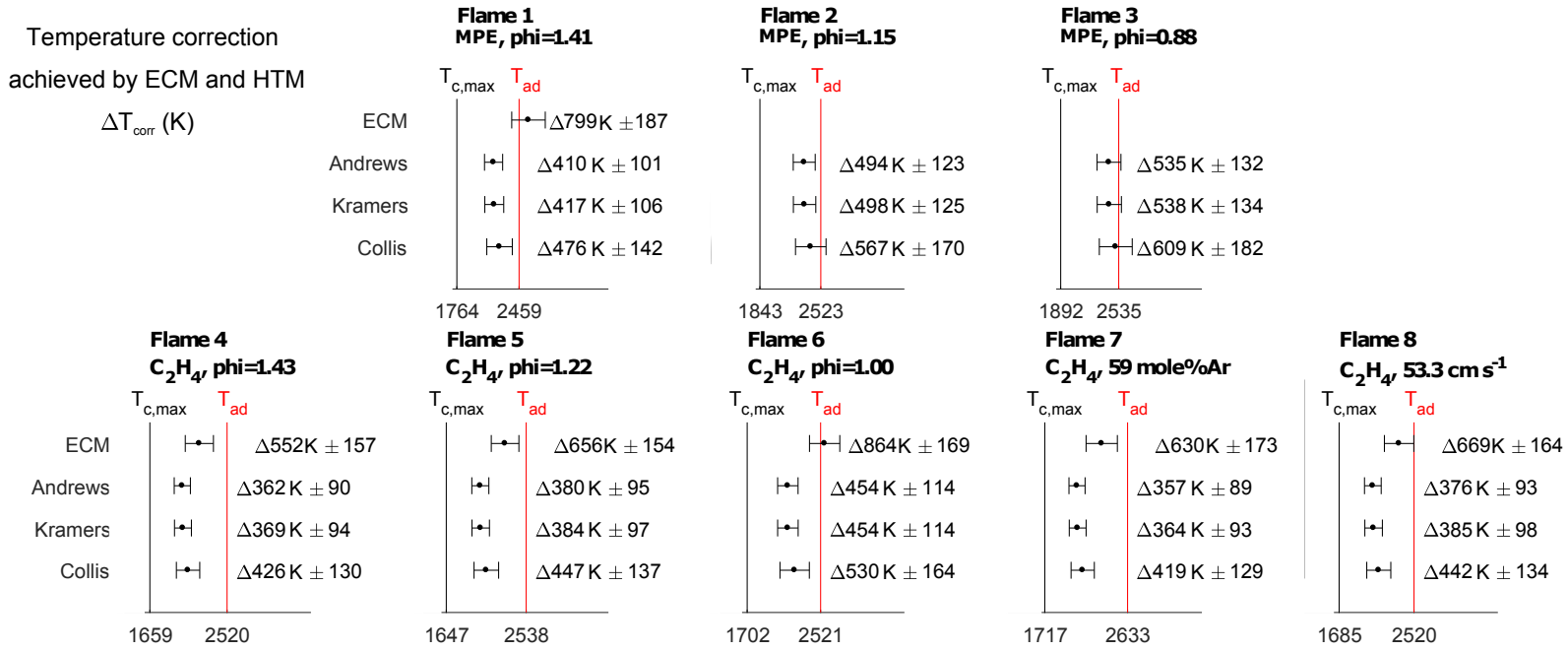

Figure 5.23: Comparison of the found temperature correction ΔT_{corr} with ECM and HTM for the eigth assessed flames. Overall, HTM performs better than ECM, since no corrections are surpassing the adiabatic temperature. Also a smaller uncertainty is found for the HTM results. The main reason for the poor performance of ECM is the uncertain extrapolation of the experimental data to flame temperatures.

5.8 Conclusion

The temperature profiles of the assessed MPE flames are needed for further kinetic modeling. Nevertheless, when the temperature profile in a laminar flat flame is measured by a fine wire thermocouple, a correction for radiation losses need to be applied. In this chapter two temperature correction methods, one based on a heat transfer model, the other method based on experiments, are assessed on different flames. The flame temperatures have been measured by a Type B thermocouple, with a wire diameter of 0.1 mm and coated by a layer of BeO-Y_2O_3 of 0.01 mm to avoid catalytic heating. Other thermocouples could lead to a better accurancy for the measured temperature, however the main cause of uncertainty is not the temperature measurement but the temperature correction for radiation losses.

Eight flames were assessed: the three MPE flames and five ethylene flames. The first method, the Heat Transfer Model (HTM), could be applied on all the assessed flames, while the experimental method, the Electrical Compensation Method (ECM), was only applicable on the rich MPE flame and the ethylene flames due to temperature limitations. During ECM, the thermocouple is heated up by the Joule heating which increases the risk of breaking the thermocouple substantially with temperature.

The performance of the ECM was worse than the HTM method, since not all the flames could be corrected by ECM. Secondly, for two of the corrected flames, the lean MPE and ethylene flame, a corrected temperature higher than the calculated adiabatic flame temperature was achieved, which is not feasible. The uncertainty on the temperature correction by ECM is around 170 K on average, which is higher than the uncertainties found by HTM (106 to 134 K). The main contribution to the uncertainty on the ECM results is the extrapolation.

The definition of the configuration of the thermocouple over which the reacting gas stream flows has an influence on the found temperature correction with the HTM. In literature, the thermocouple is seen as a sphere or as a cylinder. The difference in temperature correction for both configuration can be substantial. In this work, the transient behaviour from cylinder to sphere is taken into account by a correction factor N.

The flame temperatures are corrected by HTM based on a combination of the Kramers and the Ranz and Marschalls Nusselt correlations. The corrected temperature profiles are shown in Figure 5.24. None of the corrected flame temperature surpasses the adiabatic flame temperature. With other combination of Nusselt number correlations corrected temperature surpassing the adiabatic flame temperature can be found. The same results are found when the thermocouple configuration is set to a cylinder. The selection of the Nusselt number correlations and the thermocouple configuration should therefore be done with care, since different choices can lead to substantial temperature differences.

In conclusion, the HTM performed better than the ECM method in correcting the measured flame temperatures for radiation losses. HTM is applicable on all flames. Nevertheless, the determination of the heat transfer coefficient needs to be done with caution. In our case the transient behaviour of the thermocouple between cylinder and sphere needs to be taken into account to achieve corrected temperature below the calculated adiabatic temperature. The combination of the Kramers correlations for a cylinder and the Ranz and Marschall correlation for a sphere leaded to plausible results.

A third correction method, like multiple thermocouples with reducing bead size, could be applied in the future, to determine which combination of Nusselt number correlations and thermocouple configurations lead to the actual flame temperature.

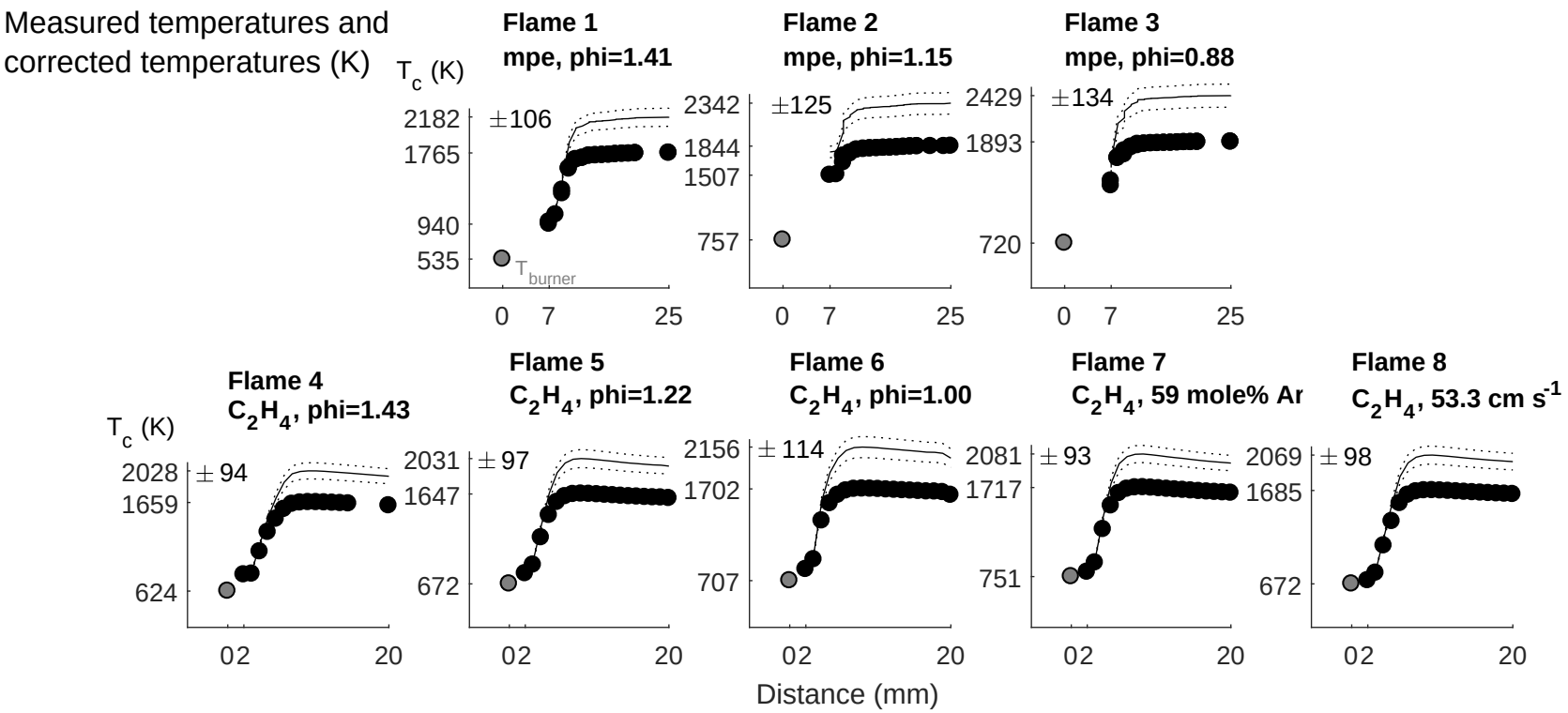

Figure 5.24: The measured and with HTM corrected temperature profiles for the eight assessed flames.

6

Results laminar flat flames

The result of the mole fraction measurements in laminar flat flames of MPE at low pressure are discussed in this chapter. The measured mole fraction profiles in the laminar flames are also compared with simulations conducted with the mechanism proposed by Dayma et al. [1].

The mole fraction profiles of 16 stable species could be measured in the MPE flames at 55 mbar with the GC-TCD/FID setup, namely MPE, propane (C_3H_8), ethanol (C_2H_5OH), acetone (CH_3COCH_3), formic acid (HOCHO), acetic acid (CH_3COOH), ethylene (C_2H_4), acetylene (C_2H_2), methane (CH_4), acetaldehyde (CH_3CHO), formaldehyde (CH_2O), CO_2, CO, H_2, O_2 and argon. However, for three of these species, formic acid, acetone and acetic acid the LoQ is not reached and the profiles cannot be used for validation (Figure 3.10). The water profile, the only main reaction product that is not experimentally measured, is calculated with the aid of the experimental data and some theoretical equations (Section 6.2).

The uncertainty on the mole fraction due to the experimental setup and the calibration is already determined in Section 3.7. However, there is also an uncertainty due to the measured flame temperatures. The flame temperature is determined in Chapter 5 and its uncertainty can affect the mole fraction profiles, therefore the effect is quantified in Section 6.1.

6.1 Uncertainty on experimental mole fraction profiles related to temperature measurements

The uncertainty on the corrected temperature profile used for the simulations can affect the obtained mole fraction profiles. A difference in the temperature in the post flame zone affects the concentration of CO and CO_2, since the equilibrium concentration is related to the temperature and kinetics. The uncertainty due to the temperature measurement on the mole fraction profiles of CO_2, CO, O_2, H_2O, CH_4, H_2, MPE, C_2H_4 and C_3H_8 will be quantified in this section. These species are chosen since their uncertainty due to experimental setup and calibration is already established in Section 3.7.

The uncertainty on the temperature profile in the rich, stoichiometric and lean MPE flame is maximal $\pm$101 K, $\pm$125 K and $\pm$134 K respectively. Simulations with the lower and higher temperature limit are conducted for the three MPE flames. The maximal Absolute Uncertainty (AU) and the Relative Uncertainty (RU) for the assessed species are calculated compared to the original simulations and are given in Table 6.1.

The uncertainty due to the temperature measurements is below 5% for the CO, O_2, CO_2 and H_2O mole fraction profiles in the rich MPE flame. However, the effect on the CH_4, C_2H_4 and C_3H_8 concentration is higher than 10% due to the low concentration of these species. The relative error on the oxygen concentration is lower in the lean flame compared to the rich flame

Table 6.1: The absolute (AU) and relative (RU) uncertainty on the mole fraction profiles of the main species and some intermediate species due to the uncertainty on the temperature profile.

Species	ϕ**=1.41**		ϕ**=1.15**		ϕ**=0.88**	
	AU (mole%)	RU (%)	AU (mole%)	RU (%)	AU (mole%)	RU (%)
CO	0.65	4.9	0.89	7.9	0.60	6.3
O_2	0.97	4.0	2.23	7.9	0.60	1.8
CO_2	0.39	4.5	1.05	9.6	0.70	5.8
H_2O	0.67	4.3	1.40	8.6	0.40	2.5
CH_4	0.06	15.0	0.10	29.9	0.02	7.1
H_2	0.16	3.7	0.25	8.1	0.13	6.3
MPE	0.36	8.3	0.42	8.2	0.12	3.2
C_2H_4	0.23	12.9	0.34	26.0	0.08	7.2
C_3H_8	0.01	11.3	0.01	18.7	0.01	10.7

due to the higher maximal oxygen concentration. The relative effect on the CO is greater in the lean flame, due to the lower CO concentration. The highest relative uncertainties are found in the stoichiometric flame.

Taking the uncertainty due the temperature measurements into account, a new total uncertainty can be calculated for the main species. The uncertainty due to calibration for the species with a concentration lower than 1 mole% is set to 25% (Section 3.7). The total uncertainty values are given in Table 6.2 for eight species. The uncertainty on the species mole fraction profiles due to the temperature is of the same order of magnitude as the uncertainty due to the experimenal setup and calibration together. The total uncertainty is the greatest in the stoichiometric MPE flame and ranges around 10% for the main species, 15% for H_2 and 30% for the intermediate species.

6.2 Water mole fraction profile

The water mole fraction profile cannot be measured experimentally in the flames. The first reason is that methane and water co-elute. Methane is also detectable with the FID detector and can be quantified. The second reason is that the measured areas are constant throughout the flame structure. The peak broadening makes it impossible to obtain the water profile. Therefore, the water concentration in the post flame zone was determined by combining experimental concentrations of CO_2, CO and H_2 and the theoretical equilibrium data of the water shift reaction:

$$CO + H_2O \rightleftharpoons CO_2 + H_2. \tag{6.1}$$

The equilibrium constant K_p of the water shift reaction can be expressed as

$$K_p = \frac{P_{CO_2} \cdot P_{H_2}}{P_{CO} \cdot P_{H_2O}} = \frac{X_{CO_2} \cdot X_{H_2}}{X_{CO} \cdot X_{H_2O}} \tag{6.2}$$

where P_{CO_2}, P_{H_2}, P_{CO} and P_{H_2O} are the partial pressure of the species, which can be substituted by their mole fraction profiles X_{CO_2}, X_{H_2}, X_{CO} and X_{H_2O} considering the law of Dalton.

Table 6.2: The total relative uncertainty on the mole fraction profiles for 8 of the measured permanent gases due to the experimental setup and calibration and the temperature measurements. The total uncertainty is calculated by error propagation.

	O_2	CO_2	CO	H_2	CH_4	C_2H_4	C_3H_8
	Rich MPE flame						
Setup + Cal (%)	3.8	6.1	5.8	6.9	25.0	25.0	25.0
Temperature (%)	4.0	4.5	4.9	3.7	15.0	12.9	11.3
TOTAL (%)	5.5	7.6	7.6	7.8	29.2	28.1	27.4
	Stoichiometric MPE flame						
Setup + Cal (%)	3.1	5.0	5.8	13.5	25.0	25.0	25.0
Temperature (%)	7.9	9.6	7.9	8.1	29.9	26.0	18.7
TOTAL (%)	8.5	10.8	9.8	15.7	39.0	36.1	31.2
	Lean MPE flame						
Setup + Cal (%)	6.8	7.9	7.2	13.3	25.0	25.0	25.0
Temperature (%)	1.8	5.7	6.3	6.3	7.1	7.2	10.7
TOTAL (%)	7.0	9.7	9.6	14.7	26.0	26.0	27.2

The mole fraction profiles of CO_2, CO and H_2 are measured experimentally, while the value of $log(K_p)$ for the different species can be extracted from the JANAF thermochemical tables if the temperature is known (Tabel 6.3) [94]. The $log(K_p)$ value of H_2 is by definition zero. The value of K_p for the water shift reaction can be calculated by

$$log(K_p) = log(K^0_{p,CO_2}(T)) - log(K^0_{p,CO}(T)) - log(K^0_{p,H_2O}(T)) \tag{6.3}$$

$$\text{with } K_p = 10^{log(K_p)} \tag{6.4}$$

where, $log(K^0_{p,CO_2}(T))$, $log(K^0_{p,CO}(T))$ and $log(K^0_{p,H_2O}(T))$ are the $log(K_p)$ values found in the JANAF thermochemical table for CO_2, CO and H_2O respectively (Table 6.3).

Table 6.3: Extracted log(K_p) values for H_2O, CO and CO_2 from the JANAF thermochemical tables [94]

Temperature	H_2O	CO	CO_2
2000	3.540	7.469	10.353
2100	3.227	7.321	9.860
2200	2.942	7.185	9.411
2300	2.682	7.061	9.001
2400	2.443	6.946	8.625
2500	2.224	6.840	8.280

Table 6.4: Mole fraction profiles for CO, CO_2 and H_2 experimentally measured after the flame front, the calculated value for K_p and the water mole fraction in the post flame zone. The uncertainty on the equilibrium water concentration due to the temperature and the CO, CO_2 and H_2 moles fractions is also given.

Equivalence ratio	CO (mole%)	CO_2 (mole%)	H_2 (mole%)	K_p (-)	H_2O (mole%)
$\phi = 1.41$	12.5	8.1	4.9	0.1948	16.4 ± 3.4 (20.7%)
$\phi = 1.15$	12.4	13.7	2.7	0.1773	17.0 ± 3.5 (20.5%)
$\phi = 0.88$	2.7	14.7	0.5	0.1698	16.2 ± 3.3 (20.4%)

Using K_p the mole fraction of H_2O in the post flame zone can be calculated by

$$X_{H_2O} = \frac{X_{CO_2} \cdot X_{H_2}}{X_{CO} \cdot K_p}. \tag{6.5}$$

The measured temperatures at the end of the combustion process are 2182, 2342 and 2429 K for the rich, stoichiometric and lean flame respectively. The K_p values related to these temperature are 0.1948, 0.1773 and 0.1698 for the rich, stoichiometric and lean MPE flame respectively. If these K_p values are combined with the experimentally measured mole fraction profiles for CO, CO_2 and H_2 after the flame front (Table 6.4), the water concentration in the post flame zone can be calculated. In the rich MPE flame, the obtained equilibrium mole fraction of water is 16.4 mole%, in the stoichiometric flame 17.0 mole% and in the lean flame 16.2 mole%.

However, only the mole fraction after the flame front, where the combustion process is in equilibrium, can be calculated in this way. To accomplish a full mole fraction profile for water, the same shape as the measured temperature profiles is implied on the mole fraction profile of water [152].

The uncertainty on the water concentration after the flame front can be calculated from the uncertainty on the flame temperature and the measured moles fractions of CO, CO_2 and H_2. The uncertainty on the mole fraction profile of CO, CO_2 and H_2 is given in Table 6.2. Taking these numbers into account, an uncertainty of 3.4, 3.5 and 3.3 mole% is found for the water concentration after the flame front in the rich, stoichiometric and lean MPE flame respectively.

6.3 Comparison experimental and simulated results

The measured mole fraction profiles can be compared with the simulated mole fraction profiles. The mole fraction profiles of the main species both achieved by experiments and simulation are given in Figure 6.1, 6.2 and 6.3 for the rich, stoichiometric and lean MPE flame. Due to the different position of the burner at the mole fraction measurements and the temperature measurements, a shift of simulated mole fraction profiles, which shape is correlated to the temperature profile, is applied during comparison to optimise the fit between experiments and simulations.

The concentrations after the flame front are predicted well by the mechanism for the rich and stoichiometric flame. The simulated values for the rich MPE flame lie within in the experimental uncertainty. Only for the oxygen profile, there is a mismatch in the flame front, which is also visible in the CO profile.

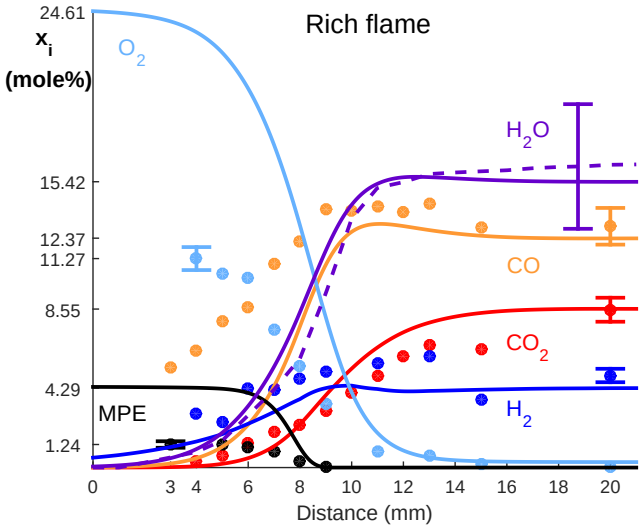

Figure 6.1: The experimental and simulated mole fraction profiles for the main intermediate species in the rich MPE flame at 55 mbar

A possible explanation can be a difference in the flame structure when the temperature and the mole fraction profiles are measured. The thermocouple is placed between the flame and the sampling cone for temperature measurements. The distance during the temperature measurements between the burner surface and the sampling cone is 5 mm more than the distance between the burner surface and the sampling cone during sampling. The sampling cone acts less as a heat sink during the temperature measurements, leading to a steeper temperature profile. However, when the mole fraction profiles are measured, the sample cone can act as a heat sink, leading to a less steep temperature profile than the measured one. Since the temperature profile affects the shape of the mole fraction profiles, the experimental mole fraction profiles shape is less steep than the simulated ones [117].

Experimentally, only the end of the flame front and the post flame zone could be measured in the stoichiometric MPE flame (Figure 6.2), since the flame is stabilised too close to the burner and the fresh gases could not be accessed by the sampling probe. The experimental measured CO peak is higher than the simulated one. Nevertheless, the simulated post flame zone concentration for the main species are within the experimental uncertainty regions. A shift of the temperature profile of 6 mm is made.

The experimental and simulated mole fraction profiles for the lean MPE are shown in Figure 6.3. The experimental post flame concentrations of CO and O_2 and the calculated H_2O concentrations are in agreement with the simulations. However, the shape of the simulated and the experimental mole fraction profiles, like O_2 and H_2O, do not match. The measured mole fraction are quite constant, the expected shape of the flame front is not visible. Possible explaination can be a different flame structure during mole fraction measurements and temperature measurements. Also the flame could be fluctuating and in reality a sample is gathered over different distances to the burner. The sample could also be unsufficiently quenched after the sampling cone resulting in quite constant mole fraction profiles. Further research is necessary the identify and solve the problem.

A shift of the water profile is also found for the MPE flames. The shape of the calculated water profile is assumed the same as the measured temperature profile, based on the findings

of Ancia [152]. Nonetheless, this assumption leads to a shift of around 2 mm between the simulated and calculated water profiles in the stoichiometric flame.

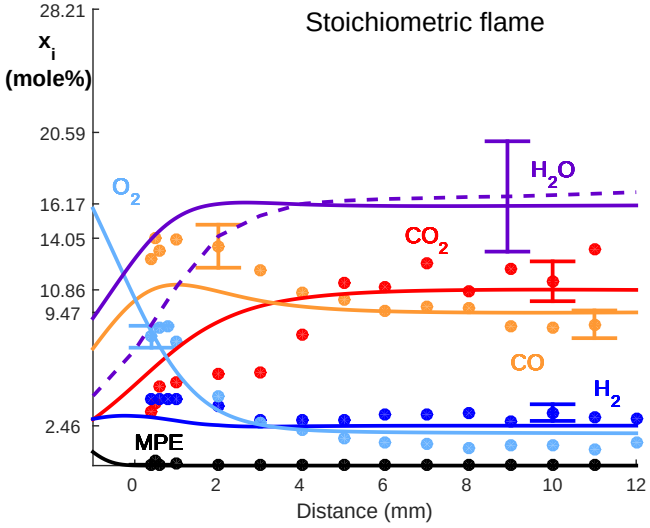

Figure 6.2: The experimental and simulated mole fraction profiles for the main intermediate species in the stoichiometric MPE flame at 55 mbar

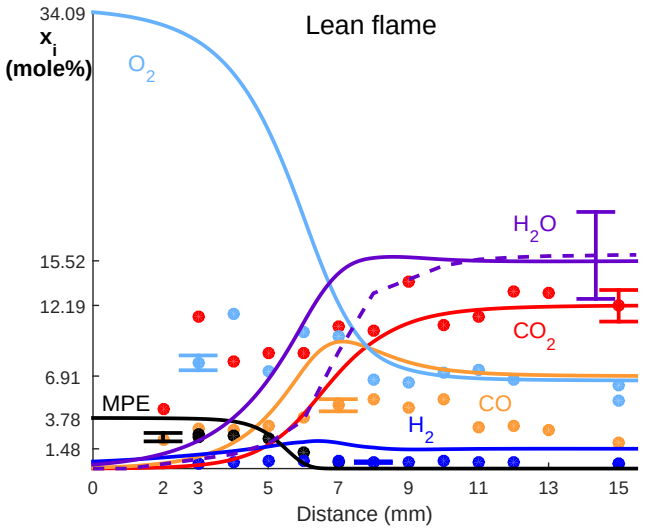

Figure 6.3: The experimental and simulated mole fraction profiles for the main intermediate species in the lean MPE flame at 55 mbar

The simulated and experimental mole fraction profiles of the measured intermediate species are compared. In Figure 6.4, the experimental and simulated mole fraction profiles of CH_4, C_2H_4, CH_2O and C_2H_2 are shown for the rich, stoichiometric and lean MPE flame. The profiles of the intermediate species in the rich flame are well captured by the simulations. Both the concentration of the species and the position of their concentration peak is described well by the model.

Only the flame front and the past flame zone could be measured in the stoichiometric MPE flame. The position of all the intermediates peak concentrations in Figure 6.4 is adequately

captured by the model. A comparison between simulations and experiments for the maximal concentration cannot be made, since it is possible that the real peak concentration is not measured. Nonetheless, the measured concentration for C_2H_2 in the stoichiometric flame is higher than the simulated one.

The concurrence of the measured and the simulated mole fraction profiles in the lean MPE flame is worse compared to the rich and stoichiometric flame. The methane and formaldehyde mole fraction profiles are overpredicted by the simulations. The ethylene and acetylene mole fraction profiles do not have the expected shape, a rather constant mole fraction is measured throughout the flame structure. The mismatch between simulations and experiments can be related to the lesser quality of the lean flame samples.

In Figure 6.5, the experimental and simulated mole fraction profiles for propane (C_3H_8), acetaldehyde (CH_3CHO), ethanol (C_2H_5OH) and argon are shown. The same conclusion can be made as for the previous intermediate species profiles. The agreement between the experimental concentration profiles and the simulated ones is satisfying in the rich MPE flame, for both the positon of the peak and the peak value. The simulations lie within the experimental uncertainty.

In the stoichiometric flame, an agreement between simulation and experiment is found for only the C_3H_8 profile. The experimental mole fraction profiles of the two other shown intermediate species do not fit with the simulations. The measured argon profile does not have the expected shape with the mole fraction decline. Nevertheless, the concentration measured in the post flame zone only differs 2 mole% with the simulated value.

The experimental data in the lean flame for C_3H_8 and argon have the same shape as the simulated mole fraction profiles. Nonetheless, the maximal simulated concentration for C_3H_8 is three times higher than the measured concentration. No defined experimental mole fraction profile was found for acetaldehyde and ethanol.

Overall, the best agreement between simulations and experiments is found for the rich MPE flame. The simulated mole fraction profiles of most of the main species lie within the experimental uncertainty range of the measurements. Only the measured oxygen concentration in the fresh gases is lower than expected. This phenomenon can be explained by a different flame structure during temperature measurements and mole fraction sampling or by sampling at different distance due to flame instability. The measured mole fraction peaks for methane, ethylene and formaldehyde agreed with the simulations. The greatest difference between measurement and simulation are found for ethanol, a difference with a factor of three is found, which cannot be explained by the uncertainty on the measured values.

The fresh gases could not be sampled in the stoichiometric MPE flame. Only experimental mole fraction profiles starting from the flame front are obtained. In most cases, the same peak position for a species is found by simulations and measurements. Nonetheless, the performance of the mechanism in predicting the peak concentration could not be assessed, since it is not clear if the peak concentration is experimentally measured.

A poor agreement between the experimental and simulated more fraction profiles in the lean MPE flame is found. Both the shape of the experimental mole fraction profiles as the experimental mole fraction values do not comply with the simulations. The the experimental variability is seen as the main reason. The measured CO and H_2 profile in the lean MPE flame are lower than what the simulations suggest and for most of the intermediates, the peak shape could not be seen in the experimental data. Since the quality of the experimental for the lean MPE flame is not guaranteed, the data will not be used further to suggest improvements for the MPE mechanism.

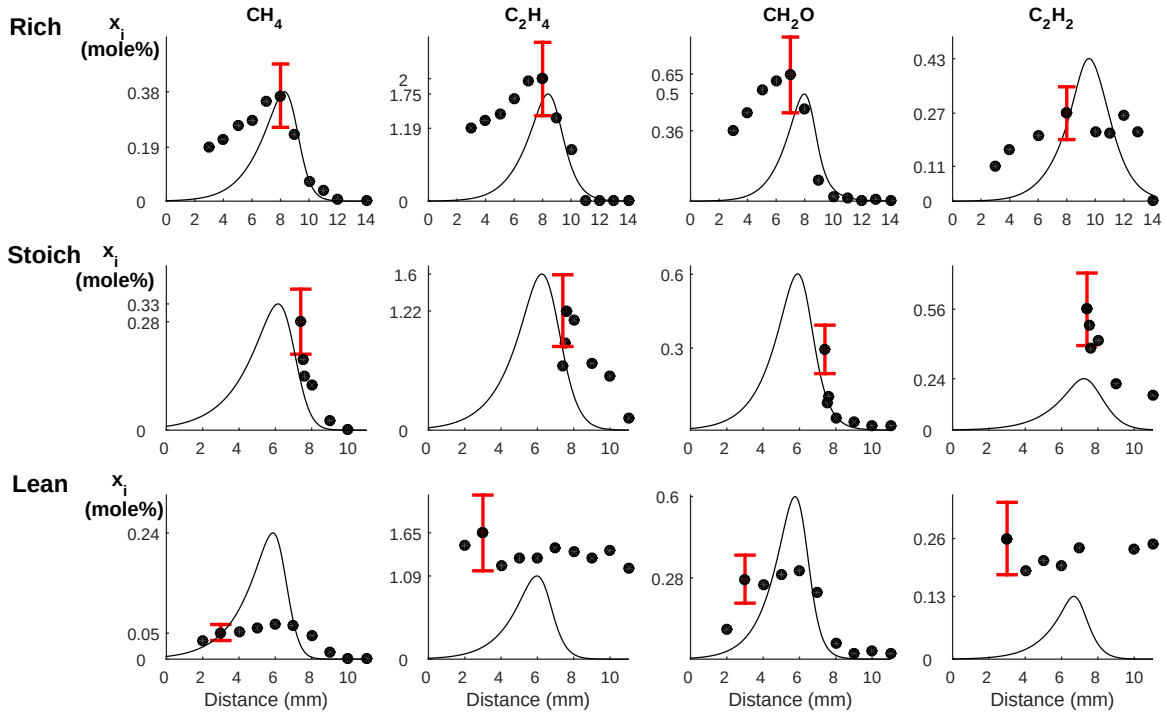

Figure 6.4: The experimental and simulated mole fraction profiles for the intermediates CH_4, C_2H_4, CH_2O and C_2H_2 measured in the MPE flames at 55 mbar.

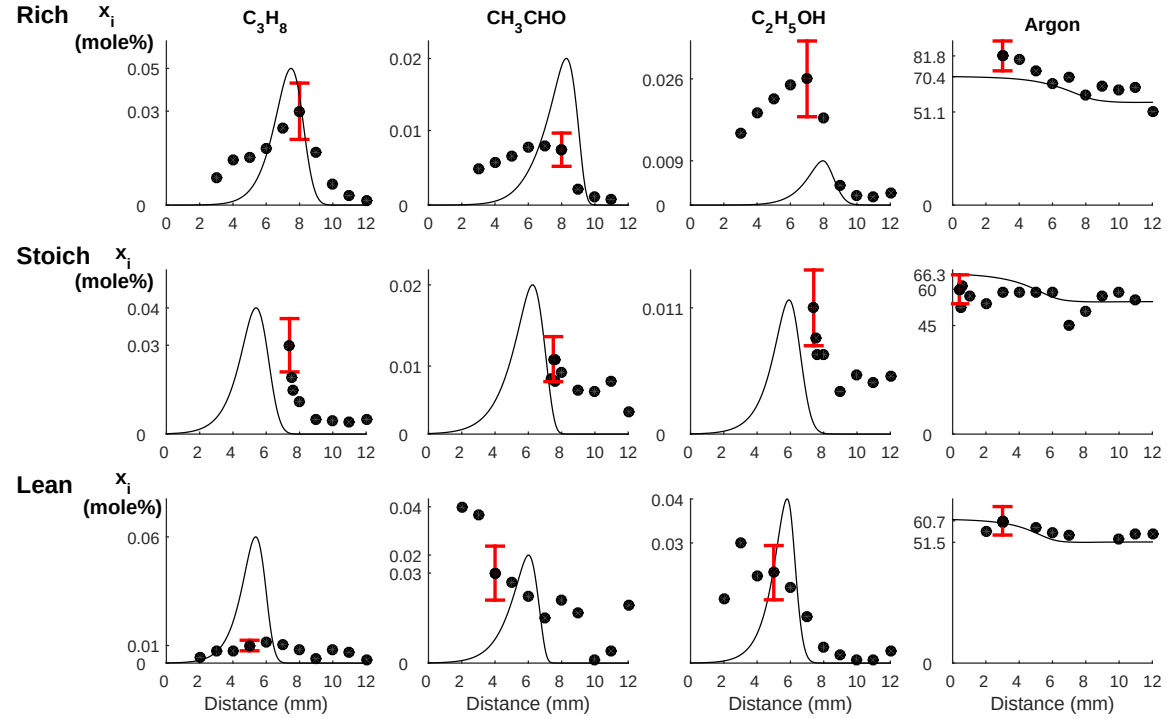

Figure 6.5: The experimental and simulated mole fraction profiles for the intermediates C_3H_8, acetaldehyde, ethanol and the dilutent argon measured in the MPE flames at 55 mbar.

6.4 Element balance

Throughout the combustion process the mass and the elements (C, H, O and Ar) are conserved. To check if the same amount of elements is found in the unburned gases as in the combustion products, the percentage for each element is calculated throughout the flame and compared with the expected theoretical number. The composition of the unburned gases is known (Section 1.1), so the theoretical element composition can be calculated (Table 6.5).

Table 6.5: Theoretical element composition for the different MPE flames, with or without argon taken into account

	With argon				Without argon		
Equivalence ratio	X_C	X_H	X_O	X_{Ar}	X_C	X_H	X_O
$\phi = 1.41$	12.7	25.3	28.0	34.0	19.2	42.4	38.3
$\phi = 1.15$	11.9	23.8	31.8	32.5	26.7	47.1	35.3
$\phi = 0.88$	11.7	23.3	33.4	31.6	17.1	34.1	48.8

The element fraction for C is depending on the mole fraction of the fuel and the reaction products CO and CO_2, while for the elements O and H, the mole fraction of water, H_2 and O_2 also play a role (Equations 6.6 to 6.8).

$$X_C = 6 \cdot C_6H_{12}O_2 + 1 \cdot CO_2 + 1 \cdot CO \tag{6.6}$$

$$X_O = 2 \cdot C_6H_{12}O_2 + 2 \cdot O_2 + 1 \cdot CO_2 + 1 \cdot CO + 1 \cdot H_2O \tag{6.7}$$

$$X_H = 12 \cdot C_6H_{12}O_2 + 2 \cdot H_2 + 2 \cdot H_2O \tag{6.8}$$

The element balance is assessed for the rich and stoichiometric MPE flames. The mole fraction profiles for all the measured species are taken into account. From the mole fraction profiles the element composition of the flame can be calculated from the fresh gases throughout the flame to the post flame zone.

To improve the element balance, species which are not experimentally measured, but have a mole fraction concentration above 1 mole% in the simulations are added to the balance. From the simulations, we could derive that the mole fractions of some radicals reach 1 mole%: $OH^\bullet$, $H^\bullet$ and $O^\bullet$ (Figure 6.6). The mole fraction of intermediate stable methyl esters (mp2d and mb3d) did not reach 1 mole% in the simulations and are therefore not taken into account.

The final element balances for the rich and stoichiometric MPE flames are visualised in Figure 6.7. The white dots are the results of the element balance without taking the $OH^\bullet$, $H^\bullet$ and $O^\bullet$ radicals into account. The black dots are the results when the radicals are considered.

The element balance is not closed in the flame front. In the rich flame, the oxygen and hydrogen profiles imply that water could be missing. Since this species is not directly measured and its mole fraction profile can differ from the implied shape. The same can be seen in the stoichiometric flame. In the stoichiometric MPE flame, there is also a shift between the simulated and the calculated water profile which can enhance the effect of missing water. The element balance improved substantially, when the simulated water profile is used for the calculations.

Nevertheless, the element balance improves in the post flame zone. In the rich MPE flame, the hydrogen balance is closed and the carbon and oxygen balance are 1 to 2% off. This can

be explained by the measured CO_2 mole fraction, which is lower than the simulated one. The hydrogen balance is also closed in the post flame zone of the stoichiometric MPE flame. A discrepancy of 3% is found for the carbon and oxygen balance, which is related to the higher CO_2 mole fraction measured than expected by simulation.

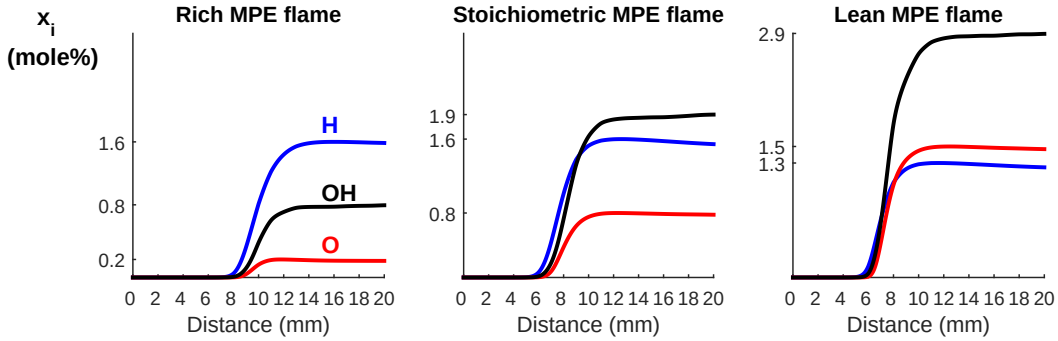

Figure 6.6: The simulated mole fraction profiles for the O, H and OH radical. Next to the main species, these radicals achieve the highest mole fractions in the simulation.

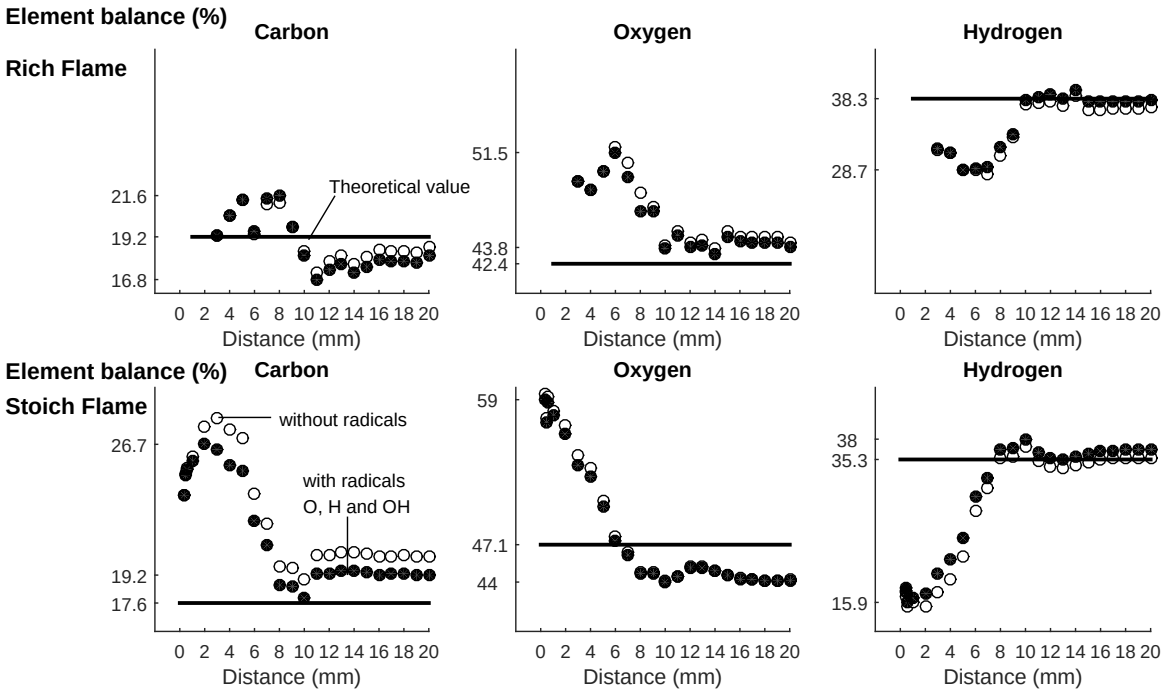

Figure 6.7: The element balance for the rich and stoichiometric MPE flame throughout the flame structure.

6.5 Conclusion

To assess the performance of a new kinetic mechanism for the oxidation of methyl pentanoate (MPE), experimental data were gathered for three laminar flames at a pressure of 55 mbar and equivalence ratios ϕ of 1.41, 1.15 and 0.88. The flames were stabilised on a Botha-Spalding burner and the mole fraction profiles of 16 stable species could be measured in the flames by means of GC-TCD/FID.

The uncertainty on the experimental mole fraction profiles is quantified, taking the uncertainty due to the experimental setup, the calibration and the temperature measurements into account. On average an uncertainty of 10% is found for the main species, except for H_2O for which an uncertainty of 20% is found. The total uncertainty on the H_2 concentration and the species with a concentration lower than 1 mole%, is 15% and 30% respectively.

The oxidation of the laminar flat MPE flames was simulated by the proposed detailed kinetic model (206 species and 1773 reactions) with the OpenSMOKE software. The results obtained by the modeling are in good agreement with the experimental results for the rich and stoichiometric MPE flame. The simulated concentrations for the main species lie within the experimental uncertainty and the position of the concentration peak is captured well by the simulations.

The experimental data measured in the lean flame is of a lower quality compared to the other two flames, due to experimental variability during sampling. The experimental mole fraction profiles of CO and H_2 do not fit with the simulations and the overall quality of the measured species concentration profiles is not good enough to be used for the mechanism validation.

7

Assessment kinetic mechanism for MPE

The performance of the mechanism proposed by Dayma et al. for the combustion of MPE [1], will be checked against different combustion configuration in this chapter. The laminar flat flames assessed in Chapter 6 are not enough to validate the MPE model over a broad temperature and pressure range. Next to the laminar flames, experimental data from literature or from other research institutes on the MPE combustion is assessed.

The other assessed combustion configurations are a Jet Stirred Reactor (JSR), a Spherical Combustion Chamber (SCC) and a Rapid Compression Machine (RCM). The mole fraction profiles obtained by a JSR and the laminar flames velocities found in a SCC are compared with the simulations results in Section 7.1.2 and 7.1.3. Experimental data regarding ignition delays achieved by experiments with a RCM [74] are compared to simulations with the proposed MPE mechanism in Section 7.1.4. In addition, experimental data for laminar flat flames from literature [72] is also simulated with the proposed mechanism in Section 7.1.1.

Once the simulations are compared with the experimental data, species for which a misfit between simulations and experiments occur can be identified. A reaction flow analysis and a sensitivity analysis are performed to identify the reactions which affect the mole fraction profile of these species the most (Section 7.2). The results of the sensitivity and reaction flow analysis indicate possible improvements for the kinetic data of the MPE mechanism.

7.1 Other experimental data

The experimental results of laminar flat flames are not enough to validate the MPE mechanism. Experimental data over a broad range of pressures and temperatures are needed to assess the performance of a kinetic mechanism. Therefore, experimental data found in literature or provided by other research institutes are assessed for different combustion conditions.

Experimental data for laminar flat MPE flames at a pressure of 27 mbar and atmospheric pressure are available in literature [72]. Next, data regarding laminar flame velocities at different temperatures and a pressure of 1 and 3 bar obtained by researchers at the CNRS of Orléans is assessed to validate the mechanism for these conditions. Another configuration for which experimental data is avaible is a jet stirred reactor in which MPE reacts adiabatically at 10 bar. These experiments have been also performed at the ICARE department of the CNRS in Orléans. The last combustion configuration for which the mechanism is compared to literature data is a RCM. With this collection of experimental data, the proposed MPE mechanism can be assessed over a broad pressure range and different combustion configurations.

7.1.1 Laminar flames

Korobeinichev et al. [72] investigated a stoichiometric (ϕ=1.0) and rich (ϕ=1.5) premixed MPE flames at 27 mbar (20 Torr) and at atmospheric pressure. The characteristics of the investigated flames are given in Table 7.1. The low pressure flames were investigated in the Lawrence Berkeley National Laboratories and samples were analysed by a time-of-flight mass spectrometer with a molecular beam flame sampling system and by photoionization with a tunable vacuum ultraviolet synchrotron radiation generated at the Advanced Light Source [153]. The atmospheric flames were studied in Novosibirsk by molecular beam mass spectrometry with soft ionization by electron impact and gas chromatography combined with mass spectrometry. No uncertainty on the experimental data is stated in the paper [72].

The experimentally measured mole fraction from [72] are compared by OpenSMOKE simulations with the MPE mechanism proposed by Dayma et al. [1]. The mole fraction profiles of the main species are given in Figure 7.1. The fit beween experimental data and the simulation for the rich flames are adequate for both pressures. This cannot be said for the stoichiometric flames, where a mismatch between the water and the CO profiles occurs in the flame at 27 mbar. It is plausible that the simulations for the stoichiometric flame at atmospheric pressure will lie within the experimental uncertainty, however the mismatch, about 5%, in the low pressure flame is quite high for the equilibrium concentrations. The equilibrium concentration is driven by the temperature, so the mismatch can be related to an error in the temperature measurements. The maximal flame temperature measured in the stoichiometric flame at 27 mbar is 1955 K, the related equilibrium mole fraction for H_2O and CO_2 is 20.9 and 16.7 mole% based on simulations. Since the equilibrium is predicted well in the other flame, it is assumed that an error occurs in the experimental measurements. This error could be in both the mole fraction measurements or in the temperature measurements.

Some of the intermediate species profiles are given in Figures 7.2, 7.3, 7.4 and 7.5. The mole fraction profiles of CH_4, C_2H_4, CH_3, C_2H_2, methyl propenoate (mp2d) and methyl-3-butenoate (mb3d) have been measured in the four flames. In the atmospheric flames, the concentration profiles of 1,3-butadiene (C_4H_6) and methyl propanoate (mp) are also shown, while in the flames at 27 mbar the mole fraction profiles of formaldehyde (CH_2O), propane (C_3H_8) or mp are given.

Most of the intermediate species profiles are well predicted by the simulations in the atmospheric rich MPE flame (Figure 7.2). The mechanism overpredicts the concentration of CH_4, C_2H_4 and CH_3, nevertheless the position of the peak corresponds with the experimental data. The profiles of the stable intermediate mp2d that is formed early in the combustion process, is simulated adequately. Both the mole fraction profiles peak and position are captured by the simulations. Nonetheless, the simulations overpredict the mole fraction profile of another stable intermediate species mb3d.

The simulated mole fraction profiles of C_2H_2 and mp do not match with the experimental data in the rich flame at atmospheric pressure. Experimentally, a C_2H_2 concentration three times lower is measured than achieved by simulations. Also the experimental equilibrium concentration tends to zero, while with the simulations an equilibrium mole fraction of 0.3 mole% is achieved. The consumption of acetylene in the rich flame at atmospheric pressure is underestimated by the kinetic mechanism. The opposite situation is found for mp: the experimental mole fraction surpasses the simulated mole fraction by a factor of 36.

For the rich MPE flame at 27 mbar, the agreement between simulations and experiments is better (Figure 7.3). The mole fraction profiles of CH_4, C_2H_4, CH_3 and C_2H_2 are well predicted

by the mechanism. The mole fraction profiles of the stable intermediates mp2d and mb3d are overpredicted by the model but the position of the peak is in agreement with the experiments. Formaldehyde and propane are also measured in the rich MPE flame at 27 mbar and both the mole fraction profiles are approximated sufficiently by the simulations.

Table 7.1: Flame characteristics of the laminar flat flames investigated by Korobeinichev et al. [72]

		Flame 1	Flame 2	Flame 3	Flame 4
Equivalence ratio	ϕ (-)	1.50	1.01	1.50	1.04
Argon dilution	mole%	50.0	50.0	70.2	80.0
Velocity	$cm{\cdot}s^{-1}$	72.1	72.1	7.6	12.5
mass flow	$g{\cdot}s^{-1}$	0.0057	0.0055	0.0278	0.0450
pressure	mbar	26.7	26.7	1000	1000
T_{ad},T_{in}=523 K	K	2495	2522	2519	2443
$T_{g,max}$	K	2040	1955	1606	1603

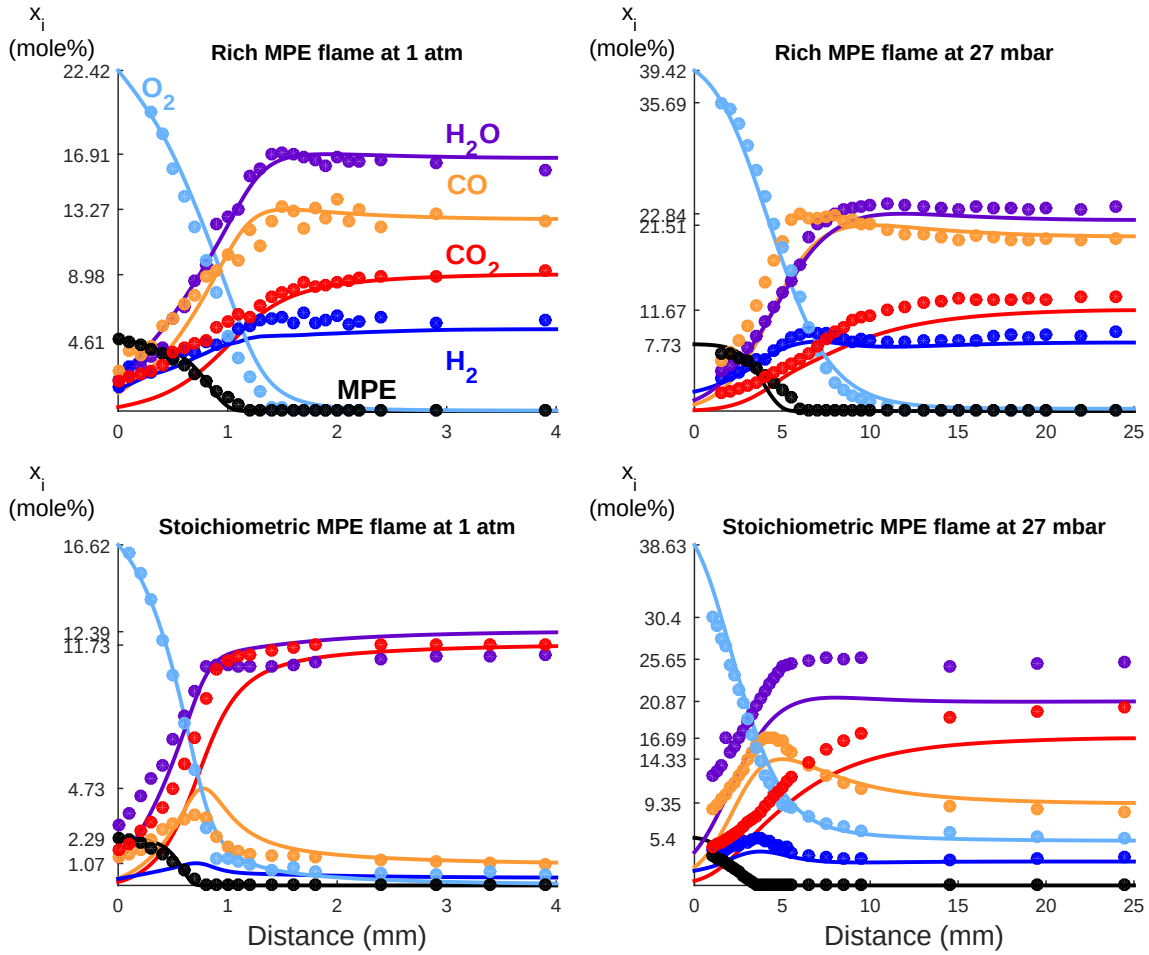

Figure 7.1: The experimental and simulated mole fraction profiles of the main species in the rich and stoichiometric MPE flames studied by [72].

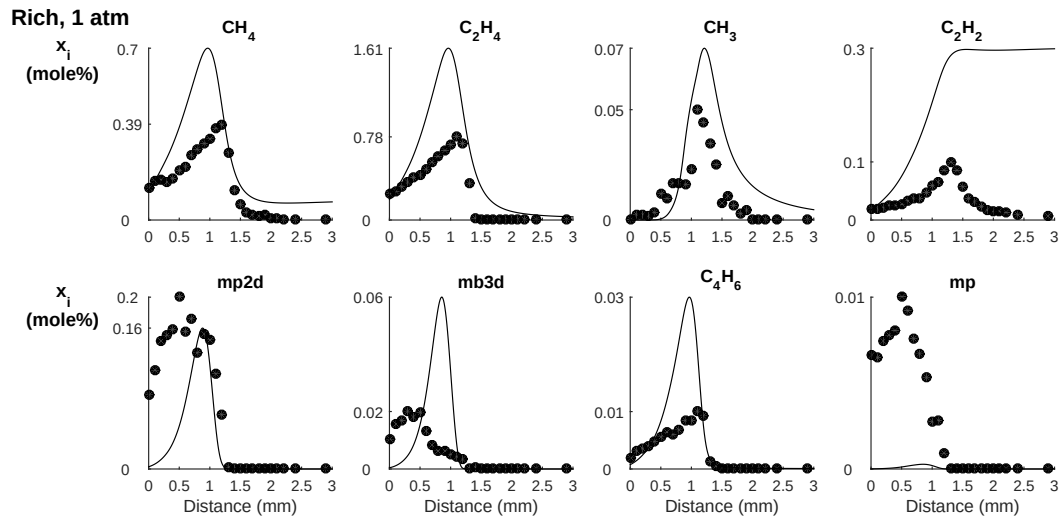

Figure 7.2: The experimental and simulated mole fraction profiles for some intermediate species in the rich MPE flame at atmospheric pressure studied by [72]. The assessed intermediates are CH_4, C_2H_4, CH_3, C_2H_2, mp2d, mb3d, C_4H_6 and mp.

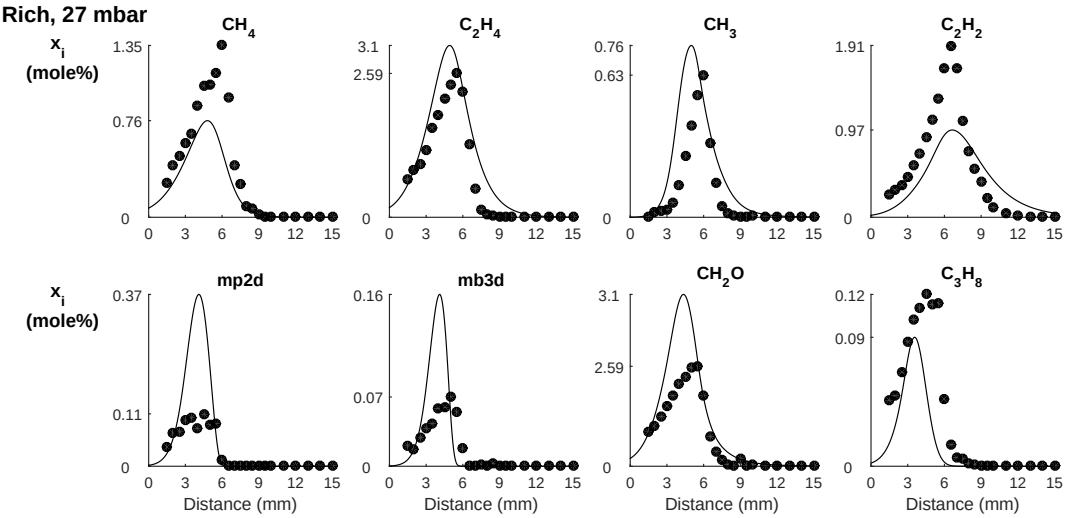

Figure 7.3: The experimental and simulated mole fraction profiles of CH_4, C_2H_4, CH_2O, C_2H_2, mp2d, mb3d, C_3H_8 and CH_3 in the rich MPE flame at 27 mbar studied by [72].

The experimental and simulated mole fraction profiles in the stoichiometric MPE flames for both pressures investigated by Korobeinichev [72], shows the same behaviour as found for the rich MPE flames (Figure 7.4 and 7.5). The mole fraction profiles of CH_4, C_2H_4 and CH_3 are predicted well by the simulations for both pressures. Also both C_2H_2 profiles are captured well by the simulations, in contrast to the rich flame at atmospheric pressure. A better fit is found for the stable intermediates mp2d and mb3d in the flame at atmospheric pressure compared to the flame at 27 mbar. Nevertheless, the position of the simulated peak is in agreement with the experiments for both flames. The mole fraction profile of mp was measured in both flames. In the stoichiometric flame at atmospheric pressure flame, the simulations underpredict the mp concentration, while at 27 mbar the concentration is overpredicted. The experimental formaldehyde concentration in the stoichiometric flame at 27 mbar is 0.35 mole% lower than the simulated peak value, while for C_4H_6 the measured concentration is 0.01 mole% lower than the simulated one.

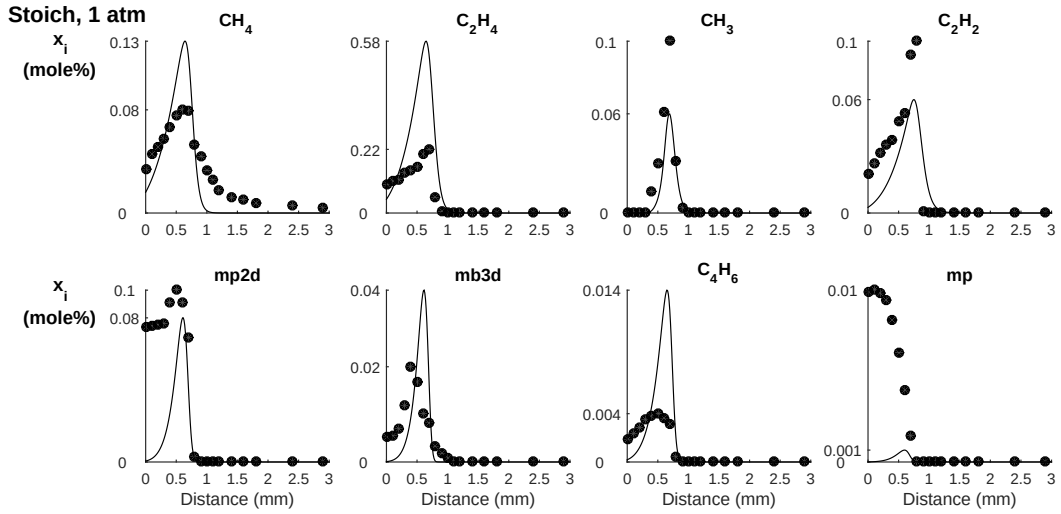

Figure 7.4: The experimental and simulated mole fraction profiles of CH_4, C_2H_4, CH_3, C_2H_2, mp2d, mb3d, C_4H_6 and mp in the stoichiometric MPE flame at atmospheric pressure studied by [72].

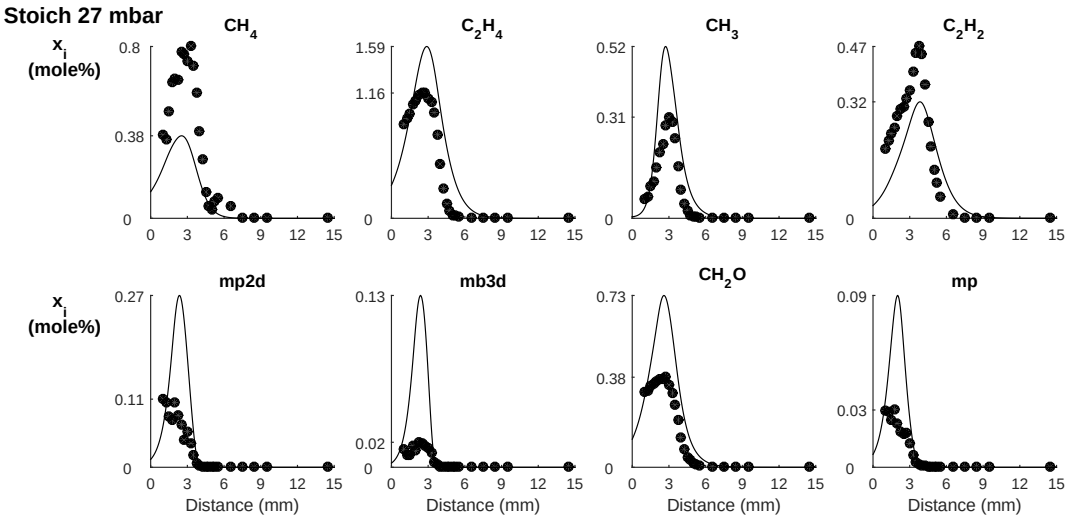

Figure 7.5: The experimental and simulated mole fraction profiles of CH_4, C_2H_4, CH_2O, C_2H_2, mp2d, mb3d, mp and CH_3 in the stoichiometric MPE flame at 27 mbar studied by [72].

Overall, an agreement is found between the simulations with the MPE mechanism and the experimenal data derived from [72]. The profiles of the main species are predicted well by the mechanism. Only the experimental equilibrium concentrations of H_2O and CO_2 in the stoichiometric flame at 27 mbar do not agree with the simulations. Also no uncertainty on the experimental concentrations is stated in the paper, so the simulations could lie within the uncertainty of the measurements in the stoichiometric flame at 27 mbar.

The mole fraction profiles of most of the intermediate species could be predicted adequately by the mechanism. Mismatches between simulations and experiments are found for C_2H_2 in the rich atmospheric flame, for mp in the atmospheric flames and for mp2d and mb3d in the low pressure flames. In Section 7.2, a sensitivity analysis is performed to assess if a change in kinetic data of the mechanism can lead to an improvement of the fit.

7.1.2 Laminar flame velocities

The laminar flame velocities S_u^0 have been measured by Fabien Halter and Fabrice Foucher of the Unversité d'Orléans in a Spherical Combustion Chamber (SCC). The used experimental setup is described in [65]. The intial temperatures are 353 K and 423 K at an inlet pressure of 1 bar and 423 K at 3 bar. At these conditions the laminar flame velocities have been gathered for equivalence ratios ranging from 0.7 to 1.4.

The SCC has a volume of 4.2 L and is filled with synthetic air ($20.5\%O_2/79.5\%N_2$) prior the experiment. The vaporized fuel was injected in the SCC and an electric fan stirred the fuel and air to obtain a homogenous mixture. Two tungsten electrodes were placed in the middle of the SCC to ignite the mixture. Only the initial flame expansion is measured, since constant pressure can only be assumed if the flame volume is small compared to the volume of the SCC. To measure the temporal expansion of the spherical flames, shadowgraphic images were taken with a high speed CMOS video camera. The streched spatial flame velocity (S_b) can be obtained from the measured flame radius (R_f) versus time (t) by

$$S_b = \frac{\mathrm{d}R_f}{\mathrm{d}t}. \tag{7.1}$$

The total stretch rate (κ) acting on a spherical expanding flame is defined as

$$\kappa = 2\frac{S_b}{R_f}. \tag{7.2}$$

The nonlinear relation between the propagation velocity and the stretch rate was used to obtain the unstretched propagation speed (S_b^0)

$$\left(\frac{S_b}{S_b^0}\right)^2 ln\left(\frac{S_b}{S_b^0}\right)^2 = -\frac{2L_b\kappa}{S_b^0}, \tag{7.3}$$

where L_b is the burned gas Markstein length. The Markstein length expresses the effect of curvature on the local burning velocity. Next the laminar burning velocity can be derived by

$$S_u^0 = \frac{\rho_b}{\rho_u}S_b^0, \tag{7.4}$$

for a flame propagating at constant pressure. Where ρ_b and ρ_u are the density of the burned and the unburned gases respectively. The densities were valuated using the EQUIL code [154].

The comparison between the experimental data and the simulations by OpenSMOKE [11] is presented in Figure 7.6. The uncertainty on the experimental velocities is 2 cm·s^{-1}, which is visualised in Figure 7.6 as a grey area. Overall, the simulated values lie within the uncertainty range of the experimental data. The experimental maximum velocity values for the three investigated conditions are 41.1 cm·s^{-1} at 1 bar and 353 K, 56.7 cm·s^{-1} at 1 bar and 423 K and 44.5 cm·s^{-1} at 3 bar and 423 K, while the simulated maximum values are 41.7, 56.8 and 45.8 cm·s^{-1} respectively. The maximum difference between simulations and experiments is 1.3 cm·s^{-1}, or 3% relatively, for the maximum values. Only at lean equivalence ratios, an underprection of maximal 5 cm·s^{-1} is found.

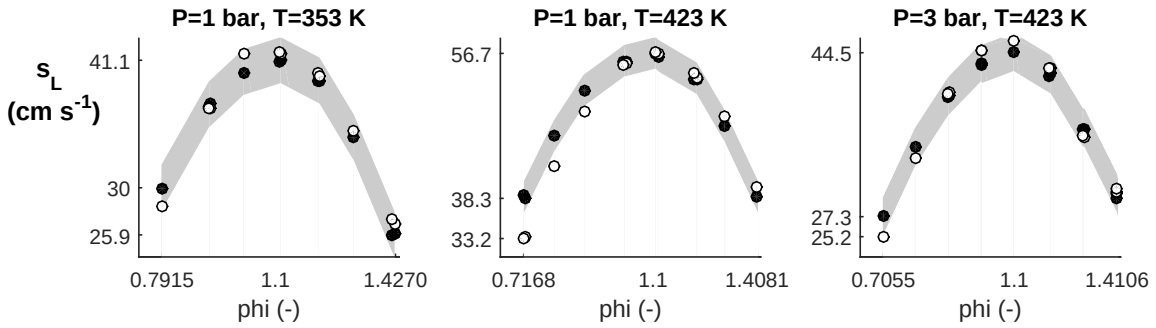

Figure 7.6: The measured laminar burning velocity S_u^0 (black dots) together with the simulated values (white dots) for different inlet conditions and as a function of the equivalence ratio. The uncertainty on the experimental results is estimated to be 2 cm·s^{-1} and is visualised by the grey area.

7.1.3 Jet stirred reactor

A Jet Stirred Reactor (JSR) is a continuous stirred-tank reactor where the combustion reaction can be investigated at a given temperature and high pressures. The used JSR is a fused silica sphere with a diameter of 4 cm and has four nozzles with an inner diameter of 1 mm. The JSR experimental setup is described in [155]. The temperature of the JSR is increased stepwise during experiments, and the mole fraction profiles of the reaction products are measured online by Fourier-Transform Infra Red spectroscopy (FTIR) and offline by GC-TCD/FID. With this analysis method, the mole fraction profiles of eleven stable species can be measured.

Three diluted mixtures of MPE, O_2 and N_2 have been analysed in the JSR at a pressure of 10 bar by Casimir Togbé and Philippe Dagaut at the Université d'Orléans. The composition of the mixtures is given in Table 7.2. The high dilution reduces the temperature changes during measurements. An uncertainty of 10% is assumed on the experimental data.

Table 7.2: Composition of the mixtures assessed in the JSR at 10 atm.

	N_2 (mole%)	O_2 (mole%)	MPE (mole%)
ϕ=2	99.4	0.5	0.1
ϕ=1	99.1	0.8	0.1
ϕ=0.6	98.3	1.6	0.1

The combustion in the JSR is simulated by OpenSMOKE [11]. The measured and simulated profiles of the main species, CO, CO_2, H_2O and O_2 are shown in Figure 7.7 for the three mixtures. The oxygen mole fraction profile is not measured in the rich and stoichiometric mixtures, but the simulated values are given. The simulations depict a higher oxygen profile in the lean flame than measured experimenally. Nevertheless, the simulated concentrations lie close to the uncertainty range of the experimental data. The mole fraction profiles of CO, CO_2 and H_2O are predicted well by the simulations. All the simulated mole fraction profiles are within the experimental uncertainty range.

In Figure 7.8, the mole fraction of MPE, H_2, CH_4 and C_2H_4 are shown for the three assessed mixtures. In the three mixtures, the MPE, CH_4 and C_2H_4 mole fraction profiles are modeled well. They lie within the experimental uncertainty and also the position of the peaks is predicted well by the mechanism.

The mole fraction profiles of formaldehyde are given in Figure 7.9. The simulations capture the formaldehyde mole fraction profiles perfectly. In the lean flame, the concentration of mp2d is also measured. Experimentally, a peak value of $1.19{\cdot}10^{-4}$ mole% is measured, while the simulated value is $0.43{\cdot}10^{-4}$ mole% higher, just outside the uncertainty range.

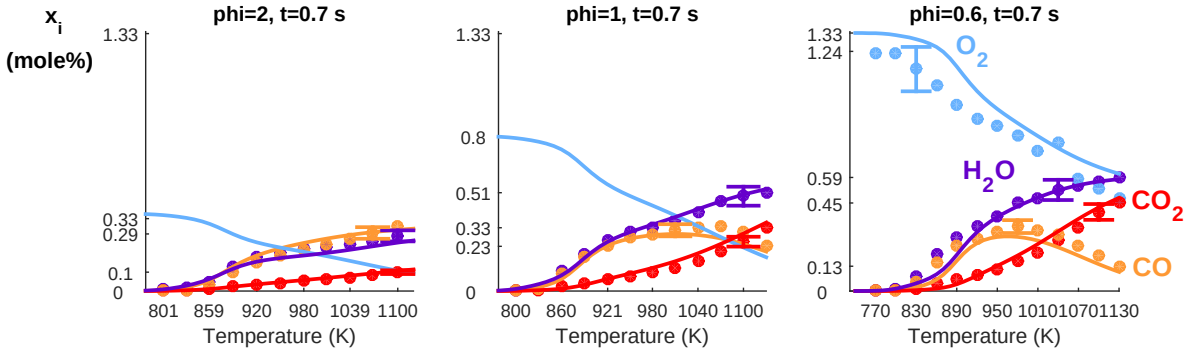

Figure 7.7: The measured and simulated mole fraction profiles of the main species for the assessed MPE combustion with an equivalence ratio of 2, 1 and 0.6 in a JSR at 10 atm and τ=0.7 s.

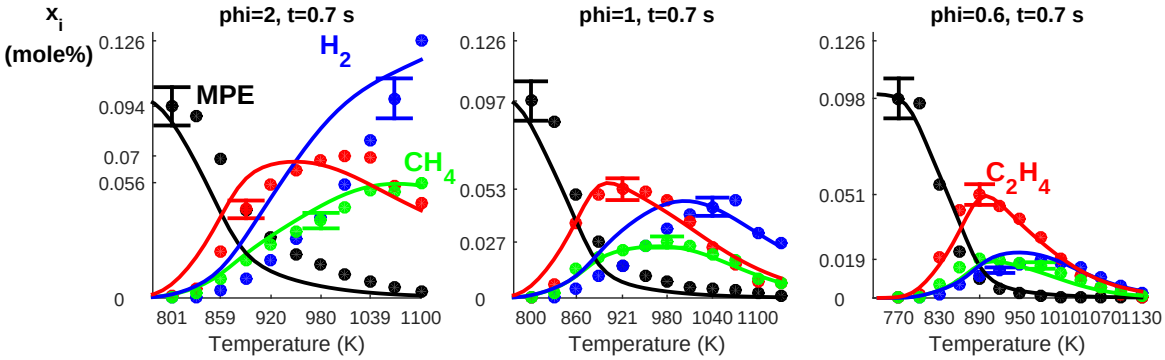

Figure 7.8: The measured and simulated mole fraction profiles of the fuel and some intermediates, found for the assessed MPE combustion with an equivalence ratio of 2, 1 and 0.6 in a JSR at 10 atm and and τ=0.7 s.

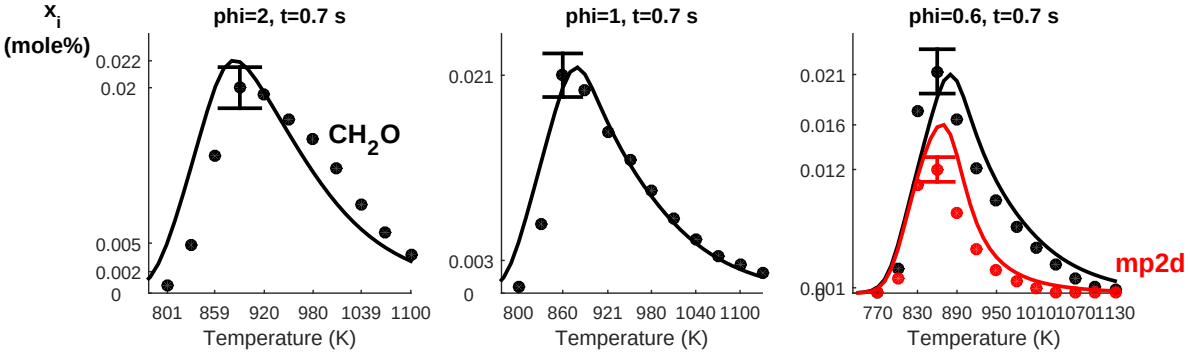

Figure 7.9: The measured and simulated mole fraction profiles of the fuel and some intermediates, found for the assessed MPE combustion with an equivalence ratio of 2, 1 and 0.6 in a JSR at 10 atm and and τ=0.7 s.

7.1.4 Rapid Compression Machine

The ignition delays of mixture with MPE, nitrogen (and for some argon) and oxygen are experimentally measured by Weber et al. at a pressure of 15 bar and 30 bar and this for different equivalence ratios in a RCM [74]. In addition, Weber et al. compared the simulation performance of different mechanisms for the combustion of MPE. They assessed if one of the three published MPE mechanisms could be used to simulate the RCM data. Two of them, investigated by Korobeinichev and Dmitriev, do not contain the low temperature chemistry and could not be used for the simulations of ignition delays [71, 72, 74]. The third mechanism established by Diévart contains low temperature chemistry and could be used for the simulations of the ignition delay data [73]. However, the mechanism was unable to reproduce the experimental results. Therefore, Weber et al. constructed their own model by the Reaction Mechanism Generator software. The achieved model contains more reactions than the Diévart model. Nevertheless, a discrepancy was found between the simulations with the new constructed model and the experimental results. Possible reasons could be missing reaction pathways, incorrect rate estimations and incorrect thermodynamic properties [74].

Some of the assessed conditions showed a two-stage ignition. A two-stage ingnition is common by alkanes and larger molecules. The fuel start to decompose at low temperature releasing some heat. The decompostion is mostly propagated by OH radicals. With the increasing temperature the chemistry changes and alkenes and HO_2 radicals are formed. The reactions release less heat and a Negative Temperature Coefficient (NTC) region is seen, where the overall reaction rate is negatively depending on the temperature. The temperature increases further due to the compression and hydrogen peroxide is formed, which enhances the decomposition reaction leading to a second peak in heat release. The heat release curve during a two-stage ignition is given in Figure 7.10 [156]. The first peak is related to the decomposition at low temperatures. The decomposition slows down in the NTC region, but when the temperature increases more due to compression a second ignition can be seen [156].

A two step ignition is found in a narrow temperature range for the rich and stoichiometric mixtures. A NTC region is found in the temperature region of 720 to 800 K for the MPE mixture with equivalence ration of 2.0 at 15 bar. The temperature range where two-stage ignition is apparent in the stoichiometric mixture at 30 bar is between 720 and 760 K (Figure 7.11) [74]. Other authors also found two-stage ignition for methyl pentanoate mixtures at stoichiometric conditions [157].

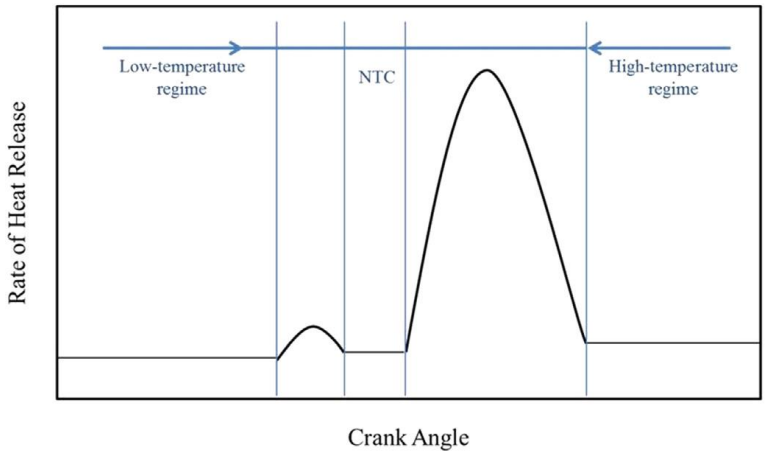

Figure 7.10: The heat release curve during a two-stage ignition [156].

In Figure 7.11, the two-stage ignition can be seen for a starting temperature T_C of 733 K in the stoichiometric mixture at 30 bar. The related pressure trace line shows a increase after 4 ms. The increase is related to the heat release and decompostion of the fuel at low temperatures. The other pressure trace lines shown only one increase in pressure and have therefore a single stage ignition.

The experimental data of Weber et al. is modeled by the reduced Diévart model [73] and the proposed MPE mechanism. The results for both models is given in Figure 7.12. The performance of the Dayma mechanism is better than the Diévart mechanism in the mixtures at 15 bar for an equivalence ratio of 0.25, 0.50 and 1.00. These mixtures have a single-step ignition.

Nevertheless, for the other two mixtures, which have a two-step ignition, the performance of the Diévart mechanism is better and some improvement of the mechanism should achieved for the mixtures with a two-step ignition.

7.2 Improving the methyl pentanoate mechanism

First of all the data of our own exeperiments are assessed. In Section 6.3, the experimental and simulated mole fraction profiles for the main species and some intermediates are discussed for the experimental assessed MPE flames at 55 mbar. A fit between simulation and experimental data is found for most of the main species. Nevertheless for some of the intermediates, a difference between the simulations and experiments is found, like for the acetylene profile in the stoichiometric flame. Next, in the flames assessed by Korobeinichev a mismatch is found for C_2H_2, mp2d and mb3d. The mole fraction profiles of these species will be investigated further. The kinetic data of the MPE mechanism can be changed to improve the fit between simulations and experiments. However, first the reactions affecting the species concentration needs to be identified.

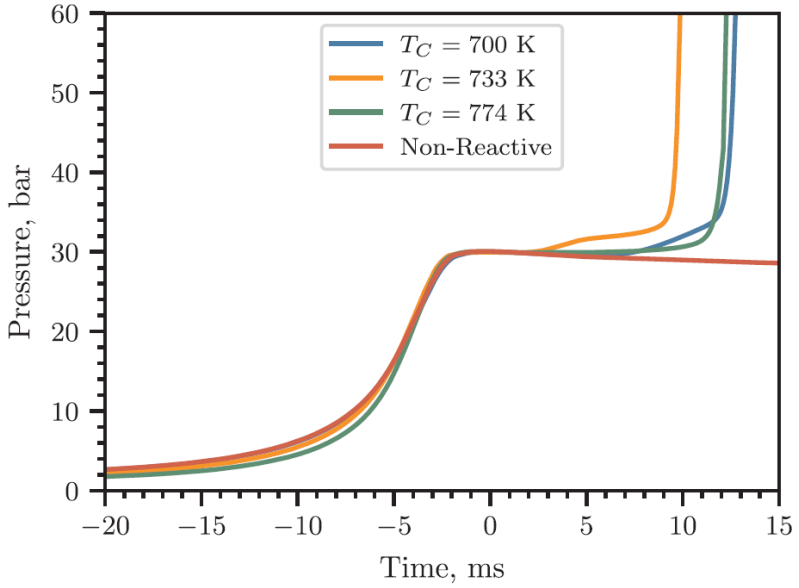

Figure 7.11: Selected pressure traces around the NTC region of ignition delay for the stoichiometric MPE mixture at 30 bar [74]

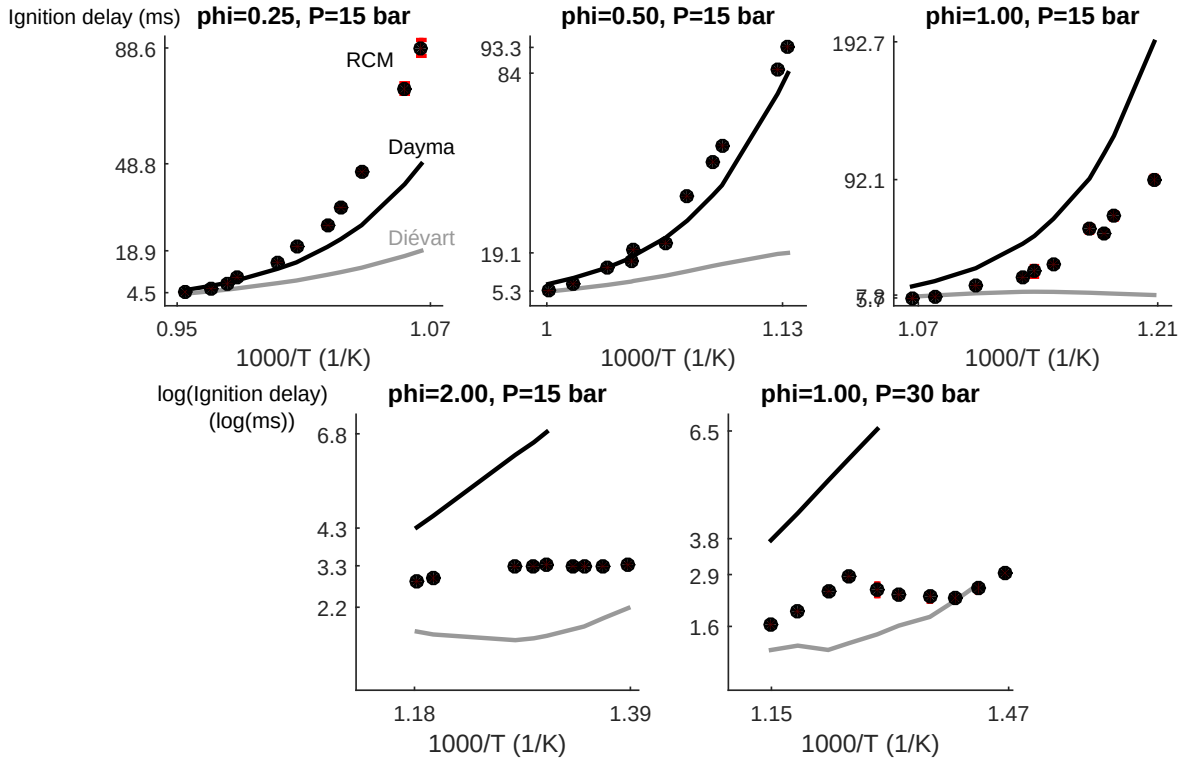

Figure 7.12: The experimental data obtained by Weber et al. for ignition delays of MPE mixtures at 15 and 30 bar for different equivalence ratios is compared to simulations with two kinetic models. The Dayma model performs better in the flames at 15 mbar with and equivalence ratio of 0.25, 0.50 and 1.00 and a single-stage ignition. Nevertheless, for the other two mixtures with a two-step ignition the Diévart mechanism predicts the ignition delay better, still there is a average difference of a factor 5 between simulations and experiments. The difference between the Dayma mechanism and the experimental data is as high as a factor of 55.

A reaction flow analysis and a sensitivity analysis are performed to identify the reactions affecting the mole fraction profiles of the species for which improvement can be achieved. After identification, the pre-exponential factor A of the reactions is changed, to see the effect on the mole fraction profiles of the assessed species. If the effect is positive and substantial, literature data about the reaction kinetics is searched and a change in kinetic data is suggested.

7.2.1 Reaction flow analysis

There are different combustion pathways through which MPE can react to CO_2 and H_2O during combustion. With a reaction flow analysis the contribution of the different pathways can be quantified (Section 4.5). The integration is done over the full domain, which make it a global rate of production analysis. In Figure 7.13, the main consumption pathways for the rich, stoichiometric and lean MPE flames at 55 mbar are shown, in percentages. The sum of the reaction pathways leaving a species cannot be higher than 100%. Only reactions which contribute more than 10% to the consumption of a species are shown to keep the schematic clear.

With this figure, the reaction sequence can be visualised and reactions where main interme-

diates are formed can be identified. The same reaction sequences are found for the rich and stoichiometric flames. The main consumption reactions in the lean flame are different after the formation of ethylene.

The first step in the combustion process of MPE is hydrogen abstraction. The C-H bond of the carbon on position 2 is weaker than the other carbon bonds and after H abstraction the mpe2j radical is formed. Other radicals formed directly from MPE by H abstraction are mpe3j, mpe4j, mpe5j and mpemj. The most abundant radical is mpe2j, since it is more stable than the other radicals due to the interaction of the free electron with the double bound of the carbonyl group. Following the mechanism around 30% of the fuel reacts to mpe2j.

The main part of the formed mpe2j radical reacts further to methyl prop-2-enoate (mp2d) and $C_2H_5^\bullet$ by β-scission, while the free electron can also delocate from position 2 to position 5 to form mpe5j. Both mp2d and mpe5j can react to mp3j, a radical of methyl propanoate. The following combustion steps are shown in Figure 7.13 and mp3j reacts further to ethylene and finally CO and CO_2.

The consumption pathway shows that intermediates like C_2H_4, C_2H_2, CH_2O and $CH_3^\bullet$ are formed early in the combustion process, just as CO and CO_2. CO_2 is formed by the reaction of $C_2H_3CO_2$ to $C_2H_3^\bullet$ and by the reaction of CH_3OCO to $CH_3^\bullet$, while in the combustion of conventional fuels CO_2 is only formed by the oxidation of CO at the end of the combustion.

The main fuel consumption pathway in the rich and stoichiometric flame is MPE ($C_6H_{12}O_2$) $\rightarrow$ mpe2j ($^\bullet C_5H_{12}O_2$) $\rightarrow$ mp2d ($CH_2{=}CH_2COOCH_3$) $\rightarrow$ mp3j ($CH_2^\bullet CH_2COOCH_3$) $\rightarrow$ mpmj ($CH_3CH_2COOCH_3^\bullet$) $\rightarrow C_2H_5CO \rightarrow C_2H_5 \rightarrow C_2H_4 \rightarrow C_2H_3 \rightarrow C_2H_2 \rightarrow$ HCCO $\rightarrow$ CO and finally CO_2. In the lean MPE flame, the reactions starting from C_2H_4 are different. More oxygenated intermediates are formed by the next patway $C_2H_4 \rightarrow C_2H_3 \rightarrow CH_2CHO \rightarrow CH_2CO \rightarrow$ CO and CO_2.

Most of the species for which the mole fraction profiles need to be improved, C_2H_2, mp2d and mb3d, are present in the consumption pathway. The species mp2d and C_2H_2 are a part of the main combustion pathway for the rich and stoichiometric MPE flame. mp2d is formed for more than 57% from mpe2j and acetylene is mainly formed out of $C_2H_3^\bullet$. The mb3d species is part of one of the other combustion pathways. It's formed by a β-scission reaction of mpe3j whereby a methyl radical is released.

Next to the consumption pathways, the formation pathways of the species can be investigated (Figure 7.14). The main formation pathways expresses from which species a certain species is formed. The sum of the arrows arriving at a species cannot be higher than 100%. The formation pathways of the rich, stoichiometric and lean flame are similar at the beginning and at the end of the combustion process, however the formation of the methyl radical is different. In the rich flame, it formed mainly from CH_2CO by the reaction $CH_2CO{+}H{=}CH_3{+}CO$ and in the stoichiometric and lean flame it is formed from C_2H_4 by the reaction $C_2H_4{+}O{=}CH_3{+}HCO$.

The consumption and formation pathways give an insight in the order of the reaction during combustion and make it possible to identify the key species of the process. In the case of MPE combustion, the main stable intermediates are mp2d, C_2H_4, CH_2O and C_2H_2. The pathways also show that CO and CO_2 are formed early in the combustion process, due the oxygenated nature of the fuel.

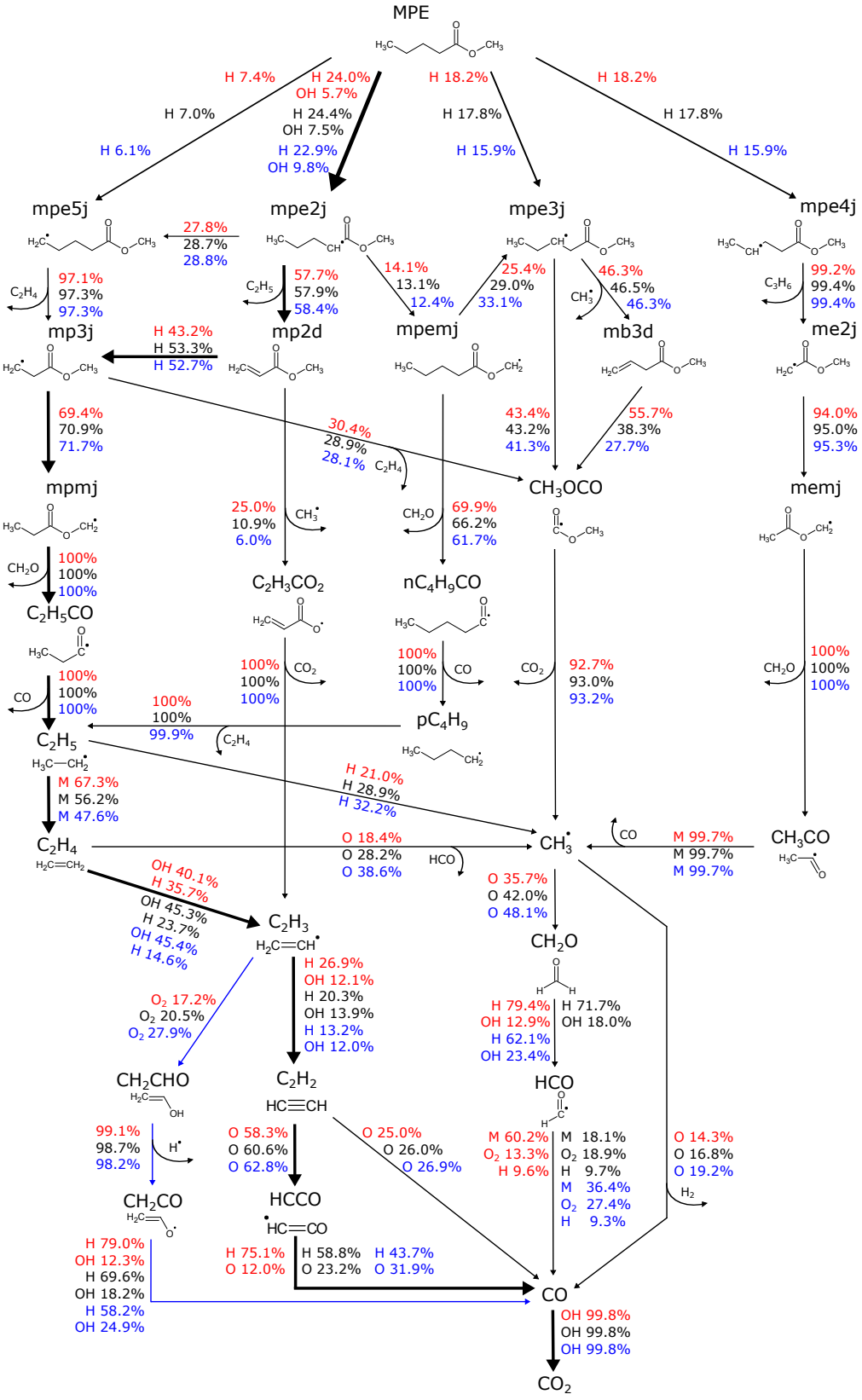

Figure 7.13: The main consumption pathway in the rich (red numbers) , stoichiometric (black numbers) and lean MPE flames (blue numbers) at 55 mbar. The rich and stoichiometric flames are decomposed by the same pathway.

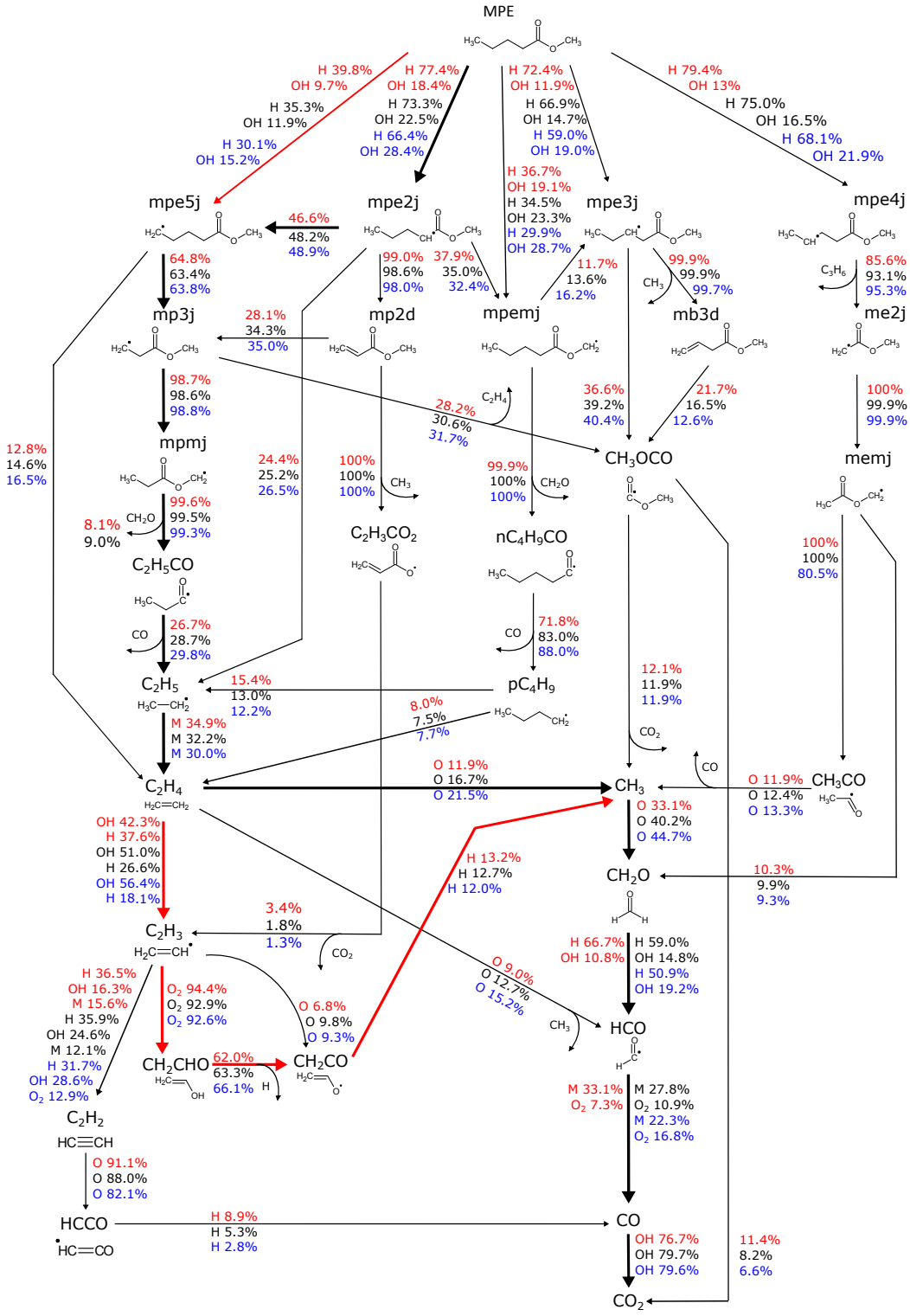

Figure 7.14: The main pathways for the production of species for the rich (red), stoichiometric (black) and lean (blue) MPE flames at 55 mbar. The production of the $CH_3^\bullet$ differs between the flames.

7.2.2 Sensitivity analysis

The reaction pathways are important to identify the main reaction sequence in the fuel oxidation. However, to alter the mole fraction profile of a species, its main formation reaction is not always the reaction to the formation is the most sensitive to. The mole fraction profile can be sensitive to other reactions, like radical reactions. To identify the reaction which influences the mole fraction profile of the species of interest, a sensitivity analysis is performed. The sensitivity analysis focusses on the pre-exponential factor of the Arrhenius equation (Equation 4.34) for the species of interest: C_2H_2, mp2d, and mb3d.

These species are chosen since they are important following the reaction flow analysis. mp2d and mb3d are stable methyl esters that are formed at the beginning of the combustion process. Acetylene is an important intermediate that is formed later in the combustion process. Mole fraction profiles for these species are measured and the fit with simulations shows some discrepancy at certain conditions. Therefore their simulated mole fraction profile can be improved by assessing the kinetic data of the reactions their mole fraction profile is sensitive to.

Acetylene (C_2H_2) is the assessed intermediate with the highest concentrations in the flames. To improve the fit between simulations and experiments, the reactions impacting most the acetylene concentration are identified and given in Figure 7.15f. The positive NSC indicates that the reaction has an effect on the formation of the species, while a negative value implies that the consumption of the species is affected by the reaction.

First the impact of the MPE submechanism is assessed. In Figure 7.15, the results of the sensitivity analysis on the C_2H_2 mole fraction are given for the rich flame at atmospheric pressure and for the stoichiometric flame at 55 mbar. The C_2H_2 concentration is not sensitive to the reactions of the MPE oxidation submechanism, but to the reactions of the methyl butanoate mechanism of Fisher [107].

In Figure 7.16 and 7.17, the sensitivity analysis for the four flames studied by Korobeinichev [72] are presented, regarding the stable intermediate mp2d. The formation of mp2d is, in the four assessed flames, sensitive to two reactions of the MPE submechanism: mpe2j=C_2H_5+mp2d and MPE+H=mpe2j+H_2. These two reactions did also come forward in the reaction flow analysis. The consumption of mp2d is affected by different reactions. Reaction H+O_2=OH+O is the most important one at high pressure, while at low pressure, this reaction affects the formation of mp2d. Similar NSC values are found for the reactions mpmj=>CH_2O+C_2H_5CO and mp3j=mp2d+H in all the flames. No other reaction of the MPE submechanism with a distinct NSC values between the flames at atmospheric and low pressure is found.

Changing the kinetic data of reaction mpmj=>CH_2O+C_2H_5CO and reaction mp3j=mp2d+H will lead to the same effect since their NSC are the same value and sign. To improve the fit of mp2d, the simulated mole fraction profile at low pressures should decrease, while the profile should stay the same at atmospheric pressure. In the mechanism, both reactions are stated as irreversible reactions without pressure dependency. Just changing the pre-exponential factor will not be enough to improve the fit of mp2d in both flames, since no pressure dependency of the reactions is implemented in the kinetic mechanism. The only pressure dependent reaction for which the NSC changes is H+O_2=OH+O.

The mole fraction profiles of mb3d are overpredicted at the low pressure of 27 mbar and atmospheric pressure. Two reactions: mp2j+H=mp and mpmj=>CH_2O+C_2H_5CO affect the formation of mb3d in all four flames (Figure 7.18 and 7.19).

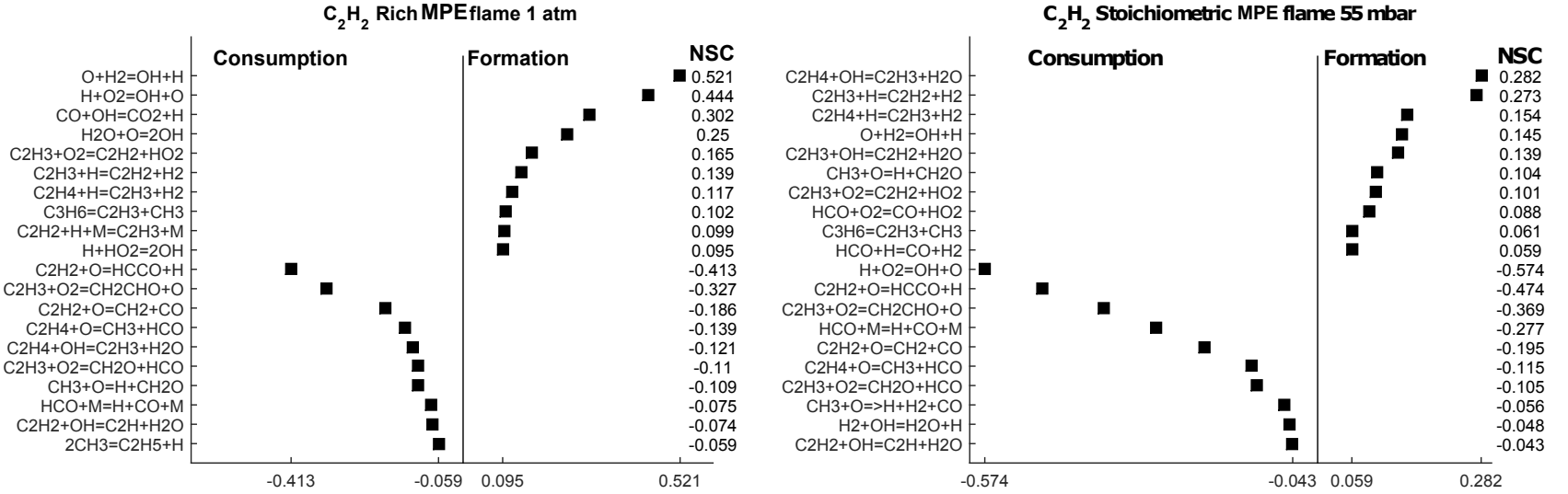

Figure 7.15: NSC for the rich MPE flame at 1 atm and for the stoichiometric MPE flame at 55 mbar regarding acetylene. The simulated acetylene concentration is not sensitive to reactions of the MPE oxidation submechanism.

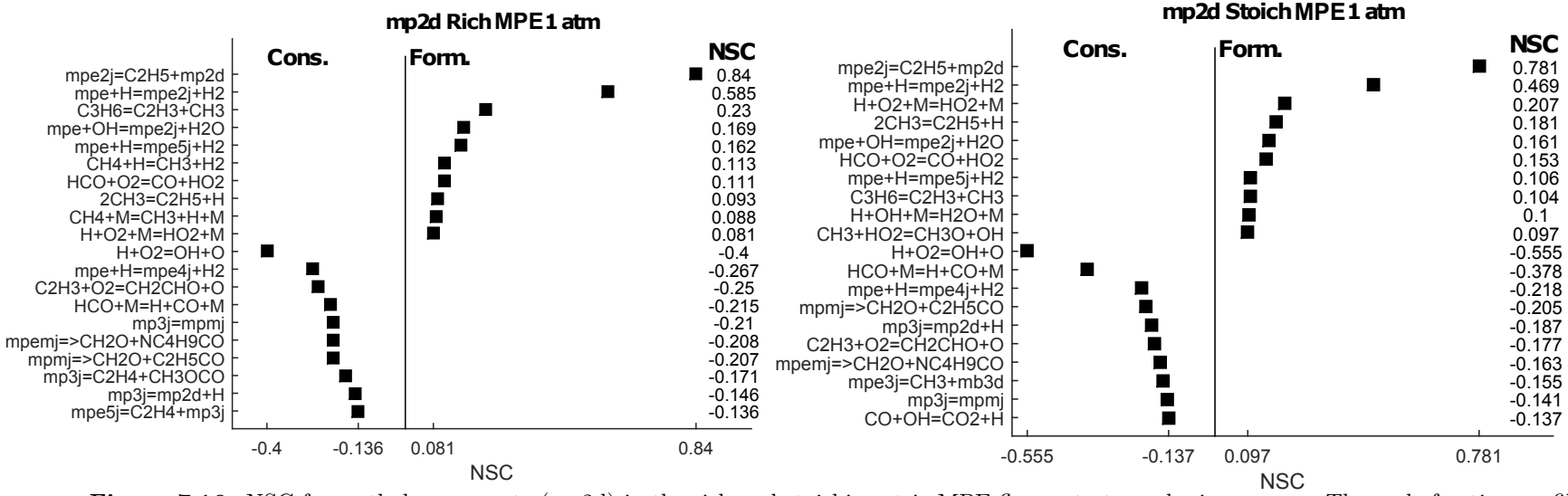

Figure 7.16: NSC for methyl propenoate (mp2d) in the rich and stoichiometric MPE flame at atmospheric pressure. The mole fraction profiles of mp2d are captured well by the mechanism at atmospheric pressure, so the thermodynamic data of the reaction that came forward in this senstivity analysis should be maintained.

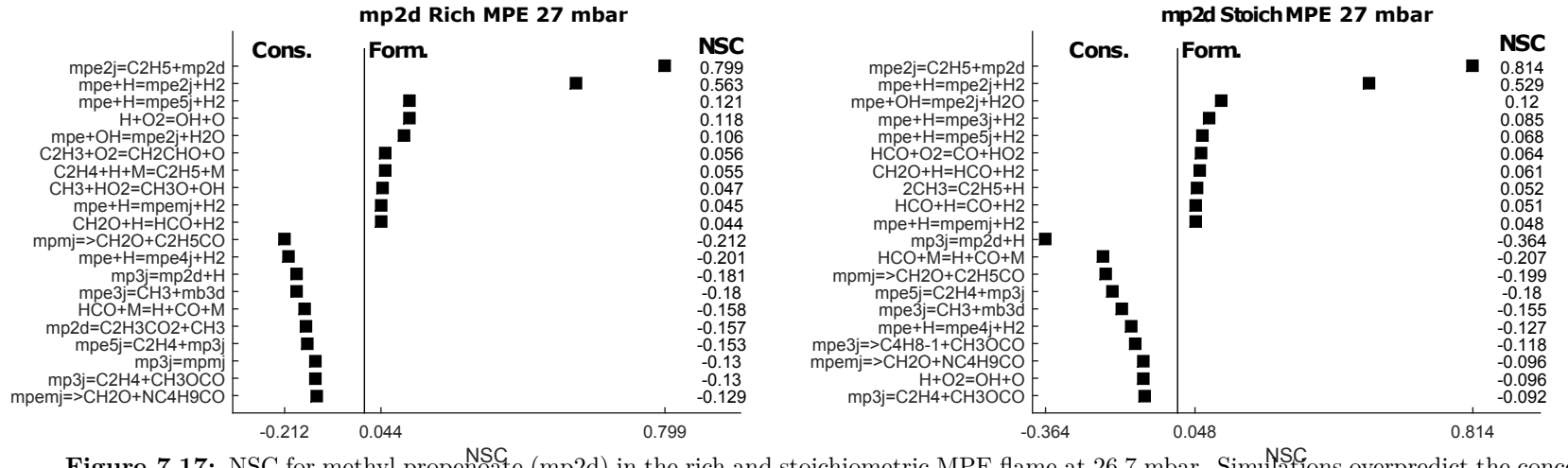

Figure 7.17: NSC for methyl propenoate (mp2d) in the rich and stoichiometric MPE flame at 26.7 mbar. Simulations overpredict the concentration of mp2d in both flames, therefore the thermodynamic data of reaction mpmj=>CH2O+C2H5CO and mp3j=mp2d+H will be assessed further.

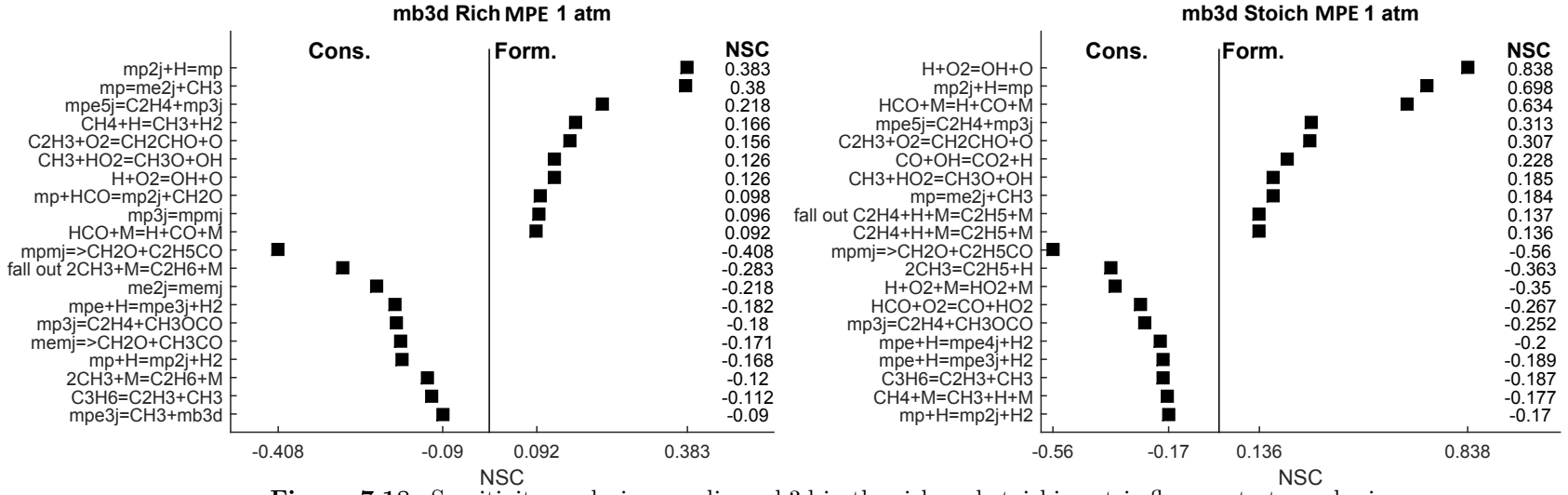

Figure 7.18: Sensitivity analysis regarding mb3d in the rich and stoichiometric flames at atmospheric pressure.

The effect of pre-exponential factor changes on the mb3d concentration for both reactions are assessed. No significant improvement between simulations and experiments was found. The mole fraction profile of mb3d is not sensitive enough to the identified reactions.

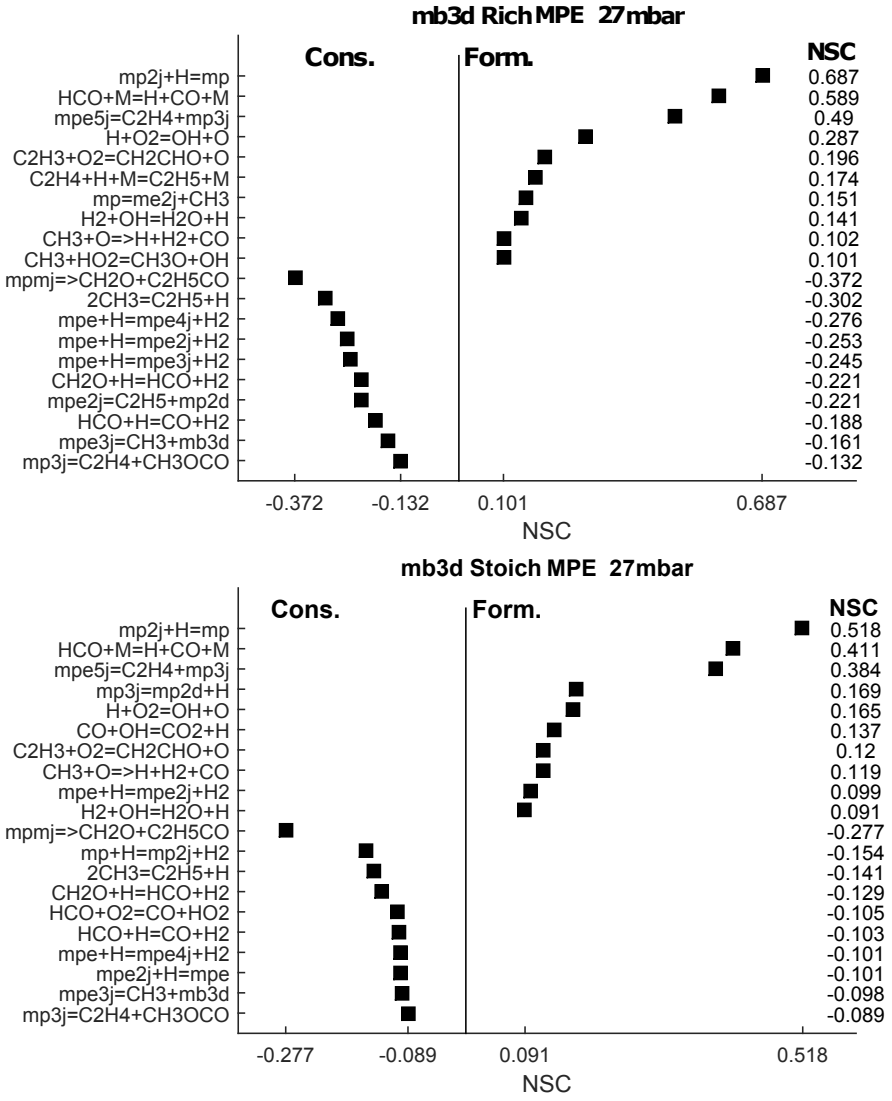

Figure 7.19: Sensitivity analysis regarding mb3d in the rich and stoichiometric flames at 26.7 mbar.

The mole fraction of most intermediates can be predicted well by the mechanism for different combustion configurations. A mismatch was found for C_2H_2, mpd2 and mb3d in some fo the laminar flames. Changes in kinetic data of the MPE mechanism for reactions that come forward in the sensitivity analysis do not lead to considerable improvements of the fit between simulated and experimental concentration profiles. On the contrary the fit for some species deteriote. Therefore the base mechanism for methyl butanoate from Fisher [107] need to be investigated further and the kinetics of the other MPE mechanisms in literature need to be assessed.

7.2.3 Performance of other MPE mechanisms

The performance of two other published MPE mechanism is assessed, to see if they have a better performance than the proposefd mechanism. Korobeinichev et al. also proposed a kinetic mechanism for the combustion of MPE [72]. The performance of the mechanism was checked by simulating the three MPE flames at 55 mbar. The result for the main species can be found in Figure 7.20. The fuel is fully consumed in the rich flame. However there is still oxygen present in the post flame zone. Also in the stoichiometric and lean MPE flame, the oxygen concentration in the post flame zone is too high and the CO and CO_2 profiles are lower than experimentally measured. The simulation results indicate that some reactions to finalise the combustion process are missing in the published mechanism, which means it cannot be used for further research.

The performance of the reduced Diévart mechanism [73] for the combustion of the laminar MPE flames at 55 mbar is assessed by simulations and the results are shown in Figure 7.21. The model can predict the mole fraction profiles of the main species well.

The rich MPE flame at atmospheric pressure investigated by Korobeinichev et al. [72] is also simulated by the Diévart model. The simulations results for the intermediates are given in Figure 7.22. The Diévart model could predict the consumption of C_2H_2 better than the Dayma mechanism and therfore the Diévart mechanism will be compared to the proposed MPE mechanism.

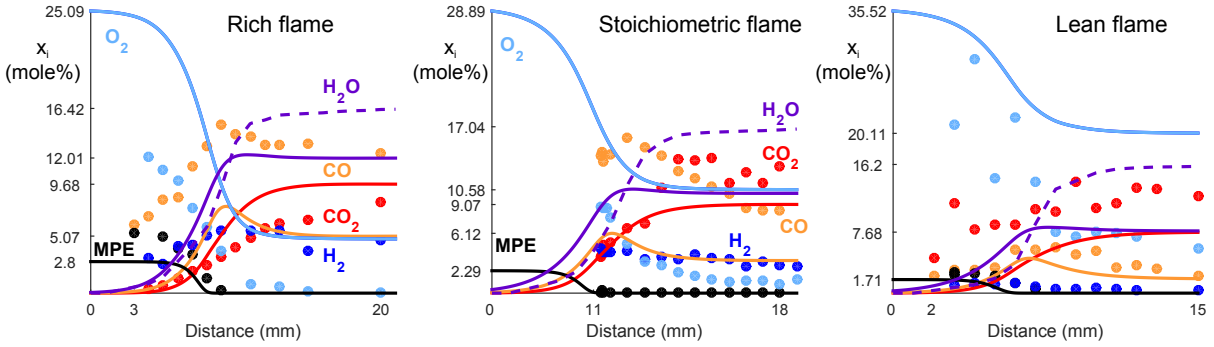

Figure 7.20: Comparison between the experimental data found in the MPE flames at 55 mbar and simulations conducted by the kinetic MPE mechanism proposed by Korobeinichev [72].

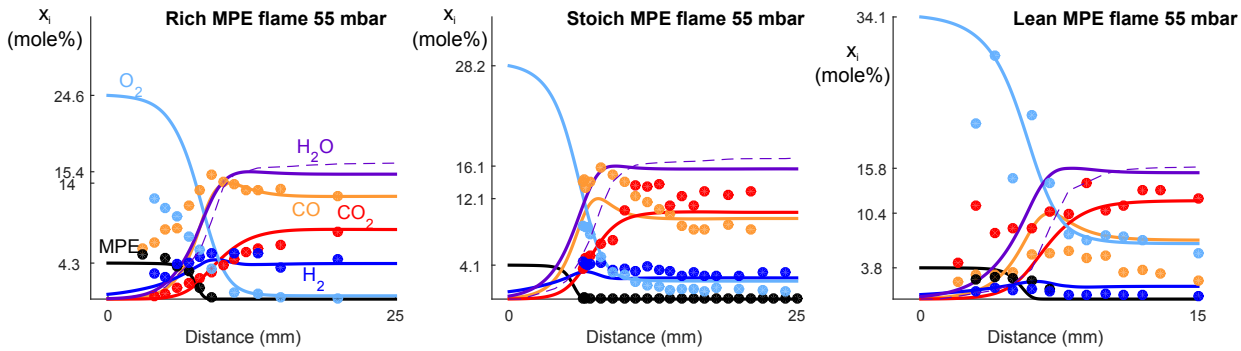

Figure 7.21: Comparison between the experimental data found in the MPE flames at 55 mbar and simulations conducted by the kinetic MPE mechanism validated in [73] for the main species.

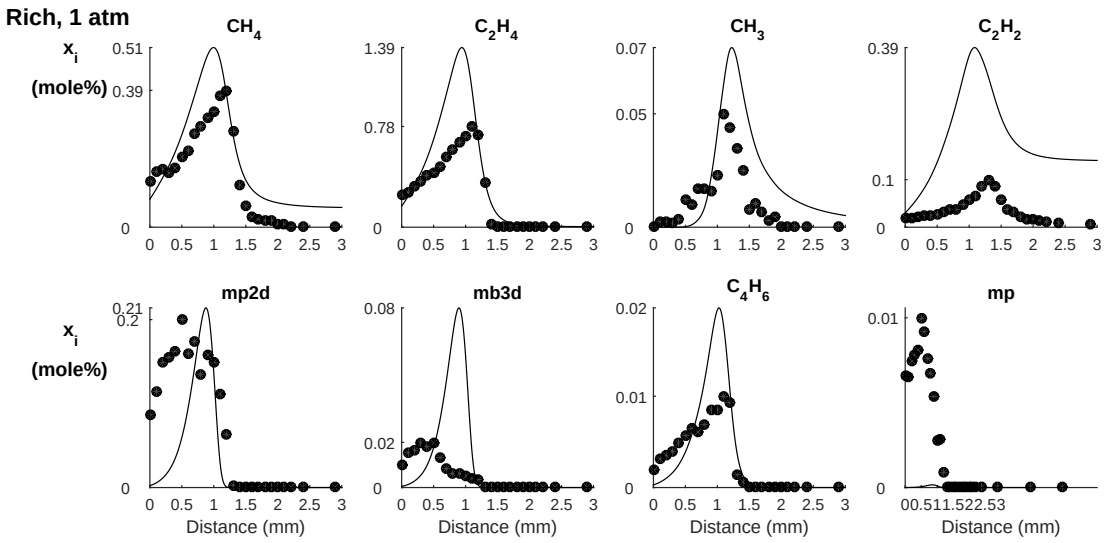

Figure 7.22: Comparison between the experimental data found by Korobeinichev [72] in a rich atmospheric MPE flame for some intermediate species and simulations conducted by the kinetic MPE mechanism validated in [73].

7.2.4 Adjustment of the Dayma mechanism

Overall, the Dayma mechanism can be improved for the simulations of the laminar flat flames mole fraction profiles and the ignition delay of mixtures with a two-stage ignition.

Since the Diévart mechanism can capture the consumption of C_2H_2 in the rich atmospheric MPE flame better, the kinetics regarding C_2H_2 in the Diévart mechanism are investigated further. Nevertheless, the consumption of C_2H_2 in the Diévart mechanism can still be improved, since the maximal peak value in experiment and simulation differs for the rich flame at atmospheric pressure. A sensitivity analysis have been performed on the Diévart results related to the C_2H_2 (Figure 7.24). The notation of the species is different in the Diévart mechanism compared to the Dayma mechanism. The fuel MPE is written as MF, also the name of other species containing the fuels name are adjusted.

The same reactions as for the Dayma mechanism come forward in the sensitivity analysis (results Dayma mechanism, see Figure 7.15). The acetylene profile is sensitive to reactions of the $O_2/H_2/CO$ mechanism. To improve the performance of the Dayma mechanism, the kinetic data of the $O_2/H_2/CO$ mechanism reactions in the Dayma mechanism are replaced by more recently published kinetic data. The kinetic data for the $O_2/H_2/CO$ mechanism published by Keromnes et al. [158] is incorporated in the Dayma mechanism.

A simulation with the adjusted Dayma mechanism, shows that the shape of the C_2H_2 profile in the rich atmospheric MPE flame slightly changes. In Figure 7.23, the simulation results with the adjusted mechanism are shown as blue lines. The simulations with the initial Dayma mechanism are shown as black lines. Only the shape of the C_2H_2 profile is affected by the implementation of the Keromnes $O_2/H_2/CO$ submechanism. To improve the performance of the Dayma mechanism further, the kinetic data of other reactions should be assessed.

The sensitivity analysis for acetylene in the rich atmospheric MPE flame (Figure 7.24) shows that the acetylene concentration is also sensitive to reaction $C_2H_4+H=C_2H_3+H_2$ and reaction $C_2H_3+H=C_2H_2+H_2$ for its formation and reaction $C_2H_2+O=HCCO+H$ affects the

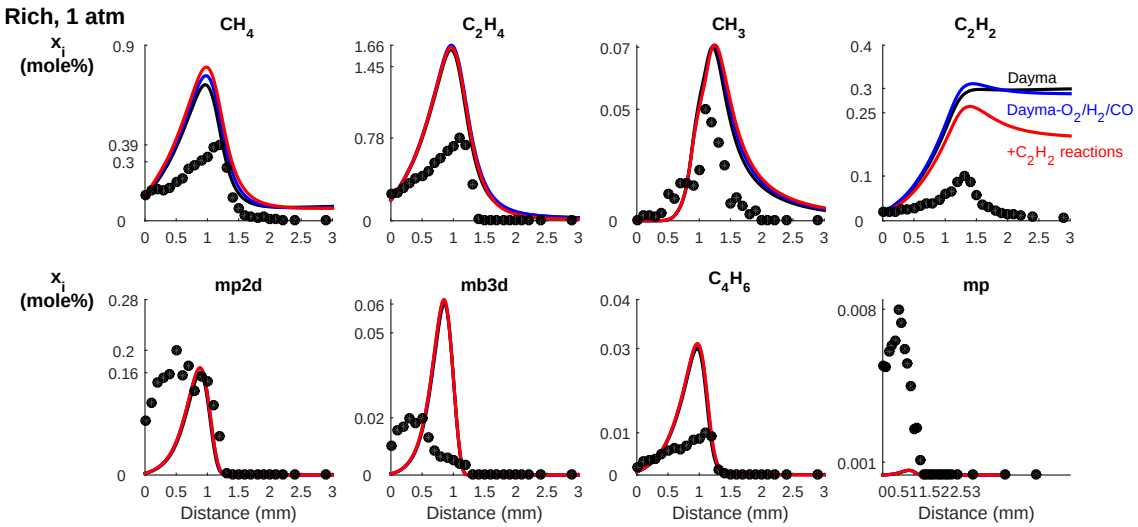

Figure 7.23: The experimental and simulated mole fraction profiles of CH_4, C_2H_4, C_4H_6, C_2H_2, mp2d, mb3d, CH_2O and CH_3 in the rich MPE flame at 27 mbar studied by [72]. The simulations are conducted by the Dayma mechanism (black lines), the Dayma mechanism with adjusted $O_2/H_2/CO$ mechanism (blue lines) and with the Dayma mechanism were also kinetic data for reaction $C_2H_4+H=C_2H_3+H_2$ and reaction $C_2H_3+H=C_2H_2+H_2$ (red lines) is changed.

consumption of acetylene. The kinetic data for these three reactions is adjusted in the Dayma mechanism. The new kinetic parameters for the Arrhenius equations of the reactions are taken from the Diévart mechanism [73] (Table 7.3).

The Arrhenius equation on itself do not visualise the reaction rate, therefore an Arrhenius plot for the three reactions is given in Figure 7.25. The Arrhenius plots tell us that changing the kinetics of reaction $C_2H_4+H=C_2H_3+H_2$, will lead to less production of acetylene at low temperature, while at high temperature the production will increase. The opposite is seen for reaction $C_2H_3+H=C_2H_2+H_2$. The reaction rate of this reaction is independent from the temperature in the Dayma mechanism, but its reaction rate lowers with temperature in the Diévart mechanism. Nevertheless, the reaction rate in the Diévart mechanism is always higher than in the Dayma mechanism. The effect of changing both reactions is a higher simulated acetylene concentration in the rich MPE flame at atmospheric pressure. The effect of the third assessed reaction $C_2H_3+O=HCCO+H$ is a higher consumption of acetylene over a broad temperature range (Figure 7.25), leading to a higher maximum acetylene concentration in the simulations that decline rapidly.

The combination of changing the three reactions leads to the best result, given in Figure 7.23 as red lines. The maximum simulated concentration of acetylene is decreased by 0.05 mole% compared to the original Dayma mechanism and the consumption in the post flame zone is increased. Nevertheless, some improvement of the acetylene profile can still be achieved.

Besides the acetylene mole fraction profiles, the RCM simulations need also improvement for the two mixtures with a two-step ignition. The ignition delays of the mixtures are overpredicted by the Dayma mechanism (Figure 7.12). In Figure 7.26, the effect of the changes in the $O_2/H_2/CO$ mechanism and the three adjusted reaction regarding the acetylene profile on the ignition delay are given as dashed lines. The mechanism adjustment of the $O_2/H_2/CO$ mechanism leads to a decrease in the simulated ignition delay. An overall improvement with a factor 3 is found. The ignition delays of the MPE mixture with a single-stage ignitions are

still close to the experimental measured ignition delays. Nevertheless, the best fit is now found for the stoichiometric mixture, while with the initial Dayma mechanism it was found for the mixture with an equivalence ratio of 0.5.

The simulations for the ignition delays of the mixtures with a two-step ignition can still be improved. A senstivity analysis is conducted for the mixture at 15 bar and an equivalence ration of 0.5 and the two mixtures with a two-step ignition. The sensitivity analysis on the first mixture will reveal reactions for which the kinetic data should not be adjusted, since adjusting them can deteriorate the performance.

To identify the reactions affecting the ignition delay, a local sensitivity analysis have been conducted on the OH mole at its peak timing with the OpenSMOKE++ software [97, 159]. This method shows very similar results to the ignition delay sensitivity analysis [160]. Different reactions come forward for the mixture with a single-stage ignition and the two-stage ignition mixtures.

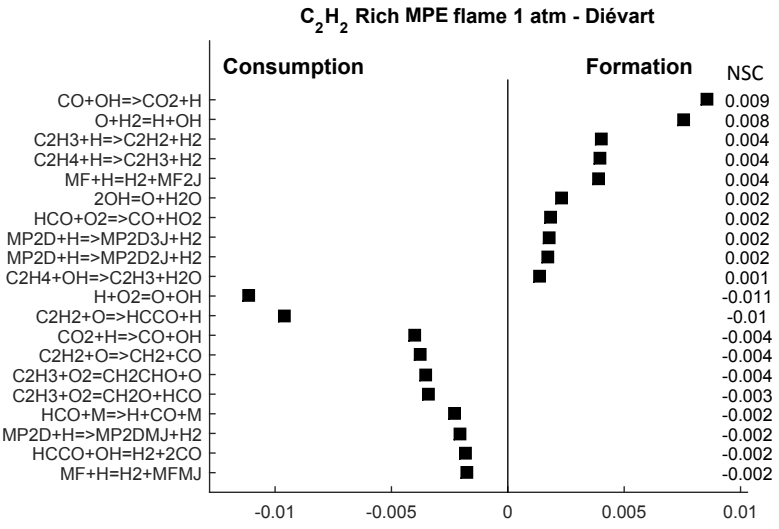

Figure 7.24: The NSC for C_2H_2 in the rich MPE flame at atmospheric pressure simulated by the Diévart mechanism [73].

Table 7.3: The original and adjusted kinetic Arrhenius equation parameters for the three adjusted reactions in the Dayma mechanism to improve the acetylene mole fraction profiles.

	Dayma			Diévart [73]			
	A	b	E_a		A	b	E_a
$C_2H_4+H=C_2H_3+H_2$	1.00E+14	0.00	15009		5.07E+07	1.93	1.30E+04
				REV	1.60E+04	2.436	5.19E+03
$C_2H_3+H=C_2H_2+H_2$	3.00E+13	0.00	0.00		9.64E+13	0.00	0.00
				REV	9.43E+13	0.253	6.92E+04
$C_2H_2+O=HCCO+H$	4.62E+04	2.60	656.00		1.43E+07	2.00	1.90E+03
				REV	2.02E+05	2.00	1.33E+04

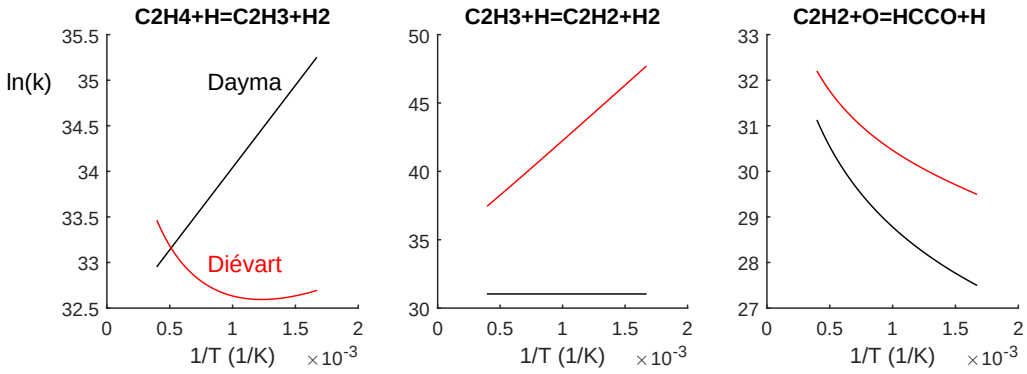

Figure 7.25: The Arrhenius plots for the assessed reactions related to C_2H_2

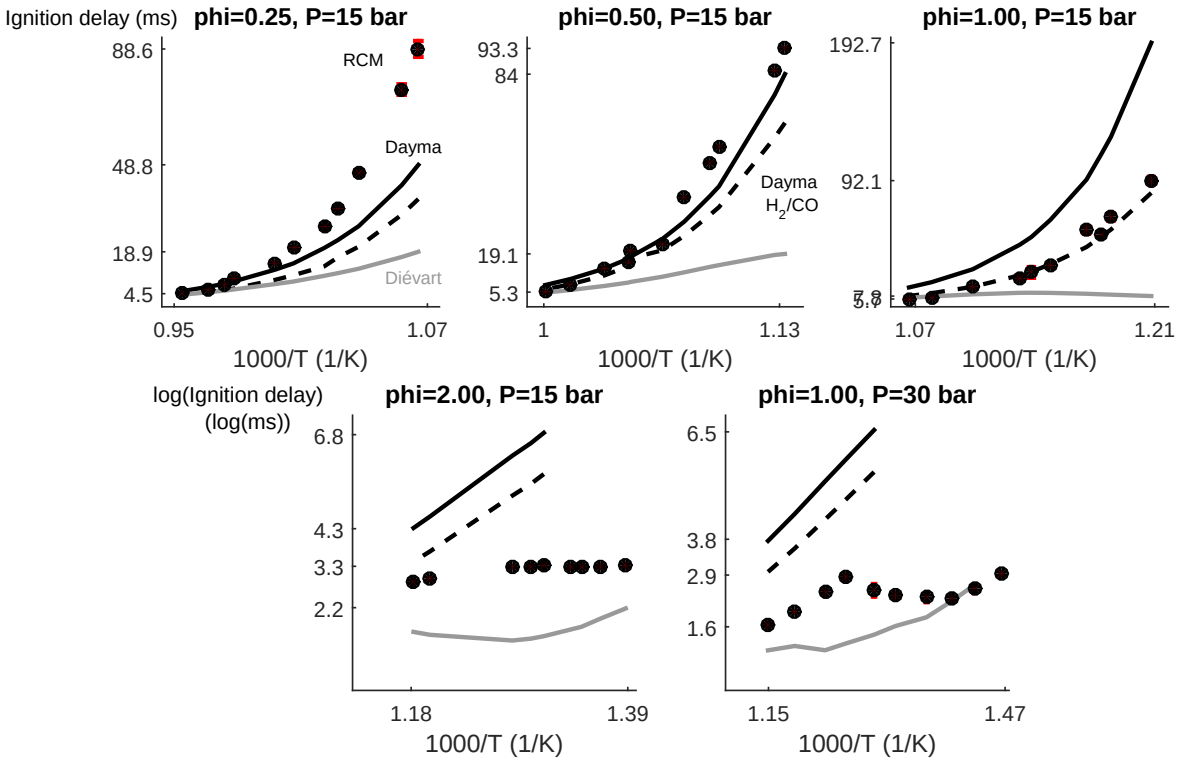

Figure 7.26: The RCM simulations obtained by the improved Dayma mechanisms. The dashed line is the Dayma mechanism with the $O_2/H_2/CO$ kinetics of Keromnes et al. [158] and the **three** reaction regarding the C_2H_2 concentration. Changing the $O_2/H_2/CO$ kinetic data lowers the ignition delays with a factor of 3.

Three reactions of the MPE submechanism delayed the ignition in the two-stage ignition mixture, while in the single-stage ignition mixture the identified reactions did not affect the OH concentration at the ignition. In Table 7.4 the three reactions affecting the OH concentration at ignition in the two-stage mixtures are given, together with their Arrhenius equation parameters found in the Dayma and Diévart mechanism. The Arrhenius plot of the reactions is given in Figure 7.27.

The reactions MPE+HO_2=mpe4j+H_2O_2, MPE+HO_2=mpe3j+H_2O_2 and MPE+HO_2=mpe2j

$+H_2O_2$ from the Dayma mechanism have a higher reaction rate than the related reactions in the Diévart mechanism over a broad temperature range. The simulated ignition delays for a two-stage ignition need to be reduced and therefore the reaction rate of one of the reactions needs to be increased.

Further investigation is needed to check if the reaction rate of the three selected reactions can be increased. No data was found in literature to substantiate an change of the reactions kinetics. Otherwise, the other reactions for which the OH concentration is sensitive should be assessed.

Table 7.4: The original and adjusted Arrhenius equation parameters for the reactions in the Dayma and Diévart mechanism selected to improve the ignition delays found by simulations.

	Dayma			Diévart [73]		
	A	b	E_a	A	b	E_a
MPE+HO_2=mpe4j+H_2O_2	5.60E+12	0.00	1.769E+04	8.19E+03	2.6	13910
MPE+HO_2=mpe3j+H_2O_2	5.60E+12	0.00	1.769E+04	8.19E+03	2.6	13910
MPE+HO_2=mpe2j+H_2O_2	6.40E+03	2.60	1.24E+04	6.14E+03	2.55	10530

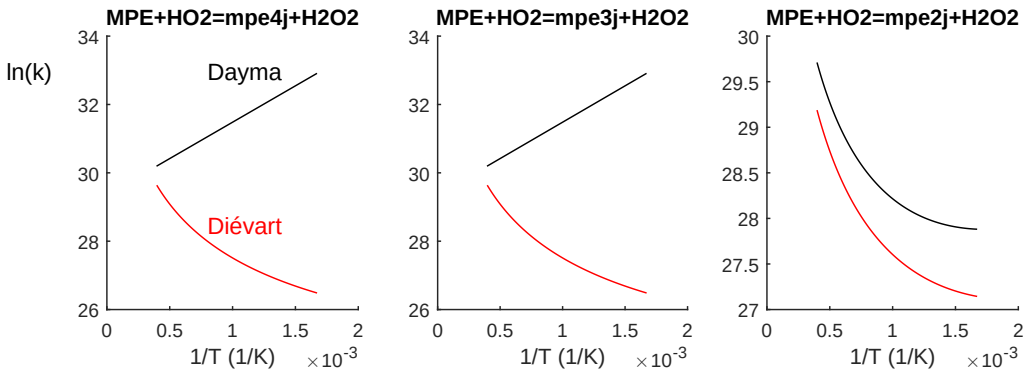

Figure 7.27: The Arrhenius plots for to the assessed reactions related to the two-stage ignition in the RCM

The implementation of the Keromnes $O_2/H_2/CO$ mechanism and the kinetic parameter changes for the three reaction related to the C_2H_2 concentration do improve the mechanism performance. The acetylene concentration in the rich atmospheric MPE flame is improved, while the mole fraction profiles of the other species do not deteriorate. The adjustment of the kinetic data also leads to lower simulated ignition delays, which is positive for the two-stage ignition mixtures.

Before the adjustments can be accepted, the performance of the adjusted Dayma mechanism should be assessed for the other combustion configuration investigated in this work.

7.2.5 Performance of the adjusted Dayma mechanism

The performance of the adjusted Dayma mechanism with the $O_2/H_2/CO$ kinetics taken from Keromnes et al. [158] and the Arrhenius equation parameters changed for the following reactions:

reaction C_2H_4+H=C_2H_3+H_2, reaction C_2H_3+H=C_2H_2+H_2 and reaction C_2H_2+O=HCCO+H, is assessed for the different combustion configurations discussed in this work.

First the adjusted mechanism is used to simulate the experimentally assessed MPE flames at 55 mbar. The changes in the mechanism did not affect the mole fraction profiles of the main species. In Figure 7.28, the effect on the simulated intermediates mole fraction profiles are shown. The initial mole fraction profiles achieved by the Dayma mechanism are shown as black lines, the mole fraction profiles achieved by the adjusted mechanism are shown as blue lines. The difference between both simulations is always smaller than the experimental error on the measured mole fractions. In the lean MPE flame a shift of the mole fraction peak is visible, but overall both mechanism are capable to simulate the laminar flat flames at 55 mbar.

The adjusted mechanism is also applied for the simulations of MPE mixtures in a JSR. The results of the simulations with both the initial and adjusted Dayma mechanism are given in Figure 7.29. The main differences between the mechanisms results are found in the H_2 mole fraction profile for all three mixtures and the CO and CO_2 mole fraction in the lean flame at high temperatures. Adjusting the kinetic data, leads to a faster consumption of the fuel as a function of the temperature, especially in the lean flame. Nevertheless, the adjusted mechanism can predict the mole fraction peaks of intermediates like mp2d and CH_2O correctly.

The laminar flame velocities for mixtures with an equivalence ratio of 0.79, 1.12 and 1.43 is also simulated by the adjusted Dayma mechanism and this for the initial condition of 353 K and 1 bar. The achieved laminar velocities are given in Table 7.5. The laminar velocities simulated by the initial Dayma mechanism lie within the experimental uncertainty of the measured value. Two of the three laminar flame velocities achieved by the adjusted Dayma mechanism are also within the uncertainty range. The third value, related to an equivalence ratio of 1.43 lies 0.6 $cm \cdot s^{-1}$ outside the uncertainty interval. The laminar flame velocities of more mixtures should be checked before drawing a conclusion about which mechanism performs best.

In addition, the adjusted mechanism can simulate all the investigated combustion configurations sufficiently. Nonetheless, there is still room for improvement of the kinetic mechanism. The consumption of acetylene in rich flames can be improved. Acetylene is a precursor for poly-aromatic hydrocarbons and soot, so the addition of a soot submechanism can lead to an improvement since it will increase the consumption of acetylene. Next, there are difference between the thermodynamic data of the Dayma and Diévart mechanism, which can have an effect of the kinetics. Therefore, the consistency of the thermodynamic data need to be checked and a mathematical optimisation of the kinetic mechanism can be conducted. The experimental ignition delays in the two-stage ignition mixtures are not in agreement with the simulated values and further research is also needed.

Therefore, the adjustments proposed for the Dayma mechanism are the implementation of the kinetic data for the $O_2/H_2/CO$ mechanism proposed by Keromnes [158] and the adjustment of the Arrhenius equation parameters of three reactions related to the C_2H_2 profile. In the end, a better simulated mole fraction profile of C_2H_2 in the rich MPE flame at atmospheric pressure is achieved, while the mole fractions of other species do not deteriorate.

The achieved adjusted MPE mechanism can be used to simulated laminar flat flames, mole fractions in JSR, laminar flame velocities and the ignition delays obtained in RCM for single-ignition mixtures. The performance of the adjusted Dayma mechanism for the oxidation of MPE is better than the mechanisms proposed by Diévart and Korobeinichev, since it is capable to capture the ignition delays of single-ignition mixtures better.

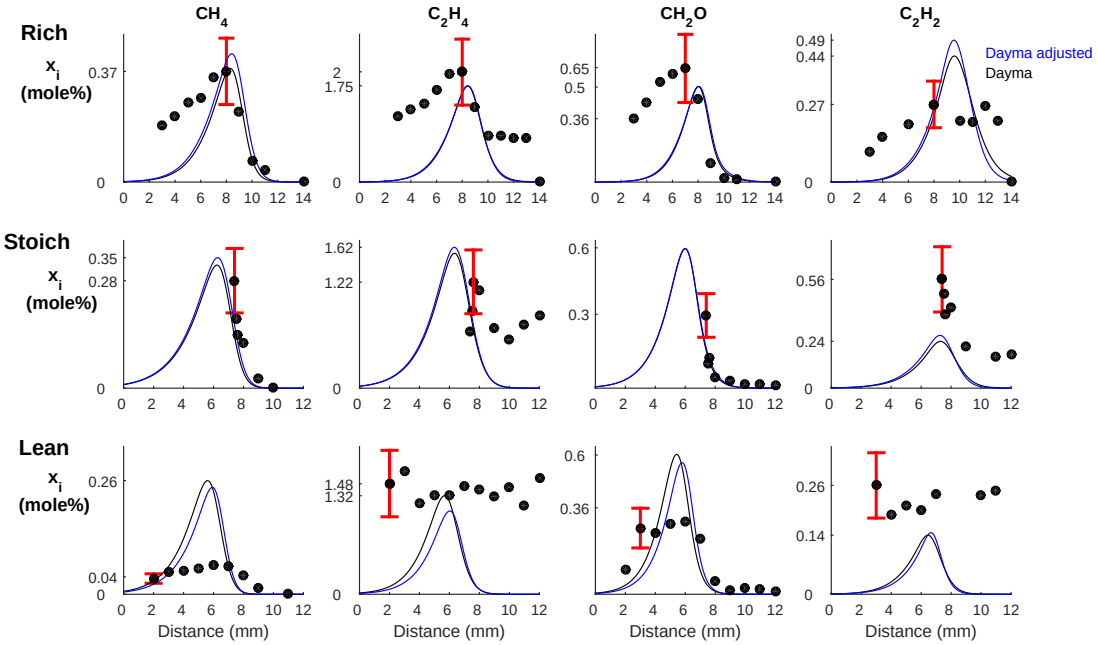

Figure 7.28: The improved Dayma model is used to simulate the MPE flames at 55 mbar. The improved Dayma model (blue lines), has the same performance as the orginal Dayma mechanism (black lines) in capturing the intermediate species mole fraction profiles.

Table 7.5: Experimental laminar flame velocities S_u^0 for the mixture of MPE and air at atmospheric pressure and a initial temperature of 353 K for an equivalence ratio of 0.79, 1.11 and 1.43. The uncertainty on the experimental data is 2 cm s^{-1}. The laminar flame velocity is simulated by the Dayma mechanism and the adjusted Dayma mechanism. The performance of both mechanisms is sufficient. Only for the rich mixture the simulation with the adjusted mechanism lies outside the experimental uncertainty range.

ϕ	S_u^0 experimental (cm s^{-1})		S_u^0 Dayma (cm s^{-1})		S_u^0 Dayma adjusted (cm s^{-1})	
0.79	29.98	±2	28.30	(-5.6%)	30.11	(+0.4%)
1.12	41.12	±2	41.78	(+1.6%)	40.45	(-1.6%)
1.43	25.94	±2	26.79	(+3.3%)	23.39	(-9.8%)

7.3 Conclusion

To assess the performance of the proposed kinetic mechanism for the combustion of MPE, experimental data over a broad pressure and temperature range and different combustion configuration is needed. Besides the experimentally investigated laminar flat flames, data from literature or other research institutes is used.

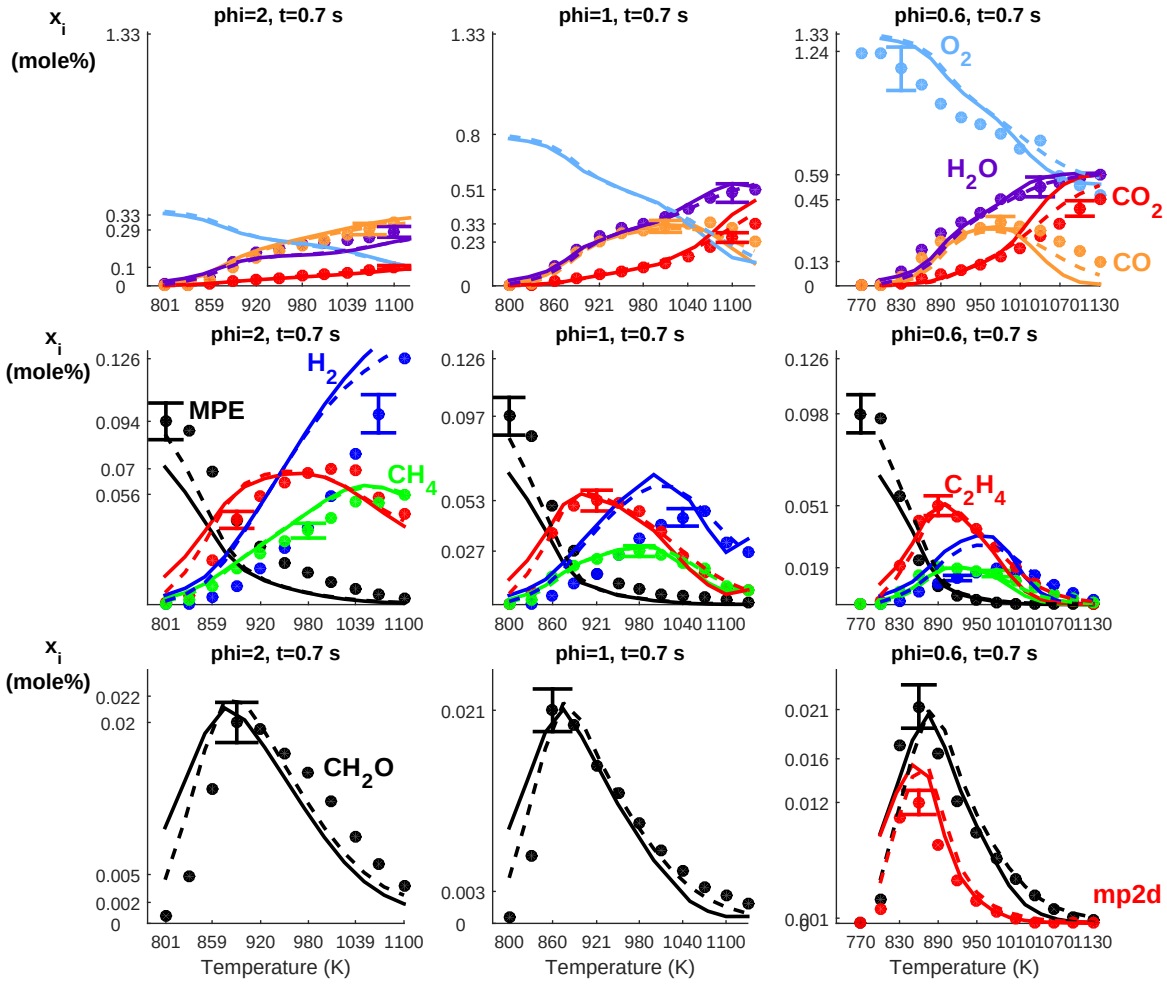

Figure 7.29: The simulations for the JSR experimental data achieved by the original Dayma mechanism (solid lines) and the adjusted Dayma mechanism (dashed lines). The performance of both mechanism differs the most in the lean mixture at high temperatures. The combustion kinetics is more temperature dependent in the adjusted mechanism. Also higher H_2 levels are achieved by the adjusted mechanism.

Experimental data obtained by [72] for a stoichiometric (ϕ=1.00) and a rich (ϕ=1.50) flat MPE flame at a pressure of 27 mbar and atmospheric pressure were compared to simulations with the proposed MPE mechanism. A difference between simulated and experimental C_2H_2 was found for the rich MPE flame at atmospheric pressure. For the stoichiometric flame at 27 mbar the concentrations of CO_2 and H_2O does not comply with the simulated values. Since for all the other flames the concentration are correctly simulated, it is assumed that experimental error is the reason for the misfit in the stoichiometric flame. More stable intermediate species could be measured by the used experimental setup in [72], like mp2d and mb3d, compared to the measurements conducted in this work. The mole fraction profiles for most of the intermediate species were calculated well by the mechanism. Only for acetylene (C_2H_2), a mismatch was found.

Data obtained in a JSR for the combustion of MPE at a pressure of 10 bar is used to validate the mechanism in the high pressure region. The mole fraction profiles of eleven stable

intermediates are measured in a JSR as a function of the temperature. Mixtures with different equivalence ratios (2, 1 and 0.6) and a mean residence time τ of 0.7 s are assessed. The combustion was simulated by OpenSMOKE. The simulated results capture the experimental data perfectly. Most of the simulated profiles are within the experimental uncertainty of 10% on the measured moles fractions.

The third combustion configuration for which experimental data is assessed, is a SCC wherein laminar flame velocities can be measured. Laminar flame burning velocities of MPE/N_2/O_2 mixtures were measured as a function of the equivalence ratio, ranging from 0.7 to 1.4. The measurements are done at pressures of 1 and 3 bar for different initial temperatures. The experimental results could be simulated very well, only at lean equivalence ratios the laminar flame velocity was underpredicted.

The last assessed combustion configuration is a RCM. Weber et al. [74] investigated the ignition delay of MPE mixtures with different equivalence ratio at pressures of 15 and 30 bar in a RCM. The ignition delays of the mixtures with a single-step ignition are predicted well by the proposed mechanism. However, the ignition of two-step ignition mixtures could not be reproduced by the mechanism.

Four species with a mismatch between experiments and simulations have been selected to assess if changes in the kinetic data of the mechanism could improve their simulated profiles. The selected species are C_2H_2, mp2d, mb3d and mp. Some reactions were selected according to a reaction flow analysis and a sensitivity analysis.

The mole fraction profiles of acetylene are not affected by reactions of the MPE submechanism added to the methyl butanoate mechanism of Fisher [107]. They are affected by the kinetics of the O_2/H_2/CO reactions. Therefore, the kinetic data from the Fisher mechanism is adjusted by recently published reaction kinetics. The implementation of the new reaction kinetics improved the acetylene profile in the rich MPE flame at atmospheric pressure, without affecting the other mole fraction profiles in a negative way.

The concentration profiles of mp2d, mb3d and mp are sensitive to reactions of the MPE submechanism. However, no selected reaction could improve the mole fraction profiles. Adjustments in the kinetic data also lead to deterioration of the mole fraction profiles of other species, or of the same species at a different pressure. The implementation of the new reaction kinetics for O_2/H_2/CO did not affect the mole fraction profiles of the assessed species.

In the end an adjusted MPE kinetic mechanism is achieved, wherein the O_2/H_2/CO kinetics is updated by recently published work and the prediction of the acetylene concentration is improved, just as the two-stage ignitions data achieved in a RCM. The obtained mechanism can predict the ignition delays of single-step ignition mixtures correctly, which makes it perform better than the MPE mechanism which are already published.

Further work can focuss on the improvement of the mechanism regarding the ignition delay of two-step ignition mixtures. The kinetic parameters of the reactions identified by the sensitivity analysis should be investigated in more detail. Also the completeness of the MPE submechanism should be checked, maybe some reaction are still missing. The addition of a poly-aromatic hydrocarbons (PAH) submechanism could be assessed, to improve the consumption of acetylene. The pressure dependency of the reaction in the MPE submechanism could also be assessed, since for some intermediates the performance of the mechanism is related to pressure.

Part II

Energy and Emission Analysis of Triacetin as biofuel

8

Part II Introduction

Triacetin is a tri-ester formed by the esterification of glycerol with acetic acid. It can be used as biofuel in diesel engines, since its chemical properties comply with diesel [161, 162]. Glycerol is formed as the coproduct in the biodiesel production and is seen as a waste stream, since its value has decreased drastically due to overproduction [163].

The production of triacetin from cheap glycerol is related to the biodiesel production. Therefore, the conventional biodiesel production is described in Chapter 9. Biodiesel from the first generation is mostly made from edible oils, which is not sustainable in different ways. The use of edible oil as fuel is not ethical and the land use change related to the feedstock production can lead to a negative effect on the Green House Gases (GHG) emissions [164]. A change of feedstock could solve these disadvantages of biodiesel. Currently, other biodiesel feedstocks like Waste Cooking Oil (WCO), non-edible oils and micro-algal oils, are investigated. The potential of micro-algae as feedstock is investigated in Chapter 9. The change in feedstock does not affect the transesterification reaction and glycerol is still formed as byproduct. The legislation about biofuels and the fuel standards they need to comply with are also discussed in Chapter 9, since they affect the future of the industry.

Different production pathways for triacetin are described in literature. Triacetin can be achieved by direct interesterification of the triglyceride with methyl acetate, or glycerol is first formed by transesterification and then esterified with acetic acid. The literature data on both production pathways is given in Chapter 10. Additionally, the use of triacetin as fuel additive in diesel engines is discussed in this chapter.

In Chapter 11 the energy needed to produce triacetin by the different production pathways is assesed and compared to the biodiesel production from micro-algae. The system boundaries are set around the production of the needed reactant (methanol, methyl acetate and acetic acid), the heating during the equilibrium reaction, the recovery of the excess reactant and the energy content of the produced biofuel. These processes are selected, since they differ between the production pathways due to the different reactant used. They are also assumed to be the most energy demanding. The uncertainty on the results are assessed by a Monte Carlo analysis and the sensitivity to the different parameters is quantified by NSC. Finally, the Normalised Net Energy Value (NNEV), the ratio of the energy needed for production and the energy content of the produced biofuel, is calculated for the four assessed production routes: the biodiesel (BD) scenario, the catalytic interesterification (IRc) scenario, the enzymatic interesterification (IRe) scenario and the esterification reaction of glycerol (ER) scenario. The highest NNEV is found for the BD scenario. Positive NNEV values are also found for the IRe and ER scenarios. The IRc scenario results in 14% of the simulations in negative NNEV, which means that more energy is needed to produce the biofuel than the energy content of the biofuel itself. The negative NNEV values are related to the high excess ratio of methyl

acetate that is needed in the IRc scenario.

Not only the energy balance is of importance regarding biofuels, also the reduction in GHG emissions plays a role. In Chapter 12 the reduction in GHG is calculated for the assessed production pathways. All the assessed production pathways lead to a reduction in GHG emissions. The greastest reduction is found for the BD scenario, 65 g $CO_{2,eq}$ per MJ fuel on average. The triacetin coproduction scenarios have a lower GHG reduction due to their higher energy demand for production. Also relatively more fuel is produced by the triacetin coproduction, than the achieved relative reduction in GHG, which means that the coproduction of triacetin cannot have a greater GHG reduction than the BD scenario, if the reduction is expressed in g $CO_{2,eq}$ per MJ fuel.

9

Current biodiesel production

Biodiesel is traditionally produced from vegetable oils via transesterfication (Figure 9.1). Untreated vegetable oils have a high viscosity and low volatility, which makes them unsuitable for internal combustion (IC) engines. Therefore the chemical properties of the vegetable oils need to be changed so they can be used directly in IC engines. Different methods can be applied to alter the oil, one of them is transesterification, others are pyrolysis, dilution and micro-emulsion. Nevertheless, via transesterification better quality fuel, biodiesel, with a good yield is achieved and therefore it is commonly used [165]. The legislation about biofuels is affecting their production industry and the implementation goals imposed by the European Union are given in Section 9.1.

The conventional biodiesel process is explained in detail in Section 9.2. The different feedstock and the reaction parameters are discussed, just as the achieved biodiesel yields for different situations and their use in conventional diesel engines. The feedstock for conventional biodiesel production is vegetable oil. However, to fulfill the demand for biodiesel production, natural land is converted to agricultural land. This land use change leads to an additional emissions of GHG, which has a negative effect on the CO_2 neutrality of biofuels. The neutral CO_2 emissions of biofuels are their main advantage compared to conventional fuels and the reason why they are produced to fight climate change. Without a reduction in CO_2 emissions, biodiesel is not sustainable and therefore other feedstocks are gaining interest.

One of them are micro-algae. Micro-algae can produce triglycerides, the main component of vegetable oil, under specific growth conditions. The conditions for algal growth, the strain selection and the biodiesel production from algal biomass are described in Section 9.3. Once the composition of the biodiesel derived from micro-algae is determined, it can be used for the further calculations of the NNEV and GHG-reduction for the different production routes in Chapter 11 and 12.

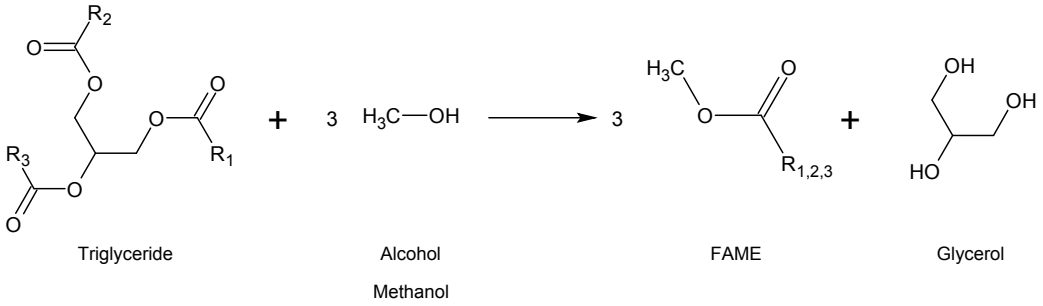

Figure 9.1: During the transesterification process, the triglyceride reacts with 3 moles of methanol to form 3 moles FAME and glycerol

9.1 Legislation

The European regulations concerning biodiesel are formulated in three Directives. The first Directive (2003/30/EC) implied a percentage of 5.75% biofuels and other renewable fuels in the transport sector by 2010 [166]. In 2009 the Renewable Energy Directive (RED, 2009/28/EC) was composed to continue the introduction of renewable energy. The RED sets an overall binding target of 20% renewable energy derived from biomass, hydro-, wind or solar power by 2020. As part of this total effort, at least 10% of the used transport fuel in the member states must come from renewable sources [167].

Next to the target goals, the RED introduced also sustainability criteria, since there are concerns about the actual GHG savings of biodiesel and the use of food crops as biofuel feedstock. To meet the sustainability criteria nowadays, a GHG saving of 35% is required, which will be increased to 60% in 2018. Social consequences such as food prices must be taken into account and land with high biodiversity value or high carbon stock may not be used as agricultural land for biofuel feedstock production [167].

The Fuel Quality Directive (2009/30/EC) refers to the European standard for biodiesel (EN 14214). This standard dictates the chemical characteristics that the biodiesel must meet and influences hereby possible future options regarding feedstock and product quality [168]. In the United States, another biodiesel standard is in force, namely ASTM D6751 [169]. This standard differs slightly from the European one. Both are given in Table 9.1 [161, 162].

Recent proposals for new European legislations limits the percentage of first generation biodiesel to 5% of the 10% renewable energy target set by the RED. The mean incentive for this, are new insights about the sustainability of first generation biodiesel in terms of GHG emissions. The European biodiesel production cannot meet the demand, therefore import of biodiesel is needed and countries such as Indonesia and Malaysia are converting nature to farmland, so they can export biodiesel or vegetable oils to Europe. This phenomenon converting nature to agricultural land causes a long-term GHG emission increase, which nullifies the main advantage of biofuels, that they are GHG-neutral [164]. In the future the Indirect Land Use Change (ILUC) will be considered when assessing the GHG performance of biofuels. The European Commission implements this legislation to provide market incentives for biofuels with no or low ILUC and GHG emissions, in particular second and third generation biofuels produced from feedstock like algae, straw and waste.

Besides the legislative aspect, the economical aspect has a strong influence as well on the development of new productions processes. The production of biodiesel is still more expensive than the production of fossil diesel, largely explained by the expensive feedstock and the low economic value of the byproduct crude glycerol [164, 163].

To enhance the biodiesel industry and make it a part of the future energy mix, a cheaper feedstock and new applications for the byproduct glycerol are needed. Due to regulations and economical aspects, first generation biofuels are no longer practicable. A switch to less valuable feedstock such as Waste Cooking Oil WCO, non-edible oils or micro-algal oil will be necessary to achieve sustainable biodiesel. In addition, a solution for the formed crude glycerol excess must be found.

As a solution for the glycerol overproduction, the use of triacetin produced from crude glycerol as biofuel is assessed in the next chapters. The different production routes are assessed to check if triacetin could be a viable solution in energy terms. Also the reduction in GHG-emissions is checked, to see if the 60% savings imposed by the European legislation from 2018 is realistic.

Table 9.1: The EN 14214 and D6751-09 standards for biodiesel [161, 162]

Property	Unit	EN 14214 Limits		D6751-09 Limits	
		Lower	Upper	Lower	Upper
Ester content	%(m/m)	96.5	-		
Cetane number		-	51	-	47
Density at 15°C	kg/m^3	860	900		
Viscosity at 40°C	mm^2/s	3.50	5.00	1.9	6
Flash point	°C	101	-	93	-
Sulfur content	mg/kg	-	10.0	-	15.0
Carbon residue (on 10% distillation residue)	%(m/m)	-	0.30	-	0.05
Sulfated ash content	%(m/m)	-	0.02	-	0.02
Water content	mg/kg	-	500		
Total contamination	mg/kg	-	24		
Copper strip corrosion (3h at 50°C)	rating	Class 1		up to Class 3	
Oxidation stability, 110°C	hours	6.0	-	3.0	-
Acid value	mg KOH/g	-	0.50	-	0.50
Iodine value	g iodine/100g	-	120		
linolenic acid methyl ester	%(m/m)	-	12.0		
Polyunsaturated methyl esters	%(m/m)	-	1		
Methanol content	%(m/m)	-	0.20	-	0.20 or flash
		-		-	point 130°C
Monoglyceride content	%(m/m)	-	0.80		
Diglyceride content	%(m/m)	-	0.20		
Triglyceride content	%(m/m)	-	0.20		
Free glycerol	%(m/m)	-	0.02	-	0.02
Total glycerol	%(m/m)	-	0.25	-	0.24
Groups I methals (Na+K)	mg/kg	-	5.0	-	5.0
Groups II methals (Ca+Mg)	mg/kg	-	5.0	-	5.0
Phosphorus content	mg/kg	-	4.0	-	10.0
Cold Filter Plugging Point (CFPP)	°C	according to climate zone			
Cloud Point (CP)	°C			according to climate zone	
Water content		500 mg/kg	-	0.05% volume	- (+sediment)

9.2 Conventional biodiesel production

Currently biodiesel is produced on a large economical scale. The biodiesel production in the US was 149 million gallons or 564 million liters in August 2017. In total 513 million kilogram of feedstocks was used to produce the biodiesel in August 2017 alone. Soybean oil remained the largest biodiesel feedstock with 276 million kilograms consumed [170].

Numbers for the production of biodiesel in Europe are available for 2016. An increase of only 0.93% was found compared to 2015. The European biodiesel production had a relapse in 2011, however by 2013 the production is recovered and increases steadily since. The numbers for some European countries and the total production are given in Table 9.2 for 2016. The production capacity of Belgium is estimated to be 846 Mkg in 2017 [171]. The production of biodiesel is related to the coproduction of glycerol. The mass of the produced glycerol is about 10% of the weight of the produced biodiesel [163], which is 1 158 Mkg in Europe yearly. The glycerol stream is substantial and a sustainable application for the crude glycerol is needed.

The fuel properties of the biodiesel are related to the Fatty Acid (FA) composition of the triglyceride feedstock. Different sources of triglycerides result in a variation of FA composition in the reaction mixture and fuel properties. In the following sections, the different feedstock of edible and non-edible oil are discussed.

The yield of the conventional biodiesel production depends on the reaction parameters, like the temperature, the catalyst loading and the alcohol to oil molar ratio. Different catalyst can be used to facilitate the transesterfication reaction. Alkaline, acidic or enzymatic catalysts are the most common. The influence of the feedstock quality, catalyst, alcohol etc. on the biodiesel yield are discussed in the next sections, together with the needed upgrading steps and the engine performance of biodiesel.

Table 9.2: The biodiesel production in some European countries in 2016, together with the total European biodiesel production [171]

Country	**Biodiesel produced (Mkg)**
Germany	3 017
France	1 703
Netherlands*	1 389
Spain	1 105
Poland	779
Italy	503
Belgium	459
Finland*	428
Denmark/Sweden	421
Austria	302
Total	11 576

* Data include Hydro-diesel production

9.2.1 Feedstock for biodiesel

The process can use a wide range of vegetable oils as feedstock. More than 350 crops are identified from which vegetable oil can be produced. The oil is mostly found in the seeds of the plant, the rest of the biomass is useless for the biodiesel production. The most commonly used edible oils are from soybeans, rapeseed, sunflower seeds, palm kernel, etc. Non-edible oils can be produced from *Jatropha curcas*, cotton seed, Jojoba, Moringa, etc. [172]. The feedstock accounts for 75 to 80% of the total cost of the biodiesel production. The other main costs are the chemicals needed (alcohol and catalyst) and the depreciation of the plant [164, 172].

The oil in the crops need to be extracted. The extraction method can be mechanical, enzymatic or a solvent can be used. Using a mechanical press to extract the oil is the most convential method. A scew press can extract 68 to 80% of the oil. The extracted oil need to be filtered and degummed. Enzymes can extract the oil from the crushed seeds. However, the long process time is the main disadvantage of this technique. The solvent extraction of oil is affected by the particle size, the type of solvent used, the temperature and the agitation of the solvent. Possible solvent extraction are hot water extraction, soxhlet extraction or ultrasonication technique [172].

All vegetable oils have the same chemical structure: a glycerol backbone esterified with three FA. This chemical structure is called a triglyceride. The FA have mostly 16 to 18 C-atoms and can be saturated or (multiple) unsaturated (Table 9.3). In Table 9.4 an overview of the fatty acids in commonly used edible and non-edible vegetable oil is given [173]. It is clear that fatty acids with 16 or 18 carbon in their chain are the most common.

The annual production yield differs between the different feedstocks and is given in Table 9.5 for some of the main edible and non-edible feedstocks [172]. *Jatropha curcas*, palm oil, rapeseed and Jojoba have a high yearly production and the crops contain a lot of oil. Especially, palm oil seems a good feedstock. However, it is edible and its production is affected by ILUC. Atabani et al. also gives some oil yields for micro-algae with different oil contents. Even for the micro-algae with the lowest oil content an annual yield ten times higher than palm oil is found. Nevertheless, these values are estimations based on small scale data [172].

Mata et al. gives some more detailed numbers about the oil production of micro algae [174]. The numbers for Chlorella vulgaris, Nannochloropsis sp. and Tetraselmis seucica are stated in Table 9.5. They show that lower oil content and oil yield are more likely in reality due to variable and suboptimal growing conditions.

WCO and animal fats are also suitable and are cheaper feedstocks [175]. The difference between the edible oils and the cheaper substitute is the percentage of Free Fatty Acid (FFA) and unsaturated FA. WCO and animal fats can contain high concentrations of FFA, which can cause saponification in the presence of water. Other impurities found in the vegetable oil are phospholipids, sterols and water [176, 177].

9.2.2 Reaction conditions for transesterification

The yield of the biodiesel production is affected by FFA content of the feedstock, the applied Alcohol to Oil Ratio (AOR), the catalyst and its concentration, the reaction temperature and the reaction time [178]. The effect of all these process parameters on the biodiesel yield is discussed in the sections below.

Table 9.3: Most common fatty acids in vegetable oil [179]

Trivial name	**Systematic name**	**CN:DB**[a]	**Structure**
Unsaturated fatty acids			
Lauric acid	Dodecanoic acid	12:0	$CH_3(CH_2)_{10}COOH$
Myristic acid	Tetradecanoic acid	14:0	$CH_3(CH_2)_{12}COOH$
Palmitic acid	Hexadecanoic acid	16:0	$CH_3(CH_2)_{14}COOH$
Stearic acid	Tetradecanoic acid	18:0	$CH_3(CH_2)_{16}COOH$
Arachidic acid	Hexadecanoic acid	20:0	$CH_3(CH_2)_{18}COOH$
Saturated fatty acids			
Oleic acid	cis-9-Octadecenoic acid	18:1	$CH_3(CH_2)_7CH{=}CH(CH_2)_7COOH$
Linoleic acid	9,12-Octadecadienoic aicd	18:2	$CH_3(CH_2)_4(CH{=}CHCH_2)_2(CH_2)_6COOH$
Linolenic acid	6,9,12-Octadecadienoic aicd	18:3	$CH_3CH_2(CH{=}CHCH_2)_3(CH_2)_6COOH$
Arachidonic acid	5,8,11,14-Eicosatetraenoic acid	20:4	$CH_3(CH_2)_4(CH{=}CHCH_2)_4(CH_2)_2COOH$

[a] CN is the number of carbon atoms in molecule, DB is the number of double bond between carbon atoms.

Table 9.4: Oil composition of non-edible and edible oils [173].

Fatty acid composition (%)	Non-edible oil					Edible oil		
	Jatropha	Rubber	Castor seed	Pongamia	Sea mango pinnata	Soybean	Palm	Rapeseed
Oleic	43.1	24.6	3.0	44.5-71.3	54.2	23.0	40.0	64.1
Linoleic	34.3	39.6	4.2	10.8-18.3	16.3	51.0	10.0	22.3
Palmitic	14.2	10.2	1.0	3.7-7.9	20.2	10.0	45.0	3.5
Stearic	6.9	8.7	1.0	2.4-8.9	6.9	4.0	5.0	0.9
Linolenic	-	16.3	0.3	-	-	7.0	-	-
Eicosenoic	-	-	0.3	9.5-12.4	-	-	-	-
Ricinoleic	-	-	89.5	-	-	-	-	-
Dihydroxystearic	-	-	0.7	-	-	-	-	-
Palmitoleic	-	-	-	-	-	-	-	0.1
Others	1.4	-	-	-	2.4	-	-	9.1

Alcohol to oil molar ratio

The transesterfication reaction can be done with any kind of alcohol. However, only methanol and ethanol are cheap enough to be used. Mostly methanol is used, which is currently produced from fossil fuels and is not a sustainable choice. Ethanol on the other hand is more expensive, but its production from biomass is already a mature industry. Besides the transesterification reaction with ethanol is more complex and a higher alcohol to oil ratio is needed [180]. The transesterification reaction is a sequence of three equilibrium reactions and to increase the biodiesel yield more methanol than stoichiometrically needed (3:1) is added. The AOR needs to be higher than 6:1 to terminate the reaction. Optimal AOR lies between 9:1 and 12:1 [176].

Nevertheless, higher alcohol to oil molar ratios can have a negative effect on the yield. The excess methanol can emulsify the formed biodiesel and glycerol, aiding the recombination of glycerol and the esters to triglycerides [178]. The separation of glycerol is also more difficult by high AOR since the solubility of glycerol increases [176].

Table 9.5: The estimated oil content for some feedstocks together with their annual productivity [172, 174]

Feedstock	Oil content (%)	Oil yield (L/ha/year)
Jatropha *curcas*	Seed: 35-50	1892
	Kernel: 50-60	
Soybean	15-20	446
Sunflower	25-35	952
Palm oil	30-60	5950
Rapeseed	38-46	1190
Cottonseed	18-25	325
Jojoba	45-50	1818
Microalgae (low oil content)	30	58 700
Microalgae (medium oil content)	50	97 800
Microalgae (high oil content)	70	136 900
Chlorella vulgaris	5-58	1 160 - 23 400
Nannochloropsis sp.	12-53	9 250 - 119 200
Tetraselmis suecica	8.5-23	65 500 - 185 500

Free fatty acid and water content

The concentration of FFA in the feedstock determines the type of catalyst that can be used. Soap can be formed if FFA are present, reducing the activity of a homogeneous alkaline catalyst. The use of an alkali catalyst is limited to oils with a FFA value lower than 3%. The FFA also has a negative effect on the biodiesel yield [176, 175, 181].

The acid value of biodiesel is a measure for the FFA content. It is the mass of potassium hydroxide (KOH) that is required to neutralise the oil and should be lower than 0.50 mg KOH per gram of biodiesel to comply with the European legislation (Table 9.1). In some feedstock the FFA content is higher than legally admitted and therefore the FFA have to be removed. They can be esterified to biodiesel, using an acid catalyst [182].

The water content of the feedstock is limited for the same reason, it increases the risk of saphonication if a alkaline catalyst is used and the emulsification of the glycerol and biodiesel phase [183]. However, if a enzymatic catalyst is used, the mixture need to contain some water to activate the enzyme [180].

Catalyst

The vegetable oil is immiscible with the used alcohol, due to the difference in polarity. There are different ways to overcome the problem: a catalyst can be used, the two phases can been stirred vigorously or the reactant can be added in supercritical state. Four types of catalyst can be used: an base catalyst, an acidic catalyst, an enzyme or a heterogeneous catalysts, which can be alkaline or acidic [176]. Alkaline homogeneous catalysts include catalysts such as NaOH, $NaOCH_3$, $KOCH_3$, KOH, NaMeO and K_2CO. This kind of catalyst is mainly used in the industrial production and more specific sodium hydroxide (NaOH) and potassium

hydroxide (KOH) are widely used. Methoxides as catalysts result in a better yield but are more expensive. Examples of acidic catalysts are sulfuric, hydrochloric, ferric sulfate, phosphoric and organic sulfonic acid.

The main advantage of an alkaline catalyst compared to an acidic one is the greater enhancement of reaction rate. Moreover, this method can achieve high purity and biodiesel yield in a short time (30 to 60 minutes), while with an acidic catalyst also high yields can be obtained but the reaction is slow (3 to 48 hours).

The use of alkaline catalysts is restricted to vegetable oils with low FFA contents. Acidic catalyst can be used to reduce the FFA content to a level safe enough for alkaline transesterification. Other drawbacks of the reaction catalysed by a homogeneous alkaline catalyst are the high energy requirements and the difficult recovery of glycerol and catalyst. The waste stream contains crude glycerol and catalyst and must be neutralized. The purification of this neutralized stream consumes high quantities of water for wet washing to remove the salt, the neutralised catalyst, and energy for removing the excess water added by the washing steps.

The reaction mechanism of the biodiesel production depends on the catalyst used. By an alkali-catalyzed transesterification reaction the catalyst reacts with the alcohol, forming an alkoxide and water. The nucleophilic alkoxide attacks the carbonyl group of the triglyceride and a tetrahedral intermediate is formed, from which the alkyl ester (FAME) and the corresponding anion of the diglyceride is generated (Figure 9.2). The diglyceride deprotonates the catalyst, regenerating its activity. The same mechanism causes the formation of monoglyceride and eventually glycerol [176].

With an acidic catalyst the carbonyl group is protonated, which leads to carbocation. The nucleophilic alcohol can attack the positive carbon and a tetrahedral intermediate is produced. This intermediate eliminates the diglyceride to form a new ester and to regenerate the catalyst (Figure 9.3). The mechanism is the same for the three reversible reactions [176].

The concentration of the catalyst has also an effect on the biodiesel yield. Adding a catalyst improves the formation of biodiesel, but the amount needs to be sufficient. Rathore et al. found out that when KOH concentration is increases from 2% to 12%, the biodiesel yield increased from 20% to 95% [184]. However, emulsions are formed if an excessive amount of catalyst is added. This leads to an increase in viscosity, which makes the recovery of the biodiesel more difficult [178].

To remove alkaline homogenous catalysts from the formed biodiesel, excessive washing is needed. This process is energy, water and time consuming and still the catalyst cannot be reused. Replacing the homogenous alkaline catalyst with a heterogeneous, solid catalyst can eliminate the need of the washing steps. The heterogeneous catalyst can be filtered off from the reaction medium and can be reused multiple times. Heterogeneous alkaline catalysts are alkaline earth metal oxides, zeolite, KNO_3 loaded on Al_2O_3, KNO_3/Al_2O_3, BaO, SrO, CaO, MgO etc. Heterogeneous acid catalysts do also exist and are able to catalyse the reaction of both triglycerides and FFA to FAME. Examples of heterogeneous acid catalysts are SO_4^{2-}/SnO_2, Amberlyst-15, ZrO_2/SO_4^{2-}, ZrO_2/WO_3^{2-} etc. [185]. High biodiesel yields can be achieved by the use of both heterogeneous catalysts (Table 9.7) [64].

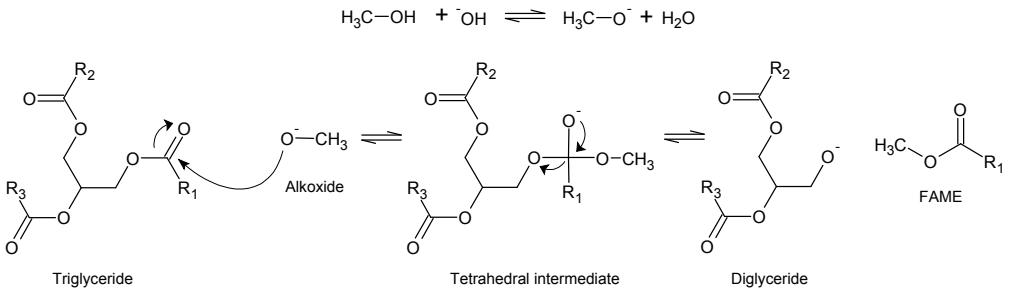

Figure 9.2: Mechanism of the alkaline-catalyzed transesterification

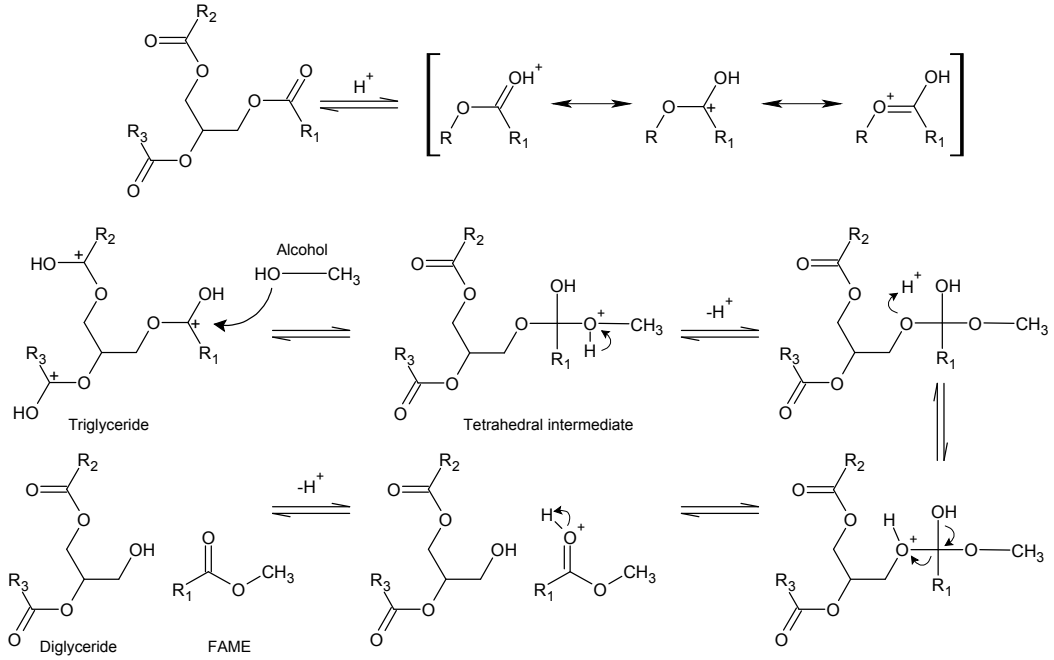

Figure 9.3: Mechanism of the acid-catalyzed transesterification

A fourth option to catalyse the transesterfication reaction is to use enzymes. Lipases can catalyse both the transesterification reaction as the esterification of FFA, which makes them usable for a wide range of feedstocks. Since they don't form soaps, subsequent washings steps are not needed, which reduces the energy need and the cost of the overall process. The product separation is also easier with lipases and a higher quality of glycerol is obtained. Nevertheless, the use of lipases has some disadvantages. Their reaction rate is slower compared to catalytic transesterication and longer reaction times are needed to obtain the equilibrium. They are also more expensive than the alkaline catalyst and they can loose their activity, typically within 100 days of operation [180].

Lipases are inhibited by methanol and methanol needs to be added stepwise, otherwise the lipase can be inactivated. Ethanol, for which no inhibition occur, seems for this reason a more appropriate acyl acceptor for enzymatic transesterification. The yields for some enzymatic transesterification reactions of non-edible oils are given in Table 9.7, higher yields are obtained with ethanol than with methanol [180].

Other aspects that need to be taken into account are the water content and the temperature. Without water the enzyme is inhibitated, while high water concentrations can decrease the lifetime of the lipase. Every lipase has it optimal temperature related to its maximal activity. Higher temperature will lead to thermal deactivation. Immobilized enzymes can work at higher temperatures, since their structure is more protected. Overall, high biodiesel yields can be obtained by the use of lipases, even for feedstocks with high amounts of FFA. The main disadvantage of lipases is that they are inhibited in mixtures with methanol and need long reaction times to achieve a good yield [180].

Temperature

The temperature of the alkaline and acidic homogeneous catalysed biodiesel production is the same and lies around 338 K (Table 9.6). Higher temperatures enhance the transesterification reaction, however they are limited by the evaporation of the alcohol [179]. The boiling point at atmospheric pressure of methanol is 338 K, explaining the widely used reaction temperature of 338 K. Higher temperature can be achieved if the reaction occurs at pressures higher than atmospheric pressure. The temperature during the supercritical biodiesel production is around 573 K and a pressure of 10 to 25 MPa is applied (Table 9.6) [172]. Overall, a lower temperature is needed for the enzymatic catalysed reactions. The temperature varies between 310 and 330 K and is limited due to thermal deactivation [180].

Table 9.6: Overview of the main reaction parameters for the alkali catalytic, acid catalytic and supercritical method [172].

	Alkali catalytic method	Acid catalytic method	Supercritical method
Reaction temperature (K)	303-338	338	523-573
Reaction pressure (MPa)	0.1	0.1	10-25
Reaction time (min)	60-360	4140	7-15
Methyl ester yield (wt%)	96	90	98
Removal of	catalyst and methanol	catalyst and methanol	only methanol
Process	Complicated	Complicated	Simple
Yield	Normal	Normal	High

Post reaction processing

The described postprocessing is valid for the commercial biodiesel production with a homogeneous alkaline catalyst. After the reaction the biodiesel and glycerol phase are separated through decantation after settling or centrifugation, mostly disk centrifugation. Decantation is possible due to density difference between the two phases. Biodiesel has a density of 880 $kg \cdot m^{-3}$ and glycerol has a density of 1050 $kg \cdot m^{-3}$. Biodiesel forms the upper layer and the glycerol the bottom layer. Most of the excess methanol, catalyst and other impurities are in the glycerol phase, however the biodiesel layer still contains some impurities. Further purification of both phases is needed. The efficiency of the separation of the biodiesel and glycerol phase can be reduced by the presence of water and intermediates like triacylglycerols,

since emulsions can be formed. The methanol is removed after the biodiesel and glycerol separation to avoid the reverse reaction to triglycerides. After separation the biodiesel phase is neutralised with H_3PO_4 if KOH is used as catalysed. The formed salt can be used as fertilizer. If other catalysts are used, like NaOH and CH_3ONa, citric acid is used to neutralise the mixture and the formed salts are seen as a waste stream [179].

The biodiesel phase contains also a part of the excess methanol. Flash vacuum vaporisation or a stripping process is applied to remove the alcohol. The salts and FFA in the biodiesel phase are removed by centrifugation followed washing with water. The biodiesel phase can also be acidified to remove soaps, so no foam or clogging occur in the further processing. The water that remains in the biodiesel phase after washing can be removed by centrifugation or drying in later washing steps. Drying can be done by flash evaporation or by a thin film evaporator under vaccuum conditions. Most of the methanol is removed from the biodiesel phase by the washing steps and to separate the methanol and the water distillation is applied. Methanol and water can be separated by continuous distillation, until the methanol contains less than 0.1 wt% of water and can be reused. When ethanol is used as alcohol, an azeotrope with water occurs, which obstructs the separation and makes it a less favourable alcohol [179].

The glycerol phase needs also purification steps before it can be used as feedstock for other processes. The glycerol phase contains most of the excess alcohol, the catalyst and the soap. An acid is added to convert the soap to FFA and salt, which are both insoluble in the glycerol phase and can be separated and removed. The alcohol is removed by first heating up the glycerol phase to 90 to 120°C and than a pressure expansion so all the volatile components, most of the alcohol, evaporates. After this step a purity of 85% glycerol is obtained. The rest of the alcohol can be removed by distillation but this step is only necessary if high purities are needed related to its use in the pharma industry [179].

Biodiesel yield

The conventional biodiesel production reaches yields above 90%. However, the main disadvantages of the current commercial biodiesel production catalysed with a homogenous alkaline catalyst, are the high feedstock cost, the low value of crude glycerol, the sensitivity to water and FFA, the high energy requirement for the reaction and the purification steps and the high costs for the waste water treatment.

Therefore a switch to new feedstocks and a heterogeneous catalyst are needed. High biodiesel yields can still be derived from different non-edible feedstocks with heterogeneous acid and alkaline catalysts (Table 9.7) [64]. The reaction parameters for the solid base catalyst are usually the same as the homogenous base catalyst, a temperature of around 60°C, a reaction time of a couple of hours at a AOR above 1:6. The reaction with the solid acid catalyst happens at a higher temperature due to the weaker catalytic acitivity of the catalyst, also a longer reaction time is needed to reach the maximum conversion [64].

9.2.3 Engine performance of conventional biodiesel

Diesel engine test of biodiesel indicate some trends. Overall, a higher brake specific fuel consumption (BSFC) is found if biodiesel is used as fuel. Due to its oxygenated nature more fuel needs to be consumed for the same energy output as diesel. The emission of CO, SO_2 and particle matter is lower for biodiesel blends than for conventional diesel fuel. The increased oxygen content of the fuel leads to a more complete combustion and less CO.

Table 9.7: The parameters for the biodiesel production from non-edible oils and the achieved biodiesel yields. The data is taken from [64].

Super solid acid catalyst	Feedstock	AOR	Cat. wt%	T (°C)	time (h)	BD Yield (%)
SO_4^{2-}/TiO_2-SiO_2	Acidified cottonseed oil	1:9	3	200	6	92
SO_4^{2-}/ZrO	*Cerberra odollam*	1:8	6	180	3	84
$SO_4^{2-}/SnO^{2-}SiO_2$	*Jatropha curcas*	1:15	3	180	2	97
	Moringa oleifera	1:5	3	150	2.5	84
	Croton megalocarpus	1:15	3	180	2	95
ZrO_2- Al_2O_3	*Jatropha curcas*	1:9	8	150	4	90
KSF clay Amberlyst	*Jatropha curcas*	1:12	5	160	6	70
Sulfated PAHs	Calophyllum inophyllum	1:15	5	180	4	99
Solid base catalyst	**Feedstock**	**AOR**	**T (°C)**	**time (h)**	**Cat. (%)**	**BD Yield (%)**
CaO	*Jatropha curcas*	1:9	70	2.5	1.5	93
CaMgO/ CaZnO	*Jatropha curcas*	1:15	65	6	4	80
CaO-NiO	*Jatropha curcas*	1:15	65	6	5	86.3
CaO-Nd_2O_3						82.2
CaO-La_2O_3	*Jatropha curcas*	1:24	65	6	4	86.5
Li/CaO	*Pongamia pinnata*	1:12	65	1-2	5	>99
MgO-ZnO	*Jatropha curcas*	1:25	120	3	3	83
Cu	*Attalea speciosa*	1:5	70	3	1.6	72
Co (II)						87
KNO_3/Al_2O_3	*Jatropha curcas*	1:12	60	6	1.5	84
		1:15	65	8	7	91.3
Na/SiO_2	*Jatropha curcas*	1:9		0.25	3	>98
MgZnAlO	*Jatropha curcas*	1:11	182	6	8	94
TiO-7-600-6	Silybum merianum	1:16	60	0.5	5	90.1
CaO	*Pongamia pinnata*	1:8	65	2.5	2.5	95
(obtained from chicken egg)	*Mahua indica*	1:8	65	2.5	2.5	95
Li doped	*Mesua ferrea Linn*	1:10	65	4	5	94
egg-derived CaO						

Enzyme	Feedstock	Alcohol	AOR	Cat. wt%	water	T (°C)	time (h)	BD Yield (%)
Pseudomonas cepacia	*Jatropha curcas*	Ethanol	4:1	5-8	50%w/w	40	24	98
Burkholderia cepacia	*Jatropha curcas*	Ethanol	10:1	24	4.5%w/w	35	24	100
Rhizopus oryzae lipase	*Jatropha curcas*	Methanol	3:1	6	5%w/w	30	60	80
	Calophyllum inophyllum	Methanol	12:1	20	15%v/v	35	25	92
Novozyme 435	*Jatropha curcas*	Methanol	3:1	2	-	30	90	75
Lipozyme TLIM	Castor oil	Methanol	3:1	15	-	45	24	68
Compound Novozyme 435 and Lipozyme TL IM	Stillingia oil	Acetonitrile and t-butanol	6:4:1	4.32	-	40	20	96

The reduction in particle matter is caused by the reduced soot formation since no aromatics are present in biodiesel and enhanced soot oxidation due to the higher oxygen content of the

fuel. There is also no sulphur in the biodiesel reducing the emissions of SO_2. Nevertheless, the emission of NO_x increases slightly. The advanced injection process when biodiesel is present, is seen as the reason for the NO_x increase. Contradictionary data to these trends are also found in literature, but this can be explained by the variability of the used experimental setups and biodiesel properties [186, 187, 188].

9.3 Biodiesel production of algal biomass

Scientist are looking for new types of feedstock for biodiesel production, since the conventional feedstock negatively affects the biodiversity and can be a food crop. Some types of micro-algae are capable of forming triglycerides when they are grown under certain circumstances.

If micro-algae are used as feedstock the conventional biodiesel production reaction will not change. The main component of vegetable and micro-algae oils are triglycerides, which are esters of glycerol with FA. The only difference is that microalgae oil have another lipid profile with more unsaturated FA, which can negatively affect the storage of the biodiesel [189]. Since micro-algal oil has the same chemical structure as vegetable oil, glycerol is still formed by the transesterification reaction.

Microalgae have some advantages compared with the current first generation feedstock. They are grown in an aqueous environment: shallow open ponds or photo-bioreactors (PBR). The algae production consumes less water than the conventional crops production and even brackish or saline water can be used. They have also the potential for a higher yield per area for oil production, they need less fertilizers and even CO_2 flue gas can be used as a carbon source [190].

Some restrictions apply for the production location. High annual temperatures and high annual irradiance are needed. Furthermore, the key inputs such as water and nutrient, p.e. CO_2 flue gas, need to be closeby to reduce the costs of supplies. Optimal climatic conditions can be found in tropical regions and even deserts. Marginal land or even salinised land are also suitable for algae production [191].

The production cost of biodiesel from microalgae is more expensive in comparison with the conventional biodiesel production. The cost to produce algae is related to the used production system. The cost to produce 1 kg of algal biomass in an open pond is 1.6 to 1.8 euros when the cost for water, carbon resource and nutrients is incorporated. A higher cost is found for PBRs which are related to a cost of 9 to 10 euros per kilogram of algal biomass. When waste water, CO_2 from flue gases is used the costs can be reduced to 0.3 to 0.4 and 3.8 euros per kilogram algal biomass for open ponds and PBRs respectively. The main cost for open ponds is the labor and the CO_2 source, while for PBRs the depreciation of the plant is the main cost [192].

To compete with the cheap fossil fuels, a biorefinery that combines the production of fuels with another more valuable product from the algae would be required. One possibility is to select a species which lipid profile contains fatty acids suitable for biodiesel production and ω3-polyunsaturated fatty acids, which can be used for the production of nutraceuticals [193].

The production process of algal biodiesel consists of three main parts. The algae cultivation itself, the harvesting and oil extraction and the biodiesel production from the extracted oil.

9.3.1 Algae cultivation

The oil content of the algal biomass is enhanced under unfavorable growth conditions. Algae can produce triglycerides in different growing conditions. The three options are:

1. **nutrient defiency,**
   By nutrient defiency, no nutrients, like nitrogen, carbon and phosphor, are added anymore after a growth phase. As a result the cell division stops and the photosynthetic energy is invested in the lipid production. This option is only available for batch production and is mostly done in a two-phase strategy, with first a nutrient-sufficient phase where the algal biomass is produced, followed by the defiency phase for lipid production [194].

2. **nutrient limitation,**
   By nutrient limitation an insufficient amount of the nutrient is still added. The algae then adapt to the harsh environment and achieve a higher lipid content compared to nutrient sufficient conditions. The nutrient limitated cultures have lower biomass production, but their lipid content is higher, which compensate for their productivity loss. This production option is able to supply a contineous stream of algal biomass [194].

3. or **nutrient-sufficient production**
   For the third option, the nutrient sufficient option, a species that combines high levels of lipid and biomass productivity can be chosen. So that, even without any depletion, algal biomass with a high lipid content can be obtained [194].

The third production option was selected within this research, due to the high continuous biomass production, which increases the possibilities for biorefinery and the natural high lipid content of the algal cells which can be used as feedstock for the biodiesel production. Also the nutrient deprivation can also lead to the accumulation of carbohydrates instead of lipids [194].

However there are some technical drawbacks for the algae cultivation. First, an alga with good lipid production and growth rate has to be selected and the monoculture has to be retained. This is easily done in PBR, since in ponds contamination can be expected. The energy demand for mixing, water pumping, harvesting and dewatering of a PBR is higher than the energy demand of open ponds. Still, the production cost of biodiesel from microalgae is more expensive for both production systems in comparison with the conventional biodiesel production [190].

Most of the investigated algae species are phototrophic. They convert the energy of the sun to biomass by photosynthesis. However some algae can be grown heterotrophic. A carbon source is than added to the mixture. The heterotrophic option is promising in areas with limiting sunlight or in large scale PBR where the high cell density hinders the light [195].

Algal strain selection

An appropriate micro-algea strain must be selected. From literature no perfect algal strain can be found that overclass all the others in terms of lipid production. Nevertheless, a good algal strain can be selected by following criteria. Since freshwater is limited in areas where algal productivity is maximal (i.e. regions of high year-round solar irradiation), it is essential that saline water sources can be used to culture the algae and that the algae can grow in a broad salinity range. If the algae have only a narrow range of salinity tolerance, as it is the case for many marine algae, then the pond water must be regularly partially or completely

dicharged. As the discharged water will still contain nutrients, especially nitrogen (N) and potassium (P), this presents a disposal challenge, a signifcant economic cost and a problem for sustainability. It is therefore almost essential that the algae strains used are able to grow at a high productivity over a wide range of salinities, unless the water source is wastewater from a sewage plant or similar [191].

Next to a broad salinity tolerance the algae must have high growth and lipid accumulation rates. Lim et al. compared the growth rates and lipid productivity of subtropical coastal and brackish microalgae and found that *Nannochloropsis sp.* had the highest triglyceride production (6.24 μg $mL^{-1}day^{-1}$) and grew exponentially the first week with an average growth rate of 0.32 μgL^{-1}. However they did not select *Nannochloropsis sp.* for an outdoor scale-up. Tetraselmis sp. M8 was chosen, based on its versatility and resourcefulness of fatty acids, its short doubling time, better extraction efficiency and the FAME profiles would also meet the criteria for a future microalgae biorefinery. The mid-scale, outdoor cultivation of Tetraselmis sp. M8 achieved a FAME productivity of 4.8 μg mL^{-1} day^{-1} , consisting mosty of palmitic methyl esters (C16:0) (20.8%), stearic methyl esters (C18:0) (10.1%) and oleic methyl ester (C18:1), an unsaturated FAME (44.6%) [196].

Roldolfi et al. compared the lipid content and their productivity of 30 micro-algal strains. She cultivated four promising strains in a bubble tube under nitrogen deprivation and only two of them accumulated lipids. The marine Nannochloropsis sp F&M-M24 achieved a lipid content of 60% and was grown in a 20-L and a 110-L PBR to study the influence of the irradiance and nutrient deprivation. In nutrient sufficient condition a lipid productivity of 117 mg/L/day is found, which increases to 204 mg/L/day under nitrogen deprivation. When a two phase growth system would be applied, first a nutrient sufficient growth phase followed by nitrogen deprivation, the oil production potential could be more than 90 kg per hectare per day, or 20 tons per hectare yearly [190].

Tetraselmis sp. came forward as a promising species in the study of Huerlimann et al. [193]. Tetraselmis sp. showed a lipid productivity of 3.9 to 4.8 g $m^{-2}day^{-1}$ and a dry biomass productivity of 33.1 to 45 g $m^{-2}day^{-1}$, which was 2 to 10 times higher than the other investigated algal strains [193].

Not only lipid content alone is a good parameter for strain selection. Lower growth rates and/or small cell size lead to lower overall productivity [190]. Therefore, lipid content alone is an unsuitable measure for yield, since the yield also depends on growth rate and cell size. Species which have been promoted for their lipid content require careful evaluation of lipid productivity, considering that selecting a suitable species for scale-up production also depends on growth rate, biomass, and lipid productivity [193].

Lipid profile and productivity

Before we can start the energy balance calculations, the lipid profile of micro-algae oil, which will be used for further calculations, should be determined. The average lipid profile of the two promising strains Nannochloropsis and Tetraselmis obtained from the literature for various growth conditions (irradiation, growth medium) are given in Figure 9.4 [196, 190, 193]

A good biofuel for a diesel engine has to have a low oxidative potential, good cold flow characteristics and a high cetane number. The optimal ratio of the FA is 5:4:1 for C16:1, C18:1 and C14:0 [197, 193]. If we apply this ratio on the average lipid profile for Nannochloropsis and Tetraselmis, a ratio of 5:1.5:1 and 1:15:1 is found respectively. The C16:1, C18:1 and C14:0 fraction of Nannochloropsis oil is 41% of the total triglycerides and for Tetraselmis oil this

Table 9.8: Lipid profile of used feedstock, FA composition of the used micro-algae oil

Fatty acid		mass%	(stdev)	mol%	MM_{FAME} ($kg \cdot kmol^{-1}$)
Miristic acid	14:0	7	(± 1)	7.8	242
Palmitic acid	16:0	46	(± 4)	46.0	270
Palmitoleic acid	16:1	35	(± 5)	35.3	268
Stearic acid	18:0	2	(± 1)	1.8	298
Oleic acid	18:1	10	(± 3)	9.1	296

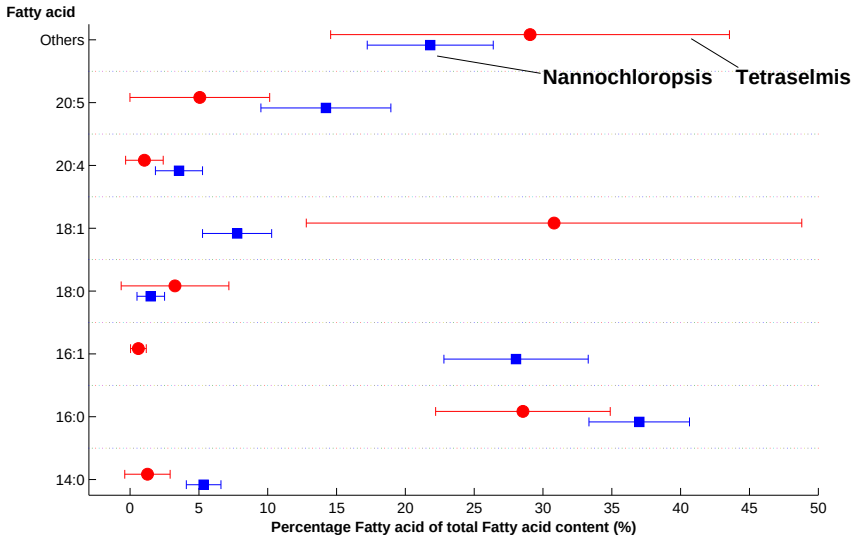

Figure 9.4: Lipid profile for Nannochloropsis and Tetraselmis [193, 190, 196]

fraction is 33%. The Poly-Unsaturated Fatty Acid (PUFA) content is also an important factor, the Tetraselmis oil contains 6% C20:4 and C20:5 and the Nannochloropsis oil 18%. The PUFAs are useful for biorefineries. The standard deviations found for the Nannochloropsis oil content are less than the variation found for the Tetraselmis oil. This can be explained by the wider range in experimental set-ups used to cultivate Tetraselmis. The Nannochloropsis experiments are all performed on lab scale, only varying the growth medium and the irradiance. The Tetraselmis data on the other hand contains some results found by an up scaled experiment.

The lipid profile of Nannochloropsis is chosen for further use, since the oil contains more PUFA which can be valorised in biorefineries. The composition of the oil selected for the further calculations is given in Table 9.8.

9.3.2 Harvesting and oil extraction

The algal biomass must be harvested before it can be used as fuel resource. The applied harvesting method is related to the characteristic of the algae and is a two-stage process. The

first step is bulk-harvesting by flocculation, flotation or gravity sedimentation. In a second step the slurry can be concentrated by centrifugation, filtration or ultrasonic aggregation. The water content after harvesting is typical 5 to 15% of the dry solid content. Further drying is needed to extend the storage time of the biomass. The biomass can be sun dried, the cheapest method, or dried by low-pressure shelf drying, drum drying etc. [198].

The dried biomass can be used as feedstock for several energy production processes. The biomass can be gasified, fermented to alcohol, pyrolysed, combusted directly, thermochemical liquefied, anaerobic digested etc. The process we are interested in the algal biomass-to-biodiesel process. An extraction of the triglycerides in the algal biomass is needed before the biodiesel production. The drying temperature can affect the triglycerides [198]. The extracted oil can than be transesterified to biodiesel with the techniques discussed in Section 9.2. To disrupt the cell wall for oil extraction four techniques can be used: high pressure homogenizatoin, bead milling, enzymatic lysis or electroporation. The micro-algae do not only contain apolar lipids like the triglycerides, but their membranes are build from polair phospholipids. There is no ideal method to extract only the apolar lipids which can be used to produce biodiesel. Organic solvents or supercritical fluid extraction can be used. Mechanical extraction methods can be oil expellers or using ultrasound and microwave radiation. New methods under investigation are ionic extraction and osmotic pressure extraction [199].

The harvesting and dewatering of the algal biomass is an energy intensive process. Sanders et al found that 3556 kJ per kg water removed is necessary to dewater the algal slurry [200]. He stated that a direct reaction to the products without dewatering is needed to keep it economical viable.

Slade et al. also concluded that to achieve a positive energy balance over the algae production technological advances and optimasation of the production systems is needed [192].

9.3.3 Engine performance of algal biodiesel

Biodiesel blends derived from micro-algae are compared to blends with biodiesel from WCO and conventional diesel by Islam et al. [201]. The algal biodiesel was derived from the marine dinoflagellae Crypthcodinium *cohnii* and the physical properties of the algal biodiesel complied with the legislation, except for the cetane number and density. Three blends of 10, 20 and 50% algal biodiesel with diesel are tested and are compared to a blend with 20% WCO biodiesel and conventional diesel. Overall, the same effects on the engine performance and the emissions are found with the micro-algal biodiesel as for conventional biodiesel. More fuel is consumed and the emissions contains more NO_x compared to diesel. The blend with 20% of algal biodiesel had the closest alignment in performance to conventional diesel [201].

Tuccar et al. came to the same conclusion as Islam et al.: micro-algal biodiesel has a cetane number too low regarding the EN 14214 standard. The other fuel properties were within the standard. This means that the algal biodiesel can be used without any problem as a fuel additive. The species from which the algal oil was derived was not stated [202].

A review of the use of (micro-)algal biodiesel in diesel engines and the comparison with the engine performance and emissions of diesel is made by Piloto-Rodriguez et al. They concluded that the high unsaturation levels of algal biodiesel had an influence on the engine performance, however the production and combustion of algal biodiesel is not well explored to deduce a conclusion [203].

10 Triacetin as biofuel

The conventional biodiesel process can be changed so that glycerol is not formed as byproduct but triacetin. Triacetin is a triglyceride, consisting of a glycerol backbone, esterified with three acetate groups. Since it is an ester, it is miscible with biodiesel and can be used as a biofuel additive. The biofuel production can increase with maximal 20 wt% when the glycerol is fully converted to triacetin. However, the European standard about biofuels (EN 14214) restrains triacetin to 10 wt% due to density limitations and to 0.2% if it is seen as a triglyceride (Table 9.1). No limitation is found for the American Society for Testing and Materials guidelines [161, 162].

Triacetin can be produced via different production routes. The different routes found in literature are given in Section 10.1. The use of triacetin as biofuel is already studied in diesel engine tests. The results of the test are given in Section 10.1, together with the effect on the fuel properties when triacetin is added.

10.1 Routes for coproduction of triacetin

To keep the biodiesel process economically viable, new applications for the surplus glycerol are needed. Triesters are a possible substitute for glycerol as byproduct and can be obtained in two ways. First, if the alcohol is replaced by an ester, the transesterification reaction changes into an interesterification reaction and a triester is directly formed (Figure 10.1). A second option is to perform first the transesterification reaction followed by an esterification reaction of the formed glycerol with a carbon acid to a triester (Figure 10.2). When methyl acetate and acetic acid are used as ester and carbon acid, triacetin is formed as byproduct.

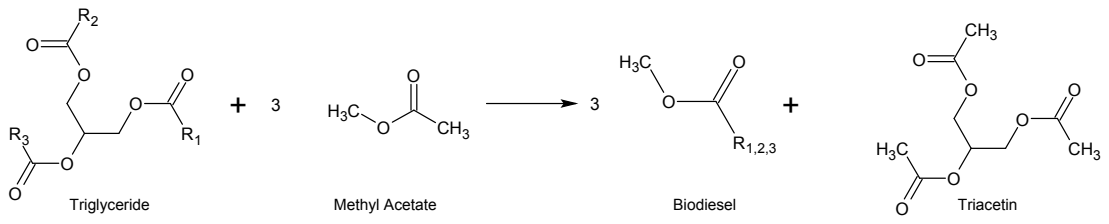

Figure 10.1: Interesterification process of triglycerides with methyl acetate to form biodiesel and triacetin.

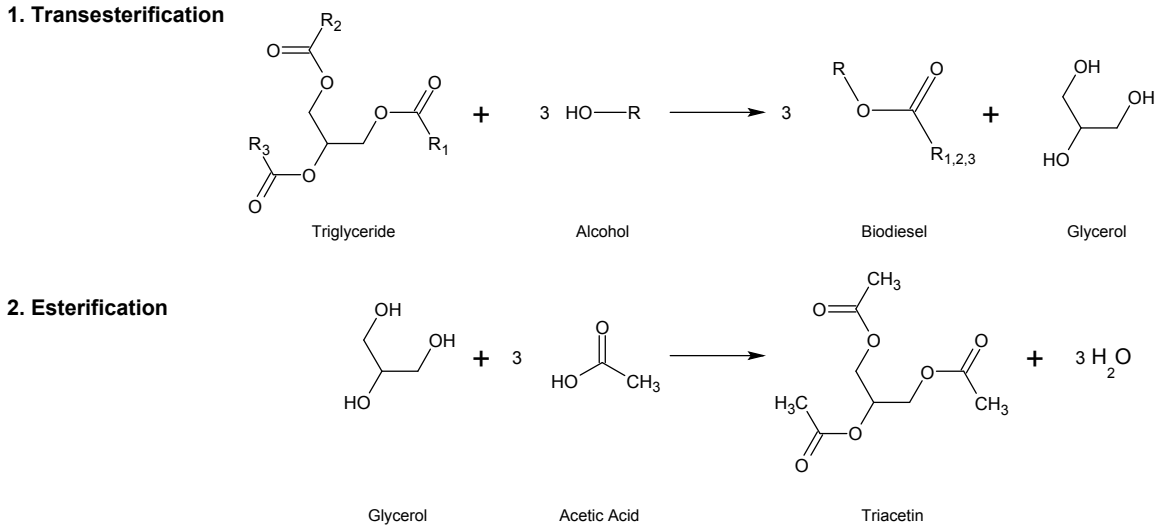

Figure 10.2: Esterification process of the glycerol formed by the transesterification reaction, with acetic acid to form triacetin and water.

10.1.1 Interesterification

During interesterification the alcohol group of two esters is exchanged. Just as the transesterification reaction, the interesterification reaction is a sequence of three equilibrium reactions. In literature three options to catalyse the interesterification reaction are described: adding an alkaline catalyst, using enzymes or supercritical methyl acetate.

Catalytic interesterification

The substitution of methanol with methyl acetate has as a consequence that the reaction mixture changes from polar to non-polar and that alkaline catalyst which are used in the conventional biodiesel production become partially insoluble and another catalyst has to be selected [204].

Casas et al. tested the chemical interesterication of sunflower oil with methyl acetate. Potassium hydroxide, potassium methoxide and polyethylene glycolate were investigated as possible catalyst. Solid potassium methoxide was found as an efficient catalyst. To dissolve the potassium methoxide, methanol was used. Methanol enhanced the biodiesel yield and improved the safety if the mole methanol to mole oil ratio is lower than 1.5. Alkaline methoxides are practical to catalyse the interesterification reaction and have a low cost compared with enzymes and supercritical conditions. However, their limited solubility in esters limits the kinetics of the overall reaction and a lag phase occurs. A solution for this delay, is to mix the catalyst first with the oil phase and then add the methyl acetate. If the catalyst is first added to the methyl acetate phase, a lower yield is found for the FAME formation, due to the Claisen condensation as a side reaction [204, 205].

The catalytic interesterification of vegetable oils requires mild conditions: 50°C and atmospheric pressure. Higher catalyst concentrations have a positive effect on the reaction rate and with a catalyst-to-oil molar ratio (COMR) of 0.2, the equilibrium composition is reached within 10 min. The presence of water and methanol has a negative effect on the triacetin yield [204].

Next to COMR the methyl acetate-to-oil molar ratio (MAOMR) is important due to the reversibility of the reaction. The complete reaction comprises three consecutive, reversible equilibrium reactions of which the reagents and products are completely miscible. Thus, it is likely that the equilibrium composition could contain high levels of intermediate compounds, such as monoacetindiglycerides and diacetinmonoglycerides. The stoichiometrical MAOMR is 3, however an higher MAOMR causes the equilibrium to shift towards triacetin and biodiesel and fewer intermediates are formed. A molar ratio of 50 was needed to remove the monoacetindiglycerides. Diacetinmonoglycerides did still exist when a MAOMR of 100 was used. These experiments demonstrate the high degree of reversibility of vegetable oil interesterification [204].

The equilibrium mass fractions found with these conditions are 76.7 wt% biodiesel, 17.2 wt% triacetin, 4.7 wt% diacetinmonoglyceride and 1.2 wt% other glycerol and triacetin intermediates. The biodiesel and triacetin yield can be calculated comparing the experimental mass fractions with the optimal ones, resulting in a yield of 96% and 86% for biodiesel and triacetin respectively. Casas also mentions that adding intermediates like diacetin, monoacetin and glycerol in the biofuel must be avoided, since hydroxyl groups can cause damage to the engine and hazardous emissions [204, 205].

He also investigated the kinetics of the total reaction, concluding that interesterification is slower than transesterification and that it follows a second-order reaction scheme. The limiting step is the formation of triacetin from diacetinmonoglyceride [206]. A purification step is needed before the recovery of the excess methyl acetate in the reaction mixture. The contaminants such as water and methanol can be adsorpted on Zeolite 5A and removed from the mixture [207].

The potassium methoxide catalyst needs to be removed from the interesterification products. Casas et al. investigated two processes to remove the catalyst: acid neutralisation and dry washing. Several acids are assessed as neutralisation agent. Phosphoric acid leads to the best results, forming monopotassium phosphate salt. The optimal concentration of the phosphoric acid is 1.5 times the catalyst concentration. Water is formed by the acid neutralisation, however no negative effect on the purification of methyl acetate was found. Different adsorbents were examined to apply dry washing. Both Magnesol and bentonite could remove the catalyst. If the undissolved catalyst was filtered off, a concentration of 1 g of adsorbent could be used per 100 g of mixture. Nevertheless, water is formed in the reaction mixture due to the humidity of the adsorbent and methyl acetate impregnates the adsorbent so it cannot be reused [208].

Ultrasound assisted chemical interesterification of waste cooking oil and methyl acetate was investigated by Maddikeri et al. A maximum biodiesel yield of 90% from waste cooking oil using sonochemical reactors was observed, which is a higher conversion compared to the reaction without ultrasound, with a molar ratio of 1:12 and temperature of 40°C [209].

The fuel interesterification reaction of triglycerides and methyl acetate is described in literature mainly by one author. Only data on experimental scale is available, which makes it difficult to assess the viability of the reaction at industrial scale. The high MAOMR of 50 needed to remove the monoacetindiglycerides from the reaction products could be the main drawback of this coproduction route, since the excess methyl acetate need to be removed. This can be done by decantation if the methyl acetate and biodiesel plus triacetin phase separate due to density, however no literature data is available for this step. If vaccuum distillation is used as separation process, which is a conservative choice, the energy demand for separation will be substantial.

Enzymatic interesterification

The enzymatic transesterification reaction of triglycerides with oil is limited by the methanol concentration. If the concentration of methanol is higher than the oil concentration the lipase is inhibited [210]. The use of methyl acetate as acyl acceptor in the biodiesel production can have a positive effect on the stability of the lipase. Ognjanovic et al. verified this phenomenon in two industrially feasible reactor designs. They used the same lipase eight consecutive times for reactions taking 8 to 10 hours and the residual activity of the lipase was still 93.6±3.75% [211].

The production of biodiesel from palm oil with a methanol/methyl acetate mixture and Novozym 435 (commercial C. *artactica*) as catalysist was investigated by Talukder et al. They found that methanol leads to a faster reaction, however it deactivates the lipase if the ratio of methanol to palm oil is greater than 1. The presence of methyl acetate has a positive effect on the Novozym 435 stability and the presence of methanol leads to a faster reaction. The highest yields were obtained with a MAOMR of 12:1 and a ratio of methanol to palm oil of 1 [210].

Usai et al. investigated the interesterification with different lipases. Candida *artactica* came forward as the most efficient lipase, with a yield as high as 80% for both the biodiesel and the triacetin production. A critical parameter is the hydratation of the enzyme, since too high water concentration can lead to enzyme inhibition or fatty acid production (saphonication) and too low water concentration can also inhibit the enzyme. Intermediate compounds, like monoacetate glycerol and diacete glycerol, were still present in the product medium. Although Usai assumed that their concentration is too low to affect the fuel properties [212].

In a second study also Candida *antarctica* was used with an excess ratio of methyl acetate to oil of 12:1. Only the yield of the biodiesel was measured and reached 92% [213]. The kinetics of the reaction was investigated in a follow-up study and the first interesterfication reaction from oil to a monoacetatediglyceride was found as the limiting step for the overall interesterication [214]. Comparable results were found by Huang et al. They found an optimal molar ratio between 14:1 and 16:1, depending of the used feedstock and biodiesel yields up to 98% [215].

A study investigating the interesterification reaction of sunflower oil with methyl acetate catalysed with two types of lipases, B. *cepacia* and C. *antartica*, both encapsulated in silica aerogels, found a final conversion of 56% with a MAOMR of 3:1. The commercially immobilized C. *antartica* showed no diffusion limitation, while the activity of B. *cepacia* is limited by diffusion. This could by explained by a change in the structure of the B. *cepacia* enzyme during encapsulation [216].

The main drawbacks of enzymatic esterification are that enzymes are expensive, need a long reaction time and are unstable at high temperatures. Usai therefore suggests to use a synthetic (organic) catalyst (either acid or alkaline) to chemical interesterificate the oil and methyl acetate, since it can resist higher reaction temperature and need a shorter reaction time [212].

Supercritical processes

Supercritical interesterification is investigated by different researchers. The main advantage of the interesterification of triglycerides with supercritical methyl acetate is that no catalyst is needed. Campanelli et al. shows that supercritical methyl acetate can be successfully used to produce biofuel from different oils [217]. All the examined oils achieved complete conversion

after 50 min at 345°C, 20 MPa and with an excess ratio (MAOMR) of 42:1. The kinetics of the reaction was faster compared with the conventional one. An important aspect is the thermal decomposition of triacetin, which lowers the overal biofuel production from the maximal value of 125 wt% to 103 to 106 wt% [217].

Saka et al. investigated the fuel characteristics of a biodiesel-triacetin blend and they concluded that triacetin has favorable effects on the drop point and oxidation characteristics, however it also lowers the cetane number. They found a yield of 105 wt% for biodiesel and triacetin together formed out of rapeseed oil with a MAOMR of 1:42, a pressure of 20 MPa and a temperature of 350°C [218].

A response surface methodology analysis of supercritical interesterification was conducted by Tcan et al. to assess the influence of various parameters on the result. The optimum conditions found with the model are 399°C for the reaction temperature, an excess ratio of 30 and a reaction time of 59 min to achieve 97.6% biodiesel yield [219].

Niza et al. investigated both the formation of biodiesel with supercritical methyl acetate and methanol. They used Jatropha curcas oil as feedstock and the reaction was carried out in a 12 mL tube reactor. The biodiesel yield with supercritical methanol was maximal 89.4%. A lower yield of 71.9% was achieved with methyl acetate. No data about the triacetin yield is given [220].

The supercritical interesterification with different carboxylate esters is investigated by Goembira et al. They investigated acetate, propionates and butyrates with a methyl, ethyl, propyl and butyl chain. The larger the chemical structure of the carboxylate esters, the more triacin can be formed in wt% which can be used as fuel additive. Nevertheless, the highest triacin yields are found with methyl acetate. The maximal product yield is 97.7 wt% when both the biodiesel and triacetin are considered as production. The reaction conditions are a pressure of 17.8 MPa at a temperature of 350°C for 45 min and a MAOMR of 42 [221].

When supercritical methyl acetate is used for the interesterification reaction resulting in triacetin and biodiesel, no catalyst is needed, which is a substantial reduction of the process costs. However, it is not clear if the absence of a catalyst compensated for the higher energy input needed to obtain supercritical conditions. Currently only literature data on small scale is available, so the real energy need at large scale is not known and cannot be compared to the energy needed to use a catalyst.

10.1.2 Esterification of glycerol

Another possible process is to perform the biodiesel production by transesterification first and then esterify the produced glycerol with the carbon acid acetic acid. The esterification reaction needs an acid catalyst. Zhou et al. compared two possibilities: ion-exchange resin like Amberlyst-15 and acid zeolites. Despite that acid zeolites schowed good selectivity towards transesterification reaction, they are less active for the acetylation reaction than Amberlyst-15. Without catalyst the conversion of glycerol can still reach 70% with an excess ratio of 9:1, a reaction temperature of 110°C and 70 minutes reaction time. However only intermediates are formed and no triacetin. With Amberlyst 15 as catalyst a selectivity to triacetin of 44.5% was found, after a reaction of 270 min with an MAOMR of 9:1 and a reaction temperature of 110°C. Diacetate monoglyceride was the main intermediate (47.7%) and 97.1% of the glycerol was converted [222].

Gelosa et al. investigated the esterification of acetic acid with glycerol using a chromatographic reactor. The advantage of this type of reactor is that the synthesis and the separation

occurs simultanoues. However there are limitations due to the chemical equilibrium that has to be overcome. Here too Amberlyst 15 was chosen as catalyst. The reaction took place at 80°C with an excess ratio (MAOMR) of 4.5:1. After 300 min around 40 wt% of the eluens is triacetin. The separation occurs due to the higher affinity of the formed esters for the packing resin, so they leave the column earlier [223].

The interesterification of glycerol with methyl acetate to triacetin is also investigated by Khayoon et al. over different heterogeneous catalysts (1 to 3.5 wt% of yttrium grafted into SBA-3 support). The optimal interesterification conditions are a MAOMR of 12:1, 3%Y/SBA-3 as catalyst, a reaction temperature of 110°C and a reaction time of 3 hours. The triacetin yield is 64%. Monoacetindiglyceride and diacetinmonoglyceride are the other reaction products [224].

The esterfication of glycerol can be done in an extra step. However this will lead to extra cost for the separation and purification of the crude glycerol formed by the biodiesel production. Also the reported yields for triacetin are lower than what is published for the other coproduction routes.

10.2 Triacetin as fuel additive in diesel engines

Melero et al. investigated the characteristic of glycerol derivates and evaluated if their addition to soybean biodiesel would improve the fuel properties. He concluded that the ethers formed of glycerol and isobutylene had a positive effect on the low temperature properties, however isobutylene is not abundant and the formation of glycerol ethers are restricted. The properties of triacetin was also assessed by them and in overall the addition of triacetin did not affect the fuel properties. The density of biodiesel needs to be between 860 and 900 $kg \cdot m^{-3}$ (Table 9.1). The density of triacetin is 1158 $kg \cdot m^{-3}$, so maximum 10 wt% can be added to biodiesel regarding the EN 14214 regulations. Nevertheless 20 wt% of triacetin is formed by stoichiometric interesterification of triglycerides. Also the viscosity increases by the addition of triacetin, but without violating the regulations. The CFPP of the mixture decreases slightly from 1 to 0°C. Triacetin does not influence the fuel properties in an adversily way and can therefore be used as biofuel additive [162].

Casas et al. also investigated the effect of triacetin on the biodiesel quality. They used different biodiesel (palm, soybean, sunflower, high-oleic sunflower, and rapeseed) for their investigation. They found the same limitation as Melero et al. Nevertheless no restriction for the addition up to 20 wt% is found regarding the American Society for Testing and Materials (ASTM) D6751 guidelines (Table 9.1) [161].

The effect of adding triacetin to biodiesel on the CP is investigated by Elias et al. They found that overall triacetin does not negatively affect the CP. A drop in CP is experienced between 0 and 10 wt% triacetin added with a maximal decrease of 3 K. Elias stated that triacetin is a promising biodiesel additive at levels below 20 wt% [225].

In addition, a patent for the use of triacetin as biofuel submitted by Delgado stated some properties of the mixtures of rapeseed methyl esters and triacetin [226]. Delgado found the same limitation due to density. Nevertheless, he claims that triacetin has a substantial positive effect on the freezing point, which is not found by other authors like Elias et al. [226].

The performance of triacetin as fuel additive is also tested in diesel engines [227, 228]. Zare et al. found that with increasing oxygen ratio, so with increasing triacetin content in biodiesel, the indicated mean effective pressure (IMEP) decreases due to the lower calorific value of the

oxygenated fuel. The emission of CO, hydrocarbons and the emitted particle number increase compared to the combustion of biodiesel, while the exhaust of CO_2, NO_x and particle matter (PM) decreases. Nevertheless, when the exhaust composition is compared to diesel, less CO_2, CO and hydrocarbons are measured, while the NO_x increases with 31% [227]. The effect on the transient and steady-state behaviour of engine running on WCO biodiesel and triacetin is investigated in [228].

10.3 Other upgrading possibilities for crude glycerol

At the momenent the crude glycerol that is coproduced by the biodiesel production is seen as a waste stream. The price of crude glycerol is not more than 0.10 euro per kilogram, while high grade glycerol can be worth 1.00 euro per kilogram [163]. Triacetin can be produced from glycerol, however there are other possibilities to valorisize glycerol. Glycerol itself cannot be used as fuel additive due to it polar affinity, it does not blend well with the apolar fuels. Burning glycerol directly forms acrolein, a hazardeous molecule. Nevertheless, by optimal combustion conditions, direct combustion seems the best option regarding Gupta et al., since the purification of raw glycerol and to process it further to fuel is currently not economically feasible [229].

Glycerol can also be catalytically oxidized or reduced to a more valuable chemical. The market of the valuable chemical need to be large enough to handle the glycerol input. Also the price of the chemical need to be higher than 0.45 euro per kg, which is the price of crude glycerol and its purification. Possible chemicals are propylene glycol, propionic acid, acrylic acid, propanol, iso-propanol and allyl alcohol. Especially propylene glycol is promising, since it can replace ethylene glycol as antifreeze and it is currently produced from natural gas [163, 230].

Glycerol can also be converted biologically. It can be used as feedstock in anaerobic digestion, however the produced natural gas contains less energy than directly cofiring glycerol. The fermentation of glycerol could lead to valuable chemicals, like 1,3-propanediol and various other coproducts. However, biological conversion is slow, which can lead to an increase in glycerol stockpile [163].

Johnson et al. concluded that both catalysis and biological conversion have the potential to convert crude glycerol to value-added products. Nevertheless, many of the conversion routes are still under research and it is not clear if they are economically viable and operationally feasible [163].

So there are other options to increase the value to the crude glycerol coproduced by biodiesel production, however none of them is currently applicable at industrial scale. The conversion of glycerol to triacetin, or the biodiesel production by interesterification with methyl acetate could be a option to valorize the glycerol stream in the future.

11 Energy balance calculations

The energy balance for the production of biodiesel with and without the coproduction of triacetin is calculated for different production routes. The coproduction of biodiesel and triacetin does not exist on industrial scale, so data from literature on experimental scale is used for the calculations. Therefore, a difference between the used parameters for the calculations and the eventually full scale parameters can occur. The assessed model is simplified to the energy in the biofuel produced and the energy needed for three processes related to the production: the heating during the reaction and the production and recovery of the reactant. A Monte Carlo analysis is applied to include the uncertainties on the input parameters and a sensitivity analysis is conducted to identify the parameters for which the model is most sensitive to.

Four production processes will be assessed in this chapter. The main process parameters are given in Table 11.1. The first assessed process is the conventional production of BD with methanol (ME) as reactant. An alkaline homogenous catalyst is chosen with a loading of 1 wt%. The process takes two hours to achieve an equilibrium and happens at a moderate temperature of 60°C. A high yield of 97% is assumed. The selected data are taken from [179].

The other three assessed production processes take the coproduction of triacetin (Tr) into account. The first production process is the catalytic interesterification as decribed by Casas et al. [204, 205, 206, 207, 208]. The triglycerides react with methyl acetate (MA) to form biodiesel and triacetin at a temperature of 50°C, an excess ratio of 1:50 with MeOK as catalyst. The reaction takes about 15 min and a biodiesel yield of 97% and a triacetin yield of 81% is achieved.

The interesterification reaction can also be catalysed by an enzyme. The commerical available C. *antartica* enzyme is chosen. Enzymatic reactions need a longer reaction time and a lower temperature to achieve a biodiesel yield of 82% and a triacetin yield of 77%. The process parameters are taken from [212].

The last production process that is assessed consists of two reaction steps. First conventional biodiesel production by transesterification is applied and then the produced glycerol is esterified to triacetin in a second step. The reaction parameters for the biodiesel production are the same as for the first production process. The process parameters for the esterification of glycerol with acetic acid (AA) are taken from [231].

The three assessed energy inputs for the production routes are (1) the production of the used reactant, (2) the heating during the reaction of the reaction mixture and (3) the recovery of the excess reactant. All three energy contributions differ between the production routes. The energy needed to produce the reactants is extracted from the EcoInvent database [232, 233]. The other energy consumptions are estimated with the use of thermodynamic properties of the assessed reactants derived from literature [85, 234, 235, 236]. No heat recovery is taken

Table 11.1: The process parameters needed to calculate the energy balance for the production of biodiesel and the coproduction of triacetin scenarios.

	Process	T (°C)	Time (h)	Reactant	Excess ratio (mole TRI:mole R)	Catalyst/ Enzyme	(wt%)	Yield BD (mole%)	Yield Tr (mole%)	Ref.
1.	BD Catalytic	60	2	ME	1:6	KOH	1	97	0	[179]
2.	IR Catalytic	50	0.25	MA	1:50	MeOK	0.8	97	81	[161]
3.	IR Enzymatic	40	96	MA	1:20	C. *antartica*	23	82	77	[212]
4.	BD Catalytic	60	2	ME	1:6	CH_3ONa	1	97	0	[179]
	+ER Catalytic	110	5	+AA	1:9	Amberlyst-15	0.5	0	45	[231]

into account as a conservative choice.

The following sections discuss the content of the EcoInvent inventory [232, 233], the applied system boundaries, the chosen functional unit and the made assumptions. The calculations about the energy produced as biofuel are given in Section 11.4, while the energy needed to heat up the reaction mixture and to produce and recover the reactant can be found in Sections 11.5.1, 11.5.2 and 11.5.3 respectively. In the end, Energy Return on Investment (EROI) is calculated for the four assessed scenarios to see if the produced energy as biofuel is greater than the energy needed for production.

11.1 EcoInvent database

The EcoInvent database contains process data for thousands of products. Life Cycle Impact Assessment (LCIA) methods are developed to quantify the impact of a process on biodiversity, climate change, fossil fuel consumption, etc., so the EcoInvent data can be used to make informed choices about the environmental impact of a process. EcoInvent version 2.0 was used for our calculations. Version 3.0 is released in 2013, which was after the start of this research and it was opted not to use the new database as the changes in the used data are minimal [232, 233].

The EcoInvent database originates from Switserland. The Swiss Centre for Life Cycle Inventories wants to offer a high quality dataset for the areas of energy, bioenergy, transportation, waste management, construction, chemicals, detergents, papers, agriculture, electronics and mechanical engineering. Life Cycle Assessement (LCA) is the study of a product, from raw material to its final disposal, the cradle-to-grave-principle. Within the LCA study the needed energy and product streams can be assessed together with their impact on the environment. The LCA methodology consists of four main steps (1) goal and scope definition, (2) inventory analysis, (3) impact assessment and (4) interpretation of the results [232, 233].

The data of the EcoInvent database mainly relies on the market in Europe in the year 2000. The processes in the database are mostly mature processes at that time, nevertheless some best available technologies and near future processes are also stated. A temporal system boundary need to be stated especially for emission impact assessment, since emissions from the past, current use and future need to be taken into account [232, 233].

Data for unit processes is gathered in the EcoInvent database, which can be aggregated to form a sequence of processes. More than one datasheet can be implemented for a unit process in the EcoInvent database, as a different supplier, production region etc. can lead to different energy needs and output parameters. Some unit processes are already aggregated if

the individual steps are not quantified or they are confidential.

To simplify the calculations, certain streams are cut off, which means that the streams are not considered for further calculations in the database. The decision to cut off a stream is done by the person who gathered the data and the decision is made based on the relevance of the stream to the mass, energy and environmental impact of the total process.

When a process has more than one output, the input and output parameters need to be allocated to the different outputs. This can be again a personal decision, or the allocation can be based on certain rules, like mass related or everything is allocated to the main or most valuable end product.

The EcoInvent database shows the mean values for the in- and output parameters of a process. The values are uncertain due to the variability of the in- and output parameters, the appropriateness of the in- and output parameters, model uncertainty and neglecting important flows since their is no data available for them. Only the first uncertainty can be quantified and is given for some processes in the inventory data. If the uncertainty on the mean value is not known a pedigree matrix can be established to estimate the uncertainty [237, 238]. The available data is scored in terms of reliability, completeness, temporal correlations, geographical correlation, further technological correlation and sample size and a default unceratinty factor is applied on the data in conjunction wit the pedigree matrix [239].

Different softwares are available to work with the EcoInvent database. CMLCA software, an free code is used in this work. The software is developed by the Institute of Environmental Sciences of Leiden Unversity [240]. The software can handle LCA calculations, just as input-output analysis. The uncertainty on the results is assessed by a Monte Carlo analysis with 100 runs. The mean paramater values and their standard deviations are stated in the EcoInvent data base, as pdf a lognormal distribution is applied.

11.2 System boundaries and assumptions

The first step in Life Cycle Assessement (LCA) is to define the system boundaries and the scope of the assessment. The scope is an energy assessment of the biodiesel production and the coproduction of triacetin within the set system boundaries and determine whether the coproduction of triacetin as biofuel is energetically advantageous or not compared to the production of only biodiesel. The system boundaries are visualised in Figure 11.1. Four scenarios are assessed. The conventional biodiesel (BD) production, the catalytic interesterification (IRc) and enzymatic interesterification (IRe) of triglycerides with methyl acetate to from biodiesel and triacetin and the esterification reaction of glycerol (ER), which is formed by the BD scenario, to triacetin. The energy inputs that are assessed in the energy balance are the heating during the equilibrium reaction, the recovery of the excess reactant and the production of the used reactant. The only energy output is the combustion energy of the produced fuels.

As functional units for the assessement the Normalised Energy Value (NEV) and the Energy Return on Investment (EROI) are chosen [241, 242]. The NEV is defined as

$$\text{NEV} = \frac{\text{Energy input proces}}{\text{Energy biofuel}} \cdot 100. \tag{11.1}$$

The NEV is used to express the energy need of each of the assessed processes separatly. The energy need of the process is expressed as a percentage of the energy content of the produced biofuel.

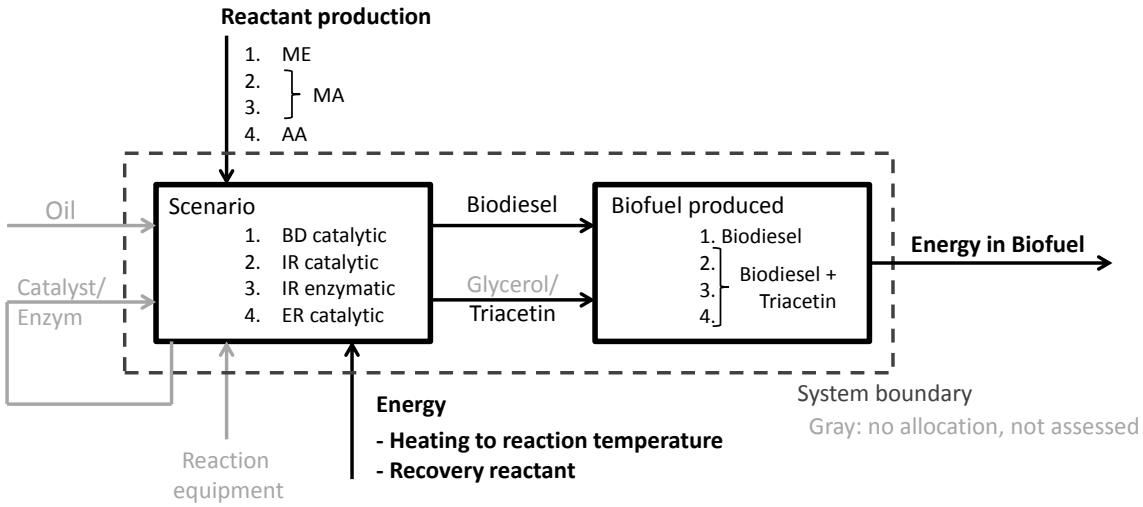

Figure 11.1: The assessed system contains the heating during the equilibrium reaction, the production and recovery of the reactant and the energy produced by the combustion of the formed biofuel. The production of the micro-algal oil and the used catalyst is not taken into account, just as the recovery of the catalyst. The glycerol produced by the transesterification reaction is seen as a waste stream and no allocation to the produced glycerol is made. Other energy contributions to the production process are neglected.

The EROI is defined as the ratio of the energy output to the energy input [242],

$$\text{EROI} = \frac{\text{Energy produced as biofuel}}{\text{Energy consumed during biofuel production}}. \tag{11.2}$$

The EROI will be used to compare the final result of the scenarios with each other. The EROI is a factor expressing how much more energy in the form of biofuel is obtained, compared to the energy input. If the EROI has a value higher than unity, energetically more biofuel is produced than that there is needed during the production process. The EROI is dimensionless and can be used to compare the energy balance of the scenarios.

An input stream of 1000 kg algal oil is chosen for the calculations. By this way the production of the oil does not need to be taken into account to make a comparison, since the oil input is the same for each scenario. The oil is derived from algae and the composition of the oil is given in Table 9.8. Some data about the energy cost to produce algal oil for biodiesel production is already published. Jorquera et al. made a LCA of algal biomass and oil production and found that 0.35 GJ of energy is needed to produce 1 GJ of biodiesel [243]. The numbers found in Slade et al. stated that the energy needed for algal biomass production is 0.24 $\text{GJ}\cdot\text{GJ}^{-1}$ biodiesel produced [192].

Other production steps, like transport and storage of the obtained biofuel, are considered the same for the different scenarios and will not be assessed. Data for these production steps are already given in literature. The energy to store and transport biodiesel from rapeseed to a service station is 0.02 and 0.04 GJ per GJ biodiesel produced respectively, according to the EcoInvent database [244]. The energy needed for these processes is only 10% of the energy needed to produce the algae.

The only outgoing energy flow is the produced biofuel. The energy content of the biofuel

is calculated by the mass of biofuel produced and the Lower Heating Value (LHV) of the biodiesel and the triacetin. Other decissions about the system boundary are:

- Not for every production route data about the catalyst recovery is available. Where possible, a hetergeneous catalyst should be chosen, which can be removed from the reaction medium by filtration, an inexpensive separation method. The catalyst or enzyme is assumed reusable and their production is not taken into account. Also the recovery of the catalyst or enzyme is not assessed.
- The resources to build the plant for the equilibrium reaction are not considered. To build an esterification plant for conventional biodiesel production, $9.11 \cdot 10^{-4}$ GJ per GJ of biodiesel produced is needed according to EcoInvent [244], however no data for the other plants is available.
- No allocation for energy is made to glycerol in the BD scenario, since glycerol is not soluble in biodiesel and cannot be directly used as a fuel additive. The economical value of glycerol is also very low, so it is treated as a waste stream.

11.3 Monte Carlo analysis and sensitivity analysis

The uncertainty of the simulations results is assessed by a Monte Carlo analysis. The basic concept of a Monte Carlo analysis is that the process is simulated multiple times and each time different starting parameter values are selected randomly from their ranges following an implied probability density function (pdf). The simulations lead to a distribution function which displays the whole area of possible outcomes [148]. The selected parameter ranges and the chosen probability distribution for sampling are given in Table 11.2. The following assumptions are made for the parameter ranges:

- The same oil composition is applied in all the scenarios.
- The minimum biodiesel yield is set to 90% for the BD, IRc and ER scenario. For enzymatic catalysed reactions the derived biodiesel yield is lower and a minimum limit of 80% is chosen.
- The triacetin yield cannot be higher than the biodiesel yield.
- As maximum reaction temperature the boiling point of the reactant is implied.
- The maximum reaction time for the IRc scenario is set to 180 min, the same as for the BD scenario. The maximum reaction time for the IRe scenario is set to 4 days.
- The minimum value for the excess ratio is set to three, the stoichiometric value.

As pdf a uniform distribution is used for all the parameters, so each value in the parameter range has the same probability to be picked in the Monte Carlo analysis. Applying another pdf could lead to different results. The number of runs in the Monte Carlo analysis has to be high enough to ensure that the desired accuracy for the end result is met. The error $|\epsilon_n|$ for a certain confidence interval can be calculated by

$$|\epsilon_n| \leq z_c \frac{\sigma}{\sqrt{n}}, \tag{11.3}$$

where n is the number of simulations, σ the found standard deviation and z_c is related to the chosen confidence interval. The constant z_c depends on the applied confidence interval and the constant z_c is 1.96 for a 95% confidence interval. After 3000 simulations the EROI of the IRc scenario has the largest spread related to a standard deviation of 26.6%. The error on this spread is 1% calculated by Equation 11.3. An error of 1% with a confidence interval of 95% is acceptable, so a Monte Carlo analysis with 3000 runs is applied [148].
The Monte Carlo analysis gives us an insight in the uncertainty of the result, however to assess the sensitivity of the result for the different input parameters another method is needed. The Normalised Sensitivity Coefficient (NSC) of the NEV are calculated by

$$\mathrm{NSC} = \frac{\mathrm{x}}{\mathrm{NEV}} \frac{\Delta \mathrm{NEV}}{\Delta \mathrm{x}} \tag{11.4}$$

for the different parameters x. The assessed parameters are the same as for which the uncertainty is assessed, namely the reaction temperature T, the biodiesel yield Y_{BD}, the triacetin yield Y_{Tr}, the composition of the oil, the excess ratio and the reaction time. The parameter values are increased by 1% separately and the simulations are run again so the difference in obtained NEV can be calculated. The NSC are achieved for the three assessed energy inputs. The achieved NSC values can be both positive or negative. Negative values imply that the NEV decreases due to the parameter change, which is an overall positive effect.

Table 11.2: Parameter ranges and the chosen pdf for the Monte Carlo analysis

Parameter		**Low value**	**High value**	**Distribution**
Oil (%)	(14:0)	5	9	Uniform
	(16:0)	44	48	Uniform
	(16:1)	33	37	Uniform
	(18:0)	0	4	Uniform
	(18:1)	8	12	Uniform
BD Yield	BD	90	97	Uniform
(%)	IRc	90	96	Uniform
	IRe	80	95	Uniform
	ER	90	97	Uniform
Tr Yield	IRc	80	BD Y	Uniform
(%)	IRe	70	BD Y	Uniform
	ER	44	BD Y	Uniform
Temperature	BD	50	64	Uniform
(°C)	IRc	40	57	Uniform
	IRe	30	50	Uniform
	ER	100	119	Uniform
Time	BD	60	180	Uniform
(min)	IRc	15	180	Uniform
	IRe	480	5760	Uniform
	ER	60	360	Uniform
Excess ratio	BD	3	9	Uniform
(mol reactant/	IRc	3	50	Uniform
(mol oil)	IRe	3	20	Uniform
	ER	3	12	Uniform

11.4 Energy produced as fuel in the scenarios

The Fatty Acid (FA) composition of our biodiesel mixture is given in Table 9.8. It is assumed that the algal oil and the FA composition of the biodiesel, Fatty Acid Methyl Esters (FAME), are the same. With this given, the optimal stoichiometric reaction to biodiesel and triacetin can be calculated. The results are given in Table 11.3. With 1000 kg of algal oil, 1005 kg of biodiesel can be produced when the yield is maximal, consuming 119 kg of methanol by conventional biodiesel production. Stoichiometrically, 275.5 kg of methyl acetate is needed to form 270.50 kg of triacetin and 1005 kg of FAME. The formation of triacetin is related to an increase of 27.5 wt% in biofuel compared with the conventional biodiesel production. When the experimental yields are applied the coproduction of triacetin still results in a biofuel increase of at least 11 wt%. The mole balance of the reaction is also given in Table 11.3.

The energy content of the produced biofuels can be calculated using the LHV. The LHV of a fuel expresses its energy content and can be calculated by

$$\mathrm{LHV} = n_{\mathrm{fuel}} \cdot \Delta H^{\circ}_{f\ \mathrm{fuel},g} - n_{\mathrm{H_2O}} \cdot \Delta H^{\circ}_{f\ \mathrm{H_2O},g} - n_{\mathrm{CO_2}} \cdot \Delta H^{\circ}_{f\ \mathrm{CO_2},g}, \tag{11.5}$$

where $\Delta \mathrm{H}^{\circ}_{f\ k,g}$ is the formation enthalpy of component k in the gaseous phase at standard conditions and n_k is the molar amount of component k that is present in the stoichiometric combustion reaction of component k.

The formation enthalpy is related to the chemical structure and can be found in chemical databases or calculated with predicting methods. Values for the formation enthalpies of the FAMEs, triacetin, the reaction products H_2O and CO_2 and the reactants, are retrieved from the National Institute for Standards and Technology (NIST) database [236]. However the NIST database did not contain all required information and vaporization enthalpies are calculated with the method described in Ceriani et al. for the FAME [234]. In addition, the enthalpy of formation is also calculated with the Benson group contribution method [245] for all the FAME. Values with the same order of magnitude are found with both methods. The formation enthalpies of the unsaturated FAMEs, palmitoleic and oleic methyl ester, differ the most between the two references, although the variation is maximum 7% (Table 11.4).

Table 11.3: The mass and mole balance for the different assessed biofuel production scenarios for a yield of 100% and taking the experimental yields given in Table 11.1 into account.

Scenario	Input			Output						
	Oil (kg)	Reactant (kg)	Glycerol (kg)	Oil (kg)	Reactant (kg)	FAME (kg)	Glycerol (kg)	Triacetin (kg)	Intermediates (kg)	Total biofuel (kg)
Yield 100%	1000	119.11		-	-	1004.96	114.15	-	-	1004.96
BD	1000	238.23		30	122.69	974.81	110.73	-	-	974.81
Yield 100%	1000	275.45		-	-	1004.96	-	270.49	-	1275.45
IRc	1000	4590.84		0	4322.70	978.27	-	219.38	75.26	1197.65
IRe	1000	1836.34		10	1588.50	904.21	-	208.28	125.35	1112.49
ER	-	649.91	110.73	-	482	-	1.69	115.70	110.86	BD+115.70
	(kmole)	(kmole)	(kmole)	(kmole)	(kmole)	(kmole)	(kmole)	(kmole)	(kmole)	(kmole)
Yield 100%	1.24	3.72		-	-	3.72	1.24	-	-	3.72
BD	1.24	7.44		0.04	3.83	3.60	1.20	-	-	3.60
Yield 100%	1.24	3.72		-	-	3.72	-	1.24	-	4.93
IRc	1.24	62.04		0	58.41	3.62	-	0.99	-	4.61
IRe	1.24	24.82		0.01	21.47	3.34	-	0.95	-	4.29
ER	-	10.83	1.20	-	8.03	-	0.02	0.53	-	BD+0.53

Table 11.4: The Enthalpy of Formation and LHV for the four discussed FAMEs in the biodiesel mixture. The LHV for the reactants and diesel are also given, just as the A/F-ratio and the energy content per volume unit [234, 236, 245].

Component	$\Delta_f H^\circ_{k,g}\left(\frac{\text{kJ}}{\text{mole}}\right)$		LHV $\left(\frac{\text{kJ}}{\text{g}}\right)$		$\frac{\text{A}}{\text{F}}$	$\text{E}_\text{V}\left(\frac{\text{kJ}}{\text{Nm}^3_{\text{air}}}\right)$	
	NIST	Benson	NIST	Benson		NIST	Benson
Miristic methyl ester	-665.87	-663.57	36.63	36.64	12.26	3865	3866
Palmitic methyl ester	-707.15	-705.43	37.38	37.39	12.52	3862	3862
Palmitoleic methyl ester	-766.66	-585.70	36.54	37.21	12.35	3824	3895
Stearic methyl ester	-748.43	-747.29	38.00	38.00	12.73	3859	3860
Oleic methyl ester	-831.08	-627.56	37.16	37.44	12.58	3818	3847
Triacetin	-1414.67		17.52		6.01	3769	
CO_2	-393.51						
H_2O	-241.83						
Diesel			43.4		14.6	3941	
Glycerol	-577		17.1				
Methanol	-205		21.0				
Methyl acetate	-410		20.2				
Acetic acid	-433		14.0				
Biodiesel Mixture			**37.02**	**37.29**	12.45	3844	3872
73% Biodiesel- 27% Triacetin Mixture			**31.76**	**31.95**	10.7	3833	3857

The LHV ($\text{kJ}\cdot\text{g}^{-1}$) for each molecule and mixture was calculated using Equation 11.5. The obtained values are given in Table 11.4. A variation of 1.7% for the LHV of the biodiesel mixtures is found between the methods of Ceriani and Benson. The LHV of conventional diesel is around 43.4 $\text{kJ}\cdot\text{g}^{-1}$. It can be concluded that the biodiesel mixture has a lower energy content by weight, due to the higher oxygen content in the chemical structure. In a diesel engine the combustion is performed at a constant volume and is characterized by the energy content of the injected mixture and used amount of air to burn the fuel, expressed by the air-to-fuel ratio (A/F-ratio). The stoichiometric A/F-ratio can be calculated by

$$\frac{A}{F}_{\text{stoich}} = \frac{m_{\text{air}}}{m_{\text{fuel}}} = \frac{\left(n_C + \frac{n_H}{4} - \frac{n_O}{2}\right) \cdot 4.76 \cdot \text{MM}_{air}}{\text{MM}_C \cdot n_C + \text{MM}_H \cdot n_H + \text{MM}_O \cdot n_O}, \tag{11.6}$$

where m_{air} and m_{fuel} are the mass of the air and fuel in the stoichiometric fuel mixture, n_C, n_H, n_O are the amount of C, H and O atoms in the fuel and MM_{air}, MM_C, MM_H and MM_O are the molar mass of air and the C, H and O atoms respectively.

The A/F-ratios needed to burn the FAME, triacetin and conventional diesel stoichiometrically, are given in Table 11.4. The LHV and the stoichiometric A/F-ratio of a molecule are positively correlated, since a molecule with a higher chemical energy content, like a less oxidized molecule, needs more oxygen to burn. This means that for the combustion of FAME and triacetin less air will be needed than for the combustion of diesel. Consequently a greater amount of biofuels can be injected in the same volume of air compared to diesel to achieve a stoichiometric combustion. When the energy content per volume unit E_V is calculated by

$$E_{\text{V}} = \frac{\text{LHV}}{{}^{A}/_{F}} \cdot 1.293, \qquad \left[\frac{kJ}{Nm^3_{air}}\right] \tag{11.7}$$

it appears that this value is quite similar for all the discussed fuels (Table 11.4). If the FAME are burned with an adjusted A/F-ratio, they will produce the same energy in a diesel engine, so no difference will be found between the biofuels and the conventional diesel in terms of delivered work. Only the consumption of the biodiesel will be greater.

The next step is to check the influence of the triacetin share on the energy content of the produced biofuel. Triacetin has a LHV of 17.52 $kJ \cdot g^{-1}$ according to the data of the NIST database, which is less than 40% of the LHV of conventional diesel. However when the A/F-ratio is taken into account to calculate the energy per volume unit E_V, the difference is reduced to 1.65%. A blend of 73% of biodiesel and 27% triacetin will have a LHV of 32 $kJ \cdot g^{-1}$ and a A/F-ratio of 11.

In the ideal case, a ton of micro-algae oil reacting with 275.5 kg methyl acetate, results in 1005 kg of biodiesel and 270.5 kg of triacetin. The biodiesel on its own has an energy content of 37.3 GJ and the formed triacetin is good for 4.7 GJ of biofuel, which means a maximal increase of 12.6% in energy produced as biofuel when triacetin is coproduced (Table 11.5). When the experimental biodiesel and triacetin yields are applied, energetically more biofuel is produced with the triacetin coproduction than with the biodiesel production alone. The catalytic interesterification leads to an energy increase of 7.6% compared to the optimal theoretical biodiesel energy content. Also the esterification of glycerol leads to a positive result of 2.4% extra fuel. With the enzymatic pathway, less energy is produced compared to the perfect biodiesel production, however if the experimental biodiesel yield is taken into account, an increase of 2.8% in biofuel energy content is found.

The previous calculations did not take the uncertainty on the process parameters into account. With a Monte Carlo analysis of 3000 runs the effect of the uncertainty on the energy content of the produced biofuels can be assessed. The results of the Monte Carlo analysis are shown in Figure 11.2 for the four assessed biofuel production scenarios. With the convential biodiesel scenario, between 33 and 36 GJ of biofuel is produced from a feedstock of 1000 kg of algal oil. In the IRc scenario energetically more biofuel is produced than the BD scenario, between 37 and 40 GJ with an average value of 38 GJ. The energy content of the produced biofuel in the IRe and ER scenario overlap with the BD scenario. 94% of the runs for the ER scenario result in an increase in the biofuel energy content, while for the IRe scenario only 44% of the simulations depicts a positive effect on the produced biofuel. For 13% of the simulations a fuel energy content lower than the BD scenario is found.

Table 11.5: The energy balance for the different assessed biofuel production scenarios taking the yields given in Table 11.1 into account.

Scenario	Input			Output						
	Oil (GJ)	Reactant (GJ)	Glycerol (GJ)	Oil (GJ)	Reactant (GJ)	FAME (GJ)	Glycerol (GJ)	Triacetin (GJ)	Intermediates (GJ)	Total biofuel (GJ)
Yield 100%	37.16	2.50		-	-	37.34	1.95	-	-	37.34
BD	37.16	5.00		1.11	2.58	36.22	1.89	-	-	36.22
Yield 100%	37.16	5.57	-	-	-	37.34	-	4.74	-	42.08
IRc	37.16	92.81	-	0	87.39	36.35	-	3.84	2.48	40.19
IRe	37.16	37.12	-	0.37	32.11	33.60	-	3.65	4.64	37.25
ER	-	9.07	1.89	-	6.73	-	0.03	2.03	1.94	BD+2.03

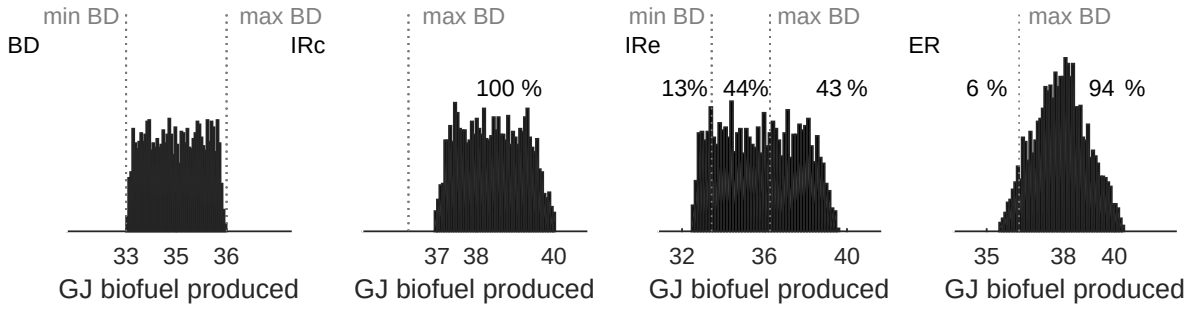

Figure 11.2: The energy content of the produced biofuel with 1000 kg of algal triglycerides as input for the four assessed production scenarios. The uncertainty on the input parameters are taken into account by a Monte Carlo analysis of 3000 runs. The conventional biodiesel production results in 33 to 36 GJ of biofuel produced. Only the catalytic interesterification, leads always to a higher energy content of biofuel.

11.5 Energy inputs for biofuel production

Three energy inputs for the production of biodiesel and triacetin are calculated and compared between the assessed scenarios. The first assessed energy input is the energy needed for the heating of the reacting mixture to the reaction temperature. The heat losses during the reaction are also taken into account.

The second contribution is the production of the used reactant (methanol, methyl acetate or acetic acid). The reactants are produced by different processes and the energy needed to produce them is not the same. Therefore, the energy needed to produce 1 kg of each is calculated using the EcoInvent database. Then the energy to produce the reactant used during the biodiesel and triacetin production can be calculated.

The last contribution is the recovery of the excess reactant. To force the equilibrium reaction to the biofuel side, more reactant is added than stoichiometrically necessary and the excess reactant need to be recovered for reuse. Distillation at atmospheric pressure is chosen as recovery method. The method is reliable and a conservative choice.

All the energy inputs are depending of the amount of reactant in the system. The total reactant in the system can be divided into excess reactant and the part of the reactant that is used in the fuel production. During the heating to the reaction temperature the total amount of reactant needs to be taken into account. For the production of the reaction, only the reactant used during the fuel production needs to be replaced and the excess reactant needs to be recovered by distillation.

11.5.1 Heating during equilibrium reaction

The energy Q needed to heat the reaction mixture up to the reaction temperature, is calculated by

$$Q = \sum_{i=1}^{n} n_i \cdot c_{p,i} \cdot (T_{amb} - T_{react}), \tag{11.8}$$

where the total heat needed (Q) is the sum of the moles of the reagentia (n_i) multiplied with their specific heat capacity ($c_{p,i}$) and the difference between the ambient temperature (T_{amb}, 20°C) and the reaction temperature (T_{react}, Tabel 11.2). The maximum reaction temperature

is the boiling point of the reactant at atmospheric pressure, so the reactant will not start to evaporate. Also, the applied excess ratio influences the heating demand. A higher excess ratio is related to a higher reactant mass, making the energy demand rise. The temperature dependency of the heat capacities for the algal oil and the reactant is taken into account for the calculations (Figure 11.3).

The heat losses for a cylindrical reactor with insulation are simulated. The density of the reacting mixture is calculated by the Haninson-Brobst-Thompson method [85]. It is assumed that the reaction occurs in a cylindrical tank with a volume of 20 m^3. The heat losses are simulated by a Monte Carlo analysis. The ranges for the thermal conductivity, the thickness and the emissivity of the insulation are set to 0.04 to 0.1 $W \cdot m^{-1}K^{-1}$, 0 to 0.2 m and 0.8 to 1 respectively. These numbers are related to an uninsulated stainless steel reactors and a stainless steel reactor insulated with 20 cm of glass wool.

In Figure 11.4 the NEV found for the different heating steps are shown. Due to our assumption for the energy losses the contribution of the losses is overall 10 times lower than the energy needed to heat up the total amount of reagentia. In reality the ratio can be different. Only for the IRe scenario the heat losses account on average for more than 0.01% of the produced biofuel energy. This is related to the long reaction time, varying between 8 hours and 4 days. The other reactions are terminated within 5 hours maximum.

The heating to the reaction temperature is maximum only 0.29% of the energy produced as biofuel for the BD scenario, with an average value of 0.2% related to 70.6 MJ.

More energy is needed for the other assessed scenarios. The IRc scenario needs on average 175.3 MJ, the IRe scenario 66.8 MJ and the ER scenario 135.2 MJ. If these values are normalised by the energy in the biofuel produced by the scenarios, it seems that the heating needs less than 1% of the energy in the biofuel produced. The maximal NEV is found for the IRc scenario. The value of 0.98 indicates that 0.98% of the energy in the produced biofuel is needed to heat up the reacting mixture in the worst case scenario.

The variability found for the IRc is related to the high methyl acetate-to-oil molar ratio (MAOMR) or excess ratio varying between 3 and 50 in the simulations. The NEV found for the IRc and the IRe scenario are higher than the BD scenario for 77 and 14% of the runs. This means that there is a chance of 77 or 14% respectively that the heating in the IRc and IRe scenario will need more energy than the BD scenario. The NEV of the ER scenario is always higher than the BD scenario, since the heating needs for the BD and ER scenario are added together. It is assumed that the FAME are removed before the esterification reaction, so they need not to be heated to 110°C during the esterification reaction.

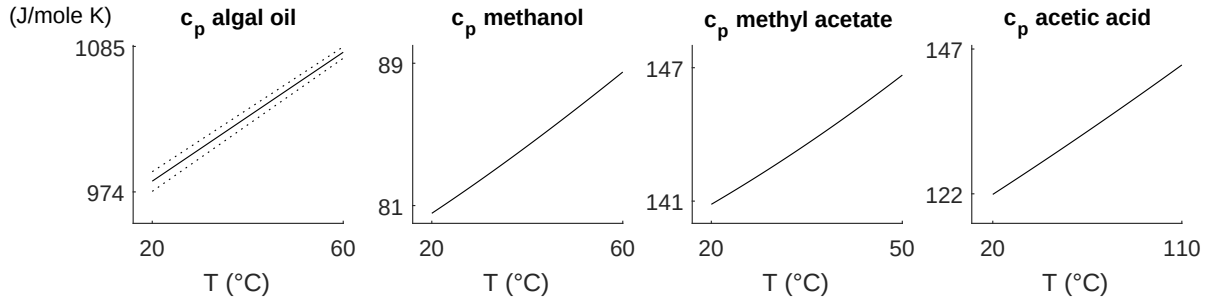

Figure 11.3: The specific heat capacity of the different reactants from the starting temperature to the reacting temperature. The uncertainty on the algal oil composition results in a variability of 12.3 $J \cdot mole^{-1}K^{-1}$ [234, 236].

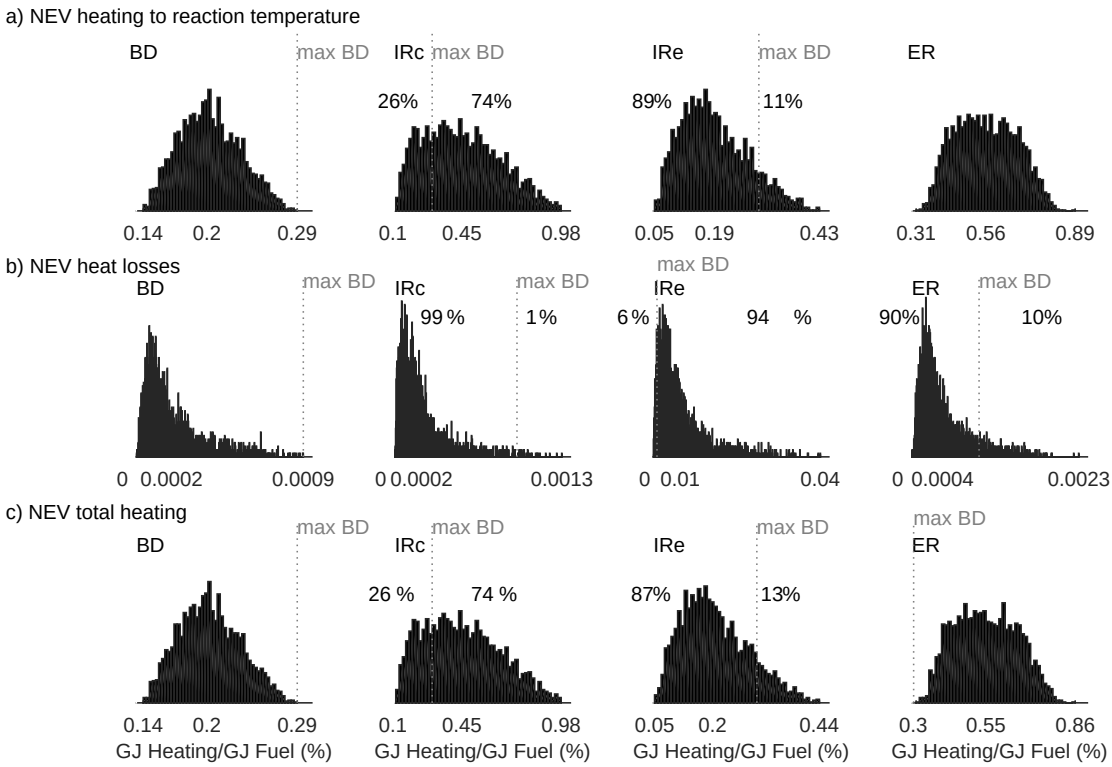

Figure 11.4: a) The energy needed to heat up the triglyceride and reactant mixture to the reaction temperature expressed as NEV, b) the energy needed to cover for heat losses during the reaction expressed as NEV and c) the total energy needed for heating to the reaction temperature expressed as NEV.

The sensitivity of the NEV value to the input parameters is quantified by NSC values given in Figure 11.5. An increase in the biodiesel yield (Y_{BD}) results in a decrease of the NEV for the heating process. The extra biofuel produced positively affect the NEV value. The increase in triacetin yield (Y_{Tr}) has the opposite effect. The extra fuel produced does not compensate for the extra heating demand. The effect of the reaction temperature, reaction time and excess ratio is as expected. An increase of them negatively affects the NEV value. The greatest effect for the time and temperature is seen by the IRe scenario. The two parameters affect the heat losses, which are 5% of the total heating in the IRe scenario.

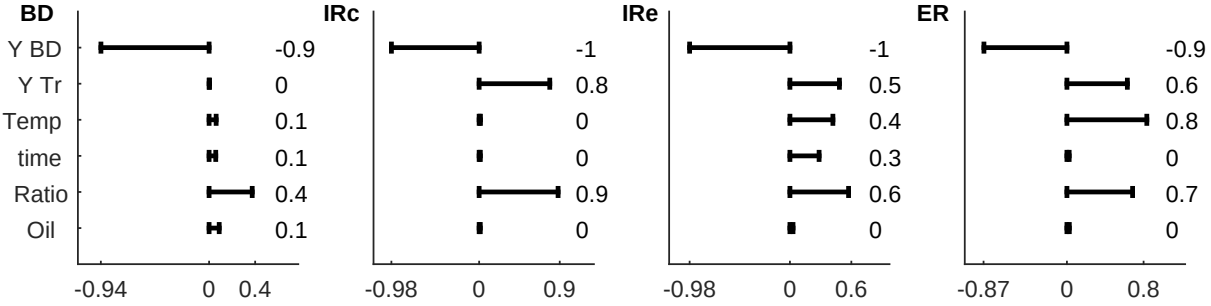

Figure 11.5: The NSC values achieved by the sensitivity analysis on the heating during the equilibrium reaction.

11.5.2 Production of reactant

The EcoInvent database contains data about the production of common chemicals. The required energy, the used resources and the emissions during production of the reactants can be deduced from the EcoInvent database. The energy needed to produce methanol, methyl acetate and acetic acid from fossil resources is extracted from the database. It is also possible to implement the uncertainties of the found values. The uncertainty on the EcoInvent data is obtained by a Pedigree matrix approach [238] and a Monte Carlo analysis of 100 samples is ran with the CMLCA software, to implement the uncertainty using the geometric mean and standard deviation stated applying a lognormal pdf distribution.

The energy used for the production of methanol, methyl acetate and acetic acid is given in (Table 11.6). Both the energy from fossil fuels and renewable energy are taken into account. The contribution of nuclear energy is seen as non-renewable source and in total fourteen energy streams are contributing. A conversion factor to MJ is applied for some of the streams (Table 11.7).

More than 98% of the energy input for the reactant production comes from non-renewable resources. It can be deduced that methanol is produced from natural gas and that methyl acetate is produced from oil. Three production pathways for acetic acid are stated in the EcoInvent inventory. Acetic acid can be produced from butane (option 1), acetaldehyde (option 3) or can be achieved as a solution of acetic acid 98% in water derived from a mixture of gas, oil and coal (option 2).

The total energy needed to produced methanol from natural gas is estimated to be 37.6±3.8 MJ·kg^{-1}, which is higher than its LHV of 21 MJ·kg^{-1}. More energy is needed to process the natural gas to methanol than the chemical energy within methanol. Most fossil fuels have already a negative energy balance, meaning that it takes more energy to refine them than their chemical energy [165]. The same is found for methyl acetate and acetic acid. The production of 1 kg of methyl acetate needs 47.3±4.3 MJ and the energy need for acetic acid production lies between 47.2 and 69.6 MJ·kg^{-1} depending on the chosen option.

Now that the energy needed to produce 1 kg of the reactant is known, the energy to produce the used reactants in the scenarios can be calculated. This is done by multiplying the mass of the used reactant with the energy needed to produce one kilogram of it. Only the energy for the reactant that is incorperated in the biofuel is accounted for. The production for the excess reactant is not taken into account except for a loss during recovery. A loss of 1 to 5% uniformly distributed of the excess reactant during recovery is taken into account using an uniform distribution, so it is assumed that between 95 to 99% of the reactant is actually recovered. All three production routes of acetic acid are taken into account equally.

The results for then energy need related to the reactant production are given in Figure 11.6. The production of the methanol used in the BD scenario needs on average 12% of the energy content of the produced biodiesel, or 4.3 GJ. Higher percentages are found for the triacetin coproduction scenarios, since the production of methyl acetate and acetic acid needs at least 25% more energy than the methanol production. The average energy needed is 15.2, 12.5 and 14.1 GJ for the IRc, IRe and ER scenario respectively. The energy demands are related to 40, 35 and 37% on average of the produced biofuel energy content for the respectively production scenarios.

Table 11.6: EcoInvent data regarding the energy needed to produce 1 kg of the needed reactants, methanol, methyl acetate and acetic acid from fossil fuels. The mean input parameters and their standard deviation are given

Energy contribution (MJ)	Methanol	Methyl acetate	Acetic acid Option 1	Acetic acid Option 2	Acetic acid Option 3
Energy, solar, converted	$0.0001 \pm 4.7{\cdot}10^{-9}$	$4.4{\cdot}10^{-4} \pm 3.7{\cdot}10^{-8}$	$4.4{\cdot}10^{-4} \pm 4.1{\cdot}10^{-8}$	$1.6{\cdot}10^{-3} \pm 6.2{\cdot}10^{-7}$	$1.3{\cdot}10^{-3} \pm 4.0{\cdot}10^{-7}$
Energy, gross calorific value, in biomass	0.02 ± 0.00014	0.11 ± 0.0050	0.11 ± 0.018	$0.28 \pm 2.7{\cdot}10^{-2}$	$3.5{\cdot}10^{-1} \pm 4.2{\cdot}10^{-2}$
Energy, potential (in hydropower reservoir), converted	0.11 ± 0.0022	0.32 ± 0.015	$3.2{\cdot}10^{-1} \pm 2.0{\cdot}10^{-2}$	0.77 ± 0.13	$7.6{\cdot}10^{-1} \pm 0.11$
Energy, gross calorific value, in biomass, primary forest	$1.2{\cdot}10^{-5} \pm 3.0{\cdot}10^{-10}$	$3.9{\cdot}10^{-5} \pm 1.1{\cdot}10^{-9}$	$3.9{\cdot}10^{-5} \pm 9.7{\cdot}10^{-10}$	$3.6{\cdot}10^{-5} \pm 8.9{\cdot}10^{-10}$	$1.8{\cdot}10^{-5} \pm 1.5{\cdot}10^{-10}$
Energy, kinetic (in wind), converted	$0.0099 \pm 2.6{\cdot}10^{-5}$	$0.027 \pm 1.9{\cdot}10^{-4}$	$0.027 \pm 2.2{\cdot}10^{-4}$	$0.11 \pm 3.2{\cdot}10^{-3}$	$8.8{\cdot}10^{-2} \pm 2.5{\cdot}10^{-3}$
Oil, crude, in ground	0.22 ± 0.00024	33.5 ± 4.3	33.3 ± 4.1	17.8 ± 1.7	31.9 ± 4.9
Gas, natural, in ground	36.2 ± 3.8	8.9 ± 0.45	8.9 ± 0.47	23.0 ± 2.6	22.9 ± 2.6
Coal, hard, unspecified, in ground	0.25 ± 0.0040	2.0 ± 0.15	2.0 ± 0.16	3.6 ± 0.52	5.3 ± 0.89
Coal, brown, in ground	0.23 ± 0.0013	$0.64 \pm 8.6\text{E-}03$	0.64 ± 0.010	2.6 ± 0.17	2.1 ± 0.11
Peat, in ground	$2.4{\cdot}10^{-5} \pm 1.4{\cdot}10^{-11}$	$3.6{\cdot}10^{-5} \pm 9.5{\cdot}10^{-11}$	$3.6{\cdot}10^{-5} \pm 8.8{\cdot}10^{-11}$	$6.2{\cdot}10^{-5} \pm 2.3{\cdot}10^{-10}$	$2.2{\cdot}10^{-3} \pm 1.2{\cdot}10^{-7}$
Gas, mine, off-gas, process, coal mining	$0.0043 \pm 8.8{\cdot}10^{-7}$	$0.041 \pm 6.1{\cdot}10^{-5}$	$0.041 \pm 4.7{\cdot}10^{-5}$	$7.2{\cdot}10^{-2} \pm 1.1{\cdot}10^{-4}$	$9.6{\cdot}10^{-2} \pm 1.8{\cdot}10^{-4}$
Uranium, in ground	$0.51 \pm 1.4{\cdot}10^{-7}$	$1.8 \pm 1.3{\cdot}10^{-6}$	$1.8 \pm 1.3{\cdot}10^{-6}$	$6.0 \pm 1.9{\cdot}10^{-5}$	$6.0 \pm 1.5{\cdot}10^{-5}$
TOTAL (MJ)	37.6 ± 3.8	47.3 ± 4.3	47.2 ± 4.1	54.2 ± 3.2	69.6 ± 5.6
Non-renewable energy (%)	99.6	99.0	99.0	97.9	98.3
Renewable energy (%)	0.4	1.0	1.0	2.1	1.7

Table 11.7: The factors to convert some energy input from the EcoInvent inventory to MJ

Energy contribution	Unit	Conversion factor
Oil, crude, in ground	kg	45.8 MJ/kg
Gas, natural, in ground	Nm^3	38.3 MJ/Nm^3
Coal, hard, unspecified, in ground	kg	19.1 MJ/kg
Coal, brown, in ground	kg	9.9 MJ/kg
Peat, in ground	kg	9.9 MJ/kg
Gas, mine, off-gas, process, coal mining	Nm^3	39.8 MJ/Nm^3
Uranium, in ground	kg	5.5 10^5 MJ/kg

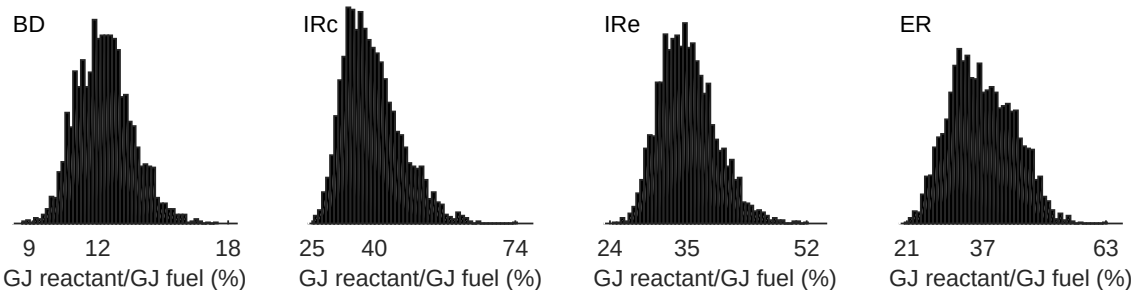

Figure 11.6: The NEV related to the production of the used reactant.

The high energy need for the reactant production is related to the use of fossil fuels. If the reactants are produced from biomass, the contribution of 'Energy, gross calorific value, in biomass' will increase, which is an renewable energy source. The total amount of energy needed for production could be higher, however the renewable aspect and sustainability will increase.

The production of methanol from fossil resources and biomass are both implemented in the EcoInvent database, so the energy consumption to produce 1 kg of methanol from biomass can be easily achieved (Table 11.8). The total energy to produce methanol from biomass is higher than the energy needed to produce it from methane. The main energy contribution is biomass, which contributes around 63.2 $MJ \cdot kg^{-1}$ methanol. The energy for the conventional production of methanol needs 37.5 $MJ \cdot kg^{-1}$, mostly fossil resources (Table 11.6). Only 7 MJ fossil resources per kg methanol are needed if methanol is produced from biomass.

The production of methyl acetate and acetic acid from biomass is not included in the EcoInvent database and therefore an estimation of the energy needed for production is made based on data found in literature.

The studies of Haro et al. investigate a biorefinery that can coproduce ethanol, dimethyleter, methyl acetate, hydrogen and electricity [246, 247]. Out of these studies can be derived that between 1.8 to 3.6 kg of wood chips are needed to produce 1 kg of methyl acetate. The production of wood chips is incorporated in the EcoInvent database and the energy needed to produce a cubic meter of wood chips is given in Table 11.8. The density of the wood chips is assumed to between 223 and 328 $kg \cdot m^{-3}$ [248], so the chemical energy from biomass needed to produce 1 kg methyl acetate lies between 20.8 and 61.2 $MJ \cdot kg^{-1}$. The energy from fossil resources needed during the process varies around 1 $MJ \cdot kg^{-1}$ methyl acetate, which is quite low due to the recuperation of heat losses in the process [246, 247]. The maximal energy demand for the production of 1 kg of methyl acetate is 62.2 $MJ \cdot kg^{-1}$, which is higher than the energy stated in the EcoInvent database. The production from biomass needs more energy, however the energy is retrieved from renewable sources.

Acetic acid can be produced during anaerobic fermentation of synthesis gas, a mixture of H_2 and CO. Data from Hu et al. is taken to assess the energy needed for this process [249]. It is assumed that between 10 to 31 g acetic $acid \cdot L^{-1}$ is achieved, related to a synthesis gas use between 3.6 and 109 $Nm^3 \cdot kg^{-1}$ acetic acid produced. The energy to produce synthesis gas from biomass is implemented in the EcoInvent database. There are three scenarios: (1) synthesis gas from wood produced with a fixed bed gasifier, (2) synthesis gas from wood produced with a fluidized bed gasifier and (3) synthesis gas produced from a mixture of feedstock and methods at the plant. The energy needed to produce synthesis gas by the three options is given in

Table 11.8 and between 35.6 and 59.8 MJ is needed to produce 1 Nm^3 of synthesis gas. The three production options of synthesis gas are taken equally into account for the calculations. Around 22.8 Nm^3 synthesis gas is needed to produce 1 kg of acetic acid. The aqueous solution of acetic acid needs to be concentrated and the total fossil energy needed to produce acetic acid is estimated to be between 13 and 96 $MJ \cdot kg^{-1}$ acetic acid [249]. These values can also be higher than the EcoInvent data related to the production of acetic acid from fossil resources.

In total more energy is needed to produce methanol, methyl acetate and acetic acid from biomass. However the contribution of fossil resources is remarkably smaller. The NEV related to the production of the reactants from biomass will be higher than the NEV achieved for the production of the reactant from fossil fuels. Nevertheless, if only the contribution of fossil resources is taken into account, a decrease will be found for the NEV. The production from biomass will also have a positive effect on the emitted GHG gases if only the energy input from fossil fuels is considered.

The sensitivity analysis on the NEV of the reactant production from fossil resources shows that the NEV is sensitive to the biodiesel yield, the triacetin yield and the excess ratio. The biodiesel yield has a positive effect on the NEV, while the needed reactant to form the extra triacetin related to the higher triacetin yield cancels out the positive effect of the extra biofuel produced. Especially in the ER scenario, since the production of acetic acid consumes the most energy. Increasing the excess ratio has also a negative effect on the achieved NSC, since losses by recovery are implemented in the code.

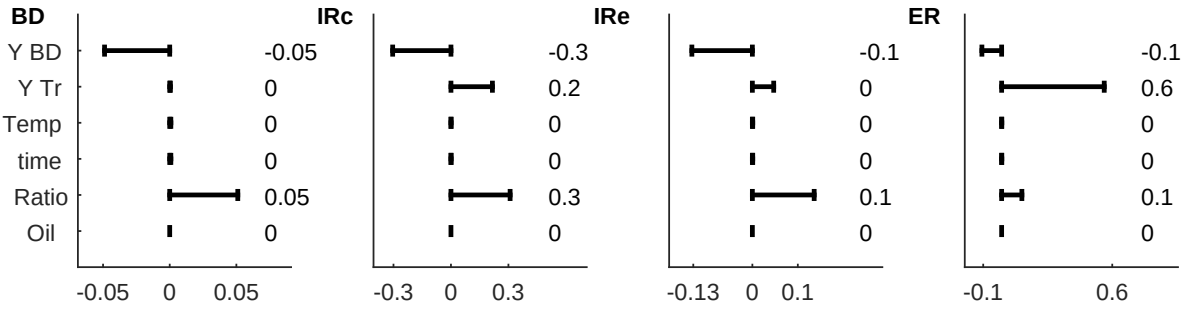

Figure 11.7: The NEV achieved by a sensitivity analysis on energy consumed by the production of the used reactants from fossil fuels.

11.5.3 Recovery of excess reactant

A conservative method is chosen to recover the reactant, namely distillation. This is an very energy intensive method, however it is reliable. The first step in the recovery cost estimation is to determine the boiling point of the reaction mixture. It is assumed that the FAME is already removed from the reaction products and that the mixture behaves ideal, so the partial pressures can be calculated with the Antoine equation,

$$log(P) = \mathrm{A} - \frac{\mathrm{B}}{T + \mathrm{C}} \tag{11.9}$$

where P is the vapor pressure, T is the temperature and A, B and C are coefficients depending on the assessed reactant, and the partial pressures may be added together for the reaction components.

Table 11.8: EcoInvent data regarding the energy needed to produce the reactants from biomass. The methanol from synthesis gas is already incorporated in the EcoInvent inventory, the other production process are estimations based on literature data [246, 247, 249]. The EcoInvent data about synthesis gas and wood chips are used in the calculations.

Energy contribution (MJ)	Methanol (1 kg)	Synthesis gas (1 Nm^3) (Option 1)	Synthesis gas (1 Nm^3) (Option 2)	Synthesis gas (1 Nm^3) (Option 3)	Wood chips (1 m^3)
Energy, solar, converted	$4.47{\cdot}10^{-4} \pm 7.76{\cdot}10^{-8}$	$3.03{\cdot}10^{-5} \pm 9.03{\cdot}10^{-10}$	$3.81{\cdot}10^{-5} \pm 1.10{\cdot}10^{-9}$	$3.42{\cdot}10^{-5} \pm 7.64{\cdot}10^{-10}$	$5.14{\cdot}10^{-3} \pm 6.47{\cdot}10^{-6}$
Energy, gross calorific value, in biomass	$63.2 \pm 1.40{\cdot}10^{48}$	59.11 ± 260.44	34.80 ± 127.88	39.06 ± 131.08	$3790 \pm$ NaN
Energy, potential (in hydropower reservoir), converted	0.78 ± 0.19	$4.97{\cdot}10^{-2} \pm 1.94{\cdot}10^{-3}$	$5.26{\cdot}10^{-2} \pm 1.80{\cdot}10^{-3}$	$5.12{\cdot}10^{-2} \pm 1.4{\cdot}10^{-3}$	2.62 ± 1.50
Energy, gross calorific value, in biomass, primary forest	$6.54{\cdot}10^{-6} \pm 3.23{\cdot}10^{-10}$	$7.79{\cdot}10^{-7} \pm 8.21{\cdot}10^{-2}$	$9.27{\cdot}10^{-7} \pm 1.18{\cdot}10^{-11}$	$8.53{\cdot}10^{-7} \pm 6.18{\cdot}10^{-12}$	$8.77{\cdot}10^{-5} \pm 7.66{\cdot}10^{-9}$
Energy, kinetic (in wind), converted	$1.69{\cdot}10^{-2} \pm 1.47{\cdot}10^{-4}$	$1.24{\cdot}10^{-3} \pm 1.95{\cdot}10^{-6}$	$1.81{\cdot}10^{-3} \pm 3.03{\cdot}10^{-6}$	$1.53{\cdot}10^{-3} \pm 1.79{\cdot}10^{-6}$	$0.36 \pm 3.51{\cdot}10^{-2}$
Oil, crude, in ground	2.17 ± 0.67	$0.25 \pm 1.46{\cdot}10^{-2}$	$0.30 \pm 2.04{\cdot}10^{-2}$	$0.27 \pm 1.21{\cdot}10^{-2}$	12.27 ± 0.83
Gas, natural, in ground	0.00 ± 0.00	$5.09{\cdot}10^{-2} \pm 3.19{\cdot}10^{-4}$	$0.10 \pm 7.17{\cdot}10^{-4}$	$7.77{\cdot}10^{-2} \pm 3.78{\cdot}10^{-4}$	9.17 ± 0.50
Coal, hard, unspecified, in ground	$0.60 \pm 1.91{\cdot}10^{-2}$	$5.31{\cdot}10^{-2} \pm 3.64{\cdot}10^{-4}$	$7.29{\cdot}10^{-2} \pm 6.83{\cdot}10^{-4}$	$6.30{\cdot}10^{-2} \pm 4.88{\cdot}10^{-4}$	10.90 ± 4.40
Coal, brown, in ground	$0.33 \pm 6.01{\cdot}10^{-3}$	$2.58{\cdot}10^{-2} \pm 9.03{\cdot}10^{-5}$	$3.97{\cdot}10^{-2} \pm 1.50{\cdot}10^{-4}$	$3.28{\cdot}10^{-2} \pm 8.96{\cdot}10^{-5}$	8.77 ± 1.83
Peat, in ground	$1.41{\cdot}10^{-5} \pm 8.79{\cdot}10^{-11}$	$1.43{\cdot}10^{-6} \pm 1.92{\cdot}10^{-12}$	$1.98{\cdot}10^{-6} \pm 2.71{\cdot}10^{-12}$	$1.70{\cdot}10^{-6} \pm 1.54{\cdot}10^{-12}$	$5.45{\cdot}10^{-5} \pm 1.12{\cdot}10^{-10}$
Gas, mine, off-gas, process, coal mining	$1.23{\cdot}10^{-2} \pm 4.44{\cdot}10^{-6}$	$1.08{\cdot}10^{-3} \pm 7.87{\cdot}10^{-8}$	$1.49{\cdot}10^{-3} \pm 1.53{\cdot}10^{-7}$	$1.29{\cdot}10^{-3} \pm 1.24{\cdot}10^{-7}$	$0.20 \pm 1.07{\cdot}10^{-3}$
Uranium, in ground	$3.66 \pm 9.68{\cdot}10^{-6}$	$0.24 \pm 8.51{\cdot}10^{-8}$	$0.26 \pm 8.21{\cdot}10^{-8}$	$0.25 \pm 6.33{\cdot}10^{-8}$	$19.66 \pm 2.02{\cdot}10^{-4}$
TOTAL (MJ)	70.77 ± 0.69	59.78 ± 260.44	35.63 ± 127.88	39.81 ± 131.08	3853.96 ± 5.09
Non-renewable energy (MJ)	6.77	0.62	0.78	0.70	60.98
Non-renewable energy (%)	9.57	1.04	2.18	1.75	1.58

The Antoine equations for methanol, methyl acetate, acetic acid, glycerol, triacetin and water are

Reactant	Antoine equation	Temperature range (K)	Reference
Methanol (ME)	$log(P) = 5.15853 - \frac{1569.613}{T - 34.846}$	353.5 - 512.63	[236]
Methyl acetate (MA)	$log(P) = 4.20364 - \frac{1164.426}{T - 52.26}$	274.91 - 328.99	[236]
Acetic acid (AA)	$log(P) = 4.68206 - \frac{1642.54}{T - 39.764}$	290.26 - 391.01	[236]
Glycerol (GLYC)	$log(P) = 3.93737 - \frac{1411.531}{T - 200.566}$	456.40 - 533.6	[236]
Triacetin (Tr)	$log(P) = 12.177 - \frac{3599.814}{T - 14.825}$	274.91 - 328.99	[250]
Water	$log(P) = 3.55959 - \frac{643.748}{T - 198.043}$	379 - 573	[236]

The partial pressures of all the reagentia from the starting temperature to their atmospheric boiling temperature are given in Figure 11.8. The boiling temperature of acetic acid is higher than water. The water need first to be removed before the acetic acid start to vaporize. Adittionally, water and acetic acid form an azeotrope. A solution could be to apply heterogeneous azeotriopic distillation by adding an entrainer. Chien et al. found that iso-butyl acetate was a promising entrainer option [251]. There is also a risk for azeotropes with the intermediate products [235]. To simplify the calculations, it is assumed that the water in the esterification reaction is removed before the acetic acid is recovered and the intermediates do not induce an azeotrope.

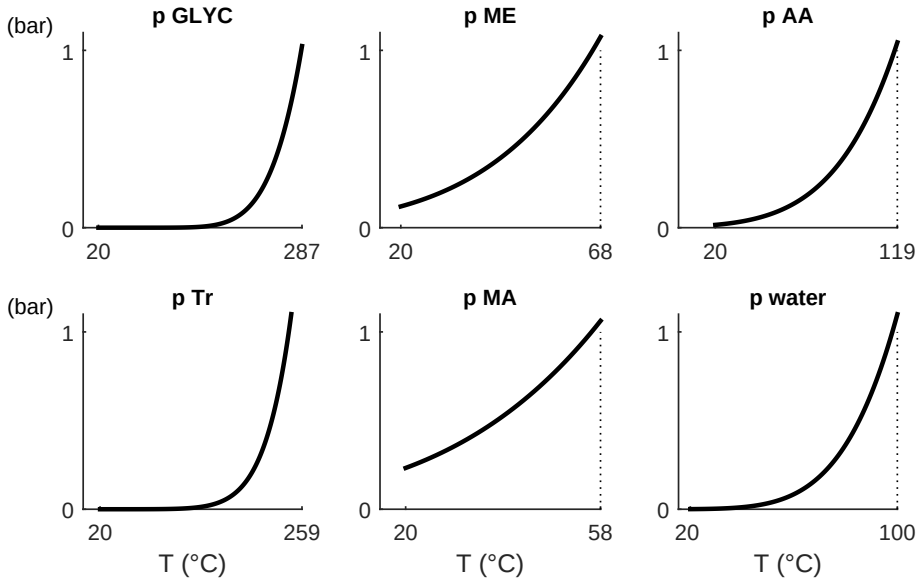

Figure 11.8: The partial pressure (bar) of the reaction products untill their boiling temperature at atmospheric pressure.

Atmospheric pressure is assumed as working pressure, so the temperature where the sum of the partial pressure of the reaction product mixture is equal to atmospheric pressure is the boiling temperature. The boiling temperatures of the mixtures at the beginning of the recovery is shown in Figure 11.9. The boiling temperature of the IRc and IRe scenario is lower due to the high excess ratio of the present methyl acetate, which has the lowest atmospheric boiling temperature of all the reaction products.

The energy needed to heat up to the boiling point is calculated in the same was as the heat required during the equilibrium reaction (Equation 11.8). The energy necessary for this step is given in Figure 11.10. The same conclusions can be drawn as for the reacting mixture heating. The heating necessary is related to the applied excess ratio and the highest values are found for the IRc scenario.

Once the mixture is boiling, evaporation enthalpies start to play a role. The enthalpy of vaporisation need to be determined for the reactants that will evaporize. The enthalpy of vaporisation is the quantity of enthalpy needed to vaporise a certain quantity of liquid at a constant temperature and can be calculated for the reactants by

$$\Delta \mathrm{H}_{\mathrm{vap}} = A \exp\left(-\alpha \frac{T}{T_c}\right)\left(1 - \frac{T}{T_c}\right)^{\beta}, \tag{11.10}$$

where A, α and β are parameters related to the assessed molecule, T is the temperature and T_c is the critical temperature.

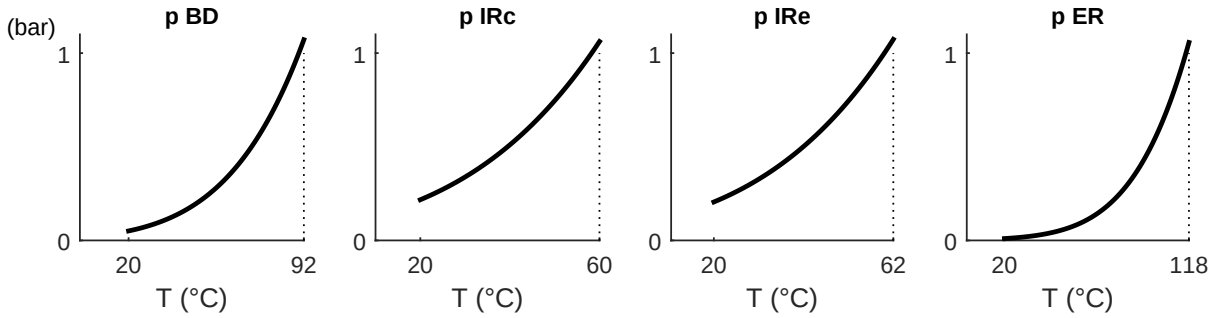

Figure 11.9: The partial pressure (bar) of the reaction products mixtures until their boiling temperature at atmospheric pressure by the start of the reactant recovery. The lowest boiling point is found for the IRc and IRe scenario, due to the presence of the excess methyl acetate.

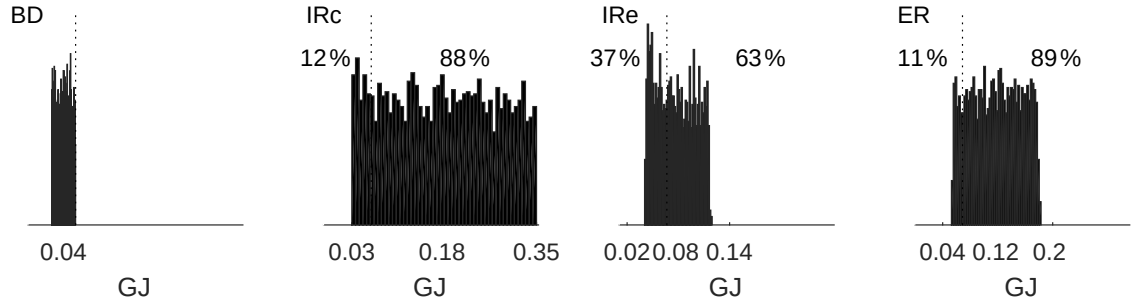

Figure 11.10: The energy in GJ needed to heat up the reaction products mixtures to their atmospheric boiling point.

Reactant	Enthalpy of vaporisation	Temperature range (K)	Ref.
Methanol	$\Delta H_{vap} = 45.3 \exp\left(0.31\frac{T}{512.6}\right)\left(1-\frac{T}{512.6}\right)^{0.4241}$	298 - 477	[236]
Methyl acetate	$\Delta H_{vap} = 48.51 \exp\left(-0.2757\frac{T}{506.8}\right)\left(1-\frac{T}{506.8}\right)^{0.2757}$	296 - 343	[236]
Acetic acid	$\Delta H_{vap} = 22.84 \exp\left(-0.0184\frac{T}{592.7}\right)\left(1-\frac{T}{592.7}\right)^{-0.0454}$	298 - 392	[236]

The boiling temperature of the reaction products mixtures increases when the reactant evaporates and the mixture needs to be heated extra. This heating is contributed to the distillation process. The enthalpy of vaporisation decreases with temperature, so at higher boiling temperature less energy will be needed to evaporate one mole of reactant. The distillation energy is calculated by an iterative method using equations from [236, 250, 252, 253, 234] and stops when all the moles reactant are vaporised. No heat recovery is implemented. The calculated energy need can also be an underprediction, since no reboiling is implemented. The calculations can be done with more accurancy in software designed to calculated the energy balances of processes, like Aspen [254]. The NEV of the distillation process is given in Figure 11.11. The IRc scenario has the highest energy demand, due the high excess ratio of 50:1. Some parameter combinations even lead to an energy need of 74% of the energy produced as biofuel. Again the BD scenario need the least energy relatively to the fuel produced, which is due to the low excess ratio of maximal 9:1.

The energy needed for the recovery of the reactant is senstivity to three parameters: the biodiesel yield, the triacetin yield and the excess ratio (Figure 11.12). NSC values with the same sign are found as for the other assessed energy contributions. However their absolute value is higher, indicating that the change in parameter value has a greater effect on the energy demand for recovery. Increasing the biodiesel yield has a positive effect, since more biofuel is produced. The higher excess ratio leads to more reactant that need to be distilled off, which is related to a higher energy demand.

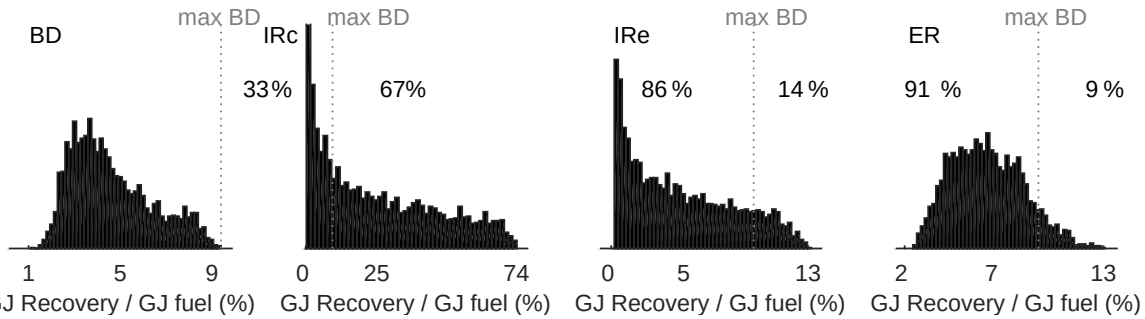

Figure 11.11: The NEV values related to the recovery of the reactant. The highest energy demand is found for the IRc scenario which is related to the high excess ratio.

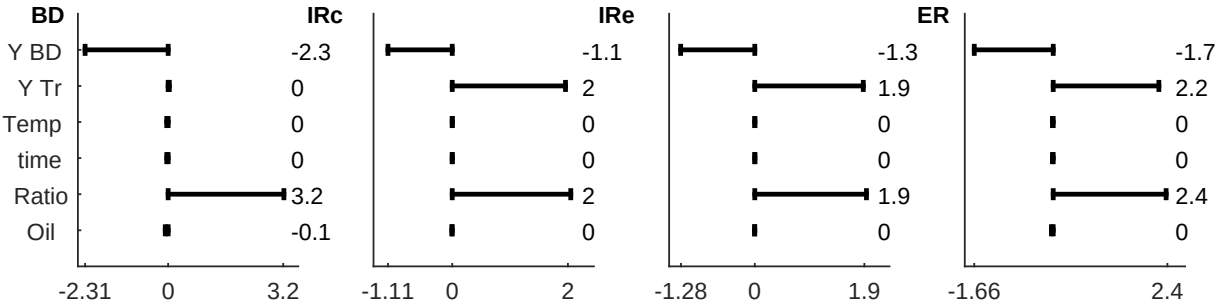

Figure 11.12: The NSC values achieved by a sensitivity analysis on the recovery of the excess reactants.

11.6 The Energy Return of Investment

The energy streams for the four assessed scenarios are summarised in Table 11.9 and 11.10. More biofuel is formed when triacetin is coproduced. An increase of 10% in energy content is found for the IRc scenario compared to the BD scenario. However, for the production and recovery of methyl acetate and acetic acid more energy is needed compared to the use of methanol and the increase in biofuel production is omitted. Nevertheless, the coproduction scenarios have still a positive net energy.

The production of the reactant is the most energy intensive production step and accounts for 72% of the energy need in the BD scenario, for 60% in the IRc scenario, 88% in the IRe scenario and for 84% in the ER scenario. The uncertainty on the IRc scenario results are related to the applied MAOMR.

Table 11.9: The mean values for the energy streams of the assessed scenarios and their standard deviation if 1000 kg of algal oil is used as feedstock.

			BD	IRc	IRe	ER
IN	Heating	(GJ)	0.07 ± 0.01	0.17 ± 0.08	0.07 ± 0.03	0.21 ± 0.04
	Reactant recovery	(GJ)	1.57 ± 0.61	9.76 ± 8.32	1.61 ± 1.22	2.45 ± 0.75
	Reactant production	(GJ)	4.30 ± 0.45	15.17 ± 2.63	12.50 ± 1.50	13.97 ± 2.69
OUT	Biofuel	(GJ)	34.84 ± 0.76	38.42 ± 0.78	35.82 ± 1.87	37.90 ± 1.02
	Net energy	(GJ)	28.90 ± 1.07	13.31 ± 8.76	21.63 ± 2.69	21.27 ± 2.98

Table 11.10: The mean values for the NEV achieved for the four scenarios, together with their standard deviation.

NEV		BD	IRc	IRe	ER
Heating	(%)	0.20 ± 0.03	0.45 ± 0.20	0.19 ± 0.07	0.55 ± 0.11
Reactant recovery	(%)	4.52 ± 1.74	25.42 ± 21.68	4.51 ± 3.42	6.47 ± 2.00
Reactant production	(%)	12.34 ± 1.26	39.49 ± 6.79	34.93 ± 3.94	36.80 ± 6.66
Total		17.06 ± 2.15	65.36 ± 22.72	39.63 ± 5.22	43.82 ± 6.96

The EROI of all the scenarios is given in Figure 11.13. For three of the four scenarios the EROI is always greater than unity, meaning that more energy is captured in the produced biofuel than the amount of energy invested during biofuel production. In 15% of the IRc runs an EROI value lower than unity is found. To make the IRc scenario vialable the maximum MAOMR value of 50 need to decrease.

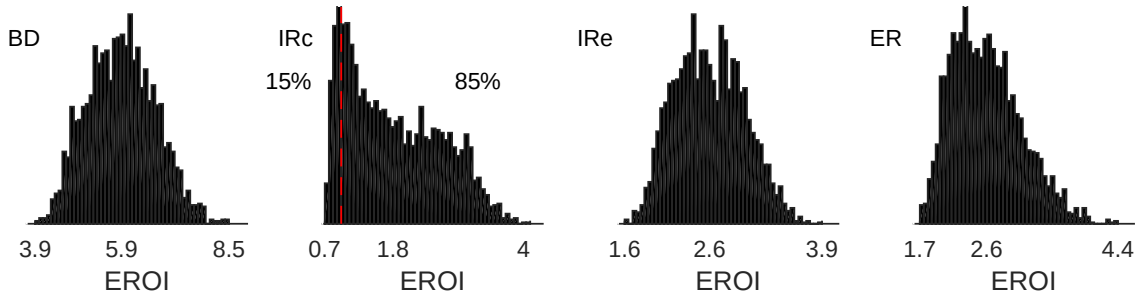

Figure 11.13: The EROIs for the different production scenarios. Three of the four scenarios have always a positive energy balance. The simulations for the IRc scenario showed that for 15% of the simulations more energy is needed for the production process than the energy content of the actual biofuel produced.

11.7 Potential for improvement

Three energy demanding steps of the production process are already taken into account. The calculation method of the energy balance can be improved by implementing more detail into the calculations, e.g. the formation of azeotropes or the production and recovery of the catalyst. This can be done if data about the process is available and by using software which can simulate the processes in more detail. However from the performed energy balance analysis, some conclusion can already be made.

With the coproduction of triacetin at least 11% more biofuel is produced in terms of energy. However the assessed production routes consumes more energy and nullify the positive biofuel production. The main reason for this is the production of the used reactant. More energy is needed to produce methyl acetate and acetic acid from fossil fuels, than methanol. Another reason why the IRc scenario performs worse than the other coproduction scenarios is the high excess ratio needed to force the equilibrium reaction to the biodiesel and triacetin side. In literature an excess ratio of 1:50 is stated. The IRc method can only be practible if a non-energy demanding process is developped to recover the excess methyl acetate from the reaction products.

It was assessed, if the production of the reactants from biomass would have a positive effect on the NNEV. Nevertheless, the production from biomass needs more energy, especially energy in the form of biomass. This energy form is renewable and the contribution of fossil fuels to the production process diminished substantially. A positive effect on the GHG emissions of the biofuel will be found if biomass is used as feedstock for the reactant production, however the NNEV will be lower compared to the production from fossil fuel when the contribution of biomass energy is taken into account.

Overall, the coproduction of triacetin could be a viable biofuel production process, if the reactant can be produced using less energy. Additionally, the reaction should be able reach high yields with a lower excess ratio, preferable not higher than the excess ratio currently found by conventional biodiesel production.

12

GHG emissions coproduction triacetin

In this chapter we assess if less GHG are emitted by the coproduction of biodiesel and triacetin than with the conventional diesel. Both the production and the combustion of the fuel are taken into account.

The main advantage of biofuels is that they are carbon neutral. The same amount of CO_2 is captured during the biomass growth as released by the combustion of the biofuel. So most of the GHG emission of the combustion of biodiesel and triacetin can be discarded. Nevertheless, during the production of biodiesel and triacetin GHG are emitted, since it is related to the consumption of fossil fuels.

Three GHG are considered: CO_2, N_2O and CH_4. N_2O and CH_4 are more severe GHG than CO_2. They have a higher Global Warming Potential (GWP) of 296 and 23 respectively, while the GWP of CO_2 is set to 1. The combination of the three GHG is stated as $CO_{2,eq}$, with applying the GWP on the N_2O and CH_4.

In a first step the GHG emissions related to the combustion of the fuel is calculated and expressed in the chosen functional unit: mass $CO_{2,eq}$ emitted normalised by the energy of the fuel burned (g $CO_{2,eq}$·MJ^{-1}). Then the GHG emitted during the production process are estimated by literature data and data from the EcoInvent database. In the end, the net GHG emissions can be calculated and compared.

12.1 GHG emission by diesel production and combustion

Diesel is a mixture of saturated hydrocarbons and aromatic hydrocarbons. The average chemical formula for diesel is $C_{12}H_{23}$ [255]. The stoichiometric combustion reaction of diesel can be written as: $C_{12}H_{23} + 17.75\cdot(O_2+3.76\cdot N_2) \rightarrow 12\ CO_2 + 11.50\ H_2O + 17.75\cdot 3.76\ N_2$. The LHV of diesel is 43.4 kJ·g diesel. Combining the LHV with the stoichiometric combustion reaction, results in a GHG emission of 73.0 g CO_2 per MJ of diesel burned.

Data about the GHG emissions during the production of diesel are published by different authors [256, 257]. Wang et al. state that 14 to 17 g $CO_{2,eq}$ per MJ of diesel at the pump is emitted. The variation in GHG emissions is related to the definitions of the system boundaries and allocations made. Lopez et al. found a value of 10.2 g $CO_{2,eq}$ per MJ of diesel, taking into account the crude oil extraction and transport, refining and distribution. From these data can be concluded that both the combustion and the production of the diesel contribute equally to the total GHG emissions.

12.2 GHG emissions coproduction scenarios

The chemical structure of the biodiesel and triacetin is known, so the CO_2 emission during their combustion can be calculated with the stoichiometric combustion reaction:

7%	$C_{15}H_{30}O_2$	$+22.5\cdot(O_2+3.76\cdot N_2)$	$\rightarrow$ 15 CO_2	+ 15 H_2O	+ 22.5·3.76 N_2
46%	$C_{17}H_{34}O_2$	$+25.5\cdot(O_2+3.76\cdot N_2)$	$\rightarrow$ 17 CO_2	+ 17 H_2O	+ 25.5·3.76 N_2
35%	$C_{17}H_{32}O_2$	$+25.0\cdot(O_2+3.76\cdot N_2)$	$\rightarrow$ 17 CO_2	+ 16 H_2O	+ 25.0·3.76 N_2
2%	$C_{19}H_{38}O_2$	$+28.5\cdot(O_2+3.76\cdot N_2)$	$\rightarrow$ 19 CO_2	+ 19 H_2O	+ 28.5·3.76 N_2
10%	$C_{19}H_{36}O_2$	$+28.0\cdot(O_2+3.76\cdot N_2)$	$\rightarrow$ 19 CO_2	+ 18 H_2O	+ 28.0·3.76 N_2
100%	$C_{17.1}H_{33.3}O_2$	$+25.4\cdot(O_2+3.76\cdot N_2)$	$\rightarrow$ 17.1 CO_2	+ 16.7 H_2O	+ 25.4·3.76 N_2

The combustion of a mole biodiesel results in the emission of 17.1 moles CO_2. One of the carbons in the biodiesel is retrieved from methanol derived from fossil fuels, the other carbons are derived from biomass.

The stoichiometric combustion of triacetin ($C_9H_{14}O_6$) is as follows

$C_9H_{14}O_6 \quad +9.5\cdot(O_2+3.76\cdot N_2) \quad \rightarrow 9\ CO_2 \quad + 7\ H_2O \quad + 9.5\cdot3.76\ N_2,$

so nine moles of CO_2 are formed by the combustion of one mole of triacetin, however three of carbon atoms are derived from biomass.

The GHG emitted per MJ fuel combusted can be calculated. In Table 12.1 the total GHG emissions during biofuel combustion are given for each scenario together with the GHG emissions related to fossil resources. The total GHG emissions of all the scenarios are higher compared to the diesel combustion (73 g $CO_2\cdot MJ^{-1}$). However, if only the emissions related to fossil resources are taken into the account, the emissions of the biofuels reduce to around 5 g $CO_2\cdot MJ^{-1}$, an improvement compared to diesel.

Next, the emission of GHG during the production of the biofuels is assessed. The heating during the equilibrium reaction, the production and the recovery of the reactant consume energy, which is assumed to come from fossil resources.

The GHG emissions related to the heating and recovery process cannot be derived directly from the EcoInvent database, first the energy source need to be defined. As energy source the combustion of natural gas in an industrial furnace is assumed. Data is available in the EcoInvent database for natural gas, burned in an industrial furnace in the European Union with a power output greater than 100 kW. The GHG emitted to produce 1 MJ of heat is given in Table 12.3. The energy needed for the heating during the fuel production and the recovery of the reactant is calculated in Section 11.5.1 and 11.5.3. Multiplying the energy needed for recovery and heating with the GHG emitted by the combustion of natural gas in a furnace gives the total GHG emitted during the processes. The total GHG emission is then normalised by the energy content of the fuel. The normalised GHG emissions can be found in Table 12.2.

The GHG-emissions during the production of the reactants can be derived directly from the EcoInvent database. The different contribution are given in Table 12.3. Emissions from biogenic sources are not taken into account. The GHG emission to produce 1 kg of methanol is 0.74 kg of $CO_{2,eq}$. The production of methyl acetate and acetic acid emits more $CO_{2,eq}$. The production of 1 kg methyl acetate emits 1.19 kg $CO_{2,eq}$ and for methyl acetate there are three production routes available, with emissions of 1.07, 2.40 and 1.35 kg $CO_{2,eq}$ per kg acetic acid produced. The GHG emissions can be multiplied with the mass of the reactant that is used during the reaction. The total GHG emitted is then normalised by the energy content of the fuel and the obtained normalised GHG emissions are given in Table 12.2.

The heating during the equilibrium reaction is related to the lowest GHG emissions of the

Table 12.1: Total GHG emission and their standard deviation during the combustion of the biofuel. The GHG emissions related to fossil resources and their standard deviation are also given.

Scenario	Total GHG emissions ($g\ CO_2 \cdot MJ^{-1}$)	GHG related to fossil resources ($g\ CO_2 \cdot MJ^{-1}$)
BD	75.0 ±0.15	4.4 ±0.01
IRc	79.5 ±0.35	5.2 ±0.11
IRe	80.2 ±0.52	5.0 ±0.16
ER	81.1 ±1.38	6.4 ±0.42

Table 12.2: Total GHG emission and their standard deviation during the combustion of the biofuel. The GHG emissions related to fossil resources and their standard deviation are also given.

Scenario	GHG emissions Heating ($g\ CO_2 \cdot MJ^{-1}$)	GHG emissions Reactant production ($g\ CO_2 \cdot MJ^{-1}$)	GHG emissions Reactant recovery ($g\ CO_2 \cdot MJ^{-1}$)	Total GHG emissions ($g\ CO_2 \cdot MJ^{-1}$)
BD	0.14 ±0.02	2.43 ±0.10	3.11 ±1.20	5.68 ±1.20
IRc	0.30 ±0.14	9.94 ±1.61	16.90 ±14.43	27.15 ±14.52
IRe	0.13 ±0.05	8.82 ±0.85	3.16 ±2.37	12.11 ±2.50
ER	0.51 ±0.08	12.00 ±1.49	4.68 ±1.44	17.84 ±2.08

three assessed processes. The GHG emissions are found for the ER scenario, since this scenario has also the highest energy demand. The greatest variation in GHG emissions is found for the IRc scenario, due to the variation in MAOMR.

The normalised $CO_{2,eq}$ emissions for the production and recovery of the reactant are higher in the coproduction scenarios, despite the higher biofuel production in these scenarios. The extra biofuel produced cannot counteract the higher emissions during the reactant production and recovery. The normalised $CO_{2,eq}$ emission for the reactant production is on average 2.43 $CO_{2,eq} \cdot MJ^{-1}$ biofuel for the BD scenario and 9.94, 8.82 and 12.00 $CO_{2,eq} \cdot MJ^{-1}$ biofuel for the IRc, IRe and ER coproduction scenarios respectively. The highest emissions are found for the ER scenario, since both methanol and acetic acid are used by this scenario. The values found for the IRc and IRe scenario are comparable. They both use methyl acetate as reactant. The lower GHG emissions in the IRe scenario are related a lower need for methyl acetate. The lower yield for the triacetin production in the IRe scenario and the lower losses during the methyl acetate recovery, result in a lower consumption of methyl acetate.

The IRc scenario has the highest GHG emissions during the recovery of the reactant. A value of 16.90 $CO_{2,eq} \cdot MJ^{-1}$ is found, due to the implied MAOMR, which can be maximal 50. The GHG emissions related to the recovery of the other scenarios are between 3 and 5 $CO_{2,eq} \cdot MJ^{-1}$.

The total GHG emissions during the production of the biofuels can be calculated by adding the emissions for the three assessed processes. The lowest emission of 5.68 $CO_{2,eq} \cdot MJ^{-1}$ is found for the BD scenario. The coproduction scenarios have all higher GHG emissions, varying from 12.1 to 27.2 $CO_{2,eq} \cdot MJ^{-1}$, mostly due to the production and recovery of the used reactant.

Table 12.3: The GHG emitted by the production of the reactants [232].

Contribution GHG-emission	Unit	Methanol (1 kg)	Methyl acetate (1 kg)	Acetic acid (1 kg)			CH_4 in furnace (1 MJ)
Carbon dioxide, fossil [air low population density]	(kg)	$9.84{\cdot}10^{-2} \pm 1.27{\cdot}10^{-3}$	0.32 ± 0.016	0.32 ± 0.018	0.43 ± 0.04	0.57 ± 0.07	$2.61{\cdot}10^{-3} \pm 1.48{\cdot}10^{-6}$
Carbon dioxide, fossil [air high population density]	(kg)	$0.53 \pm 2.27{\cdot}10^{-2}$	0.70 ± 0.074	0.70 ± 0.087	1.86 ± 0.50	0.67 ± 0.07	$6.12{\cdot}10^{-2} \pm 1.58{\cdot}10^{-4}$
Carbon dioxide, land transformation [air low population density]	(kg)	$7.23{\cdot}10^{-6} \pm 3.76{\cdot}10^{-11}$	$1.91{\cdot}10^{-5} \pm 1.36{\cdot}10^{-10}$	$1.91{\cdot}10^{-5} \pm 1.04{\cdot}10^{-10}$	$4.68{\cdot}10^{-5} \pm 6.62{\cdot}10^{-10}$	$5.90{\cdot}10^{-5} \pm 9.89{\cdot}10^{-10}$	$2.08{\cdot}10^{-7} \pm 1.86{\cdot}10^{-14}$
Carbon dioxide, fossil [air lower stratosphere + upper troposphere]	(kg)	$9.38{\cdot}10^{-10} \pm 4.57{\cdot}10^{-19}$	$3.65{\cdot}10^{-7} \pm 1.01{\cdot}10^{-13}$	$3.65{\cdot}10^{-7} \pm 1.11{\cdot}10^{-13}$	$6.43{\cdot}10^{-7} \pm 3.58{\cdot}10^{-13}$	$4.88{\cdot}10^{-7} \pm 2.10{\cdot}10^{-13}$	$1.81{\cdot}10^{-11} \pm 2.83{\cdot}10^{-22}$
Carbon dioxide, fossil [air unspecified]	(kg)	$6.71{\cdot}10^{-3} \pm 1.01{\cdot}10^{-5}$	0.042 ± 0.0007	0.042 ± 0.001	$0.11 \pm 3.34{\cdot}10^{-3}$	$0.10 \pm 3.37{\cdot}10^{-3}$	$2.65{\cdot}10^{-4} \pm 1.97{\cdot}10^{-8}$
Dinitrogen monoxide [air high population density]	(kg)	$2.80{\cdot}10^{-6} \pm 4.16{\cdot}10^{-12}$	$6.72{\cdot}10^{-6} \pm 1.02{\cdot}10^{-11}$	$6.72{\cdot}10^{-6} \pm 1.14{\cdot}10^{-11}$	$9.76{\cdot}10^{-6} \pm 2.17{\cdot}10^{-11}$	$1.20{\cdot}10^{-5} \pm 3.48{\cdot}10^{-11}$	$1.90{\cdot}10^{-7} \pm 3.57{\cdot}10^{-14}$
Dinitrogen monoxide [air low population density]	(kg)	$1.25{\cdot}10^{-6} \pm 3.82{\cdot}10^{-13}$	$3.85{\cdot}10^{-6} \pm 3.27{\cdot}10^{-12}$	$3.85{\cdot}10^{-6} \pm 4.13{\cdot}10^{-12}$	$9.79{\cdot}10^{-6} \pm 2.21{\cdot}10^{-11}$	$7.39{\cdot}10^{-6} \pm 1.36{\cdot}10^{-11}$	$2.74{\cdot}10^{-8} \pm 3.77{\cdot}10^{-16}$
Dinitrogen monoxide [air lower stratosphere + upper troposphere]	(kg)	$8.93{\cdot}10^{-15} \pm 4.51{\cdot}10^{-28}$	$3.47{\cdot}10^{-12} \pm 1.03{\cdot}10^{-23}$	$3.47{\cdot}10^{-12} \pm 1.13{\cdot}10^{-23}$	$4.64{\cdot}10^{-12} \pm 2.59{\cdot}10^{-23}$	$6.13{\cdot}10^{-12} \pm 3.24{\cdot}10^{-23}$	$1.72{\cdot}10^{-16} \pm 3.08{\cdot}10^{-30}$
Dinitrogen monoxide [air unspecified]	(kg)	$7.95{\cdot}10^{-7} \pm 1.65{\cdot}10^{-13}$	$2.74{\cdot}10^{-6} \pm 1.46{\cdot}10^{-12}$	$2.74{\cdot}10^{-6} \pm 1.82{\cdot}10^{-12}$	$8.31{\cdot}10^{-6} \pm 1.64{\cdot}10^{-11}$	$8.19{\cdot}10^{-6} \pm 1.58{\cdot}10^{-11}$	$1.43{\cdot}10^{-8} \pm 4.66{\cdot}10^{-17}$
Methane, fossil [air low population density]	(kg)	$4.20{\cdot}10^{-3} \pm 4.79{\cdot}10^{-6}$	$0.0055 \pm 1.48{\cdot}10^{-5}$	$6.72{\cdot}10^{-6} \pm 1.14{\cdot}10^{-11}$	$9.76{\cdot}10^{-6} \pm 2.17{\cdot}10^{-11}$	$1.20{\cdot}10^{-5} \pm 3.48{\cdot}10^{-11}$	$1.58{\cdot}10^{-04} \pm 1.21{\cdot}10^{-8}$
Methane, fossil [air high population density]	(kg)	$2.70{\cdot}10^{-5} \pm 5.61{\cdot}10^{-10}$	$5.99{\cdot}10^{-5} \pm 1.00{\cdot}10^{-9}$	$3.85{\cdot}10^{-6} \pm 4.13{\cdot}10^{-12}$	$9.79{\cdot}10^{-6} \pm 2.21{\cdot}10^{-11}$	$7.39{\cdot}10^{-6} \pm 1.36{\cdot}10^{-11}$	$2.64{\cdot}10^{-6} \pm 7.67{\cdot}10^{-12}$
Methane, fossil [air lower stratosphere + upper troposphere]	(kg)	$1.49{\cdot}10^{-14} \pm 1.73{\cdot}10^{-28}$	$5.79{\cdot}10^{-12} \pm 2.86{\cdot}10^{-23}$	$3.47{\cdot}10^{-12} \pm 1.13{\cdot}10^{-23}$	$4.64{\cdot}10^{-12} \pm 2.59{\cdot}10^{-23}$	$6.13{\cdot}10^{-12} \pm 3.24{\cdot}10^{-23}$	$2.87{\cdot}10^{-16} \pm 1.62{\cdot}10^{-29}$
Methane, fossil [air unspecified]	(kg)	$2.10{\cdot}10^{-7} \pm 1.43{\cdot}10^{-14}$	$1.40{\cdot}10^{-6} \pm 6.49{\cdot}10^{-13}$	$2.74{\cdot}10^{-6} \pm 1.82{\cdot}10^{-12}$	$8.31{\cdot}10^{-6} \pm 1.64{\cdot}10^{-11}$	$8.19{\cdot}10^{-6} \pm 1.58{\cdot}10^{-11}$	$5.95{\cdot}10^{-9} \pm 1.31{\cdot}10^{-17}$
Total $CO_{2,eq}$	(kg)	$0.74 \pm 2.27{\cdot}10^{-2}$	$1.19 \pm 7.40{\cdot}10^{-2}$	$1.07 \pm 8.71{\cdot}10^{-2}$	$2.40 \pm 5.05{\cdot}10^{-1}$	$1.35 \pm 7.00{\cdot}10^{-2}$	$0.07 \pm 1.58{\cdot}10^{-4}$

Table 12.4: The GHG emissions estimations found in the European directive about GHG reductions by biofuels for the production of biodiesel from different feedstocks [168].

Production traject of biofuels	Standard GHG emissions ($gCO_{2,eq}$/MJ)			
	Cultivation	Processing	Transport and distribution	Total
Biodiesel from rapeseed	29	22	1	52
Biodiesel from sunflowers	18	22	1	41
Biodiesel from soy beans	19	26	13	58
Biodiesel from vegetable and animal waste	0	13	1	14

12.3 Net GHG emissions

An overview of the total GHG emissions for diesel and the three assessed coproduction scenarios is given in Table 12.5. GHG emissions of the same order of magnitude are found for diesel, biodiesel and the coproduction scenarios, when all the CO_2 emitted during combustion is taken into account. The coproduction scenarios have even a higher CO_2 emission than the diesel and biodiesel scenario.

Nevertheless, if only the CO_2 related to fossil resources considered, the combustion contribution of both the biodiesel and the coproduction scenarios decrease. A value of 10.07 $CO_{2,eq}{\cdot}MJ^{-1}$ is found for the biodiesel scenario. Higher values ranging from 17.11 to 32.36 $CO_{2,eq}{\cdot}MJ^{-1}$ are found for the coproduction scenarios, due to their higher $CO_{2,eq}$ emission during the production and recovery of the reactant. The biofuels scenarios have now a lower GHG emissions compared to diesel. Following the EU regulations a biofuel should lead to a decrease of 60% in the GHG emissions (Section 9.1). All the assessed biofuels scenarios comply with this regulation.

Table 12.5: Total GHG emission and the related standard deviation for diesel and the three coproduction scenarios, including the combustion and fuel production. If only the emissions related to fossil resources are taken into account, the combustion contribution decreases for the coproduction scenarios, leading to GHG emissions values which are lower than the diesel emissions.

	GHG emissions ($CO_{2,eq}{\cdot}MJ^{-1}$)				
	Diesel	**BD**	**IRc**	**IRe**	**ER**
Total	86.73±3.4	80.69±1.21	106.68±14.53	92.35±2.55	98.30±2.50
Fossil	86.73±3.4	10.07±1.20	32.36±14.52	17.11±2.51	23.57±2.11

13 Conclusion

Conventional biodiesel production was compared with three possibilities to coproduce biodiesel and triacetin. To keep the comparison simple, only the main differences in energy consumption between the scenarios are taken into account. These differences are: the equilibrium reaction, the used reactant and the energy content of the derived biofuel. For the equilibrium reaction the temperature, reaction time and excess ratio differ, leading to different energy needs. The conventional biodiesel scenario requires the least energy, mainly due to the lower excess ratio and the related lower energy need for the recovery of the reactant.

The energy to produce the used reactant (methanol, methyl acetate and acetic acid) from fossil fuel was deduced from the EcoInvent database. To produce methanol less fossil resources is needed and less GHG are emitted. Therefore, the conventional biodiesel production is again the most positive option.

The amount of the produced biofuel increases when triacetin is coproduced. However, when the net energy is calculated, it seems that the extra energy produced does not meet the extra energy needs for reactant production and recovery. To make the coproduction of triacetin economically feasible another production process for methyl acetate and acetic acid is needed and the reaction parameters need to be improved, so a lower excess ratio can lead to high biodiesel and triacetin yields.

The EROI of conventional biodiesel production derived in this work varies between 3.9 to 8.5, with an average value of 5.9. Lower EROI values are found for the coproduction scenarios. The averge EROI value is 1.8, 2.6 and 2.6 for the IRc, IRe and ER scenario. Value lower than unity are even found for the IRc scenario, meaning that the production of the biofuels needs more energy than the energy content of the produced biofuel. The variability of the IRc EROI value is related to the uncertainty on the recovery of the reactant and the high maximum limit of 50 for it MAOMR.

The GHG emission of the four scenarios are also assessed and compared to diesel. The biofuel scenarios score better compared to diesel, when the CO_2 emissions during fuel combustion from biogenic origin are not taken into account. The biodiesel scenario has the lowest GHG emission of the biofuel scenarios, since less energy is needed for its production.

In conclusion, the cogeneration of triacetin needs in general more energy to produce biofuel in comparison with conventional biodiesel production. The main reason is the higher energy need for the production of methyl acetate and acetic acid. Also in terms of GHG emissions is the biodiesel scenario better, since GHG emissions are related to energy need during production. The main advantage of the coproduction scenarios is that more biofuel is produced in terms of energy and volume and that there is no waste stream of glycerol.

Perspectives

In this chapter the possibilities for future research or improvement of the results are discussed.

Experimental setup A Botha-Spalding burner combined with GC-TCD/FID is used to measure the mole fraction profiles in MPE flames at a pressure of 55 mbar. High experimental uncertainties are found for the intermediate species by propagation of the error due to the components in the experimental setup. The uncertainty on the measured mole fraction profiles is high, due to the uncertainty related to calibration. The compression of the sample to atmospheric pressure can lead to condensation of compounds in the sample and incorrectly measured mole fraction profiles.

These disadvantages of the experimental setup can be resolved by using another separation and detection method. If mass spectrometry is used, the compression system is not needed. The separation of the sample and the detection of the species would be done with more precision and in less time. Another advantage is that radicals can also be measured by mass spectrometry. Nevertheless, this will be a high investment.

Temperature measurements At the moment, the temperature profiles of the laminar flames are measured with a fine wire thermocouple. The temperature in low temperature flames can be measured and corrected for radiation losses without any problem. Nevertheless, for the high temperature flames assessed in this work, the correction for radiation losses is not easy to determine. Two correction methods are assessed in this work: ECM and HTM, and both have their disadvantages.

A current needs to be applied on the thermocouple for the experimental ECM, increasing the risk to break the thermocouple. In addition, the experimental data of the Electrical Compensation Method (ECM) needs to be extrapolated to higher flame temperatures. However due to the uncertainty on the applied polynomials order, unfeasible flame temperatures which are higher than the adiabatic flame temperature, are achieved. Future work can focus on the temperature dependency of the temperature correction.

The main disadvantage of the Heat Transfer Model (HTM) method is the selection of an appropriate Nusselt number correlation. The fine wire thermocouple can behave as a cylinder (the thermocouple wires) or as a sphere (the thermocouple junction). In this work, experimental data determined by Hibshman [138] is used to determine a correction factor N related to the transient behaviour of the thermocouple between a sphere and a cylinder. Regarding literature, the thermocouple should behave as a cylinder, however corrected temperatures higher than the adiabatic flame temperature are achieved with this method. If the correction factor N is taken into account, acceptable temperature corrections for radiation losses are achieved. A linear order is assumed for the transient behaviour of the thermocouple based on the data from Hibshman. The HTM can be improved by researching further the transient behaviour of the thermocouple between a sphere and cylinder, and determining a Nusselt number correlation which is applicable at high temperature flames.

The temperature of the laminar flames can also be measured by optical methods using infra red light and lasers. The flame is already optical accessible and no correction for radiation losses will be needed with these methods. Nevertheless, this will be a high investment.

Validation MPE mechanism The MPE mechanism is validated against several combustion configurations. Future research is needed for the ignition delay in mixtures with a two-

step igntion, the only combustion situation that could not be predicted correctly by the mechanism. Also the completeness of the MPE submechanism should be checked and the pressure dependency of the reactions in the MPE submechanism can be determined.

Currently, the proposed mechanism overpredicts the ignition delay for mixtures with a two-step ignition. Nevertheless, its performance for mixtures with a single-step ignition is better than the other MPE mechanism published in literature.

Energy balance calculations for triacetin The energy balance calculations can be improved by using commercial software which can calculate the energy need of a process in more detail. Also more production steps can be added and the possibilities to produce the needed reactants from biomass can be investigated further. Nevertheless, at the moment no data is available for the triacetin coproduction at industrial scale.

GHG emissions coproduction triacetin The GHG calculations are related to the energy demand of the assessed processes. So the improvements related to the GHG calculations are the same as the ones stated for the energy balance calculations. The calculations can be repeated in more detail, more reaction processes can be implemented and the production of reactants from biomass needs further investigation.

Appendix 1: Calibration permanent gases

The calibrated permanent gases are ethylene (C_2H_4), methane (CH_4), propane (C_3H_8), CO, CO_2, O_2 and hydrogen (H_2). In this appendix, the calibration of the gases is discussed into detail. The experimental conditions of the measurements are discussed and extra attention is given on the repeatability and accurancy of the measurements.

Gas bottles containing the permanent gases, other than O_2, H_2 and C_2H_4, are connected to the experimental setup by the ethylene or hydrogen mass flow controller. The ethylene and hydrogen MFC are not calibrated for other permanent gases, therefore a correction factor C needs to be applied on the achieved volume flow:

$$C = \frac{c_{p,1}\rho_1}{c_{p,2}\rho_2} \tag{13.1}$$

Where $c_{p,1}$ and ρ_1 are the heat capacity and density for the gas for which MFC is calibrated at normal conditions, and $c_{p,2}$ and ρ_2 are the heat capacity and density for the gas which the MFC is actually controlling at normal conditions.

Propane

The propane bottle is connected via the ethylene MFC. The correction factor implied on the volume flow is 0.569 (Table 13.1). The pressure in the combustion chamber is regulated to 55.3 mbar. During sampling, which takes 45 seconds, the pressure of the combustion chamber is measured around 45 times.

The found standard deviations on the combustion chamber pressure is maximal 0.0784 mbar, a relative variation of maximum 0.1%, implying that the burner pressure during sampling is stable (Figure 13.1, a). Next to the pressure in the combustion chamber, the maximum pressure of the collected samples is compared. If the pressure is the same in the combustion chamber, maximum pressure of the sample should also be the same. A maximal sample pressure of 52.17±0.14 mbar is found on average (Figure 13.1 b).

The pressure before the GC injection is given in Figure 13.1 c. In Section 13 the proof is given that the injection pressure affects the chromatogram substantial. The injection pressures difference with the atmospheric pressure should therefore not be higher than 0.05 bar.

In the end, a calibration curve for propane is found, with a R^2 value of 1.00.

$$Area_{C_3H_8} = 3\ 127\ 321\ 676\ X_{C_3H_8} \tag{13.2}$$

Table 13.1: Density and specific heat capacity at normal conditions for ethylene and propane. From this values a correction factor of 0.569 can be calculated, which means that if the volume flow is set to 1 $L_N \cdot m^{-1}$ the actual gas flow will be 0.569 $L_N \cdot m^{-1}$

	ρ	c_p	C
C_2H_4	1.261	0.414	0.569
C_3H_8	2.012	0.456	

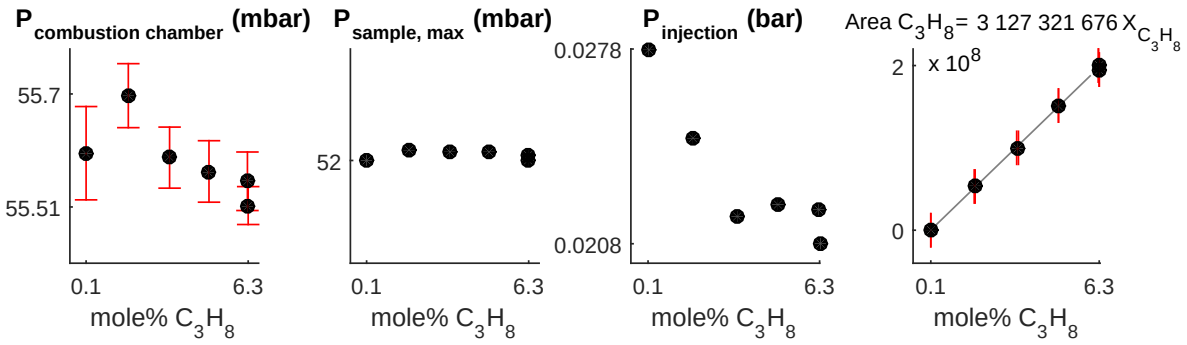

Figure 13.1: Monitoring data for the propane calibration. Six measuring points are assessed with a C_3H_8 mole fraction varying from 0.1 to 6.3 mole%. A calibration curve with a R^2 value of 1.00 is obtained.

Ethylene

Ethylene is used for the flame ignition and therefore an ethylene bottle with an MFC specially calibrated for ethylene is present in the experimental setup. No correction of the ethylene flow is needed.

For the ethylene calibrateion, 17 measurements are conducted. As for propane, the pressure in the combustion chamber is kept constant (55.6 ± 0.0572 mbar), while the average of the maximum sample pressure is 52.33 ± 0.31 mbar (Figure 13.2). The R^2 value of the achieved calibration curve is only 0.90 due to the experimental variability.

$$Area_{C_2H_4} = 1\ 153\ 860\ 089\ X_{C_2H_4} \tag{13.3}$$

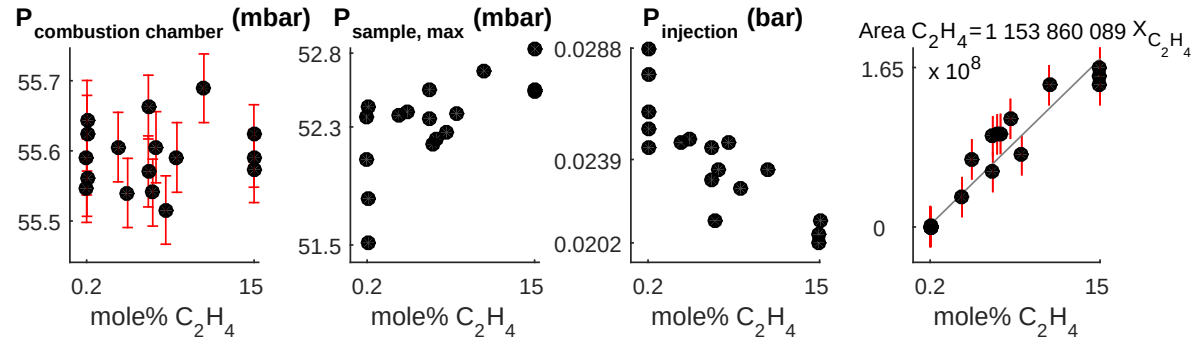

Figure 13.2: Monitoring data for the ethylene calibration. Seventeen measuring points are assessed with a C_2H_4 mole fraction varying from 0.2 to 15 mole%. A calibration curve with a R^2 value of 0.90 is obtained.

Methane

Via the MFC for ethylene, the methane bottle is connected. The correction factor for the methane volume flow is determined at 1.281 (Table 13.2). The pressure in the combustion chamber during the methane calibration is very stable, with an average pressure of 55.6 ± 0.075 mbar. The obtained calibration curve for methane is given as

$$Area_{CH_4} = \ 781\ 591\ 418\ X_{CH_4}. \tag{13.4}$$

Table 13.2: Density and specific heat capacity at normal conditions for ethylene and methane. From this values a correction factor of 1.281 can be calculated, which means that if the volume flow is set to 1 $L_N \cdot m^{-1}$ the actual gas flow will be 1.281 $L_N \cdot m^{-1}$

	ρ	c_p	C
C_2H_4	1.261	0.414	1.281
CH_4	0.7175	0.568	

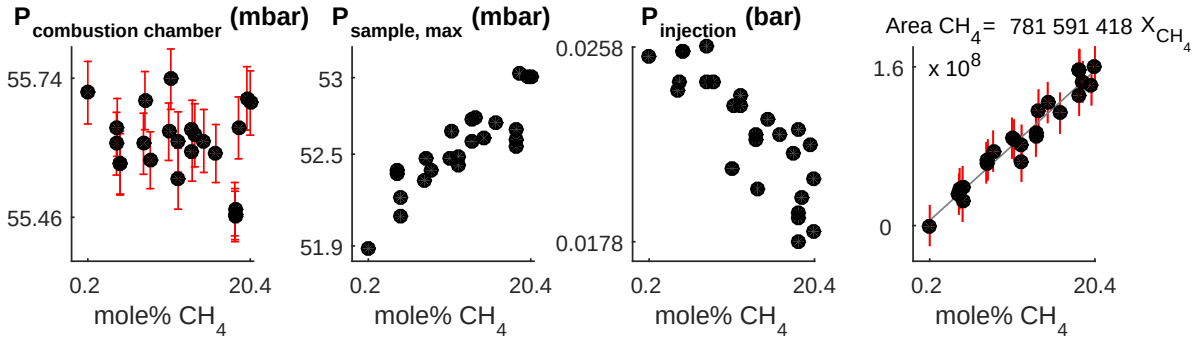

Figure 13.3: Monitoring data for the methane calibration. Seven measuring points are assessed with a CO_2 mole fraction varying from 2.2 to 18 mole%. A calibration curve with a R^2 value of 0.98 is obtained.

Carbon dioxide

The CO_2 bottle is connected to the experimental setup by the MFC for hydrogen. The corretion factor is calculated to be 0.726 (Table 13.3) and the calibration curve is

$$Area_{CO_2} = \ 759\ 885\ 791\ X_{CO_2}. \tag{13.5}$$

Table 13.3: Density and specific heat capacity at normal conditions for hydrogen and CO_2. From this values a correction factor of 0.726 can be calculated, which means that if the volume flow is set to 1 $L_N \cdot m^{-1}$ the actual gas flow will be 0.726 $L_N \cdot m^{-1}$

	ρ	c_p	C
H_2	0.088991	3.44	0.726
CO_2	1.977	0.213	

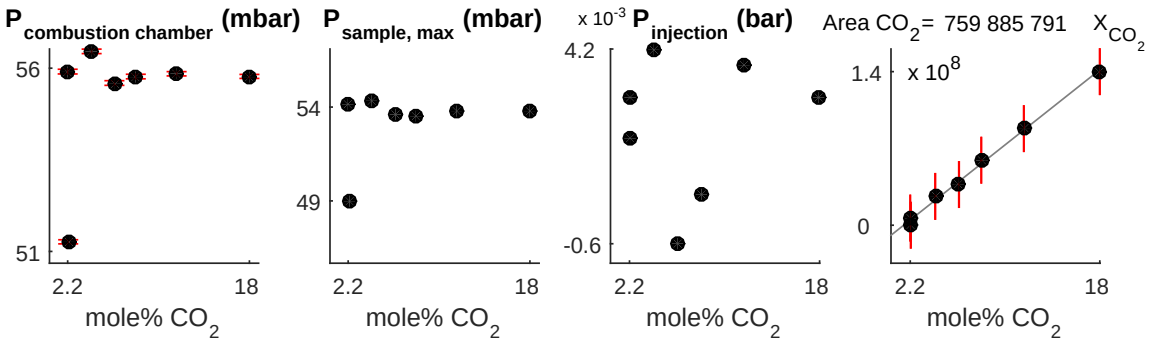

Figure 13.4: Monitoring data for the carbon dioxide calibration. Seven measuring points are assessed with a CO_2 mole fraction varying from 2.2 to 18 mole%. A calibration curve with a R^2 value of 0.98 is obtained.

Hydrogen

As ethylene, an hydrogen gas bottle is standard to the experimental set-up and no correction need to be applied on the hydrogen volume flow. Fourteen gas mixtures with a mole fraction of H_2 varying between 2.4 and 8.9 are injected (Figure 13.5). The effect of increasing the total mass flow of the gas mixture on the found GC areas is investigated. The increase of the mass flow results in an increase of the pressure in combustion chamber, from 46.7 to 55.7 mbar, but not of the injected-sample pressure.

During flame measurements, the pressure in the combustion chamber needs to be constant since it influences the shape of the flame.

In the end, a calibration curve is found for hydrogen, with a R^2 value of 0.98.

$$Area_{H_2} = 1\ 062\ 783\ 830\ X_{H_2} \tag{13.6}$$

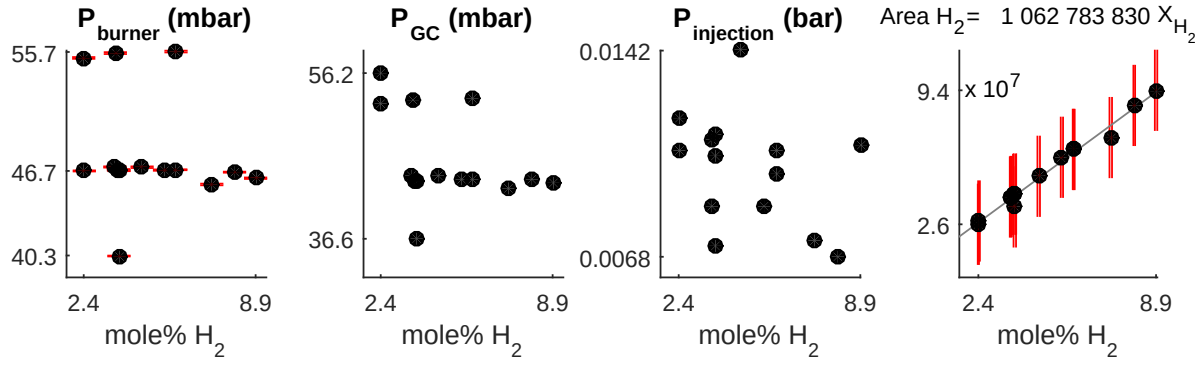

Figure 13.5: Monitoring data for the hydrogen calibration. Fourteen measuring points are assessed with a hydrogen mole fraction varying from 2.4 to 8.9 mole%. A calibration curve with a R^2 value of 0.98 is obtained.

Oxygen

To control the oxygen supply, an MFC calibrated for N_2 is used, with a correction factor C of 0.98 needs to be applied on the volume flow of oxygen (Table 13.4).

For the calibration of oxygen, 15 measurements are conducted, to obtain a calibration curve for oxygen (Equation 13.7).

$$Area_{O_2} = \ 124\ 082\ 490\ X_{O_2} \tag{13.7}$$

Table 13.4: Density and specific heat capacity at normal conditions for nitrogen and oxygen. From this values a correction factor of 0.98 can be calculated, which means that if the volume flow is set to 1 $L_N \cdot m^{-1}$ the actual gas flow will be 0.98 $L_N \cdot m^{-1}$

	ρ	c_p	C
N_2	1.250	0.249	0.98
O_2	1.429	0.222	

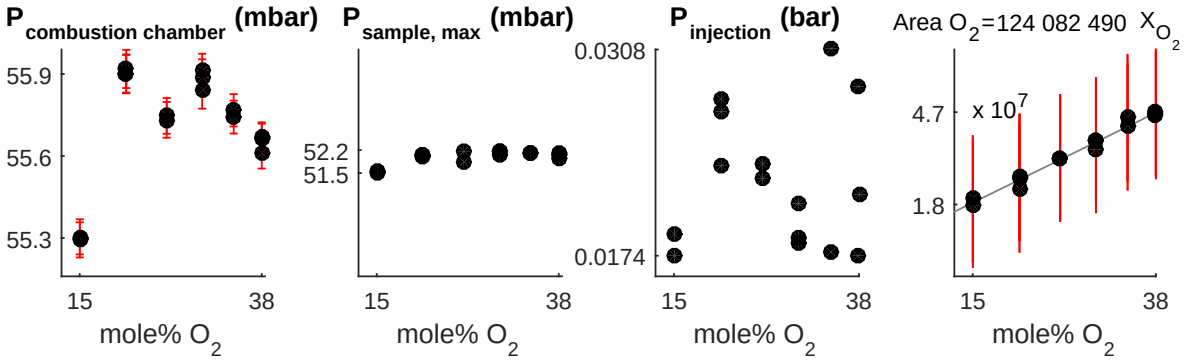

Figure 13.6: Monitoring data for the oxygen calibration. Fifteen measuring points are assessed with a oxygen mole fraction varying from 15 to 38 mole%. A calibration curve with a R^2 value of 0.98 is obtained.

Influence of the injection pressure on the calibration curve

To quantify the effect of the injection pressure on the shape of the chromotogram and the related mole fraction, samples with a known composition are injected at different pressures in the GC equipment.

The gas bottle with a known composition (Table 13.5) is directly connected to the GC-equipment, the injection is not controlled by the experimental set-up. The sensitivity of the calibration results for the injection pressure is assessed by injecting samples at 1 and 2 bar above atmospheric pressure. Due to the capillarity of the GC column, the injection pressure stays at the set pressure on the gas bottle expander. A third injection sample is also injected in the GC equipment at atmospheric pressure.

The measurements are repeated 3 times and the calibration results are given in Figure 13.7. For CH_4 and CO_2 a match is found between the experimental value and the known composition of the sampled gas bottle. The measured CO_2 mole% underpredicts the gas bottle content by 2 mole%.

An increase of the injection pressure leads to an augmentation of the measured mole fraction with a factor of 1.6 and 2.6 for 1 and 2 bar over pressure, respectively. These experimental results confirm again the influence of the injection pressure on the chromatogram results.

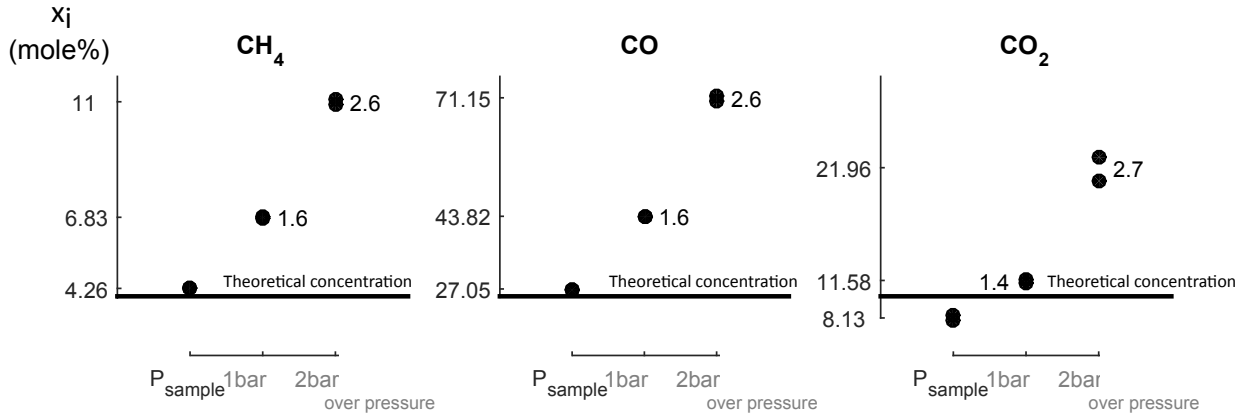

Figure 13.7: The injected pressure of a sample has an influence on the attained chromatogram areas. When a sample is injected without pressure difference over the GC capilar, P_{sample}, the measured mole fraction for CH_4 and CO have the same order of magnitude as the stated composition of the gas bottle. The measured CO_2 composition underpredicts the bottle content with 2%. However, if a pressure of 1 bar is applied, the measured mole fraction increases with a factor of around 1.6; and a factor of 2.6 if 2 bar over pressure is applied. From these results, the influence of the injection pressure on the chromatogram is proven and the injection pression should be minimal when a sample is injected.

Table 13.5: Composition of the gas bottle used to validate the calibration of CO_2 and CH_4

Component	Concentration	Standard deviation
CH_4	3.972	0.079
CO	25.36	0.51
CO_2	10.12	0.20
H_2	16.03	0.32
N_2	44.518	0

Appendix 2: Assessment of Labview data during sampling

The monitored values for the temperatures, pressures and reactants flows are assessed. Due to the velocity of the gas mixture, it is assumed that the monitored values during sampling represent the compostion and characterisitics of the sample. In Figure 13.8 and 13.9, the monitored data for 12 experimental parameters during sampling are given for the rich and stoichiometric MPE flame.

The first three parameters are all temperatures: the temperature measured at the burner surface, at the sampling cone and in the compression system.

Next, three pressures are shown. The pressure in the combustion chamber is constant during experiments. The pressure after the sampling cone, increases to a maximum pressure when the sample is gathered. When the sample is compressed, the sample pressure after the cone drops, but the pressure before the GC injection rises to 1.6 bar above atmospheric pressure and is expanded until there is no pressure gradient over the GC column.

The mole fraction and flows of the three reactants are also presented. The flow of argon and oxygen are stable during sampling. The mass flow of the fuel is affected by the sampling. The mass controller can correct the flow during sampling to the set value. The changes in fuel mass flow affect the mole fraction of the reactants.

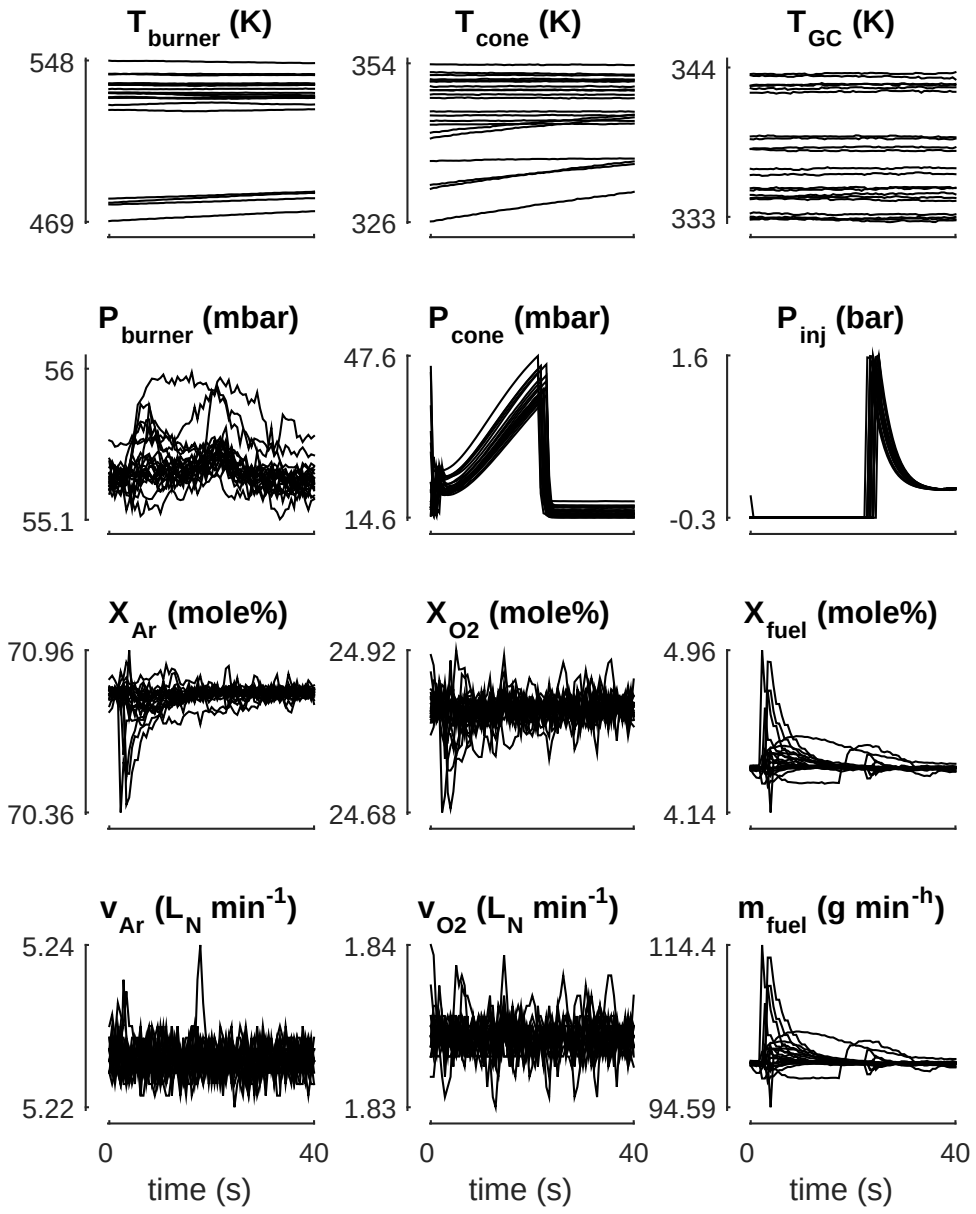

Figure 13.8: the monitored data for 12 experimental parameters during sampling are given for the rich MPE flame.

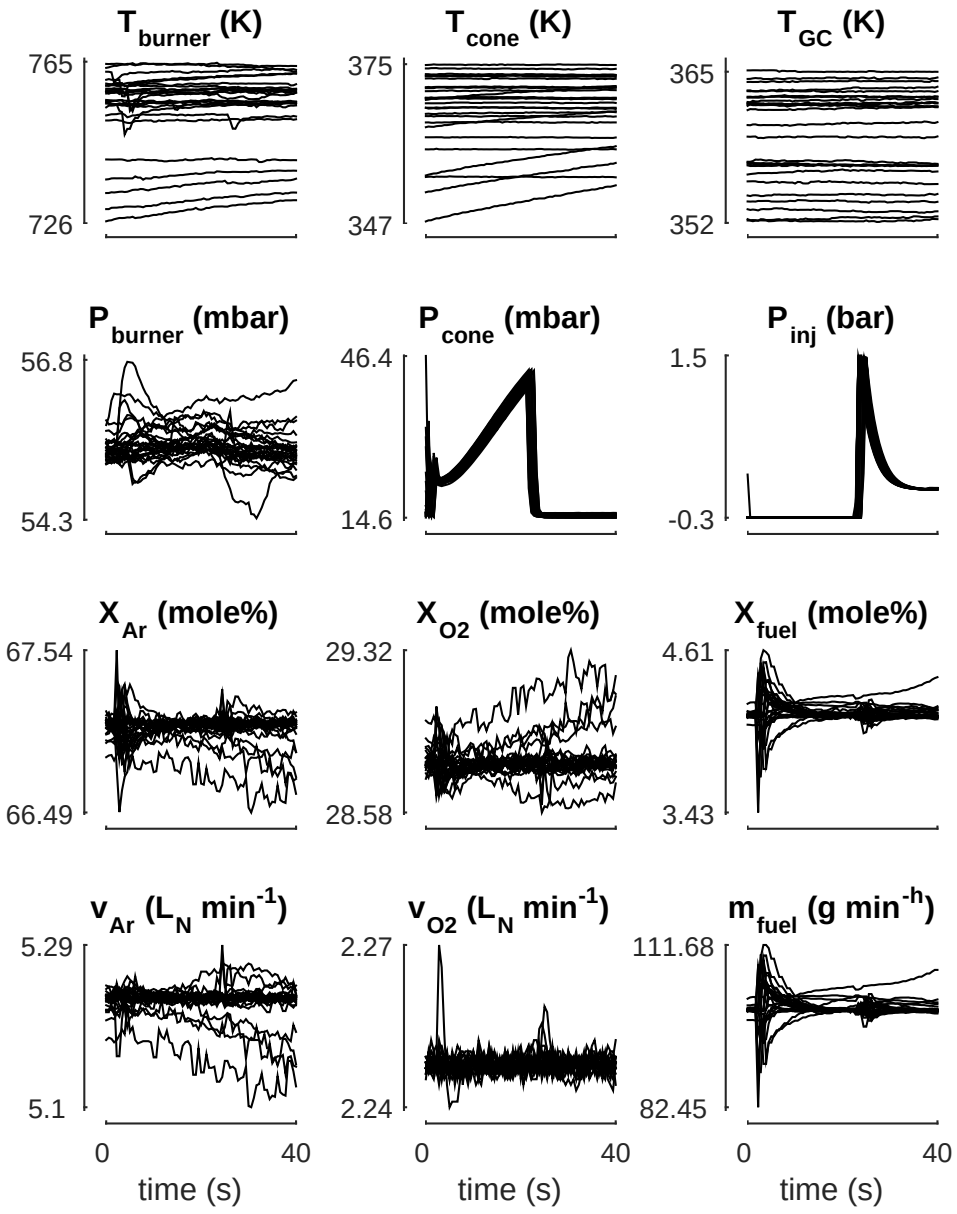

Figure 13.9: the monitored data for 12 experimental parameters during sampling are given for the stoichiometric MPE flame.

Appendix 3: Low-pass filter to the second order

The low-pass filter of the second order used for the ECM measurements (Section 5.6), consists two RC units in parallel (Figure 13.10). One RC unit consists of a resitor in series with the load and a capacitor in parallel with the load. The two resistors have both a resistance of 500Ω (R_1 and R_2) and the two capacitors have both a capacitance of 2 μF. The tension that enters the filter is V_e, while the tension that leave the filter is V_s.

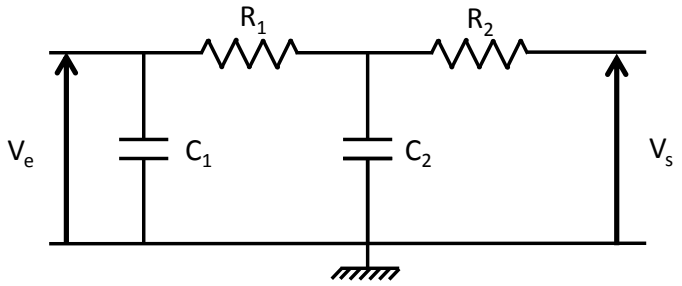

Figure 13.10: Two RC units in parallel forming a low-pass filter of the second order used to transform current with high frequency to a lower frequency.

The time constant τ of one RC circuit is defined as the multiplication of the resistor and the capacitor (Equation 13.8). It expresses the time required to charge the capacitor by 63.2% regarding the related initial and final state through the resistor.

$$\tau = R \cdot C \tag{13.8}$$

From the time constant the cut-off frequency f_c can be calculated (Equation 13.9). An ideal low-pass filter eliminates all frequencies above the cut-off frequency. The cut-off frequency can also be expressed in radians per second (Equation 13.10).

$$f_c = \frac{1}{2\pi\tau} \tag{13.9}$$

$$\omega_c = \frac{1}{\tau} = \frac{1}{R \cdot C} \tag{13.10}$$

The time constant of one low-pass circuit is 0.001s, while the cut-off frequency of is 159.24 Hz. These values mean that the capacitor needs 0.001 s to charge for 63.2%. If the current has a frequency higher than 159.24 Hz, the capacitor will not have time enough to charge and the transmitted current will be reduced. If the frequency is sufficient higher than the cut-off frequency the capacitor will act as a short cut and no signal will pass to the load.

The frequency of the current applied for ECM is 8000 Hz, well above the cut-off frequency and the applied current will hereby not affect the thermo-electric voltage which is DC.

Bibliography

[1] G. Dayma. Private communication, 2015.

[2] D. Hayes, S. Fitzpatrick, M. Hayes, and J. Ross. The Biofine Process-Production of Levulinic Acid, Furfural, and Formic Acid from Lignocellulosic Feedstocks. In *Biorefineries-Industrial Processes and Products*, pages 139–164. Wiley-VCH Verlag GmbH, 2005.

[3] J-P. Lange, R. Price, P. Ayoub, J. Louis, L. Petrus, L. Clarke, and H. Gosselink. Valeric Biofuels: A Platform of Cellulosic Transportation Fuels. *Angewandte Chemie International Edition*, 49(26):4479–4483, 2010.

[4] A. Morone, M. Apte, and R. Pandey. Levulinic acid production from renewable wast resources: bottlenecks, potential remedies, advancements and applications. *Renewable and Sustainable Energy Reviews*, 51:548–565, 2015.

[5] X. Tang, X. Zeng, Z. Li, L. Hu, Y. Sun, Sh. Liu, T. Lei, and L. Lin. Production of γ-valerolactone from lignocellulosic biomass for sustainable fuels and chemicals supply. *Renewable and Sustainable Energy Reviews*, 40:608–620, 2014.

[6] C. Chan-Thaw, M. Marelli, R. Psaro, N. Ravasio, and F. Zaccheria. New generation biofuels: γ-valerolactone into valeric esters in one pot. *RSC Adv.*, 3(5):1302–1306, 2013.

[7] F. Contino, P. Dagaut, G. Dayma, F. Halter, F. Foucher, and C. Mounaïm-Rousselle. Combustion and Emissions Characteristics of Valeric Biofuels in a Compression Ignition Engine. *Journal of Energy Engineering*, 140(3):A4014013, 2014.

[8] E. Koivisto, N. Ladommatos, and M. Gold. Compression Ignition and Exhaust Gas Emissions of Fuel Molecules Which Can Be Produced from Lignocellulosic Biomass: Levulinates, Valeric Esters, and Ketones. *Energy & Fuels*, 29(9):5875–5884, 2015.

[9] J. Botha and D. Spalding. The laminar flame speed of propane/air mixtures with heat extraction from the flame. *Proceeding of the royal society A*, 225:71–96, 1954.

[10] F. Contino, F. Foucher, F. Halter, G. Dayma, P. Dagaut, and C. Mounaïm-Rousselle. Engine Performances and Emissions of Second-Generation Biofuels in Spark Ignition Engines: The Case of Methyl and Ethyl Valerates. *11^{th} International Conference on Engines & Vehicles*, 2013. DOI: 10.4271/2013-24-0098.

[11] A. Cuoci, A. Frassoldati, T. Faravelli, and E. Ranzi. OpenSMOKE: numerical modeling of reacting systems with detailed kinetic mechanisms. *Meeting of the Italian Section of the Combustion Institute*, 2011.

[12] M. Himmel, S. Ding, D. Johnson, W. Adney, M. Nimlos, J. Brady, and T. Foust. Biomass recalcitrance: Engineering plants and enzymes for biofuels production. *Science*, 315:804–807, 2007.

[13] T. Flannelly, M. Lopes, L. Kupiainen, S. Dooley, and J. Leahy. Non-stoichiometric formation of formic and levulinic acids from the hydrolysis of biomass derived hexose carbohydrates. *Royal Society of Chemistry Advance*, 6:5797–5804, 2016.

[14] C. Chang, P. Cen, and X. Ma. Levulinic acid production from wheat straw. *Bioresource Technology*, 98:1448–1453, 2006.

[15] J. Cha and M. Hanna. Levulinic acid production based on extrusion and pressurized batch reaction. *Industrial Crops and Products*, 16:109–118, 2002.

[16] Q. Fang and M. Hanna. Experimental studies for levulinic acid production from whole kernal grain sorghum. *Bioresource technology*, 81:187–192, 2002.

[17] B. Girisuta. Levulinic acid from lignocellulosic biomass. *Chemical Engineering, PhD thesis, University of Groningen, Netherlands*, 2007.

[18] A. Efremov, G. Pervyshina, and B. Kuznetsov. Thermocatalytic transformations of wood and cellulose in the presence of HCl, HBr and H_2SO_4. *Chemistry of Natural Compounds*, 33:84–88, 1997.

[19] M. Chalid. Levulinic acid as a renewable source for novel polymers. *University of Groningen, Netherlands*, 2012.

[20] L. Yan, N. Yang, H. Pang, and B. Liao. Production of Levulinic Acid from Bagasse and Paddy Straw by Liquefaction in the Presence of Hydrochloride Acid. *Clean*, 36:158–163, 2008.

[21] D. Bevilaqua, M. Rambo, T. Rizzetti, A. Cardoso, and A. Martins. Cleaner production: levulinic acid from rice husks. *Journal of Cleaner Production*, 47:96–101, 2013.

[22] A. Efremov, G. Pervyshina, and B. Kuznetsov. Production of levulinic acid from wood raw material in the presence of sulfuric acid and its salts. *Chemistry of Natural Compounds*, 34:182–185, 1998.

[23] J. Tan-Soetedjo, H. van de Bovenkamp, R. Abdilla, C. Rasrendra, J. van Ginkel, and H. Jan Heeres. Experimental and kinetic modeling studies on the conversion of sucrose to levulinic acid and 5-hydroxymethylfurfural using sulfuric acid in water. *Industrial & Engineering Chemistry Research*, 2017.

[24] H. Mehdi, V. Fábos, R. Tuba, A. Bodor, L. Mika, and I. Horváth. Integration of homogeneous and heterogeneous catalytic processes for a multi-step conversion of biomass: from sucrose to levulinic acid, γ-valerolactone, 1,4-pentanediol, 2-methyltetrahydrofuran, and alkanes. *Top. Catal.*, 48:49–54, 2008.

[25] L. Wiggins. The utilization of sucrose. *Advances in carbohydrate chemistry*, 4:293–336, 1949.

[26] R. Weingarten, W. Conner, and G. Huber. Production of levulinic acid from cellulose by hydrothermal decomposition combined with aqueous phase dehydration with a solid acid catalyst. *Energy & Enverionmental Science*, 5:7559–7574, 2012.

[27] N. Ya'aini, N. Amin, and S. Endud. Characterization and performance of hybrid catalysts for levulinic acid production from glucose. *Microporous and Mesoporous Materials*, 171:14–23, 2013.

[28] H. Chen, B. Yu, and S. Jin. Production of levulinic acid from steam exploded rice straw via solid superacid,$S_2O_8^{2-}$/ZrO_2-SiO_2-Sm_2O_3. *Industrial Crops and Products*, 16:109–118, 2002.

[29] L. Peng, L. Lin, H. Li, and Q. Yang. Conversion of carbohydrates biomass into levulinate esters using heterogeneous catalysts. *Applied Energy*, 88(12):4590 – 4596, 2011.

[30] C. Chang, G. Xu, and X. Jiang. Production of ethyl levulinate by direct conversion of wheat straw in ethanol media. *Bioresource Technology*, 121(Supplement C):93 – 99, 2012.

[31] J. Zhang, S. Wu, B. Li, and H. Zhang. Advances in the catalytic production of valuable levulinic acid derivatives. *ChemCatChem*, 4(9), 2012.

[32] S. Saravanamurugan and A. Riisager. Zeolite catalyzed transformation of carbohydrates to alkyl levulinates. *ChemCatChem*, 5(7):1754–1757, 2013.

[33] I. Horvath, H. Mehdi, V. Fabos, L. Boda, and L. Mika. γ-valerolactone-a sustainable liquid for energy and carbon-based chemicals. *Green Chemistry*, 10:238–242, 2008.

[34] G. Dautzenberg, M. Gerhardt, and B. Kamm. Bio based fuels and fuel additives from lignocellulose feedstock via the production of levulinic acid and furfural. *Degruyter*, 65:439–451, 2010.

[35] J. Serrano-Ruiz, D. Wang, and J. Dumesic. Catalytic upgrading of levulinic acid to 5-nonanone. *Green chemistry*, 12:574–577, 2010.

[36] L. Xin, Z. Zhang, J. Qi, D. Chadderdon, Y. Qiu, K. Warsko, and W. Li. Electricity storage in biofuels: Selective electrocatalytic reduction of levulinic acid to valeric acid or γ-valerolactone. *Green Chemistry*, 6:674–686, 2013.

[37] Y. Qiu, L. Xin, D. Chadderdon, J. Qi, C. Liang, and W. Li. Integrated electrocatalytic processing of levulinic acid and formic acid to produce biofuel intermediate valeric acid. *Green Chemistry*, 16:1305–1315, 2014.

[38] Z. Yang, Y. Huang, Q. Guo, and Y. Fu. RANEY Ni catalyzed transfer hydrogenation of levulinate esters to γ-valerolactone at room temperature. *Chemical Communications*, 46:5328–5330, 2013.

[39] L. Manzer. Biomass derivatives: a sustainable source of chemicals. *Feedstocks for the Future, Renewables for the Production of Chemicals and Materials*, 921:40–51, 2006.

[40] L. Manzer and K. Hutchenson. Production of 5-methyldihydrofuran-2-one from levulinic acid in supercritical media. *US patent US20040254384*, 2004.

[41] R. Bourne, J. Stevens, J. Ke, and M. Poliakoff. Maximising opportunities in supercritical chemistry: the continuous conversion of levulinic acid to γ-valerolactone in CO_2. *Chemical Communications*, 44:4632–4634, 2007.

[42] F. Geilen, B. Engendahl, A. Harwardt, W. Marquadt, J. Klankermayer, and W. Leitner. Selective and flexible transformation of biomass-derived platform chemicals by a multifunctional catalytic system. *Angewandte Chemie International Edition*, 49:5510–5514, 2010.

[43] G. Braca, A. Raspolli Galletti, and G. Sbrana. Anionic Ruthenium iodorcarbonyl complexes as selective dehydroxylation catalysts in aqueous solution. *Journal of Organometallic Chemistry*, 417:41–49, 1991.

[44] K. Osakada, T. Ikariya, and S. Yoshikawa. Preparation and properties of hydride triphenyl-phosphine ruthenium complexes with 3-formyl (or acyl) propionate [RuH(ocochrchrcor')(PPh_3)$_3$] (R=H, $CH3_3$, C_2H_5; R'=H, CH_3, C_6H_5) and with 2-formyl (or acyl) benzoate [RuH(o-$OCCOC_6H_4COR'$)(PPh_3)$_3$] (R'=H, CH_3). *Journal of organometallic chemistry*, 231:79–90, 1982.

[45] H. Broadbent, G. Campbell, W. Bartley, and J. Johnson. Rhenium and its compounds as hydrogenation catalysts. III. rhenium heptoxide. *Journal of organic chemistry*, 24:1847–1854, 1959.

[46] Schütte, H. and Thomas, R. Normal III. its preparation by the catalytic reduction of levulinic acid with hydrogen in the presence of platinum oxide. *Journal American Chemical Society*, 52:3010–3012, 1930.

[47] R. Christian, H. Brown, and R. Hixon. Derivatives of γ-valerolactone, 1,4-pentanediol and 1,4-di-(β-cyanoethoxy)-pentane. *Journal of the american chemical society*, 69:1961–1963, 1947.

[48] L. Kyrides, W. Groves, and J. Craver. Process for the production of lactones. *US Patent US2368366 to Monsanto Chemical Company, a corporation of Delware, St. Louis, MO, US*, 1945.

[49] D. Kopetzki and M. Antonietti. Transfer hydrogenation of levulinic acid under hydrothermal conditions catalyzed by sulfate as a temperature-switchable base. *Green Chemistry*, 12:656–660, 2010.

[50] C. Ortiz-Cervantes and J. García. Hydrogenation of levulinic acid to γ-valerolactone using ruthenium nanoparticles. *Inorganica Chimica Acta*, 397(Supplement C):124 – 128, 2013.

[51] L. Deng, J. Li, D. Lai, Y. Fu, and Qing-X. Guo. Catalytic conversion of biomass-derived carbohydrates into γ-valerolactone without using an external h_2 supply. *Angewandte Chemie International Edition*, 48(35):6529–6532, 2009.

[52] L. Deng, Y. Zhao, J. Li, Y. Fu, B. Liao, and Q. Guo. Conversion of levulinic acid and formic acid into γ-valerolactone over heterogeneous catalysts. *ChemSusChem*, 3(10):1172–1175, 2010.

[53] X. Du, L. He, S. Zhao, Y. Liu, Y. Cao, H. He, and K. Fan. Hydrogen-independent reductive transformation of carbohydrate biomass into γ-valerolactone and pyrrolidone derivatives with supported gold catalysts. *Angewandte Chemie International Edition*, 50(34):7815–7819, 2011.

[54] P. Son, S. Nishimura, and K. Ebitani. Production of γ-valerolactone from biomass-derived compounds using formic acid as a hydrogen source over supported metal catalysts in water solvent. *RSC Adv.*, 4:10525–10530, 2014.

[55] J. Yuan, S. Li, L. Yu, Y. Liu, Y. Cao, H. He, and K. Fan. Copper-based catalysts for the efficient conversion of carbohydrate biomass into γ-valerolactone in the absence of externally added hydrogen. *Energy & Environmental Science*, 6:3308–3313, 2013.

[56] V. Fábos, L. Mika, and I. Horváth. Selective conversion of levulinic and formic acids to γ-valerolactone with the shvo catalyst. *Organometallics*, 33(1):181–187, 2014.

[57] H. Heeres, R. Handana, D. Chunai, C. Borromeus Rasrendra, B. Girisuta, and H. Jan Heeres. Combined dehydration/(transfer)-hydrogenation of c_6-sugars (d-glucose and d-fructose) to γ-valerolactone using ruthenium catalysts. *Green Chemistry*, 11:1247–1255, 2009.

[58] M. Chia and J. Dumesic. Liquid-phase catalytic transfer hydrogenation and cyclization of levulinic acid and its esters to [gamma]-valerolactone over metal oxide catalysts. *Chem. Commun.*, 47:12233–12235, 2011.

[59] X. Tang, L. Hu, Y. Sun, G. Zhao, W. Hao, and L. Lin. Conversion of biomass-derived ethyl levulinate into γ-valerolactone via hydrogen transfer from supercritical ethanol over a zro_2 catalyst. *RSC Adv.*, 3:10277–10284, 2013.

[60] X. Tang, H. Chen, L. Hu, W. Hao, Y. Sun, X. Zeng, L. Lin, and S. Liu. Conversion of biomass to γ-valerolactone by catalytic transfer hydrogenation of ethyl levulinate over metal hydroxides. *Applied Catalysis B: Environmental*, 147(Supplement C):827 – 834, 2014.

[61] J. Wang, S. Jaenicke, and G. Chuah. Zirconium-beta zeolite as a robust catalyst for the transformation of levulinic acid to γ-valerolactone via meerwein-ponndorf-verley reduction. *RSC Adv.*, 4:13481–13489, 2014.

[62] L. Bui, H. Luo, W. Gunther, and Y. Román-Leshkov. Domino reaction catalyzed by zeolites with bronsted and lewis acid sites for the production of γ-valerolactone from furfural. *Angewandte Chemie International Edition*, 52(31):8022–8025, 2013.

[63] F. Contino, P. Dagaut, F. Halter, J-B. Masurier, G. Dayma, C. Mounaim-Rousselle, and F. Foucher. Screening method for fuels in homogeneous charge compression ignition engines: Application to valeric biofuels. *Energy Fuels*, 31:607–614, 2016.

[64] H. Mardhiah, H. Ong, S. Masjuki, H. Lim, and H. Lee. A review on latest developments and future prospects of heterogeneous catalyst in biodiesel production from non-edible oils. *Renewable and Sustainable Energy Reviews*, 67:1225–1236, 2017.

[65] S. Sarathy, M. Thomson, W. Pitz, and T. Lu. An experimental and kinetic modeling study of methyl decanoate combustion. *Proceedings of the Combustion Institute*, 33:399–405, 2011.

[66] P. Glaude, O. Hervinet, S. Bax, J. Biet, V. Warth, and F. Battin-Leclerc. Modeling of the oxidation of methyl esters - validation for methyl hexanoate, methyl heptanoate, and methyl decanoate in a jet-stirred reactor. *Combustion and Flame*, 157:2035–2050, 2010.

[67] G. Dayma. Experimental and kinetic modeling study of the oxidation of methyl hexanoate. *Energy & Fuels*, 22:1469–1479, 2008.

[68] G. Dayma, C. Togbé, and P. Dagaut. Detailed kinetic mechanism for the oxidation of vegetable oil methyl esters: new evidence from methyl heptanoate. *Energy & Fuels*, 23:4254–4268, 2009.

[69] G. Dayma, F. Halter, F. Foucher, C. Togbé, C. Mounaim-Rousselle, and P. Dagaut. Experimental and detailed kinetic modeling study of ethyl pentanoate (ethyl valerate) oxidation in a jet stirred reactor and laminar burning velocities in a spherical combustion chamber. *Energy Fuels*, 26:4735–4748, 2012.

[70] H. Mbuyi Katshiatshia, V. Dias, and H. Jeanmart. Experimental and numerical study of ethyl valerate flat flames at low pressure. *Combustion Science and Technology*, 190:632–622, 2017.

[71] A. Dmitriev, D. Knyazkov, T. Bolshova, A. Shmakov, and O. Korobeinichev. The effect of methyl pentanoate addition on the structure of premixed fuel-rich n-heptane/toluene flame at atmospheric pressure. *Combustion and Flame*, 162:1964–1975, 2015.

[72] O. Korobeinichev, I. Gerasimov, D. Knyazkov, A. Shmakov, T. Bolshova, N. Hansen, C. Westbrook, G. Dayma, and B. Yang. An experimental and kinetic modeling study of premixed laminar flames of methyl pentanoate and methyl hexanoate. *Zeitschrift fur Physikalische Chemie*, 229:1–22, 2015.

[73] P. Diévart, S. Won, J. Gong, S. Dooley, and Y. Ju. A comparative study of the chemical kinetic characteristics of small methyl esters in diffusion flame extinction. *Proceedings of the Combustion Institute*, 34:821–829, 2013.

[74] B. Weber, J. Bunnell, K. Kumar, and C. Sung. Experiments and modeling of the autoignition of methyl pentanoate at low to intermediate temperatures and elevated pressures in a rapid compression machine. *Fuel*, pages 479–486, 2018.

[75] R. Brown and S. Stein. *Boiling Point Data*. NIST Chemistry WebBook, NIST Standard Reference Database Number 69, Eds. P.J. Linstrom and W.G. Mallard, National Institute of Standards and Technology, Gaithersburg MD, 20899, 2016.

[76] K. Eisazadeh-Far, A. Moghaddas, H. Metghalchi, and J. Keck. The effect of diluent on flame structure and laminar burning speeds of JP-8/oxidizer/diluent premixed flames. *Fuel*, 90:1476–1486, 2011.

[77] Bronkhorst. CEM liquid delivery system with vapour control.

[78] Properties methyl valerate 99% | Sigma-Aldrich, 2016.

[79] Bronkhorst. *Definition Normal Conditions*, 2016.

[80] Bronkhorst. *General instructions digital Mass Flow/ Pressure instruments laboratory style / IN-FLOW*, 2016.

[81] F. Vercheval. Pid du brûleur basse pression - chromotographe, 2012.

[82] R. Brown and S. Stein. *Antoine equation for water*. NIST Chemistry WebBook, NIST Standard Reference Database Number 69, Eds. P.J. Linstrom and W.G. Mallard, National Institute of Standards and Technology, Gaithersburg MD, 20899, 2016.

[83] R. Brown and S. Stein. *Antoine equation for n-butyl acetate*. NIST Chemistry WebBook, NIST Standard Reference Database Number 69, Eds. P.J. Linstrom and W.G. Mallard, National Institute of Standards and Technology, Gaithersburg MD, 20899, 2016.

[84] R. Brown and S. Stein. *Antoine equation for methyl hexanoate*. NIST Chemistry WebBook, NIST Standard Reference Database Number 69, Eds. P.J. Linstrom and W.G. Mallard, National Institute of Standards and Technology, Gaithersburg MD, 20899, 2016.

[85] B. Poling, J. Prausnitz, and J. O'Connell. *The properties of gases and liquids, fifth edition*. McGraw-Hill, 2001.

[86] J. Parcher. Fundamental relationships in gas chromatography. *Journal of Chemical Physics*, 35:1676, 1961.

[87] A. Littlewood. *Gas Chromatography*. New York: Academic Press, 1970.

[88] A. Shrivastava and V. Gupta. Methods for the determination of limit of detection and limit of quantitation of the analytical methods. *Chronicles of Young Scientists*, 2:21, 2011.

[89] Bureau International des Poids et Mesures. *Evaluation of measurement data-Guide to the expression of uncertainty in measurement*. Joint Committee for Guides in Metrology (JCGM), 2008.

[90] U. Struckmeier, P. Oßwald, T. Kasper, T. Böhling, M. Heusing, A. Köhler, and K. Kohse-Höinghous. Sampling probe influences on temperature and species concentration in molecular beam mass spectroscopic investigations of at premixed low-pressure flames. *Zeitschrift für Physikalische Chemie*, 223:503–537, 2009.

[91] A. Hartlieb, B. Atakan, and K. Kohse-Höinghous. Effects of a sampling quartz nozzle on the flame structure of a fuel-rich low pressure propene flame. *Combustion and Flame*, 121:610–624, 2000.

[92] R. Kee, F. Rupley, and J. Miller. Chemkin-ii: A fortran chemical kinetics package for the analysis of gas-phase chemical kinetics. *Sandia Report SAND89-8009.UC-401*, 1989.

[93] J. Warnatz, U. Maas, and R. Dibble. *Combustion - Physical and chemical fundamentals, modeling and simulation, experiments, pollutant formation*. Springer, 2006.

[94] M. Chase, C. Davies, D. Downey, R. McDonald, and A. Syverud. Janaf thermochemical tables, fourth edition. *Journal of Physical Chemistry*, 1985.

[95] J. Hirschfelder, C. Curtiss, and R. Bird. *Molecular Theory of Gases and Liquids*. John Wiley and Sons, 1954.

[96] L. Monchick and E. Mason. Fundamental relationships in gas chromatography. *Chromatographia*, 9/10:570–574, 1998.

[97] A. Cuoci, A. Frassoldati, T. Faravelli, and E. Ranzi. Opensmoke plus plus : An object-oriented framework for the numerical modeling of reactive systems with detailed kinetic mechanisms. *Computer Physics Communication*, 192:237 – 265, 2015.

[98] R. Kee, M. Coltrin, and P. Glarborg. Chemical reacting flows: Theory and practice. *Wiley-Interscience*, 192:237 – 265, 2003.

[99] C. Wilke. A viscosity equation for gas mixtures. *Journal of Chemical Physics*, 18:517 – 519, 1950.

[100] R. Bird, W. Stewart, and E. Lightfoot. *Transport Phenomena.* John Wiley and Sons, 1960.

[101] J. Warnatz. *Numerical Methods in flame propagation, edited by N. Peters and J. Warnatz.* Friedr. Vieweg and Sohn, Wiesbaden, 1982.

[102] J Parker. Rotational and vibrational relaxation in diatomic gases. *Physics of Fluids*, 2:449–462, 1959.

[103] C. Brau and R. Jonkman. Classical theory of rotational relaxation in diatomic gases. *Journal of Chemical Physics*, 52:477–484, 1970.

[104] S. Mathur, P. Tondon, and S. Saxena. Thermal conductivity fo binary, ternary and quaternary mixtures of rare gases. *Molecular Physics*, 12:569–579, 1967.

[105] J. Troe. Fall-off curves of unimolecular reactions. *Berichte der Bunsen-Gesellschaft*, 78:478–488, 1974.

[106] J. Troe and V. Ushakov. Revisiting falloff curves of thermal unimolecular reactions. *Journal of Chemical Physics*, 135:054304, 2001.

[107] E. Fisher, W. Pitz, H. Curran, and C. Westbrook. Detailed chemical kinetic mechanisms for combustion of oxygenated fuels. *Proceedings of the Combustion Institute*, 28:1579–1586, 2000.

[108] R. Ancia. Etude de la formation des précurseurs des suies dans les flammes riches d'acetylene et d'ethane. *PhD thesis, Unversité catholique de Louvain*, 1998.

[109] The Combustion Simulation Laboratory. COSILAB. *Rotexo GmbH & Co KG, Haan (Germany).*

[110] V. Dias and J. Vandooren. Experimental and modeling studies of $C_2H_4/O_2/Ar$, C_2H_4/methylal/O_2/Ar and C_2H_4/ethylal/O_2/Ar rich flames and the effect of oxygenated additives. *Combustion and Flame*, 158:848–859, 2011.

[111] V. Dias, H. Mbuyi Katshiatshia, and H. Jeanmart. The influence of ethanol addition on a rich premixed benzene flame at low pressure. *Combustion and Flame*, 161:2297–2304, 2014.

[112] D. Goodwin, H. Moffat, and R. Speth. Cantera: An object-oriented software toolkit for chemical kinetics, thermodynamics, and transport processes. `http://www.cantera.org`, 2017. Version 2.3.0.

[113] P. Childs, J. Greenwood, and C. Long. Review of temperature measurement. *Review of Scientific Instruments*, 71(8):2959–2978, 2000.

[114] C. Shaddix. Correcting thermocouple measurements for radiation loss: a critical review. *Proceedings of the 33rd National Heat Transfer Converence*, pages 1–10, 1999.

[115] V. Dias, C. Duynslaegher, F. Contino, J. Vandooren, and H. Jeanmart. Experimental and modeling study of formaldehyde combustion in flames. *Combustion and Flame*, 159:1814–1820, 2012.

[116] N. Bahlawane, U. Struckmeier, T. Kasper, and P. Oßwald. Noncatalytic thermocouple coatings produced with chemical vapor deposition for flame temperature measurements. *Review of scientific instruments*, 78:013905, 2007.

[117] M. Heitor and A. Moreira. Thermocouples and sampe probes for combustion studies. *Progress in Energy and Combustion Science*, 19(3):259–278, 1993.

[118] U. Bonne, T. Grewer, and G. Wagner. Messungen in der reaktionszone von wasserstoff-sauerstoff- und methan-sauerstoff- flammen. *Zeitschrift fur Physikalische Chemie Neue Folge*, 26:93–110, 1960.

[119] A. Bakali, J-L. Delfau, and C. Vovelle. Experimental study of 1 atmosphere, rich, premixed n-heptane and iso-octane flames. *Combustion Science and Technology*, 140:69–91, 2007.

[120] A. Hayhurst and D. Kittelson. Heat and mass transfer considerations in the use of electrically heated thermocouples of iridium versus an iridium/rhodium alloy in atmospheric pressure flames. *Combustion and Flame*, 28:301–317, 1977.

[121] D. Bradley and K. Matthews. Measurement of high gas temperatures with fine wire thermocouples. *Journal of Mechanical Engineering Science*, 115:468–480, 1968.

[122] H. Kramers. Heat transfer from spheres to flowing media. *Physica*, 12:61–80, 1946.

[123] J. Greig. The sodium d-line reversal method of temperature measurement in ionized flame gases. *British Journal of Applied Physics*, 16:957–964, 1965.

[124] L. Tran, P. Glaude, and F. Battin-Leclerc. An experimental study of the structure of laminar premixed flames of ethanol/methane/oxygen/argon. *Combustion, Explosions, and Shock Waves*, 49:11–18, 2013.

[125] E. Pousse, P. Glaude, R. Fournet, and F. Battin-Leclerc. Experimental study of the structure of a lean premixed Indane/CH_4/O_2/Ar flame. *Combustion, Explosions, and Shock Waves*, 46:132–139, 2010.

[126] N. Lamoureux, K. Marschallek-Watroba, P. Desgroux, J-F. Pauwels, M. Sylla, and L. Gasnot. Measurements and modelling of nitrogen species in CH_4/O_2/N_2 flames doped with no, NH_3 or NH_3+NO. *Combustion and Flame*, 176:48–59, 2017.

[127] M. Gilbert and J. Lobdell. Resistance-thermometer measurements in a low-pressure flame. *Symposium (International) on Combustion*, 4:285–294, 1953.

[128] A. Sato, K. Hashiba, S. Sugiyama, and J. Kimura. A correctional calculation method for thermocouple measurements of temperature in flames. *Combustion and Flame*, 24:35–41, 1975.

[129] A. Abid, N. Heinz, E. Tolmachoff, D. Phares, C. Campbell, and H. Wang. An evolution of particle size distribution functions of incipient soot in premixed ethylene-oxygen-argon flames. *Combustion and Flame*, 154:775–788, 2008.

[130] G. Andrew, D. Bradley, and G. Hundy. Hot wire anemometer calibration for measurements of small gas velocities. *International Journal of Heat and Mass Transfer*, 15:1765–1786, 1972.

[131] C. Baukal. *Temperature*, chapter 5, pages 103–108. CRC Press, 2010.

[132] K. Lin and G. Faeth. Structure of laminar permanently blue, opposed-jet ethylene-fueled diffusion flames. *Combustion and Flame*, 10:299–305, 1998.

[133] J. Kent. Noncatalytic coating for platinum-rhodium thermocouples. *Combustion and Flame*, 14(1-3):279, 1970.

[134] Omega. ITS-90 Thermocouple Direct and Inverse Polynomials. https://www.omega.com/techref/pdf/z198-201.pdf.

[135] Keysight Technologies. Service rapport multimeter 3458a, 2015.

[136] Keysight Technologies. Data sheet keysight 3458a multimeter, 2014.

[137] R. Peterson and N. Laurendeau. The emittance of yttrium-beryllium oxide thermocouple coating. *Combustion and Flame*, 60:279–284, 1985.

[138] J. Hibshman. An experimental study of soot formation in dual mode laminar wolfhard-parker flames. *M.S. Thesis, Dept. of Mechanical Engineering, Virginia Polytechnic Institute and State University, 1998*, 1998.

[139] V. Hindasageri, R. Vedula, and S Prabhu. Thermocouple error correction for measuring the flame temperature with determination of emissivity and heat transfer coefficient. *Review of Scientific Instruments*, 84:1–11, 2013.

[140] Omega. Physical properties of thermoelement materials. *Omega*, 2016.

[141] C. Davisson and J. Weeks. The relation between the total thermal emissive power of a metal and its electrical resistivity. *Journal of the Optical Society of America and Review of Scientific Instruments*, 8:581–605, 1924.

[142] D. Bradley and A. Entwistle. Determination of the emissivity, for total radiation, of small diameter platinum-10% rhodium wires in the temperature range 600-1450 °c. *British journal of applied physics*, 12:708–711, 1961.

[143] R. Seifert. The spectral emissivity and total emissivity of beryllium oxide. *Physical Review*, 73:1181–1187, 1948.

[144] W. McMahon and D. Wilder. High temperature spectral emissivity of yttrium, samarium, gadolinium, erbium and lutetium oxides. *United States Atomic Energy Commision*, pages 1–48, 1963.

[145] D. Collis and M. Williams. Two-dimensional convection from heated wires at low reynolds numbers. *Journal of Fluid Mechanics*, 6:357–384, 1959.

[146] S. Whitaker. Forced convection heat transfer correlations for flow in pipes, past flat plates, single cylinders, single spheres, and for flow in packed beds and tube bundles. *American Institute of Chemical Engineers*, 18:361–371, 1972.

[147] inc. Mathworks. Global optimization toolbox: User's guide (r2017a). http://www.mathworks.com/help/pdf_doc/gads/gads_tb.pdf, 2017.

[148] A. Saltelli, Stefano Tarantola, Francesca Campolongo, and Marco Ratto. *Sensitivity Analysis in Practice: A Guide to Assessing Scientific Models*. John Wiley & Sons, 2004.

[149] W. Ranz and W. Marshall. Evaporation from drops. *Chemical Engineering Progress*, 48:141–146 and 173–180, 1952.

[150] Agilent Technologies. Agilent 34401a multimeter data sheet, 2013.

[151] C. McEnally, U. Koylu, D. Pfefferle, and D. Rosner. Soot volume fraction and temperature measurements in laminar nonpremixed flames using thermocouples. *Combustion and flame*, 109:701–720, 1997.

[152] R. Ancia, J. Vandooren, and P.J. Van Tichelen. Experimental study of the structure of rich ethane flames. *International Symposium on Combustion*, 26:1009–1016, 1996.

[153] T. Cool, A. McIlroy, F. Qi, P. Westmoreland, L. Poisson, D. Peterka, and M. Ahmed. Photoionization mass spectrometer for studies of flame chemistry with a synchrotron light source. *Review of Scientific Instruments*, 76:094102:1–7, 2005.

[154] A. Lutz, F. Rupley, and R. Kee. Equil: A Chemkin implementation of Stanjan for computing chemical equilibria. *Sandia National Laboratories Livermore, CA 94551*.

[155] P. Dagaut, M. Cathonnet, J.P. Rouan, R. Foulatier, A. Quilgars, J. Boettner, F. Gaillard, and H. James. A jet-stirred reactor for kinetic studies of homogeneous gas-phase reactions at pressures up to ten atmospheres (=1 MPa). *Journal of Physics E: Scientific Instruments*, 19:207–209, 1986.

[156] J. Chung, S. Lee, H. An, S. Song, and K. Chun. Rapid-compression machine studies on two-stage ignition characteristics of hydrocarbon autoignition and an investigation of new gasoline surrogates. *Energy*, 93:1505–1514, 2015.

[157] K. Hadj Ali, M. Crochet, G. Vanhove, M. Ribaucour, and R. Minetti. A study of the low temperature ignition of methyl esters. *Proceedings of the Combustion Institute*, 32:239–246, 2009.

[158] A. Keromnes, W. Metcalfe, K. Heufer, N. Donohoe, A. Das, C. Sung, J. Herzler, C. Naumann, P. Griebel, O. Mathieu, M. Krejci, E. Petersen, W. Pitz, and H. Curran. An experimental and detailed chemical kinetic modeling study of hydrogen and syngas mixtures oxidation at elevated pressures. *Combustion and Flame*, 160:995–1011, 2013.

[159] A. Cuoci, A. Frassoldati, T. Faravelli, and E. Ranzi. A computational tool for the detailed kinetic modeling of laminar flames: Application to C_2H_4/CH_4 coflow flames. *Combustion and Flame*, 160:870–887, 2013.

[160] O. Mathieu and E. Petersen. Experimental and modeling study on the high-temperature oxidation of ammonia and related nox chemistry. *Combustion and Flame*, 162:554–570, 2015.

[161] A. Casas, J. Ruiz, M. Ramos, and Á. Pérez. Effects of triacetin on biodiesel quality. *Energy & Fuels*, 24(8):4481–4489, 2010.

[162] J. Melero, G. Vicente, G. Morales, M. Paniagua, and J. Bustamante. Oxygenated compounds derived from glycerol for biodiesel formulation: Influence on EN 14214 quality parameters. *Fuel*, 89(8):2011–2018, 2010.

[163] D. Johnson and K. Taconi. The glycerin glut: Options for the value-added conversion of crude glycerol resulting from biodiesel production. *Environmental Progress*, 26(4):338–348, 2007.

[164] A. Demirbas. Political, economic and environmental impacts of biofuels: A review. *Applied Energy*, 86:S108–S117, 2009.

[165] M. Balat and H. Balat. Progress in biodiesel processing. *Applied Energy*, 87:1845–1835, 2010.

[166] The European Parliament and the Council of the European Union. Directive 2003/30/EC of the European Parliament and of the Council of 8 May 2003 on the promotion of the use of biofuels or other renewable fuels for transport. *Official Journal of the European Union*, 2003.

[167] The European Parliament and the Council of the European Union. Directive 2009/28/EC of the European Parliament and of the Council of 23 April 2009 on the promotion of the use of energy from renewable sources and amending and subsequently repealing directives 2001/77/EC and 2003/30/EC. *Official Journal of the European Union*, 2009.

[168] The European Parliament and the Council of the European Union. Directive 2009/30/EC of the European Parliament and of the Council of 23 April 2009 amending directive 98/70/EC as regards the specification of petrol, diesel and gas-oil and introducing a mechanism to monitor and reduce greenhouse gas emissions and amending council directive 1999/32/EC as regards the specification of fuel used by inland waterway vessels and repealing directive 93/12/EEC. *Official Journal of the European Union*, 2009.

[169] ASTM International. Standard specification for biodiesel fuel blend stock (b100) for middle distillate fuels. 2008.

[170] US Energy Information Administration. Overview and methodology data v2.0, 2007.

[171] European Biodiesel Board. Statistics on the eu biodiesel industry, http://www.ebb-eu.org/stats.php, 2017.

[172] E. Atabani, A. Silitonga, I. Badrudding, T. Mahlia, H. Masjuki, and S. Mekhilef. A comprehensive review on biodiesel as an alternative energy resource and its characteristics. *Renewable and Sustainable Energy Reviews*, 16:2070–2093, 2012.

[173] M. Gui, K. Lee, and S. Bhatia. Feasibility of edible oil vs. non-edible oil vs. waste edible oil as biodiesel feedstock. *Energy*, 33(11):1646–1653, 2008.

[174] T. Mata, A. Martins, and N. Caetano. Microalgae for biodiesel production and other applications: A review. *Renewable and Sustainable Energy Reviews*, 14:217–232, 2010.

[175] F. Ma, D. Clements, and M. Hanna. Biodiesel fuel from animal fat. ancillary studies on transesterification of beef tallow. *Industrial & Engineering Chemistry Research*, 37:3768–3771, 1998.

[176] L. Meher, V. Sager, and S. Naik. Technical aspects of biodiesel production by transesterification - a review. *Renewable and Sustainable Energy Reviews*, 10:248–268, 2006.

[177] Y. Sharma, B Singh, and S. Upadhyay. Advancements in development and characterization of biodiesel: A review. *Fuel*, 87:2355–2373, 2008.

[178] P. Verma and M. Sharma. Review of process parameters for biodiesel production from different feedstocks. *Renewable and Sustainable Energy Reviews*, 62:1063–1071, 2016.

[179] G. Santori, G. Di Nicola, M. Moglie, and F. Polonara. A review analyzing the industrial biodiesel production practice starting from vegetable oil refining. *Applied Energy*, 92:109–132, 2012.

[180] L. Fjerbaek, K.. Christensen, and B. Norddahl. A review of the current state of biodiesel production using enzymatic transesterification. *Biotechnology and Bioengineering*, 102(5):1298–1315, 2009.

[181] J. Pullen and K. Saeed. Investigation of the factors affecting the progress of base-catalyzed transesterification of rapeseed oil to biodiesel fame. *Fuel Processing Technology*, 130:127–135, 2015.

[182] A. Ramadhas, S. Jayaraj, and C. Muraleedharan. Biodiesel production from high ffa rubber seed oil. *Fuel*, 84(4):335–340, 2005.

[183] J. Calero, D. Luna, E. Sancho, C. Luna, F. Bautista, A. Romero, A. Posadillo, J. Berbel, and C. Verdugo-Escamilla. An overview on glycerol-free processes for the production of renewable liquid biofuels, applicable in diesel engines. *Renewable and Sustainable Energy Reviews*, 42:1437–1452, 2015.

[184] V. Rathore, S. Tyagi, B. Newalkar, and R. Badoni. Jatropha and Karanja oil derived dmc-biodiesel synthesis: A kinetics study. *Fuel*, 140:597–608, 2015.

[185] E. Shahid and Y. Jamal. Production of biodiesel: A technical review. *Renewable and Sustainable Energy Reviews*, 15(9):4732 – 4745, 2011.

[186] M. Lapuerta, O. Armas, and J. Rodrǵuez-Fernández. Effect of biodiesel fuels on diesel engine emissions. *Progress in Energy and Combustion Science*, 34(2):198 – 223, 2008.

[187] M. Dorado, E. Ballesteros, J. Arnal, J. Gómez, and F. López. Exhaust emissions from a diesel engine fueled with transesterified waste olive oil. *Fuel*, 82(2):1311–1315, 2003.

[188] E. Alptekin. Emission, injection and combustion characteristics of biodiesel and oxygenated fuel blends in a common rail diesel engine. *Energy*, 119(Supplement C):44 – 52, 2017.

[189] Y. Chisti. Biodiesel from microalgae. *Biotechnology advances*, 25:294–306, 2007.

[190] L. Rodolfi, G. Chini Zittelli, N. Bassi, G. Padovani, N. Biondi, G. Bonini, and M. Tredici. Microalgae for oil: Strain selection, induction of lipid synthesis and outdoor mass cultivation in a low-cost photobioreactor. *Biotechnology and Bioengineering*, 102(1):100–112, 2009.

[191] M. Borowitzka and N. Moheimani. Sustainable biofuels from algae. *Mitigation and Adaptation Strategies for Global Change*, 18(1):13–25, 2013.

[192] R. Slade and A. Bauen. Micro-algae cultivation for biofuels: cost, energy balance, environmental impacts and future prospects. *Biomass and Bioenergy*, 53:29–38, 2013.

[193] R. Huerlimann, R. de Nys, and K. Heimann. Growth, lipid content, productivity, and fatty acid composition of tropical microalgae for scale-up production. *Biotechnology and Bioengineering*, 107(2):245–257, 2010.

[194] X. Huang, Z. Huang, W. Wen, and J. Yan. Effects of nitrogen supplementation of the culture medium on the growth, total lipid content and fatty acid profiles of three microalgae (tetraselmis subcordiformis, nannochloropsis oculata and pavlova viridis). *Journal of Applied Phycology*, 25(1):129–137, 2013.

[195] C. Chen, K. Yeh, R. Aisyah, D. Lee, and J. Chang. Cultivation, photobioreactor design and harvesting of microalgae for biodiesel production: A critical review. *Bioresource Technology*, 102:71–81, 2011.

[196] D. Lim, S. Garg, M. Timmins, E. Zhang, S. Thomas-Hall, H. Schuhmann, Y. Li, and P. Schenk. Isolation and evaluation of oil-producing microalgae from subtropical coastal and brackish waters. *PLoS ONE*, 7(7):e40751, 2012.

[197] P. Schenk, S. Thomas-Hall, E. Stephens, U. Marx, J. Mussgnug, C. Posten, O. Kruse, and B. Hankamer. Second generation biofuels: High-efficiency microalgae for biodiesel production. *Bioenergy Resources*, 1:20–43, 2008.

[198] L. Brennan and P. Owende. Biofuels from microalgaeâĂŤa review of technologies for production, processing, and extractions of biofuels and co-products. *Renewable and Sustainable Energy Reviews*, 14:557–577, 2010.

[199] S. Dickinson, M. Mientus, D. Frey, A. Amini-Hajibashi, S. Ozturk, F. Shaikh, D. Sengupta, and M. El-Halwagi. A review of biodiesel production from microalgae. *Clean technologies and environmental policy*, 19:637–668, 2017.

[200] Kyle Sander and Ganti S. Murthy. Life cycle analysis of algae biodiesel. *The International Journal of Life Cycle Assessment*, 15(7):704–714, 2010.

[201] M. Islam, M. Rahman, K. Heimann, M. Nabi, A. Ristovski, Z. Dowell, G. Thomas, B. Feng, N. von Alvensleben, and R. Brown. Combustion analysis of microalgae methyl ester in a common rail direct injection diesel engine. *Fuel*, 143:351–360, 2015.

[202] G. Tuccar and K. Aydin. Evaluation of methyl ester of microalgae oil as fuel in a diesel engine. *Fuel*, 112(Supplement C):203 – 207, 2013.

[203] R. Piloto-Rodríguez, Y. Sánchez-Borroto, E. Melo-Espinosa, and S. Verhelst. Assessment of diesel engine performance when fueled with biodiesel from algae and microalgae: An overview. *Renewable and Sustainable Energy Reviews*, 69(Supplement C):833 – 842, 2017.

[204] A. Casas, M. Jesus Ramos, and Á. Pérez. New trends in biodiesel production: Chemical interesterification of sunflower oil with methyl acetate. *Biomass & Bioenergy*, 35(5):1702–1709, 2011.

[205] Abraham Casas, Maria Jesus Ramos, and Ángel Pérez. Methanol-enhanced chemical interesterification of sunflower oil with methyl acetate. *Fuel*, 106:869–872, April 2013.

[206] A. Casas, M. Jesus Ramos, and A. Perez. Kinetics of chemical interesterification of sunflower oil with methyl acetate for biodiesel and triacetin production (vol 171, pg 1324, 2011). *Chemical Engineering Journal*, 195:403–403, 2012.

[207] A. Casas, M. Ramos, and A. Perez. Adsorption equilibrium and kinetics of methyl acetate/methanol and methyl acetate/water mixtures on zeolite 5a. *Chemical Engineering Journal*, 220:337–342, 2013.

[208] A. Casas, A. Perez, and M. Ramos. Catalyst removal after the chemical interesterification of sunflower oil with methyl acetate. *Organic process research & development*, 21:1253–1258, 2017.

[209] Ganesh L. Maddikeri, Aniruddha B. Pandit, and Parag R. Gogate. Ultrasound assisted interesterification of waste cooking oil and methyl acetate for biodiesel and triacetin production. *Fuel Processing Technology*, 116:241–249, 2013.

[210] M. Talukder, P. Das, T. Fang, and J. Wu. Enhanced enzymatic transesterification of palm oil to biodiesel. *Biochemical Engineering Journal*, 55:119–122, 2011.

[211] N. Ognjanovic, D. Bezbradica, and Z. Knezevic-Jugovic. Enzymatic conversion of sunflower oil to biodiesel in a solvent-free system: Process optimization and the immobilized system stability. *Bioresource Technology*, 100:S146–S154, 2009.

[212] E. Usai, E. Gualdi, V. Solinas, and E. Battistel. Simultaneous enzymatic synthesis of FAME and triacetyl glycerol from triglycerides and methyl acetate. *Bioresource Technology*, 101(20):7707–7712, 2010.

[213] W. Du, Y. Xu, D. Liu, and J. Zeng. Comparative study on lipase-catalyzed transformation of soybean oil for biodiesel production with different acyl acceptors. *Journal of Molecular Catalysis B-Enzymatic*, 30(3-4):125–129, 2004.

[214] Y. Xu, W. Du, and D. Liu. Study on the kinetics of enzymatic interesterification of triglycerides for biodiesel production with methyl acetate as the acyl acceptor. *Journal of Molecular Catalysis B-Enzymatic*, 32(5-6):241–245, 2005.

[215] Ying Huang and Yunjun Yan. Lipase-catalyzed biodiesel production with methyl acetate as acyl acceptor. *Zeitschrift FÃijr Naturforschung. C, Journal of Biosciences*, 63(3-4):297–302, 2008.

[216] O. Orcaire, P. Buisson, and A Pierre. Application of silica aerogel encapsulated lipases in the synthesis of biodiesel by transesterification reactions. *Journal of Molecular Catalysis B: Enzymatic*, 42:106–113, 2006.

[217] P. Campanelli, M. Banchero, and L. Manna. Synthesis of biodiesel from edible, non-edible and waste cooking oils via supercritical methyl acetate transesterification. *Fuel*, 89(12):3675–3682, 2010.

[218] S. Saka and Y. Isayama. A new process for catalyst-free production of biodiesel using supercritical methyl acetate. *Fuel*, 88(7):1307–1313, 2009. WOS:000265228800023.

[219] K. Tan, K. Lee, and A. Mohamed. A glycerol-free process to produce biodiesel by supercritical methyl acetate technology: An optimization study via response surface methodology. *Bioresource Technology*, 101(3):965–969, 2010.

[220] N. Niza, K. Tan, Z. Ahmad, and K. Lee. Comparison and optimisation of biodiesel production from jatropha curcas oil using supercritical methyl acetate and methanol. *Chemical Papers*, 65(5):721–729, 2011.

[221] F. Goembira, K. Matsuura, and S. Saka. Biodiesel production from rapeseed oil by various supercritical carboxylate esters. *Fuel*, 97:373–378, July 2012.

[222] Limin Zhou, Essam Al-Zaini, and Adesoji A. Adesina. Catalytic characteristics and parameters optimization of the glycerol acetylation over solid acid catalysts. *Fuel*, 103:617–625, January 2013.

[223] D. Gelosa, M. Ramaioli, G. Valente, and M. Morbidelli. Chromatographic reactors: Esterification of glycerol with acetic acid using acidic polymeric resins. *Industrial & Engineering Chemistry Research*, 42(25):6536–6544, 2003.

[224] M. Khayoon and B. Hameed. Yttrium-grafted mesostructured sba-3 catalyst for the transesterification of glycerol with methyl acetate to synthesize fuel oxygenates. *Applied Catalysis A: General*, 460-461:61–69, 2013.

[225] R. Elias, M. Senra, and L. Soh. Cold flow properties of fatty acid methyl ester blends with and without triacetin. *Energy & fuels*, 30:7400–7409, 2016.

[226] J. Delgado. Use of glycerine tri-acetate as additive of biodiesel fuel compositions. *European Patent Specification, Application number: 02380270.5*, 2008.

[227] A. Zare, M. Nabi, T. Bodisco, F. Hossain, M. Rahman, Z. Ristovski, and R. Brown. The effect of triacetin as a fuel additive to waste cooking biodiesel on engine performance and exhaust emissions. *Fuel*, 182:640–649, 2016.

[228] A. Zare, T. Bodisco, M. Nabi, F. Hossain, M. Rahman, Z. Ristovski, and R. Brown. The influence of oxygenated fuels on transient and steady-state engine emissions. *Energy*, 121:841–853, 2017.

[229] M Gupta and N. Kumar. Scope and opportunities of using glycerol as an energy source. *Renewable and Sustainable Energy Reviews*, 16:4551–4556, 2012.

[230] G. Suppes, W. Sutterlin, and M. Dasari. Method of producing lower alcohols from glycerol, 2005. US Patent App. 11/088,603.

[231] L. Zhou, E. Al-Zaini, and A. Adesina. Catalytic characteristics and parameters optimization of the glycerol acetylation over solid acid catalysts. *Fuel*, 103(0):617 – 625, 2013.

[232] H.-J. Althaus, M. Chudacoff, R. Hischier, N. Jungbluth, M. Osses, and A. Primas. Life cycle inventories of chemicals. *Final report ecoinvent data v2.0*, 8, 2007.

[233] J. Sutter. Life cycle inventories of petrochemical solvents. *Final report ecoinvent data v2.0*, 22, 2007.

[234] R. Ceriani, R. Gani, and A. Meirelles. Prediction of heat capacities and heats of vaporization of organic liquids by group contribution methods. *Fluid Phase Equilibria*, 283(1-2):49 –55, 2009.

[235] A. Casas, M. Jesus Ramos, and A. Perez. Product separation after chemical interesterification of vegetable oils with methyl acetate. part II: liquid-liquid equilibrium. *Industrial & Engineering Chemistry Research*, 51(30):10201 – 10206, 2012.

[236] *NIST Chemistry WebBook, NIST Standard Reference Database Number 69*. Linstrom, P.J. and Mallard, W.G.

[237] R. Frischknecht and N. Jungbluth. Overview and methodology, data v2.0, ecoinvent report no.1. swiss centre for life cycle inventories, dübendorf, 2007.

[238] S. Muller, P. Lesage, A. Ciroth, C. Mutel, B. Weidema, and Samson S. The application of the pedigree approach to the distributions foreseen in ecoinvent v3. *The International Journal of Life Cycle Assessment*, 2014.

[239] R. Frischknecht, N. Jungbluth, H-J. Althaus, G. Doka, R. Dones, T. Heck, S. Hellweg, R. Hischier, T. Nemecek, G. Rebitzer, and M. Spielmann. The ecoinvent database: Overview and methodological framework. *International Journal of LCA*, 10:3–9, 2005.

[240] R. Heijungs. CMLCA: Scientific software for LCA, IOA, EIOA, and more , http://www.cmlca.eu/, CML university of leiden, netherlands, 2017.

[241] L. Batan, J. Quinn, B. Willson, and T. Bradley. Net energy and greenhouse gas emission evaluation of biodiesel derived from microalgae. *Environmental Science technology*, pages 7975–7980, 2010.

[242] C. Hall, J. Lambert, and S. Balogh. Eroi of different fuels and the implications for society. *Energy Policy*, pages 141–152, 2014.

[243] O. Jorquera, A. Kiperstok, E. Sales, M. Embirucu, and M. Ghirardi. Comparative energy life-cycle analyses of microalgal biomass production in open ponds and photobioreactors. *Bioresource Technology*, 101:1406–1413, 2010.

[244] N. Jungbluth, M. Emmenegger, F. Dinkel, C. Stettler, G. Doka, M. Chudacoff, A. Dauriat, E. Gnansounou, M. Spielmann, J. Sutter, N. Kljun, M. Keller, and K. Schleiss. Life Cycle Inventories of Bioenergy. *Final report ecoinvent data v2.0*, 17:109–132, 2007.

[245] M. Lapuerta, J. Rodriguez-Fernandeze, and F. Oliva. Determination of enthalpy of formation of methyl and ethyl esters of fatty acids. *Chemistry and Physics of Lipids*, 163(2):172 – 181, 2010.

[246] P. Haro, P. Ollero, A. L. Villanueva Perales, and A. GÃşmez-Barea. Thermochemical biorefinery based on dimethyl ether as intermediate: Technoeconomic assessment. *Applied Energy*, 102:950–961, February 2013.

[247] P. Haro, P. Ollero, A. L. Villanueva Perales, and C. Reyes Valle. Technoeconomic assessment of lignocellulosic ethanol production via DME (dimethyl ether) hydrocarbonylation. *Energy*, 44(1), August 2012.

[248] V. Francescato, E. Antonini, and L. Bergomi. Wood fuels handbook, 2008.

[249] P. Hu, H. Rismani-Yazdi, and G. Stephanopoulos. Anaerobic CO2 fixation by the acetogenic bacterium moorella thermoacetica. *AIChE Journal*, 59(9):3176–3183, 2013.

[250] A. Casas, M. Jesus Ramos, and A. Perez. Product separation after chemical interesterification of vegetable oils with methyl acetate. part i: Vapor-liquid equilibrium. *Industrial & Engineering Chemistry Research*, 51(23):8087–8094, 2012.

[251] I. Chien, K. Zeng, H. Chao, and J. Liu. Design andcontrol of acetic acidd ehydration system via heterogeneous azeotropic distillation. *Chemical Engineering Science*, 59:4547–4567, 2004.

[252] Robert C. Reid. *The Properties of Gases and Liquids*. McGraw-Hill, January 1987.

[253] R. Ceriani and A. Meirelles. Predicting vapor-liquid equilibria of fatty systems. *Fluid Phase Equilibria*, 215(2):227–236, 2004.

[254] Inc. Aspen Technology. Aspen plus v8.8. *www.aspentech.com*.

[255] A. Date. *Analytic Combustion With Thermodynamics, Chemical Kinetics and Mass Transfer*. Cambridge University Press, 2011.

[256] M. Wang, H. Lee, and J. Molburg. Allocation of energy use in petroleum refineries to petroleum products implications for life-cycle energy use and emission inventory of petroleum transportation fuels. *International Journal for LCA*, pages 34–44, 2004.

[257] J. Lopez, A. Gomez, F. Aparicio, and J. Sanchez. Comparison of GHG emissions from diesel, biodiesel and natural gas refuse trucks of the city of madrid. *Applied Energy*, 86:610–615, 2009.

[258] F. Egolfopoulos, N. Hansen, Y. Ju, K. Kohse-Hoinghaus, C. Law, and F. Qi. Advances and challenges in laminar flame experiments and implications for combustion chemistry. *Progress in Energy and Combustion Science*, 43:36–67, 2014.